London South Bank University

School of Engineering

PhD Thesis

Digital Beamforming Techniques for Passive UHF RFID Tag Localization

Markus Cremer

A thesis submitted to London South Bank University in partial fulfilment of the requirements for the degree of *Doctor of Philosophy*

August 2016

Acknowledgements

This thesis represents the achievements of nearly six years of work at the London South Bank University (LSBU) and at the Signal Processing and Digital Communications Group of Cologne University of Applied Sciences (CUAS). I am grateful that I was given the opportunity to play a part in several research projects. The time at LSBU and CUAS has been challenging but also amazing and fulfilling. I have always enjoyed the working atmosphere that made me feel almost at home. This thesis is also a result of many experiences I have encountered at both universities, from dozens of remarkable individuals who I wish to acknowledge.

First and foremost, I would like to cordially thank my supervisor at LSBU, Dr. Anjum (Jim) Pervez. He has been supportive since the days I began working on this project and helped me to stay on an academical course through the years. I highly appreciate his patience and endurance with me, especially during the last few months. His advice has always been invaluable and I am grateful that he was able to solve all problems that stood in my way. I really enjoyed our travelling together and the time that I stayed in London.

My deepest heartfelt appreciation goes to Prof. Dr.-Ing. Uwe Dettmar, my supervisor at CUAS and my mentor. I am forever indebted to him for recognizing my potential earlier on when he supervised my master's thesis. Thank you for your invaluable advice, the motivational talks, the constructive feedback and the continuous encouragement. Without you, this thesis would never have become reality. I am very proud that I have been your first PhD student and I hope that many more will follow to benefit from your knowledge and your experience.

I owe a very important debt to Prof. Dr.-Ing. Rainer Kronberger who has been my advisor in all questions related to high-frequency technology and applications. His meticulous comments were an enormous help to me and his knowledge and experience have always encouraged me to give my best.

I would also like to express my gratitude to my whole supervisory team and to Prof. Dr. Klaus Becker, Vice President for Research at CUAS, for caring about my financial worries during the last years.

Special thanks also goes to the present and past members of the research groups at LSBU and CUAS for creating a healthy and vibrant working atmosphere during my time. Specifically, I would like to thank Carsten Hudasch, M.Sc., Dipl.-Ing. Thomas Knie, Dipl.-Ing. Roberto Leonardi, Robin Lerche, M.Sc., Dr. Oladimeji Onalaja, and Dipl.-Ing. Martin Seckler. Thank you for the fruitful discussions, the invaluable suggestions

and the warm encouragement. I will continue to cherish the fun, intense and often stressful times we have spent together for as long as I live.

I have greatly benefited from the excellent craftsmanship of the staff at the CUAS faculty workshop, Aaron Finkenthei and Michael Söntgerath, who have provided me with everything I needed for my experiments and prototypes. You always did a perfect job.

I would like to finish the acknowledgements with my home country Germany, where the most basic source of my life energy resides: my family. Their support has been unconditional during the last years and especially during the challenging PhD time. I have to express my gratitude in my native language, German:

Zunächst möchte ich meiner Mutter Anna-Maria Cremer herzlich dafür danken, dass sie mir durch ihre fortwährende Unterstützung meine akademische Laufbahn überhaupt erst ermöglicht hat. Ohne ihre Hilfe hätte ich meine Promotion nicht realisieren können. Meiner Schwester Melanie Kastenholz danke ich vor allem für ihre moralische Unterstützung in den schweren Phasen, die ich in der Promotionszeit durchlebt habe. Meiner Nichte Nina und meinem Neffen Jan danke ich für ihre Motivation während der letzten Jahre. Die Zeit, die ich trotz meiner Verpflichtungen für diese Arbeit mit ihnen verbringen dürfte, hat mir stets neue Kraft gegeben und mich an den Erfolg glauben lassen. Ich wünsche mir, dass Ihr meinem akademischen Weg eines Tages folgen werdet und Ihr den Erfolg in Eurem Leben haben werdet, den Ihr Euch wünscht! Ich danke ebenfalls den Familienmitgliedern, die leider meine Promotion bzw. die Endphase meiner Promotion nicht miterleben konnten: Meinem Vater Peter Cremer und Herrn Hans Richterich. Sie haben meine Ideen und Vorhaben immer unterstützt und mir klargemacht, dass ich alles schaffen kann, wenn ich hart arbeite und an mich glaube. Vielen Dank auch an alle Freunde und Bekannte, die Verständnis für meine begrenzte Zeit in den letzten Jahren hatten und trotzdem zu mir gestanden und mich fortwährend motiviert haben.

Ich danke Euch allen von Herzen!

Abstract

Radio-frequency identification (RFID) technology is on the way to substitute traditional bar codes in many fields of application. Especially the availability of passive ultra-high frequency (UHF) RFID transponders (or tags) in the frequency band between 860 MHz and 960 MHz has fostered the global application in supply chain management. However, the full potential of these systems will only be exploited if the identification of objects is complemented by accurate and robust localization.

Passive UHF RFID tags are cost-effective, very small, extremely lightweight, maintenance-free, rugged and can be produced as adhesive labels that can be attached to almost any object. Worldwide standards and frequency regulations have been established and a wide infrastructure of identification systems is operated today. However, the passive nature of the technology requires a simple communication protocol which results in two major limitations with respect to its use for localization purposes: the small signal bandwidth and the small allocated frequency bandwidth. In the presence of multipath reflections, these limitations reduce the achievable localization accuracy and reliability. Thus, new methods have to be found to realize passive UHF RFID localization systems which provide sufficient performance in typical multipath situations.

In this thesis, an enhanced transmission channel model for passive UHF RFID localization systems has been proposed which allows an accurate estimation of the channel behaviour to multipath. It has been used to design a novel simulation environment and to identify three solutions to minimize multipath interference: a) by varying the channel interface parameters, b) by applying diversity techniques, c) by installation of UHF absorbers. Based on the enhanced channel model, a new method for tag readability prediction with high reliability has been introduced. Furthermore, a novel way to rate the magnitude of multipath interference has been proposed. A digital receiver beamforming localization method has been presented which uses the Root MUSIC algorithm for angulation of a target tag and multipath reducing techniques for an optimum localization performance. A new multiangulation algorithm has been proposed to enable the application of diversity techniques. A novel transmitter beamforming localization approach has been presented which exploits the precisely defined response threshold of passive tags in order to achieve high robustness against multipath. The basic technique has been improved significantly with respect to angular accuracy and processing times. Novel experimental testbeds for receiver and transmitter beamforming have been designed, built and used for verification of the localization performance in real-world measurements.

All the improvements achieved contribute to an enhancement of the accuracy and especially the robustness of passive UHF RFID localization systems in multipath environments which is the main focus of this research.

Contents

List of Figures

List of Tables

Abbreviations

ACK	**Ack**nowledgement
ADC	**A**nalogue-to-**D**igital **C**onverter
AoA	**A**ngle-**o**f-**A**rrival
AoAct	**A**ngle-**o**f-**Act**ivation
ASK	**A**mplitude-**S**hift **K**eying
CAD	**C**omputer-**A**ided **D**esign
CUAS	**C**ologne **U**niversity of **A**pplied **S**ciences
CW	**C**ontinuous **W**ave
DAC	**D**igital-to-**A**nalogue **C**onverter
DECT	**D**igital **E**nhanced **C**ordless **T**elecommunications
DSP	**D**igital **S**ignal **P**rocessing
ECDF	**E**mpirical **C**umulative **D**istribution **F**unction
EIRP	**E**quivalent **I**sotropically **R**adiated **P**ower
EPC	**E**lectronic **P**roduct **C**ode
ERP	**E**ffective **R**adiated **P**ower
ESPRIT	**E**stimation of **S**ignal **P**arameters via **R**otational **I**nvariance **T**echniques
ETSI	**E**uropean **T**elecommunications **S**tandards **I**nstitute
FCC	**F**ederal **C**ommunications **C**ommission
FEKO	**Fe**ldberechnung für **K**örper mit beliebiger **O**berfläche (German for 'field calculations involving bodies of arbitrary shape')
FM	**F**requency **M**odulation
FQ	**F**ading **Q**uantification
FR4	**F**lame **R**etardant 4 (composite material)
GSM	**G**lobal **S**ystem for **M**obile Communications
GPS	**G**lobal **P**ositioning **S**ystem

IC	**I**ntegrated **C**ircuit
IEEE	**I**nstitute of **E**lectrical and **E**lectronics **E**ngineers
IET	The **I**nstitution of **E**ngineering and **T**echnology
INS	**I**nertial **N**avigation **S**ystem
IoT	**I**nternet **o**f **T**hings
IR	**I**nfra**r**ed
ISM	**I**ndustrial, **S**cientific and **M**edical Band
ISO	**I**nternational **O**rganization for **S**tandardization
LANDMARC	Location Identification Based on Dynamic Active RFID Calibration
LHCP	**L**eft **H**and **C**ircular **P**olarisation
LNA	**L**ow-**N**oise **A**mplifier
LO	**L**ocal **O**scillator
LOS	**L**ine-**o**f-**S**ight
LSBU	**L**ondon **S**outh **B**ank **U**niversity
MoM	**M**ethod **o**f **M**oments
MUSIC	**Mu**ltiple **Si**gnal **C**lassification
NLOS	**N**on **L**ine-**o**f-**S**ight
NP	**N**earest **P**oint Algorithm
PA	**P**ower **A**mplifier
PC	**P**ersonal **C**omputer
PIE	**P**ulse **I**nterval **E**ncoding
PoA	**P**hase-**o**f-**A**rrival
PVC	**Polyv**inyl **C**hloride
RADAR	**Ra**dio **D**etection **a**nd **R**anging
RF	**R**adio-**F**requency
RFID	**R**adio-**F**requency **ID**entification
RHCP	**R**ight **H**and **C**ircular **P**olarisation
RMS	**R**oot **M**ean **S**quare
RN16	**R**andom **N**umber, 16 Bit
RSS	**R**eceived **S**ignal **S**trength
SNR	**S**ignal-to-**N**oise **R**atio
TDoA	**T**ime-**D**ifference-**o**f-**A**rrival
ToA	**T**ime-**o**f-**A**rrival

TS	**T**echnical **S**pecification
μ**C**	**M**icro**c**ontroller
UHF	**U**ltra-**H**igh **F**requency
ULA	**U**niform **L**inear **A**rray
UMTS	**U**niversal **M**obile **T**elecommunications **S**ystem
US	**U**ltra**s**ound
USB	**U**niversal **S**erial **B**us
UWB	**U**ltra-**W**ide**b**and
WLAN	**W**ireless **L**ocal **A**rea **N**etwork
WSN	**W**ireless **S**ensor **N**etwork

In loving memory of my dad, dedicated to my family.

Chapter 1

Introduction

In the automation age, the demands for technologies that facilitate the spatial localization of objects and people have gained a significant degree of attention in industry, research and private life, in recent years [1–4]. Well-established technologies, such as the Global Positioning System (GPS) [5] are almost ubiquitous today and are indispensable in the modern society. They allow the localization and tracking of people and objects on a global scale and have found their way into various supply chain management applications [6]. With upcoming technologies like the Internet of Things (IoT) [7] and Industry 4.0 [8], the need for indoor localization systems with an accuracy in the decimetre-range seems a natural next step in this arena [9–11]. The popularity of localization systems like GPS is based on the fact that they are wireless and provide sufficient accuracy for the target applications. However, for indoor applications, the microwave frequency (satellite signals) used in GPS systems is blocked by walls and other objects which makes localization almost impossible [12]. Additionally, the achieved localization errors lie in a metre-range which is far too high for indoor applications. Not only the localization environment but also the localization targets are much smaller and their relative density with respect to the available space is much higher. The early approaches utilized existing infrastructures (e.g. Wireless Local Area Networks, WLAN) to realize indoor localization [13]. The main disadvantage was that the target devices needed to have an on-board power supply and sufficient processing capabilities. Furthermore, the active devices are generally more expensive and often large in size which limits their suitability for localization applications. The same is true for technologies like Ultra-Wideband (UWB) that were developed with high-accuracy indoor localization applications in mind [14].

Passive Ultra-High Frequency[1] (UHF) Radio-Frequency Identification (RFID) technology is well-established, reliable, cost-effective, maintenance-free, works indoor, and is widely used for identification and tracking in worldwide supply chain management applications [15]. Due to the success of passive UHF RFID systems for identification, global standards like the EPCglobal [16] (also standardized as ISO 18000-6c [17]) were introduced and global frequency regulations were established [18]. At the first glance, this technology seems to be the ideal candidate for wireless indoor localization systems. However, a deeper investigation reveals that the passive UHF RFID technology has two major limitations with respect to an application for localization: a) the small bandwidth of the signals transmitted for communication purposes which is defined in the relatively simple communication protocol EPCglobal [16], b) the small allocated frequency bandwidth of the signals which is defined by local regulation authorities [18]. As a consequence, the achievable localization accuracy, reliability, and robustness are limited [19]. The main focus of the work presented in this thesis is to investigate whether, despite the technological limitations of passive UHF RFID systems, it is possible to use passive UHF RFID transponders (or tags) for object localization with sufficient accuracy in real-world application scenarios.

In 1999, the term 'Internet of Things'was first mentioned by the British entrepreneur Kevin Ashton [20] and it is expected that, by 2020, it will consist of almost 50 billion objects [21]. The main goal of IoT is to interconnect devices, systems, services and the internet for global availability [22]. This is the basis for applications like the smart grid, the smart home or smart cities [22]. Industrial IoT, which is also called Industry 4.0, was introduced by the German government in 2011. It aims at interconnecting machines and goods in manufacturing in order to optimize mass production processes [23]. One important requirement in IoT and Industry 4.0 is the availability of location informtion, not only for goods and tools within the production process but also for people, e.g. in hazardous environments [11, 24, 25]. It is obvious that the bulk of localization applications can be found in indoor environments (warehouses, production halls, etc.). The first solution for indoor localization was to utilize the well-established WLAN technology in 2000 [13]. Due to various disadvantages as well as insufficient accuracy and reliability, other technologies like Bluetooth were also tested but with rather unsatisfying results [26]. In 2002, the use of Ultra-wideband systems was permitted by the Federal Communications Commission (FCC). Because of its high frequency bandwidth, this technology was thought to solve the indoor localization problem. However, like WLAN, it requires active target devices which are very complex, expensive and rather bulky. In addition, the need for maintenance of the active hardware (especially exchanging the batteries) excludes these technologies from mass production applications.

[1] Frequency range in RFID applications: 860 MHz - 960 MHz

Although they were developed for identification purposes, passive UHF RFID systems seem to fulfil all technological demands for localization applications. Today, RFID systems have substituted traditional barcodes in various fields of application that are primarily found in supply chain management. In comparison to barcodes, RFID transponders offer various benefits like the capability to identify multiple objects simultaneously over relatively long distances ($\leq$ 10 m) without the need for a line-of-sight (LOS) that have led to an explosive growth in the worldwide application of RFID technology [27].

The first use of the RFID principles for localization dates back to the LANDMARC system introduced in 2003 which uses active target devices [28]. A localization accuracy of approximately 1 m was achieved. Although research focused on finding techniques to improve the localization accuracy in RFID systems in the following years, no system could be realized that achieves sufficient accuracy and reliability in real-world application scenarios.

1.1 Wireless Localization Principles

In general, localization (or positioning) is the process of estimating the spatial location of a target, e.g. a box in a warehouse. The most important performance criterion of localization systems is the localization accuracy (or localization error) which is the Euclidean Distance between the estimated target position and the actual target position. Other requirements for practical application are the target size, the target cost, or the maximum localization range.

Localization techniques, in general, can be categorized into two basic groups: target distance estimation (lateration) and target direction estimation (angulation). In a passive UHF RFID localization system, this target can be the interrogator or the tag. For clarity reasons, the following explanation of lateration and angulation assumes a target tag but is also valid for a target interrogator.

In lateration approaches, the interrogator-to-tag distances are estimated from different interrogator locations, e.g three interrogator locations in a trilateration system figure 1.1(a)). For two-dimensional localization of a target tag T, at least three interrogators I_1, I_2, I_3 are required that estimate the three distances to the tag d_1, d_2, d_3. From these distances and the interrogator positions, three circles can be constructed that intersect in the tag position.

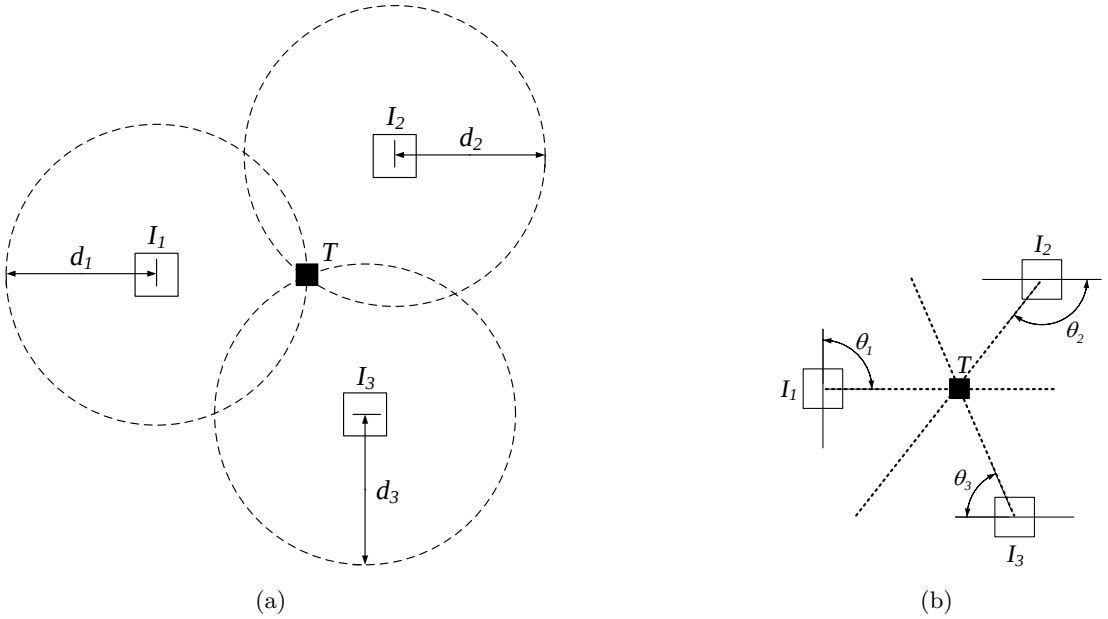

FIGURE 1.1: Localization principles in an RFID system:
(a) Trilateration, (b) Triangulation

For angulation in an RFID system, at least two interrogators are required for two-dimensional target tag localization. For example, in a triangulation system figure 1.1(b)), three interrogators estimate the tag direction angles $\theta_1, \theta_2, \theta_3$ (also referred to as angles-of-arrival, AoA). From these angles and the interrogator positions, straight lines can be constructed that intersect in the tag location. Because the lateration technique requires an additional interrogator position, the angulation technique is more economic with regard to the localization system cost and complexity.

Wireless localization systems, in general, evaluate the parameters of the received wireless signals at a base station to estimate the target device distance or direction. The following measurements are utilized:

- Received signal power level (Received Signal Strength, RSS)
- Received signal phase (Phase-of-Arrival, PoA)
- Received signal time or time-difference (Time-of-Arrival, ToA, or Time-Difference-of-Arrival, TDoA)

However, the passive UHF RFID technology and the indoor application scenarios introduce the following limitations to possible signal measurements. To travel the distance of the maximum communication range of passive UHF RFID systems (10 m), a wireless signal needs approximately $t_{\max} = 33$ ns. Because the measurement of such short time durations (ToA) or even time-differences (TDoA) requires complex and expensive measurement equipment in addition to a high signal bandwidth, this technique cannot be used in passive UHF RFID localization systems [29].

RSS-based lateration approaches estimate the interrogator-to-tag distance d from the measured power $P_{\mathrm{Rx,int}}$ of a received tag signal at the interrogator location. Using the known transmitter power of the interrogator $P_{\mathrm{Tx,int}}$, an equation for d can be derived from the Friis Transmission Equation [30]:

$$d = \frac{\lambda}{4\pi} \sqrt[4]{\frac{P_{\mathrm{Tx,int}} G_{\mathrm{int}}^2 G_{\mathrm{tag}}^2}{P_{\mathrm{Rx,int}}}}, \tag{1.1}$$

where λ is the signal wavelength, G_{int} is the gain of the interrogator antenna and G_{tag} is the gain of the tag antenna.

PoA-based localization approaches measure the phase, $\varphi_{\mathrm{Rx,int}}$, of a received target tag signal at the interrogator location to estimate the tag distance d. Assuming that the tag transmits with an initial phase of $\varphi_{\mathrm{Tx,tag}} = 0°$, d is calculated as

$$d = \varphi_{\mathrm{Rx,int}} \frac{c}{2\pi f}, \tag{1.2}$$

where c is the speed of light and f is the signal frequency. It must be noted that distinct values for $\varphi_{\mathrm{Rx,int}}$ are only measured for interrogator-to-tag distances in a range of $0 \leq d < \lambda/2$ (phase ambiguity).

The introduction of the basic localization approaches that can be utilized in passive UHF RFID systems presented above was limited to two-dimensional techniques. However, in all cases, an extension to the third dimension is possible by using the same principles. In lateration approaches, three-dimensional spheres would be constructed from the estimated interrogator-to-tag distances. With four available interrogator positions, these spheres intersect in the tag position. For the angulation approach two interrogator positions suffice for three-dimensional localization. To find the target position, the target direction is first estimated in the azimuth plane and then estimated in the elevation plane. Both tag directions can then be combined to calculate the three-dimensional target location.

The decision whether to use a two- or three-dimensional localization system depends on the targeted application (three-dimensional if an estimation of the target elevation is required). However, the previously introduced technological limitations of passive UHF RFID systems equally effect both system types and two-dimensional localization has a lower degree of complexity. Therefore, the work presented in this thesis focuses on two-dimensional localization.

1.2 Motivations and Achievements

The main focus of this research is to investigate the limitations of a practical application of passive UHF RFID localization systems in typical multipath environments and to find methods which improve the localization performance to a level which is sufficient for the targeted applications.

There are numerous passive UHF RFID localization systems using RSS-based, phase-based or biparameter-based signal evaluation for lateration or angulation of a target tag. RSS-based systems require a dedicated infrastructure of reference tags or interrogators and the development of a reference database which makes them rather unattractive for practical application [31–33]. Phase-based methods are proposed to relax the limitations of RSS-based methods but their localization range is limited by the phase ambiguity [34, 35]. Hybrid systems are capable of achieving a higher coverage range than phase-based approaches and higher accuracies than RSS-based approaches because they combine the passive UHF RFID technology with other wireless technologies (e.g. WLAN or cameras) [36, 37]. However, the system complexity, cost and processing times are highly increased compared to the above methods. Other systems use a-priori knowledge (e.g. movement of a target in a restricted and predefined area) to improve the localization accuracy but they are limited to one specific application scenario [38, 39]. To overcome the limitations of power- and phase-based localization systems, biparameter-based approaches are proposed which generally provide a high angular accuracy for target tag direction estimation [40, 41]. Amongst this class of techniques, digital receiver beamforming and digital transmitter beamforming provide the highest angular accuracy [42, 43] and are therefore identified as the most promising candidates for an application in passive UHF RFID localization.

Supposing a decision has been made to carry out target tag localization based on digital beamforming techniques. The widely used receiver beamforming algorithms MUSIC (Multiple Signal Classification) and ESPRIT (Estimation of Signal Parameter via Rotational Invariance Techniques) have a very high computational complexity and require high processing times [44]. The Root MUSIC algorithm is a variation of MUSIC and has the advantage of achieving the same high degree of angular resolution with reduced processing times [45]. It has not been used in passive UHF RFID localization systems because it is restricted to two-dimensional localization problems. However, it appears that the Root MUSIC approach is well suited to achieve sufficient localization accuracy in typical application scenarios. Digital transmitter beamforming localization techniques have not been used to date because they require very complex signal generation devices [42]. However, since they provide the same high angular accuracy as the receiver

beamforming, the notion of applying transmitter beamforming to passive UHF RFID localization seems to have a high potential and is worthy of further investigation.

In indoor application environments, signal reflections at walls or other objects generate multiple signal paths (multipath) which interfere at the interrogator. Under these conditions, a precise target tag localization can only be achieved by an evaluation of the tag's line-of-sight receiver signal. However, the limited available signal and frequency bandwidths of the passive UHF RFID technology which are defined in the protocols used and the local regulations incapacitate the interrogator to resolve the line-of-sight signal from multipath reflections [46]. Therefore, the achievable localization accuracy is highly reduced.

An accurate transmission channel model is required for an accurate estimation of the channel behaviour to multipath signals in localization systems. A statistical channel model can be used but has the disadvantage of requiring a large amount of complex, time-consuming measurements and being only valid for specific environments [47, 48]. The deterministic full-wave analysis or the brute-force ray-tracing approach deliver very high estimation accuracies but at the expense of substantial computational effort [49]. It appears that deterministic models which are based on a modified version of the classical Friis Transmission Equation best suited for application because they highly reduce the computational load [50]. However, it is shown that they achieve only a coarse approximation of the signal parameters in real-world situations because they include only a limited consideration of the channel and the channel interface (i.e. the antenna) characteristics. Several enhancements of the modified Friis model have been proposed to achieve a better estimation accuracy: the consideration of a higher number of signal paths, complex reflection coefficients, antenna polarizations, antenna orientations as well as three-dimensional antenna gain and phase pattern. It is shown that the enhanced transmission channel model provides a very high estimation accuracy of the real-world signal parameters compared to the modified Friis model. Furthermore, the enhanced channel model provides a low computational complexity and low computing times compared to the full-wave analysis or the brute-force ray-tracing. A further benefit of the enhanced channel model is the possibility to reliably predict the tag readability in identification applications which is confirmed by real-world measurements.

In order to address the previously mentioned reduction of the achievable localization accuracy caused by multipath, the multipath interference has to be minimized. Since the characteristics of the wireless transmission channel in the space between the tag antenna and the interrogator antenna are fixed, only the parameters of the channel interfaces seem to offer a starting point for an investigation of multipath reducing techniques. Variations of the interrogator and tag antenna parameters, well-established

diversity combining techniques [51] and the installation of UHF absorbers should be able to highly reduce the effects of multipath. Consequently, directional patch antennas, circular polarization, different antenna orientations, frequency diversity, spatial diversity and polarization diversity have been proposed. It is shown that directional antennas and circular polarization highly reduce the effects of multipath. However, both techniques reduce possible applications of the localization system because they require large and costly antennas. A change of the antenna orientation changes the multipath characteristic but does not reduce multipath interference. The application of frequency diversity is highly effective but restricted by the available system frequency bandwidth. The use of spatial diversity is highly beneficial and requires a minimum antenna displacement on the order of the system wavelength which is easily manageable. Polarization diversity achieves a reduction of multipath interference but is not suited for practical application because it requires additional antennas. The installation of high-frequency absorbers is highly effective because certain reflection paths are cancelled out but it is only practically feasible in small localization areas. One issue associated with the implementation of diversity techniques is the availability of a multiangulation algorithm which can be used on any number of estimated target tag directions, has a low computational complexity and can handle complicated constellations (e.g. parallel tag direction lines which do not intercept). A new multiangulation algorithm 'Nearest Point'has been proposed and it is shown to be a reliable tool for any diversity localization system.

The digital receiver beamforming localization technique Root MUSIC has been identified as one candidate for passive UHF RFID localization with sufficient localization accuracy and low processing times. Since it has not been used before, a principle localization approach has to be designed. The tag direction information which is provided by the Root MUSIC algorithm and the nearest point multiangulation algorithm should be ideally suited to implement a classical angulation system. An angle-of-arrival (AoA) angulation approach is presented and its effectiveness is demonstrated in simulations. However, further simulations confirm the above mentioned degradation of the localization accuracy in the presence of multipath. The previously introduced techniques for a reduction of multipath interference should increase the localization accuracy in multipath situations. Therefore, the application of directional antennas, circular polarization, different antenna orientations, frequency diversity, spatial diversity and reflection cancellation has been proposed. Simulations show that all of the above multipath reducing techniques increase the achievable localization accuracy. As result, an optimum receiver beamforming localization system with respect to multipath robustness and achievable localization accuracy has been proposed. In order to verify the above simulation results in real-world measurements, an experimental receiver beamforming localization testbed is required but commercially available interrogators do not provide received signal phase

information. Therefore, a novel experimental testbed has been developed and built which implements the optimum receiver beamforming localization approach in a novel 'AoA unit'. Measurements in multiple real-world scenarios and under severe multipath conditions show that the AoA localization approach achieves a highly improved localization accuracy compared to existing passive UHF RFID localization system.

The digital transmitter beamforming was previously identified as a second candidate for application in passive UHF RFID localization systems. One major challenge is the design of a feasible angulation technique because digital transmitter beamforming has never been used before. Due to its computational simplicity and ease of practical implementation, the idea of using RSS-measurements of the target tag seems to be highly attractive. An RSS-based angulation technique has been proposed but it is shown that the achievable tag direction estimation accuracy is severely degraded by multipath interference and that multipath reducing techniques are not able to sufficiently improve the situation. A tag angle estimation process which exploits the precisely defined response threshold of passive UHF RFID tags using very simple tag readability measurements should improve the robustness against multipath because it requires only a minimum interrogator transmitter power, thereby assuring that the readability is caused by the line-of-sight interrogator transmitter signal only. A new transmitter beamforming angulation approach has been proposed (angle-of-activation, AoAct). Simulations show that AoAct provides better robustness against multipath interference and improved direction estimation accuracy than the RSS-based approach. However, the simulations also reveal high processing times and the potential for further angular accuracy improvement. Various enhancements of the basic AoAct approach such as the consideration of unsymmetrical beampattern or an optimized algorithm for finding the appropriate interrogator transmitter power have been proposed and their superior performance is demonstrated in simulations. For a practical verification of the AoAct localization performance, an experimental testbed is required but off-the-shelf interrogators do not provide beamforming capabilities. A novel experimental testbed is designed and built which is based on very cost-effective components and achieves a very high angular beam pattern accuracy. Localization measurements in different real-world scenarios show a better mean localization performance compared to the receiver beamforming approach and compared to any other existing passive UHF RFID localization system, especially in severe multipath situations. However, compared to the receiver beamforming system, the AoAct system requires higher overall processing times.

The main aim of this research, i.e. the realization of a passive UHF RFID localization system which achieves sufficient localization accuracy in typical multipath application scenarios, has been fully accomplished. Two different passive UHF RFID localization systems have been designed, developed and simulated as well as tested in real-world

measurements under severe multipath conditions. All results confirm the superior localization accuracy of the beamforming techniques compared to existing localization systems. For high-accuracy applications, transmitter beamforming should be favoured, whereas receiver beamforming is more appropriate for applications where fast response times are required.

1.3 Thesis Structure

Following the introduction chapter, a literature review of localization systems which are based on well-established wireless technologies is presented in chapter 2. The functionality of the localization approaches is explained and the benefits of the passive UHF RFID technology are highlighted. The operational principles of passive UHF RFID systems are explained in detail and the technological limitations pointed out. Existing passive UHF RFID localization systems, which can be classified in three categories (power-based, phase-based and biparameter based) are presented and their practical application and drawbacks are discussed. The benefits of the biparameter-based localization techniques, namely receiver beamforming and transmitter beamforming are described and the theoretical principles of operation introduced. The advantages of the Root MUSIC algorithm and the digital transmitter beamforming are explained. Finally, existing statistical and deterministic transmission channel models are discussed in detail. The ability of the modified Friis-based modelling approach to overcome the limitations of other deterministic approaches is pointed out.

In chapter 3, the performance of a number of existing modified Friis-based channel models is compared by simulations. For a close estimation of the real-world situation in localization systems, a very accurate estimation of the channel behaviour to multipath signals is required. Thus, an enhanced channel model is presented which considers important parameters of the channel and the channel interfaces. The superior performance of the enhanced channel model is demonstrated by comparison of simulations with measurements. Based on the enhanced model, the influence of multipath interference on the signal power and phase is shown and a novel simulation environment developed. Finally, the quality of tag readability predictions using the new simulation environment is tested in real-world measurements.

In chapter 4, a new equation to rate the magnitude of multipath effects, referred to as the 'Fading Quantification'(FQ) is derived. FQ is then used as the quality criterion for multipath interference. Three solutions to minimize the effects of multipath interference are presented: a) by varying the channel interface parameters, b) by applying diversity

techniques, c) by installation of UHF absorbers. The performance of these techniques is compared by simulations in a typical application scenario.

A digital receiver beamforming localization approach ('AoA') which is based on the Root MUSIC algorithm is presented in chapter 5. The localization principle is explained and the localization performance analysed by simulations. The degradation of the achievable localization accuracy by multipath interference is demonstrated and techniques for the reduction of multipath interference are applied. The effects on the achievable localization accuracy are compared by simulations in a typical localization scenario. A new multiangulation algorithm ('Nearest Point') is presented to overcome the limitations of existing angulation algorithms. For the verification of the localization performance in real-world measurements, a novel experimental testbed is established. The development of a novel antenna array which is required for the testbed is described in detail. Finally, real-world measurements in different multipath scenarios are utilized to investigate the localization performance of the enhanced receiver beamforming technique.

Chapter 6 first proposes a transmitter beamforming localization principle which is based on RSS measurements. The reduced localization performance compared to the receiver beamforming technique is revealed by simulations. Therefore, a novel localization approach is proposed which utilizes the very precisely defined response threshold of passive tags ('AoAct'). The technique is explained in detail and analysed in simulations which show further possibilities for improvement of the angular accuracy and processing times. Thus, several enhancements of the basic technique are developed and their performance compared by simulations. The improved AoAct localization approach is implemented in the design of a novel experimental testbed. The construction ideas and the physical realizations of the testbed are explained. The achievable AoAct localization performance is investigated in multiple real-world measurements and compared with the receiver beamforming technique.

Finally, chapter 7 summarizes the research presented in each chapter and the overall achievements of the project. Multiple directions are recommended for future work.

1.4 Published Work

Conference Papers

1. Markus Cremer, Anjum Pervez, Uwe Dettmar, Thomas Knie, and Rainer Kronberger, **"Using a Circularly Polarized Patch Antenna to Optimize the Passive UHF RFID Indoor Channel"**, in *IEEE International Symposium on Antennas and Propagation*, Orlando, Florida, July 2013, pp. 1730-1731.

2. Markus Cremer, Anjum Pervez, Uwe Dettmar, Thomas Knie, and Rainer Kronberger, **"An Improved Channel Model for Passive UHF RFID Systems"**, in *IEEE International Conference on RFID Technologies and Applications*, Johor Bahru, Malaysia, September 2013, pp. 1-7.

3. Uwe Dettmar, Rainer Kronberger, Thomas Knie, Markus Cremer, and Carsten Hudasch, **"Passive UHF RFID Transponders for Switching and Controlling"**, in *IEEE International Conference on RFID-Technologies and Applications*, Johor Bahru, Malaysia, September 2013, pp. 1-4.

4. Markus Cremer, Anjum Pervez, Uwe Dettmar, Thomas Knie, and Rainer Kronberger, **"Improved UHF RFID Localization Accuracy Using Circularly Polarized Antennas"**, in *IEEE International Conference on RFID-Technologies and Applications*, Tampere, Finland, September 2014, pp. 175-180.

5. Markus Cremer, Anjum Pervez, Uwe Dettmar, Carsten Hudasch, Thomas Knie, Rainer Kronberger, and Robin Lerche, **"Transmit Beamforming for Angle-of-Activation (AoAct) Estimation in Passive UHF RFID Systems"**, in *IEEE International Conference on RFID-Technologies and Applications*, Tokyo, Japan, September 2015, pp. 1-7.

6. Rainer Kronberger, Uwe Dettmar, Carsten Hudasch, Robin Lerche, Markus Cremer, and Anjum Pervez, **"Multichannel Digital Transmit Beamforming Experiments for RFID Tag Localization"**, in *International EURASIP Workshop on RFID Technology*, Rosenheim, Germany, October 2015, pp. 126-131.

7. Rainer Kronberger, Uwe Dettmar, Carsten Hudasch, Robin Lerche, Markus Cremer, and Anjum Pervez, **"A Transmitter Beamforming System for the Localization of Passive RFID Tags"**, in *IEEE Radio and Wireless Week*, Austin, Texas, January 2016, pp. 252-255.

Journal Papers

1. Markus Cremer, Uwe Dettmar, Rainer Kronberger, and Anjum Pervez, **"Modeling of the Passive UHF RFID Multipath Channel for Tag Read Region Estimation"**, in *International Journal of Wireless Information Networks*, Springer, Volume 22, Issue 3, September 2015, pp. 188-204.

2. Markus Cremer, Uwe Dettmar, Carsten Hudasch, Rainer Kronberger, Robin Lerche, and Anjum Pervez, **"Measurement Results for Multichannel Transmit Beamforming Tag Direction Detection in Passive Ultra-High Frequency Radio-Frequency Identification Systems"**, in *IET Electronics Letters*, Volume 51, Issue 21, October 2015, pp. 1632-1634.

3. Markus Cremer, Uwe Dettmar, Carsten Hudasch, Rainer Kronberger, Robin Lerche, and Anjum Pervez, **"Localization of Passive UHF RFID Tags Using the AoAct Transmitter Beamforming Technique"**, in *IEEE Sensors Journal*, Volume 16, Issue 6, March 2016, pp. 1762-1771.

Publications Before PhD Registration

1. Markus Cremer, Salah Azzouzi, Uwe Dettmar, Thomas Knie, Rainer Kronberger, and Roberto Leonardi, **"UHF RFID Localization System Based on a Phased Array Antenna"**, in *IEEE International Symposium on Antennas and Propagation*, Spokane, Washington, July 2011, pp. 525–528.

2. Markus Cremer, Salah Azzouzi, Uwe Dettmar, Rainer Kronberger, and Thomas Knie, **"New Measurement Results for the Localization of UHF RFID Transponders Using an Angle of Arrival (AoA) Approach"**, in *IEEE International Conference on RFID*, Orlando, Florida, April 2011, pp. 91–97.

3. Markus Cremer, Salah Azzouzi, Uwe Dettmar, Thomas Knie, and Rainer Kronberger, **"Improved AoA Based Localization of UHF RFID Tags Using Spatial Diversity"**, in *IEEE International Conference on RFID-Technologies and Applications*, Sitges, Spain, September 2011, pp. 174–180.

4. Rainer Kronberger, Roberto Leonardi, Thomas Knie, Uwe Dettmar, Markus Cremer, and Salah Azzouzi, **"Design and Measurement Results of an UHF Localization System"**, in *4th International Symposium on Applied Sciences in Biomedical and Communication Technologies*, Barcelona, Spain, October 2011, pp. 1-5.

1.5 Contributions

Amongst others, the main contributions of this work are as follows:

- An enhanced transmission channel model for passive UHF RFID systems which considers multiple signal paths, complex reflection coefficients and channel interface parameters such as three-dimensional antenna gain and phase pattern. It allows a reliable simulation of the signal parameters (i.e. power and phase) in any passive UHF RFID system setup and any indoor application scenario with low computing times.
- A reliable method for predicting read and no-read zones in any passive UHF RFID system setup and any indoor application scenario. It can be used in preliminary system designs to maximize tag read zones and to optimize the tag readability in identification systems.
- An investigation of techniques for a minimization of multipath effects in passive UHF RFID systems: frequency diversity, spatial diversity, polarization diversity, optimized antenna types, optimized antenna polarisations and reflection cancellation. These techniques help to improve the localization accuracy in passive UHF RFID systems.
- A Root-MUSIC-based digital receiver beamforming localization approach for passive UHF RFID systems that achieves a high localization accuracy in real-world application scenarios. It has low complexity, low computing times and can be implemented in low-cost hardware. Due to the application of techniques for a reduction of multipath effects, it has a high reliability, even in severe multipath environments.
- A new multiangulation algorithm that can be used on any number of measured target directions and enables the use of diversity techniques. It can handle complicated situations such as parallel target tag direction lines.
- A digital transmitter beamforming localization approach for passive UHF RFID systems that allows the generation of high-accuracy antenna array gain patterns. It utilizes the very defined sensitivity of passive UHF RFID tags and achieves a high localization accuracy and reliability, even in severe multipath environments.

- The design and implementation of various hardware devices for passive UHF RFID localization systems:
  - A three-element, circularly polarized patch antenna array for the European UHF RFID frequency range. It has a high gain, a low axial ratio and a small size.
  - A low-cost hardware unit that implements the new digital receiver beamforming localization approach. It is composed of off-the-shelf components and shows a high tag direction estimation accuracy in real-world measurements and very low processing times.
  - A low-cost, small-size hardware unit that implements the new digital transmitter beamforming localization approach. It is composed from off-the-shelf components and shows a high tag direction estimation accuracy in real-world measurements.
  - All devices are developed up to a mass-production-ready state.

Chapter 2

Related Work

In this chapter, a review of the existing localization techniques, with particular emphasis on passive UHF RFID based localization methods, is presented. The performance criterion for these systems is highly application dependent. However, the most important performance measures are the localization accuracy, the cost (device cost as well as maintenance and setup costs), the required infrastructure (base stations, access points and the provision for reference measurements), the update rate (the number of consecutive localization measurements per second) and the possible number of localization targets in a given application. It is argued that passive UHF RFID localization systems have the potential to overcome most of the limitations of the other localization technologies, particularly, for indoor localization applications.

The concept and operational principles of passive UHF RFID localization are explained. Three different approaches (power-based, phase-based and biparameter-based) for system realization are discussed and it is concluded that two biparameter-based approaches, namely, receiver beamforming and transmitter beamforming are the most promising techniques to realize passive UHF RFID localization systems that provide sufficient accuracy in typical application scenarios.

The communication link between an interrogator and a tag in a passive UHF RFID system constitutes a wireless transmission channel. The transmission characteristics of the channel are commonly described either statistically or deterministically. The existing models for both approaches are discussed and it is concluded that a deterministic approach would be the preferred channel model for passive UHF RFID localization systems.

2.1 Existing Localization Systems

Existing localization systems are based on a wide range of technologies that include:

Image-based techniques that rely on multiple cameras distributed over the space of interest [52–59]. These systems have a coverage range of 10 m, update rates of up to 50 Hz and do provide high localization accuracy (in millimetre-range) but their accuracy depends on the distance from the target. The main disadvantage of image-based approaches is the need for an elaborate infrastructure that causes high system cost.

Inertial Navigation Systems (INS) use specific sensors like accelerometers to measure the velocity and orientation of moving objects and to estimate their relative location [60]. For the initial positioning, tracking applications and multiple targets, an external infrastructure is needed, such as GPS and others [61–65]. Due to error accumulation, the localization accuracy range lies between 0.1% and 20% of the travelled target distance and also depends on the possible update rate of the absolute position [63, 66, 67]. The sensors used in INS are rather bulky, which is a limiting factor for their applications.

Magnetic localization systems use two different measurement techniques: a) tracking of the phase relationship between the electrical and magnetic fields of the received target signals, b) measurement of the magnetic flux density. The former technique needs large antennas and its range is limited by phase ambiguities and the latter requires a local infrastructure of permanent magnets or coils and complex mathematical calculations. Neither of the two techniques necessitates line-of-sight operation or is affected by multipath [67, 68]. These techniques are capable of achieving a maximum coverage of up to 20 m, an update rate of 240 Hz and a localization accuracy of several centimetres. The main drawback is that magnetic localization systems are unable to identify individual targets [69].

Infrared (IR) localization systems require a cost-intensive local infrastructure of IR receivers or thermal cameras and do not have target identification capabilities [70–72]. Although IR signals have the advantage of being invisible to the human eye, they are not able to penetrate opaque materials such as walls or other objects in the area of interest which limits their application. The update rates are high (max. 50 Hz) and a maximum localization accuracy in the decimetre-range is reported depending on the localization method used [71, 73]. Natural sources of infrared light like the sun or human bodies compromise the localization performance but the main disadvantage is the limited coverage of only 5 m.

Localization systems that use ultrasound (US) sensors achieve an accuracy in the centimetre range (dependent on the positioning accuracy of receivers in the localization environment), an operational range of 10 m and a maximum update rate of 30 Hz [74–77]. They are prone to be influenced by sounds in the localization environment, multipath, and the signal Doppler-shift. The identification of single localization targets is not possible and signal superposition makes a localization of multiple targets almost impossible [74, 75]. The use of audio frequencies has been proposed [78], but these frequencies suffer more severely from the above effects.

Due to low receiver sensitivity and signal attenuation caused by walls and other objects, GPS systems are not suitable for indoor localization applications. High sensitivity GPS localization systems seem unattractive for indoor applications as they are highly complex and only achieve a localization accuracy of 10 m or less [79–81]. The use of open frequency bands e.g. ISM (Industrial, Scientific and Medical Band) for transmission of GPS-like signals needs an infrastructure of local base stations [82, 83]. Other disadvantages of GPS and GPS-like systems are the bulky target hardware and the absence of a return channel that would allow target identification.

The operation of WLAN-based localization systems is cost-effective because the widely available infrastructure of base stations (access points, routers, etc.) and mobile targets (laptops, mobile phones, etc.) can be utilized [84–93]. Another advantage is the high coverage (up to 50 m) and the fact that no line-of-sight to the target is needed. However, since all WLAN-based localization approaches use RSS measurements, their accuracy deteriorates because of: multipath effects (e.g. fast fading), the low density of access points and inconsistent measurement values due to variations in equipment supplied by different vendors [91, 94]. The maximum achieved localization accuracy is only one metre and the processing times lie in the range of several seconds [94–96].

Ultra-wideband localization systems use the time-of-arrival technique and nano-second signal pulses. The high resolution in time allows a high accuracy in distance estimation and localization that lies in the centimetre range [97–100]. Another advantage is the ability to isolate the target's line-of-sight signal from reflections, thus achieving an excellent multipath suppression. The high bandwidth also helps to minimize interference from other wireless systems [101, 102]. Other features include: high update rates of more than 100 Hz, large coverage (up to 50 m), target identification capabilities and low power consumption. On the minus side, UWB localization systems are complex, cost-intensive and need large broadband antennas as well as a dedicated local transmitter-receiver infrastructure [103].

Bluetooth and ZigBee localization systems utilize the open ISM band which makes them vulnerable to interfering signals from external other systems in the vicinity that operate

in the ISM band (e.g. WLAN). ZigBee uses RSS-based distance estimation that is highly prone to be influenced by multipath effects and thus only achieves low accuracies in the metre range [104, 105]. The maximum coverage of 30 m is relatively high but the update time of 5 s is very low. Although Bluetooth devices are of low-power and of low-cost, the cost for the overall infrastructure is high. Furthermore, the achievable localization accuracy is 4 m or less [106, 107]. The coverage is limited to 10 m and the update time to several seconds (rather low). Bluetooth as well as ZigBee are able to identify individual localization targets but the size and structure of the target hardware limit possible applications.

Localization systems that are based on the Digital Enhanced Cordless Technology (DECT), Digital Television signals, FM radio signals or cellular networks (e.g. GSM[1] or UMTS[2]) benefit from the existing infrastructure of base stations and cost-effective target devices [108–111]. Although various lateration and angulation approaches have been used, signal attenuation makes the indoor localization process difficult and allows only low accuracies in the metre-range. The coverage is very high and ranges from 500 m for DECT to 100 km for digital television. In Power Line Positioning, low frequency signals are modulated onto the existing power lines in a building [112, 113]. The maximum coverage area and the number of localization targets are very limited, other electrical devices deteriorate the localization signals and the maximum achieved accuracy is only one metre. The capacitance between multiple floor tiles or the force on single tiles is measured to localize persons within a room [114, 115]. A special, cost-intensive preparation of the environment with a high number of interconnected sensors is necessary and the identification of specific targets is not possible. The light of fluorescent lamps is modulated with data signals to localize targets that are equipped with light sensors [116]. It requires a constant connection to a database containing the lamp coordinates using WLAN or other technologies and a line-of-sight operation.

The use of active RFID technology in localization systems was first introduced in 2003 [28]. The proposed localization system, referred to as 'Location Identification Based on Dynamic Active RFID Calibration'(LANDMARC) deployed active target tags and reference tags in localization environment. In this system, the RSS from the target is measured and compared with reference RSS values obtained from the reference tags. From this comparison, the distance between the target in question and the interrogator is estimated. The process takes about 7.5 s to execute and achieves a mean accuracy in the range of 1 - 2 m. Further improvements were made in the original LANDMARC system [81, 117–121] which achieved a localization accuracy of 0.8 m, but at the expense of very high system complexity. Active RFID localization systems offer a high coverage

[1] Global System for Mobile Communications
[2] Universal Mobile Telecommunications System

of up to 100 m and a relatively high update rate of 10 Hz [122–126]. The localization methods commonly used in these systems are RSS-based, consequently they suffer from multipath effects which tend to limit their localization accuracy [19, 124]. The main advantages are the target identification capabilities and the low power consumption of RFID tags.

The growing interest in indoors applications of localization systems led to the notion of the use of passive UHF RFID technology for localization. The main advantage is the availability of passive UHF RFID tags as adhesive labels that are small, extremely light, rugged and cost-effective. Furthermore, they can be attached to almost any object and need no maintenance. In addition, the ability to simultaneously communicate with a large number of targets, without the need for line-of-sight communication, and the available identification capabilities are the other useful features offered by the passive UHF RFID technology.

On the other hand, the passive UHF RFID technology does have a number of limitations. Passive tags do not have an on-board energy source and therefore power is provided by a remote interrogator. This limits on-board computational and signal processing capabilities of the tags. Consequently, signal processing is carried out at the interrogator on the basis of return signals from the tag that is being interrogated.

However, on balance, passive UHF RFID technology seems to offer an ideal solution for low-cost and high density indoor localization system applications.

The first passive UHF RFID localization system was introduced in 2006 [127]. This system uses interrogator antennas with rotation abilities, a variable interrogator transmitter power and an evaluation of the tag readability to determine the target direction and to angulate its position (similar to the AoA technique introduced in section 1.1). This complex approach requires a high processing time and achieves a relatively low mean localization accuracy of 0.68 m.

Numerous passive UHF RFID localization system designs, with the aim to improve localization accuracy, have been proposed over the past decade. A maximum accuracy in the centimetre range has been reported with experiments conducted in idealized environments (reduced or no multipath), using very small testbeds or over very short range [128–131]. In more realistic experiments, an accuracy between 15 cm and 60 cm is achieved with a coverage of up to 10 m and an update rate up to 10 Hz [35, 132–135].

A more detailed overview on all existing indoor localization systems can be found in [103].

2.2 Operational Principles of Passive UHF RFID Systems

An RFID system consists of an interrogator (or reader), a connectionless data carrier called transponder (or tag) and interrogator and tag antennas. Typically, the tag antenna is physically integrated with the tag IC (a special silicon Integrated Circuit) while the interrogator antenna is isolated from the interrogator and electrical connection is provided via a connecting cable. The tag IC stores a worldwide unique identification number, the Electronic Product Code (EPC). Each communication cycle is handled by the interrogator in accordance to the EPCglobal Generation 2 Class 1 protocol [16] that utilizes a country-specific frequency band in the range between 860 MHz and 960 MHz [18] (e.g. in Europe: 865.6 MHz - 867.6 MHz). Also, the maximum interrogator transmitter power is specified by local regulations [18] (e.g. 2 W Effective Radiated Power, ERP, in Europe). In most cases, the aim is to read the EPC from one or multiple tags in the communication range of the interrogator but it is also possible to read or write internal register data of the tag IC. Figure 2.1 shows the basic communication cycle between the interrogator and the tag as it is defined in the EPCglobal protocol.

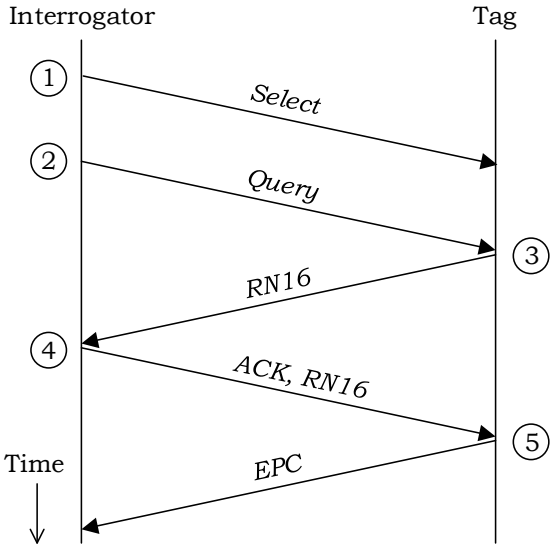

FIGURE 2.1: Basic EPCglobal communication cycle

Since the passive tag draws its energy from the transmitted interrogator signal (modulated data signal or sinusoidal signal), it stays deactivated until the interrogator initiates the communication cycle with a Select command ①. Through this command, single tags can be addressed with their full EPC, a limited group of tags can be addressed with a partial EPC or all tags in range can be addressed. In the two latter cases, the tags are assigned to different time slots by using random numbers so that only one tag communicates with the interrogator at a time (anti-collision protocol). To transmit data (especially commands) to the tag, the interrogator uses Pulse Interval Encoding (PIE)

and digital Amplitude Shift Keying (ASK) with a modulation depth of 90% at a constant bit rate between 26.7 kBit/s and 128 kBit/s. Following the Select phase ①, the interrogator transmits a Query command on which only the addressed tag or the tag that is assigned to the current time slot reacts ②. This tag replies to the interrogator's Query command with a 16-bit random number (RN16) that is used to identify the tag in the following process ③. During this response phase, the tag is powered by a sinusoidal, high-frequency interrogator signal which is partially reflected back to transmit[3] data (backscatter principle). The tag digitally encodes the response data using the FM0 code[4] (40 kBit/s - 640 kBit/s) or the Miller-modulated subcarrier code (5 kBit/s - 320 kBit/s). Then, the tag antenna tuning is switched between matched (the received interrogator signal is fully absorbed) and unmatched (the received interrogator signal is partially reflected back) in accordance with the digital code sequence. This switching of the antenna tuning generates the ASK of the backscattered signal, which eventually arrives at the interrogator. After the interrogator received the RN16 from the tag, it transmits an Acknowledgement command (ACK) and the current tag's RN16 ④. All tags in the coverage range of the interrogator receive the ACK and the RN16 but only the tag with a matching RN16 responds by transmitting its EPC using the described backscatter principle ⑤. At this point, the basic communication cycle is completed and the tag will stay deactivated until the next Select phase is initiated. If the interrogator continues with a new Query command, the tag that is assigned to the next time slot will respond.

The communication channel between the interrogator and the tag is established by two links: the uplink (tag → interrogator direction) and the downlink (interrogator → tag direction). Although the wireless transmission channel is the same for both links, the link power budget is different in each direction because the power transmitted by the interrogator is defined and fixed but the power transmitted by the tag depends on its backscatter loss. The sensitivities of the tag receivers and interrogator receivers are typically -15 dBm and -80 dBm, respectively.

A simple protocol, simple signal processing at the tag and the passive tag construction give the benefit of design simplicity, small size and low-cost. However, there are a number of limitations, i.e., relatively low communication range ($\leq$ 10 m), low bit rate and hence high communication cycle times, and small memory size. However, it is widely recognized that the benefits of the passive UHF RFID technology

[3] Although a passive UHF RFID tag does not actively transmit a data signal, the term 'transmit'is used in this work for clarity reasons.

[4] Also known as biphase space encoding.

outweigh its limitations when considering indoor applications (e.g. identification of goods in a warehouse).

2.3 Passive UHF RFID Localization Systems

The basic principle of communication between a tag and interrogator in a passive UHF RFID localization system is as follows:

The interrogator transmits a sinusoidal signal (carrier) of a fixed frequency, f_c to the passive tag to be interrogated. The passive tag is energized by the carrier and the tag digitally modulates the carrier amplitude. The modulated signal is reflected back to the interrogator (backscatter principle). Without loss of generality and assuming an initial phase of $\varphi = 0°$ (where $\varphi = 2\pi f_c t$), the modulated carrier, $s_{\text{tag}}(t)$, can be expressed as:

$$s_{\text{tag}}(t) = \text{Re}\left\{b(t)e^{j2\pi f_c t}\right\}, \tag{2.1}$$

where $b(t)$ is the time-dependent binary signal amplitude that represents information transmitted by the tag and Re{} denotes the real part of a complex number. The communication channel between the tag and the interrogator assumes a simple communication protocol (EPCglobal [16]), specially designed for passive UHF RFID systems.

During the transmission from the tag to the interrogator, $s_{\text{tag}}(t)$ is reflected at walls or other objects in the localization area. Thus, the overall received signal, $s_{\text{int}}(t)$, at the interrogator is a superposition of the direct backscatter signal (line-of-sight) and the N reflected signals and is given by:

$$s_{\text{int}}(t) = \text{Re}\left\{\sum_{n=1}^{N+1} b(t)l_n e^{j2\pi f_c t+\varphi_n}\right\}, \tag{2.2}$$

where l_n and φ_n are the attenuation factor and phase shift for each individual received signal, respectively.

It is common practice to measure the received signal, $s_{\text{int}}(t)$, in terms of instantaneous signal power $P(t)$, given by

$$P(t) = |s_{\text{int}}(t)|^2. \tag{2.3}$$

$P(t)$ is often referred to as the received signal strength (RSS).

From equations (2.2) and (2.3), it can be deduced that the received signals can be measured either in terms of power, phase or both. This has facilitated the power-based, phase-based and biparameter-based (evaluation of power and phase) system designs.

From equation (2.2), it can be seen that the reflected signals will have different phase angles and amplitudes (due to different path lengths) when arriving at the interrogator. This would, inevitably, result in constructive and destructive interference. Consequently, any evaluation of the received signal power or phase in a localization system will deteriorate via multipath because the interrogator is not able to filter out the line-of-sight target tag signal from the overall receiver signal. This is caused by the low available signal bandwidth of passive UHF RFID systems which is defined in the EPCglobal protocol (section 2.2). Furthermore, the application of the well-established frequency diversity technique to reduce the influence of multipath on the interrogator receiver signal is not possible due to the restricted frequency bandwidth in passive UHF RFID localization systems which is defined by local regulations [18].

With the help of a typical application scenario, the two bandwidth limitations of passive UHF RFID systems shall be quantified and explained in detail.

In a room of size 10 m × 5 m × 3 m (length × width × height) (figure 2.2), a tag is located at $L_{\text{tag}} = (2.5, 2.0, 1.5)$ m and an interrogator is positioned to $L_{\text{int}} = (2.5, 7.0, 1.5)$ m. The interrogator transmitter power is $P_{\text{Tx,int}} = 30$ dBm (1 W) and the tag and interrogator antenna gains are $G_{\text{ant,int}} = G_{\text{ant,tag}} = 2$ dBi. Assuming a ray signal model and considering the geometric relations, the lengths R_n of the $n = 1...N$ different signal paths can be calculated. Table 2.1 lists the signal path lengths and the signal path arrival times τ_n with respect to the LOS path (τ_1). In this example, only the first-order[5] reflections are taken into account with a fixed reflection coefficient of 0.5 (-3 dB). The received signal power P_n of the tag response of the nth path at the interrogator antenna is calculated using the Friis Transmission Equation [30]. It can be observed that the received signal power of the reflection paths is close to the power of the LOS path (e.g. the floor and the ceiling reflections have a 2.7 dB lower power than the LOS). Thus, the impact of the received reflection signals on the overall received signal is very high.

[5]The signal is only reflected once on its way from the transmitter to the receiver antenna

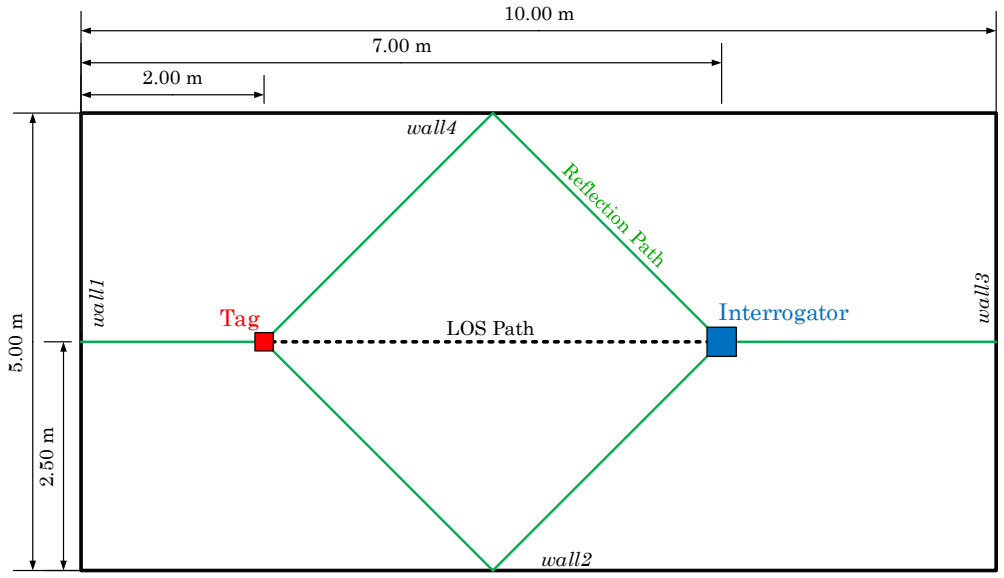

FIGURE 2.2: RFID system and reflections in a typical application example (top view)

TABLE 2.1: Characteristic values for different indoor signal distribution paths

Path	R_n **[m]**	τ_n **[ns]**	P_n **[dBm]**	P_n **[nW]**
LOS	5	0	-34.3	372
***wall1* Reflection**	9	13.3	-44.5	35
***wall2* Reflection**	7.07	6.9	-40.3	93
***wall3* Reflection**	11	20.0	-48.0	16
***wall4* Reflection**	7.07	6.9	-40.3	93
Ceiling Reflection	5.83	2.8	-37.0	201
Floor Reflection	5.83	2.8	-37.0	201

According to the EPCglobal communication protocol [16], the maximum data rate in the uplink (tag → interrogator) of a passive UHF RFID system is 640 kBit/s. Depending on the chosen baseband coding scheme, this translates to a maximum signal bandwidth of $B_s = 640$ kHz and a bit time duration (or signal pulse length) of $t_{\text{bit}} = \frac{1}{B_s} = 1.56\ \mu$s. Accurate localization measurements depend on the isolation of the tag's line-of-sight signal which is the earliest arriving signal and thus the first arriving signal pulse. In the considered scenario, the maximum received time difference of the LOS path and a reflection path is $\tau_{\max} = 20$ ns $\approx 0.01 \cdot t_{\text{bit}}$ (*wall3* reflection) and the mean received time difference $\tau_{\text{mean}} = 8.8$ ns $\approx 0.006 \cdot t_{\text{bit}}$ (table 2.1). Thus, all arriving multipath signal pulses overlap almost coherently thereby making it impossible to distinguish. In an optimum case, the multipath signal pulses would arrive at the interrogator one after another. For the mean received time difference $\tau_{\text{mean}} = 8.8$ ns, this would require a signal bandwidth of $B_s = \frac{1}{\tau_{\text{mean}}} = 114$ MHz.

Depending on the path lengths of the different multipath signal components transmitted by the tag and arriving at the interrogator, their phase shifts with respect to the direct tag signal are different. In a worst case, this phase shift is $\Delta\varphi = 180°$ which results in destructive interference and deep signal power fading. Thus, the influence of the reflection on the overall receiver signal is at maximum. The signal carrier frequency used (f_c) determines the signal wavelength and thus the phase of the received signal components. By switching between two carrier frequencies $f_{c,1}$ and $f_{c,2}$, the experienced signal fading and thus, the influence of multipath signals can be reduced (frequency diversity). However, the total available spectrum of the system $B_f = |f_{c,1} - f_{c,2}|$ has to be large enough to significantly change the received signal phase of the multipath components. The minimum required frequency bandwidth is called coherence bandwidth, B_c, and is calculated as follows. From the received tag signal power of the nth path P_n and signal arrival times τ_n (table 2.1), the root mean square (RMS) delay spread τ_{rms} for the application example is derived as [136, 137]

$$\tau_{\text{rms}} = \sqrt{\frac{\sum_{n=1}^{N+1} P_n \tau_n^2}{\sum_{n=1}^{N+1} P_n} - \frac{\left(\sum_{n=1}^{N+1} P_n \tau_n\right)^2}{\left(\sum_{n=1}^{N+1} P_n\right)^2}} = 4.53 \text{ ns}. \tag{2.4}$$

Using τ_{rms}, the coherence bandwidth B_c is estimated as [138]

$$B_c \approx \frac{1}{4\pi\tau_{\text{rms}}} = 17.6 \text{ MHz}. \tag{2.5}$$

In the European UHF RFID frequency band (865.6 MHz - 867.6 MHz), a frequency bandwidth of only 2 MHz ($\approx 0.1 \cdot B_c$) is available which makes frequency diversity effectless.

The explained bandwidth-related problems are common to all passive UHF RFID localization systems, and the situation is further complicated if there are movements in the localization area (i.e. movements of persons or objects in the localization environment).

Additionally, the presence of multipath in the localization environment gives rise to formation of 'dead-zones'(locations where tags are not readable). This condition occurs when either a tag cannot be activated or the tag signal power arriving at the interrogator is below interrogator sensitivity. Thus, minimization of the effects of multipath is one of the major challenges in passive UHF RFID localization system designs.

The performance of a passive UHF RFID localization system is measured in terms of the coverage range, the update rate but, most commonly, the localization accuracy.

General overviews on RFID-based localization approaches can be found in [3, 31, 139, 140].

2.3.1 Power-Based Passive UHF RFID Localization Systems

Power-based passive UHF RFID localization systems can be categorized as the target interrogator type and target tag type. In a target interrogator type localization system, the interrogator is assumed to be the target that is surrounded by a number of passive tags located at pre-defined fixed positions. More specifically, a square grid of reference tags is attached to the floor or ceiling of the area of interest. In most cases, the target interrogator is mounted onto a mobile robot.

In the readability-based localization technique, tags are only activated and readable when the received signal power at the tag exceeds the tag's sensitivity. Due to the limited coverage range of interrogators which is dependent on the maximum allowed interrogator transmitter power, only a subset (a small number) of the existing reference tags is readable from the target location. The coordinates of these reference tags are then used to estimate the target position. Accuracies in the range between 7 cm and 50 cm have been reported, depending on density of reference tags [128, 129, 132, 141–144]. The main disadvantage is the time-consuming and cost-intensive preparation of the localization environment that has to be repeated for each new scenario. A higher density of reference tags increases the localization accuracy but also increases the preparation effort and cost. In addition, the maximum density is limited by the mutual interaction between adjacent reference tags [145].

The presence of reflections gives rise to generation of multipath, which degrades the readability of reference tags [128]. For a system with a given reference tag density, fingerprinting has been suggested to alleviate the effects of multipath. An accuracy improvement of 20 cm has been achieved [133, 143, 146]. Fingerprinting is a technique that matches the subset of readable reference tags with an existing database of reference measurements conducted prior to the operation of the localization system. However, the technique does require additional preparation time for measurements and storage of the reference data corresponding to each

individual reference tag in the system. In addition, the localization accuracy is highly deteriorated in dynamic environments.

The effects of multipath on the tag readability measurements may also be alleviated by the use of highly directive reference tag antennas [147]. This approach increases the localization accuracy to 10 cm compared with fingerprinting. However, these types of antennas tend to be large and bulky and incur additional cost.

The averaging of multiple readability measurements with different interrogator transmitter power levels has also been proposed [144, 148], but this approach only gives a minor accuracy improvement at the expense of significant reduction in the update rate.

An example of the angulation technique described in section 1.1 requires rotation of the interrogator antenna which significantly reduces the update rate compared with the readability-based methods [132, 149, 150]. The direction of the reference tag is estimated from the interrogator antenna angle at which readability of the reference tag changes. This technique can achieve localization accuracy of 20 cm, however, it requires additional devices (e.g. a digital compass) to determine the interrogator antenna angle, which increases system complexity, size and costs.

In RSS-based (here RSS refers to the received signal strength at the interrogator) lateration systems (section 1.1), the reference tag distance is estimated by the interrogator from the power reflected (backscatter) by the reference tag [122, 134, 144, 151–153]. The achievable localization accuracy in RSS-based systems can be in the range 20 cm to 40 cm. In practice, however, the achievable accuracy is degraded due to the spatial orientation and type of the tags.

An improvement in the above RSS-based system is possible by adjusting the transmitter power of the target interrogator to multiple levels and then averaging the corresponding reference tag RSS measurement values. However, this approach increases the processing time [122].

Hybrid approaches either combine two measurement parameters (e.g. reference tag readability and RSS measurements) or two different technologies (e.g. passive UHF RFID and motion sensors, cameras, WLAN or others) [130, 131, 135, 152, 154–160]. These types of systems have the ability to provide relatively higher localization accuracy (3 cm - 10 cm) but at the expense of system complexity and high data processing time, which, inevitably, adds cost.

Target tag type systems require a local infrastructure of interrogators to be deployed at pre-defined positions in the area of interest.

In tag readability approaches, the interrogators increase their transmitter power level to a point where the target tag becomes activated. A comparison of this power level with a reference database allows an estimation of the target tag distance which is then used for lateration [31, 161, 162]. For this method, a localization accuracy of 15 cm is reported. The processing time is very high compared to all aforementioned localization systems (e.g. 54 seconds in [31]). Other disadvantages are the cost-intensive preparation of the localization environment with interrogators and the time-consuming reference measurements that have to be repeated for each new scenario.

An alternative approach that avoids reference measurements is to use additional reference tags in the localization area with known distances to the interrogator [32]. In the measurement process, the interrogator transmitter power levels that activate the target tag are matched with the reference tag activation power levels. In addition to high system cost, this approach has a high complexity and a high processing time. Localization accuracy in the range 6 cm to 46 cm has been reported [32].

In the RSS approach (already described for the target interrogator case), the interrogators measure the received signal power of the target tag's backscatter signal to estimate its distance which is then used for lateration [163, 164]. The approach has a higher error deviation compared with all the target tag type systems discussed above. Consequently, the achievable localization accuracy is limited to 40 cm [124, 165–168].

The above RSS approach may be improved by first creating a database of RSS values measured from reference tags arranged at known locations in the localization area. The RSS from a given target tag is compared with the database RSS values and the position of the target tag is determined by the closest RSS match [33, 169]. Using this approach, localization accuracy of 21 cm has been achieved.

Several RSS-based target tag localization systems use auxiliary information, e.g. a limited number of possible target positions, which achieves an accuracy of 14 cm [38, 39, 170, 171]. Unfortunately, the auxiliary information is always application-specific.

The angulation technique that was described for target interrogator localization is also used for target tags. It achieves an accuracy of 16 cm and requires high processing times [172–174].

Hybrid approaches combine RSS measurements with other technologies such as WLAN, Wireless Sensor Networks (WSN) or cameras. Localization accuracies of up to 30 cm have been reported [36, 37, 175, 176]. The processing of additional data decreases the update rates and the required hardware increases the system cost, size and installation time.

As an alternative to the usual target interrogator and target tag localization systems, a combined interrogator/tag target on a mobile robot is used in [31, 177]. The localization process is divided into two steps. First, the readability of reference tags in the localization environment is used to coarsely localize the target's on-board interrogator. Second, interrogators arranged in the localization environment use RSS measurements to laterate the target's on-board tag location. A localization accuracy of 23 cm is achieved but the localization process is more time-consuming compared to single-target approaches. In addition, the on-board interrogator increases the size, complexity and cost of the target compared to tag-only methods.

Device-less passive UHF RFID localization systems do not require individual targets in the conventional sense [178–180]. Instead, they use a local infrastructure of reference tags and interrogators to measure the changes in the RSS values as a result of an intruder (the target). The position of the target is determined by matching the measured RSS values with an existing database of reference RSS measurements. The main disadvantages are the complex and cost-intensive installation of the local infrastructure as well as the inability of target identification. In addition, the required reference measurements further increase the set up time and cost and dynamic environments deteriorate the localization accuracy.

2.3.2 Phase-Based Passive UHF RFID Localization Systems

As for the power-based systems, phase-based passive UHF RFID localization systems can also be categorized as the Target Interrogator type and Target Tag type. The target interrogator type systems require a local infrastructure of reference tags in the area of interest. The received signal phase is compared with the phase value of the reference tags in a pre-recorded database. From the phase comparison, the location of the target is estimated. Localization accuracy of 18 cm has been

reported [34, 35]. The main problem associated with all phase-based approaches is the phase ambiguity (see section 1.1). Because the measurement of the reference tag phase delivers distinct values only for a maximum target distance of $d = \lambda$ (e.g. 34 cm in the European UHF RFID band), the reference measurements have to be conducted with a high spatial resolution. This increases the initial system installation time and the time-consuming database search in the localization process reduces the update rates.

Hybrid target interrogator localization systems (e.g. a combination of phase measurements with motion sensors) increase the localization accuracy to 5 cm. However, the additional sensor devices increase the target cost and size as well as the complexity of the measurement data processing [181–183].

In phase-based target tag localization systems, a local infrastructure of interrogators is setup that estimates the distance to the target from received signal phase measurements. Additional a-priori information (e.g. the known path and speed of the targets) has to be used to avoid phase ambiguities and to extend the possible distance estimation range [184, 185]. This information is application-specific but achieves an accuracy in the centimetre-order.

A different approach to extend the distance estimation range is the use of additional reference tags in the localization environment. It uses an estimation of the distance between the target tag and the reference tags to determine the target location [186]. However, compared to all other phase-based localization systems, this technique achieves the lowest localization accuracy (metre-range). Furthermore, it demands a high number of reference tags because the distance between the target and the reference tags has to be smaller than the system's wavelength to avoid phase ambiguities. The proposed use of target arrays consisting of multiple tags achieves a high localization accuracy but requires complex, cost-intensive and bulky target devices [187–189].

The measurement of phase-differences for target tag localization is not influenced by phase ambiguities [190–192]. Existing systems are only used for target distance estimation (not a full lateration) and achieve an accuracy of 14 cm. They need a high bandwidth that cannot be realized in the UHF RFID frequency range and the tag has to remain static during the measurements. Multiple interrogator antennas as well as time-consuming calibration measurements are required [190].

2.3.3 Biparameter-Based Passive UHF RFID Localization Systems

In biparameter-based systems, the two signal parameters (power and phase) are jointly evaluated. In this class of passive UHF RFID localization systems, only the target tag localization is generally considered. The most probable reason is the fact that using interrogators as the localization target increases the overall target size, cost and complexity. In addition, the active interrogator devices need a constant power-supply and individual targets cannot be identified.

A localization scheme that combines the phase difference measurements with tag readability has been presented in [40]. A mean localization accuracy of 30 cm has been achieved, but at the expense of requiring high processing time.

In another scheme, the fusion of separately measured RSS and phase data, using an artificial neural network, has achieved a mean accuracy of 7 cm but the neural network needed to be trained with a high number of reference measurements and the reliability could only be ensured if the localization environment was static [41].

The other two biparameter localization methods are receiver beamforming and transmitter beamforming. In general, receiver beamforming (or spatial filtering) is a technique that uses antenna arrays for signal reception and combines the array element signals in a way that particular spatial angles experience constructive interference and other angles destructive interference. In a localization system, multipath reflections and the direct target tag signal (LOS) arrive at the interrogator antenna at different angles. Thus, the receiver beamforming technique can be used to amplify the LOS target tag signal while attenuating the reflection signals thereby mitigating the effects of multipath on localization accuracy. There are two approaches that have been employed in receiver beamforming: a) Analogue receiver beamforming, b) Algorithmic beamforming.

In analogue receiver beamforming, the receiver scans the angular range of the interrogator antenna array and finds the incidence angle of the target tag signal [193–195].

Algorithmic beamforming facilitates digital receiver beamforming. The main signal processing algorithm that is used in this method is the Multiple Signal Classification (MUSIC). By evaluating the received target tag signals from the antenna array elements, a high resolution angle-of-arrival can be estimated [43, 196–198]. Localization of the target position is realized by angulation using angle-of-arrival information from multiple interrogators located at different positions. Algorithmic

receiver beamforming is capable of achieving localization accuracy in the order of centimetres. Comparing the two approaches, the analogue receiver beamforming is cost-intensive in terms of receiver design, requires high processing time, has a limited receiver scanning range and offers low angular resolution. However, despite all its strengths, the performance of algorithmic receiver beamforming is severely degraded in the presence of multipath [43, 199] and, in addition, it relies on custom-designed multiple antenna array receivers used at the interrogators.

Transmitter beamforming is a well-established technique that is used in RADAR, UMTS base stations, and other applications [200, 201]. However, its use in passive UHF RFID systems has been limited to identification systems only. In principle, transmitter beamforming is realized by manipulating the directivity (or beam pattern) of an antenna array, which is achieved by changing the phase and/or amplitude of the individual array element feeding signals. In passive UHF RFID applications, the main lobe interrogator transmitter power is directed towards the tag, which helps to minimize signal reflections [42, 193, 195, 202–212]. This improves the signal-to-noise ratio (SNR) and hence, enhances the tag readability.

Almost all passive UHF RFID transmitter beamforming systems to date have only used analogue beamforming.

The principles of digital transmitter beamforming in RADAR applications have been explained in [213]. In [42] analogue transmitter beamforming has been used to enhance readability in passive UHF RFID identification systems, however, it has been suggested that digital transmitter beamforming, in principle, would improve angular resolution but at the expense of design complexity. It could be argued intuitively that high angular resolution would improve the target tag angle estimation accuracy in localization systems. This makes the digital transmitter beamforming a more compelling argument for localization systems.

With regards to the use of transmitter beamforming in passive UHF RFID localization, only one attempt has been made to date. The transmitter beamforming has been used for tag direction estimation [201]. In this experiment, an accuracy of 1.6° (difference between the estimated tag angle and the actual value) has been reported.

2.3.4 Discussion

The above review of the current state of passive UHF RFID localization techniques suggests that in the power-based category, target interrogator type systems are less attractive compared with target tag type, due to a number of disadvantages: large target size is restrictive (e.g. difficult to attach to a person or a small object); the need for additional devices in order to identify individual targets (implementation of multiple targets and targets of different types becomes difficult); the need for a constant power supply; the need for a dedicated local infrastructure of tags and in some cases development of a references database (high cost operations). The passive structure of targets in target tag type systems overcomes all the above constraints. As a result, there seems to be a trend to opt for target tag type localization systems.

Phase-based localization systems have limited coverage range due to phase ambiguities.

Hybrid systems are capable of achieving higher localization accuracies but at the expense of additional devices that increase the target size, complexity and increased processing time.

Biparameter-based systems generally provide a high accuracy for angle-of-arrival estimations. Among this class, systems based on receiver beamforming techniques appear to be more promising, in particular, algorithmic receiver beamforming is worthy of further investigations.

Analogue transmitter beamforming is an interesting concept and has been used to improve the tag readability in passive UHF RFID identification systems. A natural extension of this work would be to investigate possibilities of transmitter beamforming techniques in passive UHF RFID localization systems.

2.4 Receiver and Transmitter Beamforming

2.4.1 Receiver Beamforming

As algorithmic receiver beamforming techniques seem to have the potential to outperform all other localization methods used for passive UHF RFID localization systems, it is appropriate to look into the principles of algorithmic receiver beamforming in some detail.

In algorithmic receiver beamforming techniques, antenna arrays that consist of multiple elements with some arbitrary three-dimensional arrangements are generally employed. In a Uniform Linear Array (ULA), however, the antenna elements are arranged in a straight line with equal distance between adjacent elements.

The quality of receiver beamforming techniques is measured in terms of angular resolution, i.e. the ability to distinguish between different signal sources, and computational complexity.

The principle of receiver beamforming, based on a ULA, is depicted in figure 2.3. In this two-dimensional formation, the beamforming can only be considered in the azimuth plane of the antenna array (two- dimensional beamforming).

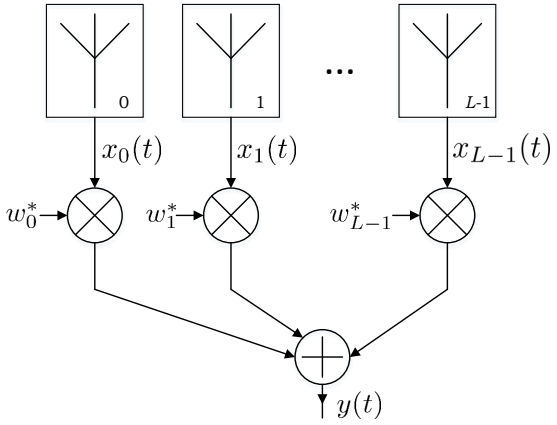

FIGURE 2.3: Receiver beamforming principle

The received signals $x_0(t), x_1(t), ..., x_{L-1}(t)$ of an L-element ULA are multiplied with complex weighting factors $w_0, w_1, ..., w_{L-1}$ and added together to achieve a receiver signal $y(t)$ as

$$y(t) = \sum_{l=0}^{L-1} w_l^* x_l(t), \tag{2.6}$$

where * denotes the complex conjugate.

The average output power $P(w)$ of the beamformer output signal $y(t)$ over N time samples of $y(t)$ as a function of the weighting factors w_l is given by [214]

$$P(w) = \frac{1}{N} \sum_{n=1}^{N} |y(nT)|^2 , \tag{2.7}$$

where T is the sampling period. The power, $P(w)$, is maximized, for the desired signal direction, as a function of the weighting coefficients w_l.

In all cases, these weights include the array steering vector

$$\mathbf{a}(\theta) = \begin{bmatrix} 1 & e^{-j\phi} & e^{-j2\phi} & ... & e^{-j(L-1)\phi} \end{bmatrix}^T, \tag{2.8}$$

with $\phi = \frac{2\pi s}{\lambda} \sin\theta$ which then relates the beamformer output power to the azimuth angle θ of the antenna array. The incident angle of the desired signal, θ_0, corresponds to the maximum in $P(\theta)$.

There are two existing techniques for receiver beamforming, namely, Classical and Subspace-Based (also known as the Super-Resolution method) [44].

In the Classical technique, the most prominent approaches are the Conventional Beamformer and the Minimum Variance Distortionless Response (MVDR).

The Conventional Beamformer (also referred to as Delay-And-Sum method or Barlett method), defines the constraint that $|\mathbf{w}| = 1$, where $\mathbf{w}$ is a vector containing all weighting factors w_l [215]. The search for peaks over $P(\theta)$ after setting the appropriate weights identifies the direction of the incident signals (beam scanning). However, the angular resolution of the Conventional Beamformer is limited to $\phi_B = \frac{2\pi}{L}$ (e.g. $\phi_B = 180°$ for a two-element array or $\phi_B = 120°$ for a three-element array), i.e. two signals that incident from a segment smaller than ϕ_B cannot be distinguished [214].

The MVDR method (also known as the Capon Beamformer) defines a linear power constraint which sets the power incident from the direction of the desired signal to $P(\theta_0) = 1$ [44, 216]. Optimising the weighting coefficients to achieve that is equivalent to minimizing the total received power of all directions but the desired one. Thus, the average interference is minimized. However, the resolution capability is still dependent on the array aperture (given by L) and the SNR [214]. Another disadvantage is that the computation of an inverse matrix is needed which may become ill-conditioned if the incident signals are highly correlated [44].

In the subspace technique, there are two approaches: a) Multiple Signal Classification (MUSIC), b) Estimation of Signal Parameter via Rotational Invariance Techniques (ESPRIT).

Both approaches achieve higher angular resolution than the classical beamforming techniques. They decompose the observation space into a signal subspace and a noise subspace and exploit the orthogonality of the two subspaces. In addition, the specific properties of the received signal covariance matrix are utilized, which enables them to achieve high angular resolution in $P(\theta)$.

MUSIC derives $P(\theta)$ from the noise signal eigenvectors which are calculated from an estimation of the received signal covariance matrix. Because it involves a search for peaks over $P(\theta)$ that requires various matrix calculations, it has a high computational complexity. In the presence of correlated interferers (i.e. multipath reflections), the estimated signal covariance matrix may become ill-conditioned, which will prevent detection of incident signals [43]. An exemplary calculation of a covariance matrix for correlated receiver signals is given in appendix A.1. Spatial smoothing has been proposed to overcome this problem [199]. It divides the array into smaller subarrays and averages the covariance matrix for each subarray. All subarray covariance matrices are then used to form a single, spatially smoothed covariance matrix. Although this technique may improve the performance in the presence of multipath, it further increases the computational complexity.

The Root MUSIC algorithm is a variation of MUSIC and only applicable to uniform linear arrays. It constructs a specific polynomial whose roots correspond to the maxima in $P(\theta)$ [217]. Thus, it avoids the peak search over $P(\theta)$ and provides a direct calculation of the signal incidence angles. As a result, it has much lower computational complexity and much shorter processing time. Its performance is asymptotically equal to that of MUSIC but is better than MUSIC if a relatively smaller number of signal samples for each signal is taken [45].

ESPRIT is very similar to MUSIC because it also involves an eigendecomposition of the received signal covariance matrix [218]. Based on the rotational invariance property of the signal space, it is able to directly calculate the incidence angle of the desired signal. The computational complexity of ESPRIT is lower than in the MUSIC method because it does not need a search for maxima over $P(\theta)$. However, it still relies on computation of the signal covariance matrix and is thus prone to correlated source signals. Its performance is almost identical to MUSIC for unmodulated sine signals and it is less sensitive to noise [219]. All subspace-based receiver beamforming approaches have the limitation that the number of source signals M has to be smaller than the number of antenna array elements L (reflections are included into the M source signals). Increasing L directly leads to higher computational and system complexity which increases the size of the hardware devices (i.e. signal processing hardware and antenna array) and cost.

The MUSIC algorithm has been widely used in the existing receiver beamforming systems. These systems aim to realize three-dimensional localization, which can only be achieved with MUSIC [220]. The angular accuracy is improved by increasing the number of antenna array elements [43, 197], using arbitrary antenna array

arrangements (e.g. elements arranged in a circular pattern). Root MUSIC, on the other hand, can only deal with two-dimensional localization, based on ULAs which, in turn, only allow a small number of array elements, due to the ULA size constrain. As a result of these limitations, Root MUSIC has not been used in any existing localization system. However, despite its limitations, Root MUSIC has the advantage of low computation and fast response time [44], together with better performance over a certain range of sampling frequencies [45]. It seems that these features have never been exploited to date. It would be of interest to investigate the possible benefits of these features in passive UHF RFID localization applications.

More detailed mathematical descriptions of all receiver beamforming methods are given in appendix A.1 and in [44, 200, 214, 219, 221, 222].

2.4.2 Transmitter Beamforming

In principle, the transmitter beamforming is an opposite operation to the conventional receiver beamformer because it requires the generation of weighted antenna array signals instead of acquiring them. Figure 2.4 shows the principle of a transmitter beamforming system.

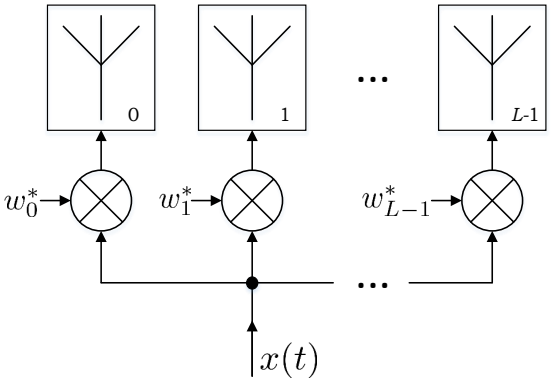

FIGURE 2.4: Transmitter beamforming principle

The transmitter signal $x(t)$ is distributed to the feeding lines of an L-element antenna array and multiplied with individual complex weight factors w_l. At the antenna array output, the L transmitter signals with different amplitudes and phases superpose and generate the radiation pattern

$$B(\theta) = e^{-j\left(\frac{L-1}{2}\right)\phi} \sum_{l=0}^{L-1} w_l^* e^{jl\phi}, \text{ with } \phi = \frac{2\pi s}{\lambda} \sin\theta, \tag{2.9}$$

where θ is the azimuth angle of the antenna array, λ is the system wavelength and s is the distance between the antenna array elements. Only in the 'visible region'with $0 \leq \theta \leq \pi$, does $B(\theta)$ deliver distinct values. To set a specific beam pattern, the corresponding weights are calculated by fixing L values of $B(\theta)$ and solving equation (2.9) for w. Thus, the degree of freedom in the manipulation of the beam pattern is limited by the number of antenna array elements L.

As has been discussed previously, only analogue transmitter beamforming has been used to date, mainly in passive UHF RFID identification systems. In these systems, the analogue signals feeding to individual antenna array elements are generated by various techniques, for example: activation and deactivation of different parasitic elements in the feeding lines of the antenna array allows the generation of a small number of fixed beam pattern [205]; Phase shifters and power dividers achieve more degrees of freedom and a higher angular accuracy [195, 201, 203, 204, 207, 208, 211, 223].

However, despite its ability to achieve high angular accuracy, analogue transmitter beamforming has three main limitations: the angular range for the main lobe in the generated beam pattern is restricted to $\pm 30°$; offers low angular resolution of the order of a few degrees; splitting of the transmitter signal into L branch results in signal attenuation.

As has been suggested by others (see section 2.3.3) that digital transmitter beamforming, in principle, would improve angular resolution, the notion of applying digital transmitter beamforming to localization systems is certainly intriguing. It is of great interest to investigate whether all the above limitations of the analogue beamforming can be removed by digital transmitter beamforming.

The full derivation of the transmitter beamforming theory can be found in [200]. Appendix A.3 gives a detailed mathematical description of transmitter beamforming, using a uniform linear array.

2.5 Existing Transmission Channel Models for Passive UHF RFID

In a passive UHF RFID system, communication between an interrogator and target tag constitutes a bi-directional, short-haul wireless transmission channel. The signal parameters of interest (e.g. amplitude and phase), in any one direction, can be evaluated by considering the channel behaviour between the transmitting and receiving antennas. One of the most important channel parameters is the power loss incurred during transmission (referred to as the path loss).

From the basic Friis equation, the path loss, L_{path}, is given by [30]:

$$L_{\text{path}} = \left(\frac{\lambda}{4\pi d}\right)^2, \tag{2.10}$$

where λ is the transmission wavelength and d is the distance between the two antennas.

It is important to note that the above equation is only valid under idealized conditions, i.e. there is no multipath interference, the distance d is much greater than the wavelength, the antennas are equally aligned with matching polarizations, both the transmitter and receiver antennas have a unity gain, and the system bandwidth is narrow enough for a single value for λ to be assumed. As has been discussed previously, the effects of multipath in indoor passive UHF RFID systems are of vital importance (precise analysis by solving Maxwell E-M equations is neither desired nor necessary for localization applications, as localization systems require simple and fast methods for estimations).

As an alternative to the precise analysis, two general approaches, namely the statistical approach and the deterministic approach to model and evaluate the effects of multipath on the system performance can be found in the literature.

The basic statistical model expresses the path loss in terms of proportionality as a function of distance, d, and is given by [224]:

$$L_{\text{path}} \propto d^{-\alpha} \tag{2.11}$$

The exponent α is derived from measurements and thus only valid for a specific set of measurements, scenario and frequency. For example, the following empirical values for α have been proposed in the literature: $\alpha = 3$ for a university office room

at 1.5 GHz [224], $\alpha = 1.8$ for a building hallway at 910 MHz [225], $\alpha = 1.2...2.8$ for different factory buildings at 1.3 GHz [47]. More values can be found in [226].

Numerous other statistical channel models, in the literature, have proposed a variety of different distributions for the signal amplitude based on specific environments (e.g. Rician distribution for factories [47, 227] or for university office rooms [228, 229], Nakagami-m distribution for general indoor environments [230], or Rayleigh distribution for general indoor environments [231, 232]).

In a more complex approach, the wireless indoor channel is assumed to be a linear filter with the impulse response $h(t)$ [48]:

$$h(t) = \sum_{n=1}^{N} a_n \delta\left(t - t_n\right) e^{j\theta_n}, \tag{2.12}$$

where N is the number of multipath signal components and a_n, t_n, θ_n are the nth signal's random amplitude, arrival time, and phase, respectively. Convolving a transmitted signal $s(t)$ with $h(t)$ and adding noise $n(t)$ gives the received signal

$$y(t) = \int_{-\infty}^{\infty} s(t)h(t-\tau)d\tau + n(t). \tag{2.13}$$

From the analysis of a high amount of measurement data in two specific office rooms at a frequency range of 900 MHz to 1 GHz in [233], the following statistical distributions are proposed for the signal parameters in equation (2.12):

- Gaussian distribution for the number of multipath components N
- Modified Poisson distribution for the signal arrival times t_n
- Log-normal distribution for the signal amplitudes a_n
- For the signal phases θ_n, no distribution is proposed because the authors are unable to measure the individual multipath signal phases

From the study of statistical channel models, it can clearly be deduced that they have four main issues of concern with respect to their application to passive UHF RFID systems:

1. A large amount of complex and time-consuming measurements are necessary to derive the required statistical parameters,
2. The derived parameters are only valid for specific environments and specific frequencies,
3. The choice of statistical distribution is dependent on a given environment,

4. Statistical models cannot deal with the signal phase information, which is a very important signal parameter in some localization techniques.

In deterministic approaches, different physical signal propagation paths from the geometry of the environment are considered and amplitude or power of individual signals is added at the receiver. This method is also known as 'ray-tracing'and was first used in optics.

Thus, the Friis basic equation may be modified to superpose the path loss of N signals (where N is any natural number). The path loss, L_{path}, for the superposition of the LOS path with $N-1$ reflected paths, is then given by:

$$L_{\text{path}} = \left(\frac{\lambda}{4\pi d_0}\right)^2 \left|1 + \sum_{n=1}^{N} \Gamma_n \frac{d_0}{d_n} e^{-jk(d_n - d_0)}\right|^2 , \tag{2.14}$$

where d_0 is the length of the LOS path, d_n is the length of the nth reflection path, Γ_n is the reflection coefficient for the nth signal path, and k is the wavenumber with $k = \frac{2\pi}{\lambda}$. This model can be extended to include higher-order reflections.

Recalling the attenuation factor, l_n, in equation (2.2) (Section 2.3), l_n is represented by L_{path} in equation (2.14).

There are several examples of the use of equation (2.14) in the literature. However, in most cases, only two paths ($N = 2$), LOS and one reflected signal, have been considered.

In [50, 234–236], the second signal path is assumed to be the ground reflection and a wall reflection has been considered in [237]. In [50, 235], the reflection coefficient Γ_n is assumed to be real valued and set to -1, which corresponds to a full reflection of the incidence signal energy with an inverted phase. Other models calculate a complex reflection coefficient $\underline{\Gamma}_n$ from the dielectric properties of the reflection surface, the signal incidence angle, and the polarization of the incidence signal [234, 236, 237]. Some of the models have included antenna polarization, but only linear polarization states (vertical or horizontal) have been considered. In all the above examples, the antenna gain (transmitter or receiver) is set to a fixed maximum value.

A more elaborate approach to deterministically model the wireless channel is called 'brute-force ray-tracing' [238]. Instead of deriving the signal path lengths from the geometry of the environment under test, a very high number of possible signal paths originating from the transmitter antenna is calculated (e.g. 10^6 in [239]).

After considering the interaction (reflection, transmission, or diffraction) of each possible signal path with any surface in the environment, the signal paths that intersect with the receiver antenna are superposed to get the overall receiver signal.

Different brute-force ray-tracing models consider different properties of the environment and the transmitter and receiver structures. Examples are the dielectrical properties of the reflection surfaces [240], diffraction effects at objects [49, 240, 241], antenna polarizations [238, 240], or second-order reflections in addition to first-order reflections [49].

The brute-force ray-tracing approach can produce very close results to that obtained by full-wave analysis (based on Maxwell E-M theory), but requires detailed specifications and modelling of the environment (e.g. a full three-dimensional CAD blueprint) and huge computational effort (e.g. 1.5 hours for the calculation of signal amplitude values for 50 different receiver antenna locations in [49]).

It is possible to use one of the simplified methods: a) by considering a local coordinate system for each surface interaction simplifies the required matrix calculations for transmission, reflection and diffraction effects [240], b) the use of a geometrical pre-processing phase helps to exclude surface interaction calculations for most signal paths that do not intersect with the receiver antenna [49]. Both methods significantly reduce computational times but they are still higher than in the modified Friis-based model.

The full benefits of brute-force ray-tracing models can only be realized in large environments with a high number of surfaces that interact with the transmitted signals (e.g. a large office room full of furniture and other typical objects). This is not the case in passive UHF RFID system applications, due to the limited communication range of such systems. Thus, signal paths for individual signals can easily be determined from the geometry of the environment in question.

Furthermore, it may be necessary to use several interrogators in an identification or localization system and there may be multiple locations for tags. This formation leads to a large number of transmitter-receiver-constellations and hence a large number of signal calculations.

From the above review, it can be deduced that, although brute-force ray-tracing can provide very accurate results, it is not a practical solution for passive UHF RFID identification and/or localization systems for the reasons already given (simple and faster operations are needed).

Reverting to the models, based on equation (2.14), it is noted that all the models discussed above [50, 234–237] consider the wireless transmission channel, with no or little regard to the channel interfaces (receiver and transmitter antennas). A few have considered the channel interface effects in a limited way e.g. considering linear polarization for the antennas. However, there is sufficient evidence in the literature to suggest that more parameters associated with the channel interfaces should be included to build a more realistic picture.

For example, a three-dimensional gain pattern with individual gains for each signal path and the antenna impedance mismatch at the interrogator and tag have been considered in [242], all possible states of antenna polarizations, antenna orientation and polarization mismatch loss have been suggested to be important parameters [243].

After having reviewed the existing approaches, it seems that in order to construct a more realistic channel model that mimics closely to the real-world situations, with simplicity and fast response, it is sensible to consider equation (2.14) and assume a suitable number (N) of first-order signal paths with the provision of including second-order paths and the received signals phase information, in conjunction with a complex reflection coefficient and all the channel interface related parameters.

2.6 Summary

Numerous existing localization techniques, based on a variety of technologies, have been reviewed. It is emphasized that passive UHF RFID based localization methods are of particular interest for indoors localization applications. The concept, operational principles and different methods of realization of passive UHF RFID localization have been explained. The receiver beamforming and transmitter beamforming have been identified to be the most promising techniques to realize passive UHF RFID localization systems that provide sufficient accuracy in typical applications. The existing receiver beamforming approaches employ both analogue and digital techniques; however, digital receiver beamforming offers much higher localization accuracy. MUSIC is the most commonly used algorithm for digital beamforming techniques. A variation of MUSIC, called Root MUSIC, has the advantage of much reduced processing time compared with MUSIC, but has not been employed in localization application to date. Analogue transmitter beamforming has been used in identification systems but has not been employed in localization systems. Further, it has been suggested in the literature that digital transmitter

beamforming, in principle, would provide higher angular resolution (hence higher accuracy) but, due to implementation complexities, digital transmitter beamforming has not been considered, to date, for passive UHF RFID applications.

Despite their advantageous features, all passive UHF RFID indoors systems suffer from multipath reflection problems. Therefore an accurate transmission channel model is essential for an accurate estimation of the channel behaviour to multipath signals. A study of various existing channel models for passive UHF RFID applications has been carried out and it has been concluded that the modified Friis channel model, with a suitable number (N) of first order signal paths, the provision of including second order paths and the received signals phase information, in conjunction with a complex reflection coefficient and all the channel interface related parameters, would be an appropriate choice for passive UHF RFID localization systems.

Chapter 3

Enhancement of the Transmission Channel Model

The study of existing channel models in chapter 2 led to the belief that the modified Friis channel model with further enhancements would be an appropriate channel model for passive UHF RFID localization system performance estimations.

A number of existing models, based on the modified Friis channel model [50, 234–237] are simulated and their performance compared. The simulation environment is based on a physical setup. The simulated results are also compared with actual measurements carried out using the same physical set up.

Further channel parameters (channel interface related as pointed out in section 2.5 of chapter 2) are included in the modified Friis channel model. Each additional parameter is included one by one in the simulation process and at each step, the improvement of the signal power estimation observed. The ultimate aim is that by including all the channel interface related parameters and signal phase information in the modified Friis channel model, a general channel model may be derived that gives a close estimation of the real-world situations and may also be used for any given localization environment (i.e. not dedicated to a specific localization environment).

It is verified by the simulation results that the enhanced Friis channel model can be regarded as the general channel model for received signal power and phase estimations in passive UHF RFID localization systems. This approach has the advantage of simplicity and low computational time.

Finally, the general channel model is used to predict the tag readability in a simulated localization environment (based on a physical setup). The simulated results are found to be in close agreement with the physically measured results.

3.1 Verification of Existing Channel Models

In order to identify a suitable existing channel model that can be used as the basis for an enhanced channel model, simulations of the received signal power in a typical application scenario are conducted.

In the previous chapter, the path loss, L_{path}, was introduced (section 2.5) which describes the signal distribution between the interrogator antenna and the tag antenna. However, the channel interface (i.e. the antennas) introduces additional gains and losses at the interrogator, G_{int} and L_{int}, and at the tag, L_{tag} and G_{tag}, which influence the transmitted signal power (the interrogator transmitter power, $P_{\text{Tx,int}}$, in the downlink and tag backscatter power, $P_{\text{Tx,tag}}$, in the uplink). Thus, a general form of the channel model equation for the received signal power, $P_{\text{Rx,tag}}$, at the tag in the downlink is

$$P_{\text{Rx,tag}} = P_{\text{Tx,int}} \cdot G_{\text{int}} \cdot L_{\text{int}} \cdot L_{\text{path}} \cdot G_{\text{tag}} \cdot L_{\text{tag}} \tag{3.1}$$

and for the received signal power, $P_{\text{Rx,int}}$, at the interrogator in the uplink,

$$P_{\text{Rx,int}} = P_{\text{Tx,tag}} \cdot G_{\text{int}} \cdot L_{\text{int}} \cdot L_{\text{path}} \cdot G_{\text{tag}} \cdot L_{\text{tag}}. \tag{3.2}$$

The simulations in this section are limited to existing transmission channel models which provide full equations for $P_{\text{Rx,tag}}$ (table 3.1). All existing models consider only the downlink.

TABLE 3.1: Subset of existing transmission channel models for simulation

Authors	Signal Paths	Antenna Gains	Antenna Polarizations	Reflection Coefficients	Ref.
Tam and Tran	2 (LOS, Floor Reflection)	Fixed Max. Gain	Linear	Complex	[234]
Marrocco et al.	2 (LOS, Wall Reflection)	Fixed Max. Gain	Linear	Complex	[237]
Kvaksrud	2 (LOS, Floor Reflection)	Fixed Max. Gain	Linear	Complex	[236]
Nikitin et al.	2 (LOS, Floor Reflection)	Fixed Max. Gain	Not Included	Fixed (-1)	[50]
Banerjee et al.	2 (LOS, Floor Reflection)	Fixed Max. Gain	Not Included	Fixed (-1)	[235]

The corresponding model equations are

1. The Model by Tam and Tran:

$$E_{\mathrm{Rx,tag}} = \frac{1}{d} E_{\mathrm{Tx,int}} e^{-jkd} + \underline{\Gamma} \frac{1}{d_1} E_{\mathrm{Tx,int}} e^{-jkd_1}, \tag{3.3}$$

   with

   $E_{\mathrm{Rx,tag}}$: Received electrical field strength at the tag location
   $E_{\mathrm{Tx,int}}$: Transmitted electrical field strength of the interrogator
   d: Distance between the interrogator and the tag
   d_1: Length of the floor reflection path
   $\underline{\Gamma}$: Complex reflection coefficient
   $k = \frac{2\pi}{\lambda}$

   The received electrical field strength, $E_{\mathrm{Rx,tag}}$, is converted to received signal power, $P_{\mathrm{Rx,tag}}$, using

$$P_{\mathrm{Rx,tag}} = G_{\mathrm{int}} G_{\mathrm{tag}} \frac{\lambda^2}{4\pi} \left| \frac{E^2_{\mathrm{Rx,tag}}}{Z_0} \right|, \tag{3.4}$$

   where Z_0 is the intrinsic impedance of the transmission medium (e.g. $Z_0 = 377\ \Omega$ for air), G_{int} is the antenna gain of the interrogator and G_{tag} is the gain of the tag antenna.

2. The Model by Marrocco et al.:

$$P_{\mathrm{Rx,tag}} = P_{\mathrm{Tx,int}} G_{\mathrm{int}} G_{\mathrm{tag}} \left| \frac{1}{d} e^{-jkr} + \underline{\Gamma} \frac{1}{d_1} e^{-jkd_1} \right| \tag{3.5}$$

   Here, d_1 is the length of the reflection path from the wall behind the tag. In all other models, d_1 is the length of the ground reflection path.

3. The Model by Kvaksrud:

$$P_{\mathrm{Rx,tag}} = P_{\mathrm{Tx,int}} G_{\mathrm{int}} G_{\mathrm{tag}} \left(\frac{\lambda}{4\pi} \right)^2 \left[\frac{1}{d^2} + \frac{1}{d_1^2} \operatorname{sign}(\underline{\Gamma}) |\Gamma| \cos\left[(d - d_1)\, k \right] \right] \tag{3.6}$$

4. The Model by Nikitin et al.:

$$P_{\mathrm{Rx,tag}} = P_{\mathrm{Tx,int}} G_{\mathrm{int}} G_{\mathrm{tag}} \left(\frac{\lambda}{4\pi d} \right)^2 \left| 1 - \frac{d}{d_1} e^{-jk(d_1 - d)} \right|^2 \tag{3.7}$$

5. The Model by Banerjee et al.:

$$P_{\mathrm{Rx,tag}} = P_{\mathrm{Tx,int}} G_{\mathrm{int}} G_{\mathrm{tag}} \left(\frac{\lambda}{4\pi}\right)^2 \left|\frac{1}{d} - \frac{1}{d_1} e^{jk(d_1-d)}\right|^2 \tag{3.8}$$

All models include two signal paths (LOS and floor reflection in all models except Marrocco et al. who use a wall reflection) and the antenna gains are assumed as the maximum available gain. Nikitin et al. as well as Banerjee et al. do not include antenna polarizations and use a fixed reflection coefficient for the floor of $\Gamma = -1$. Tam and Tran, Marrocco et al. as well as Kvaksrud calculate a complex reflection coefficient based on the material properties of the reflection surface. For a valid comparison of the following RSS simulations, the non-matching properties of all models are equalized to: two signal paths (LOS, floor reflection), complex reflection coefficients and linear antenna polarizations.

In a typical application scenario, the passive UHF RFID system is placed into an office room of size 7.25 m × 2.30 m × 3.00 m (figure 3.1). The floor, the ceiling and *wall2* are made of concrete. *Wall3* consists of glass windows and all other reflection surfaces are made of gypsum board (*wall1* and *wall4*). A sinusoidal signal (frequency $f = 867.1$ MHz, transmitter power $P_{\mathrm{Tx,int}} = 24.5$ dBm) is transmitted from a vertically polarized interrogator patch antenna (maximum gain $G_{\mathrm{ant,int}} = 7$ dBi) to a vertically polarized tag dipole antenna (maximum gain $G_{\mathrm{ant,tag}} = 2.1$ dBi). The coordinates (x, y, z) of the antennas are chosen as (1.15, 0.85, 1.50) m for the interrogator and $(1.15, y_{\mathrm{tag}}, 1.50)$ m for the tag. By moving the tag on a straight line from its initial position in y-direction, y_{tag} is varied from 1.45 m to 6.15 m ($d = 0.60$ m...5.30 m). All properties of the application scenario (geometric relations, antenna gains, antenna polarizations, material properties of the reflection surfaces) and the existing transmission channel models are used to simulate the RSS development, $P(d)$ (figure 3.2).

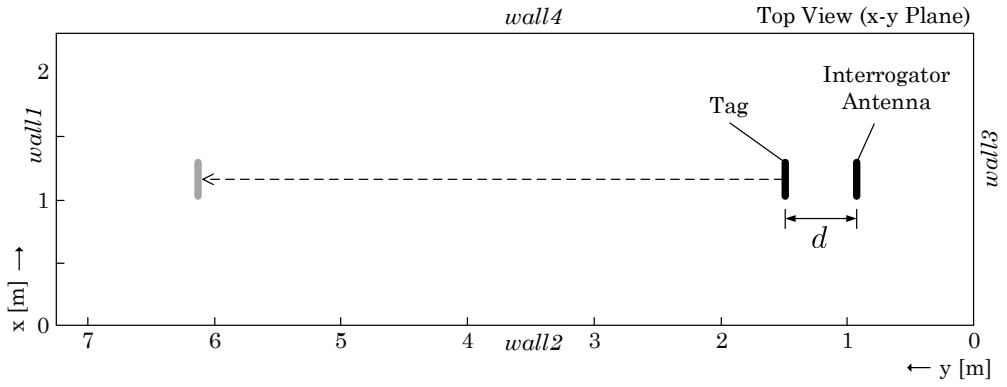

FIGURE 3.1: Setup for the received signal power simulation (top view)

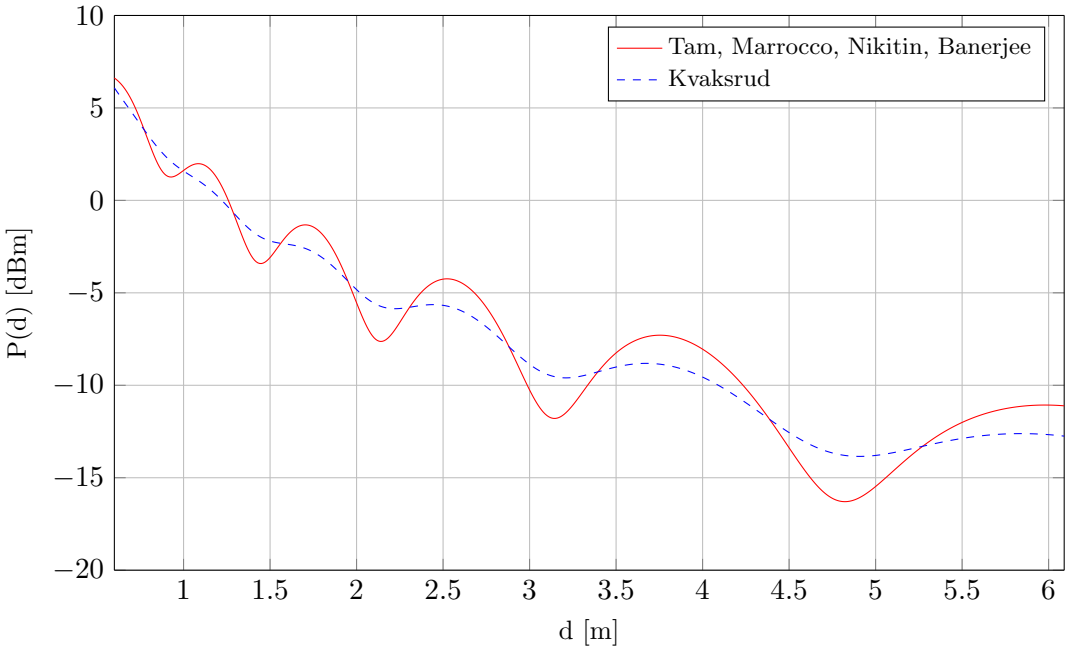

FIGURE 3.2: Simulation of the received signal power using existing transmission channel models

All simulated $P(d)$ characteristics show local maxima and minima (signal fading) at the same distances d but with different amplitudes. The models by Tam, Marrocco, Nikitin and Banerjee produce identical simulation results. After converting the model equations, it becomes obvious that they are also identical for this case. In the following, they are denoted by the single term 'modified Friis model'. The reason for the lower fading amplitudes in the model by Kvaksrud is a transformation of the complex reflection coefficient to a real valued number by taking its absolute value.

For comparison of the simulated RSS development with measured RSS values, a novel testbench is designed that automatically records $P(d)$ in a real-world scenario. A detailed description of the measurement setup and process is given in appendix B.1. In principle, a signal generator feeds the sinusoidal transmitter signal into a vertically polarized interrogator patch antenna. The dipole tag antenna is connected to a spectrum analyzer that records $P(d)$ while the tag is moved away from the interrogator antenna.

The comparison of the measured RSS values with a simulation of the modified Friis model (figure 3.3) shows that the model only gives a coarse approximation of the measured $P(d)$ development and is not able to predict the small local minima and maxima. The reason is an imprecise consideration of the channel interface

parameters (i.e. the antenna parameters) and the characteristics of the environment.

Therefore, the objective is to enhance the modified Friis model in a way that it matches the real-world RSS values as close as possible.

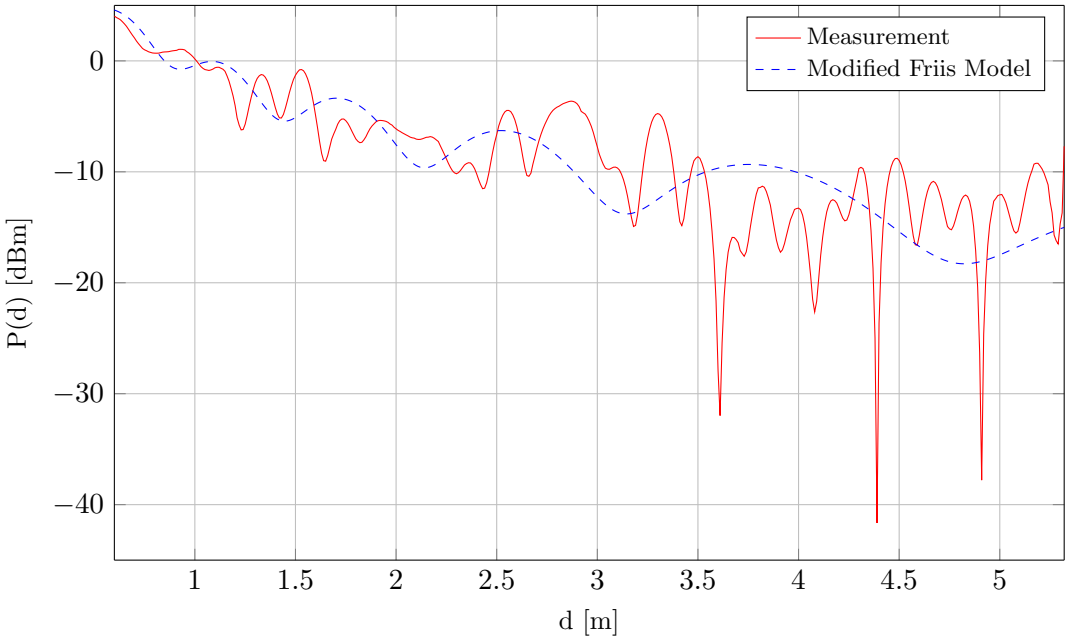

FIGURE 3.3: Comparison of RSS measurement and modified Friis model simulation

3.2 Enhancement of the Modified Friis Model

3.2.1 Number of Signal Paths

The number of signal paths considered in the modified Friis model is limited to $N = 2$ (LOS and floor reflection). However, in reality, reflections of multiple orders are existent. Table 3.2 lists the path lengths, d_n, and the received signal power levels, P_n, of the first- and second-order reflection paths at the receiver antenna in the previously introduced application scenario. As a simplification, a mean reflection coefficient for concrete of $\overline{\Gamma} = 0.5$ is assumed. The received signal power levels, P_n, for the first-order reflections lie in a close range to the power of the LOS path, P_1. Especially the floor and the ceiling reflections contribute a high power to the overall receiver signal that is only 2.7 dB lower than P_1. Thus, all first-order reflections must be considered in the enhanced channel model. From the second-order reflections, the ceiling and floor reflections deliver the highest signal powers

which are 13.7 dB lower than P_1. Due to the low influence of second-order reflections on the overall receiver signal and the complex signal path calculations, the second-order reflections are not considered in the enhanced transmission channel model.

TABLE 3.2: Path lengths and received signal powers for first- and second-order reflections

Path	**First-Order Reflections**		**Second-Order Reflections**	
	d_n [m]	P_n [dBm]	d_n [m]	P_n [dBm]
LOS	5.0	-34.3	-	-
***wall1* Reflection**	9.0	-44.5	15.0	-59.4
***wall2* Reflection**	7.1	-40.3	11.2	-54.3
***wall3* Reflection**	11.0	-48.0	25.0	-68.3
***wall4* Reflection**	7.1	-40.3	11.2	-54.3
Ceiling Reflection	5.8	-37.0	7.8	-48.0
Floor Reflection	5.8	-37.0	7.8	-48.0

For the $N = 7$ signal paths (LOS and six first-order reflections), the basic model equation (3.7) is modified to

$$P_{\mathrm{Rx,tag}} = P_{\mathrm{Tx,int}} G_{\mathrm{ant,int}} G_{\mathrm{ant,tag}} \left(\frac{\lambda}{4\pi d_1}\right)^2 \left| \sum_{n=1}^{7} \underline{\Gamma}_n \frac{d_1}{d_n} e^{-jk(d_n - d_1)} \right|^2 , \tag{3.9}$$

where $\underline{\Gamma}_n$ is the complex reflection coefficient of the nth signal path and d_n is the length of the nth signal path.

3.2.2 Complex Reflection Coefficients

For each of the $n = 1...7$ signal paths in the modified model equation (3.7), a complex reflection coefficient $\underline{\Gamma}_n$ has to be considered individually, depending on the material of the reflection surface. Since the LOS path ($n = 1$) is not reflected, $\Gamma_1 = 1$. The other $\underline{\Gamma}_n$ are derived as follows.

Observing the occurrence of a reflection, the incoming signal that travelled through a medium with the permeability μ_1 and the permittivity $\underline{\varepsilon}_1$ reaches the surface of another medium with the permeability μ_2 and the permittivity $\underline{\varepsilon}_2$. The incidence angle of the incoming signal with respect to the normal of the surface is θ_i. One part of the signal energy is reflected by the surface and the other part is transmitted through the material behind the surface. The reflection angle is θ_r and the transmission angle is θ_t. The three angles are connected to each other as follows:

$$\theta_i = \theta_r \tag{3.10}$$

$$\underline{n}_1 \sin\theta_i = \underline{n}_2 \sin\theta_t, \tag{3.11}$$

where $\underline{n}_1 = \sqrt{\underline{\varepsilon}_1 \mu_1}$ and $\underline{n}_2 = \sqrt{\underline{\varepsilon}_2 \mu_2}$ are the refractive indexes of the two materials.

The complex reflection coefficient $\underline{\Gamma}_n$ that specifies the part of energy of the incoming signal which is reflected from the surface can be derived from the Fresnel Equations [244]:

$$\underline{\Gamma}_\perp = \frac{\underline{n}_2 \cos\theta_i - \underline{n}_1 \cos\theta_t}{\underline{n}_2 \cos\theta_i + \underline{n}_1 \cos\theta_t} \tag{3.12}$$

$$\underline{\Gamma}_\parallel = \frac{\underline{n}_2 \cos\theta_t - \underline{n}_1 \cos\theta_i}{\underline{n}_2 \cos\theta_t + \underline{n}_1 \cos\theta_i} \tag{3.13}$$

$\underline{\Gamma}_\parallel$ denotes the reflection coefficient for parallel incidence of a signal's electric field vector on a surface (e.g. horizontally polarized signal impinges on a wall) and $\underline{\Gamma}_\perp$ for a perpendicular incidence (e.g. vertically polarized signal impinges on a wall).

For the typical application scenarios of passive UHF RFID systems, equations (3.11), (3.12) and (3.13) can be simplified. The reflected signal has travelled through the medium air with $\varepsilon_1 \approx 1$. The material of the reflection surface and the medium air are both non-magnetic with $\mu_1 \approx 1$ and $\mu_2 \approx 1$. With $n_1 = 1$ and $\underline{n}_2 = \sqrt{\underline{\varepsilon}_2}$, equations (3.11), (3.12) and (3.13) can be rewritten as:

$$\underline{n}_1 \sin\theta_i = \underline{n}_2 \sin\theta_t \Rightarrow \sin\theta_i = \sqrt{\underline{\varepsilon}_2} \sin\theta_t \tag{3.14}$$

$$\underline{\Gamma}_\perp = \frac{\underline{\varepsilon}_2 \sin\theta_i - \sqrt{\underline{\varepsilon}_2 - \cos^2\theta_i}}{\underline{\varepsilon}_2 \sin\theta_i + \sqrt{\underline{\varepsilon}_2 - \cos^2\theta_i}} \tag{3.15}$$

$$\underline{\Gamma}_\parallel = \frac{\sin\theta_i - \sqrt{\underline{\varepsilon}_2 - \cos^2\theta_i}}{\sin\theta_i + \sqrt{\underline{\varepsilon}_2 - \cos^2\theta_i}} \tag{3.16}$$

The complex permittivity $\underline{\varepsilon}_2$ of the reflection surface material can be expressed as

$$\underline{\varepsilon}_2 = \varepsilon' + j\frac{\sigma}{\omega}, \text{ with } \omega = 2\pi f, \tag{3.17}$$

where σ is the material conductivity, $j = \sqrt{-1}$, $\varepsilon' = \mathrm{Re}\{\underline{\varepsilon}_2\}$.

The consideration of individual complex reflection coefficients for each first-order reflection in an enhanced transmission channel model mimics the small local maxima and minima in the $P(d)$ measurement but with a much higher amplitude in most cases (figure 3.4). The reason is that the power levels of the reflection paths are estimated too high and thus their influence on the overall receiver signal is

estimated too high. Most probably, this is caused by the assumption that all signal paths experience the same, maximum antenna gain at the transmitter and the receiver.

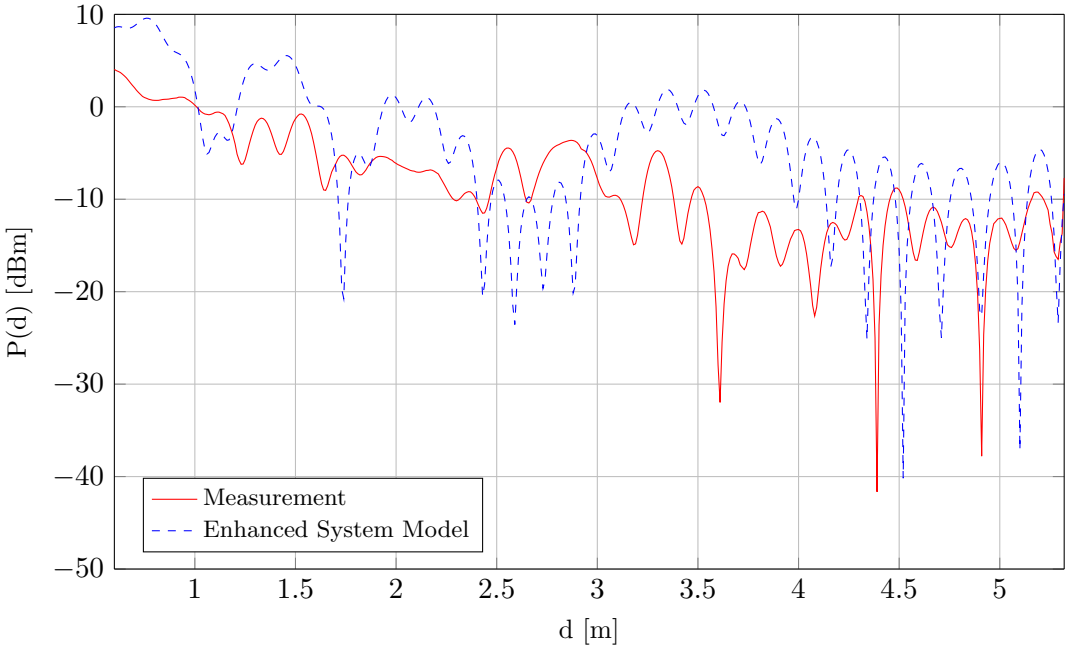

FIGURE 3.4: Comparison of RSS measurement and enhanced transmission channel model ($N = 7$ signal paths)

Up to this point, each surface of the environment is assumed as homogeneous with respect to the material properties. Thus, the calculation of the reflection coefficients for all reflections at one surface is based on the same complex permittivity. In reality, walls have built-in windows, doors, metal structures or other areas which are constructed from different materials. However, the preparation of the simulation with detailed wall structures would demand a very complex and time-consuming mapping of the environment. Thus, these structures are not considered in the enhanced transmission channel model.

3.2.3 Three-Dimensional Antenna Gain Pattern

Figure 3.5 depicts polar plots of a representative gain pattern (azimuth and elevation plane) for a typical patch antenna and four reflection signal paths that leave the antenna in $\pm 30°$ elevation and azimuth angles. The maximum antenna gain ($G_{\max} = 8.5$ dBi) is only available for the zero degree azimuth and elevation angles whereas the reflection signal paths experience a much lower gain.

As a conclusion, three-dimensional gain patterns have to be considered for the interrogator antenna,

$$G_{\text{ant,int}} = G_{\text{ant,int}}\left(\theta_n, \phi_n\right), \tag{3.18}$$

and for the tag antenna,

$$G_{\text{ant,tag}} = G_{\text{ant,tag}}\left(\theta_n, \phi_n\right), \tag{3.19}$$

where θ_n is the azimuth angle and ϕ_n is the elevation angle of the nth signal path with respect to the normal of the antenna.

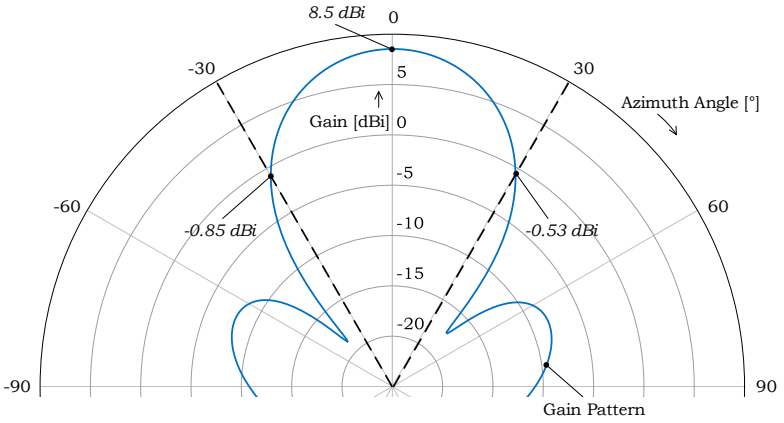

(a)

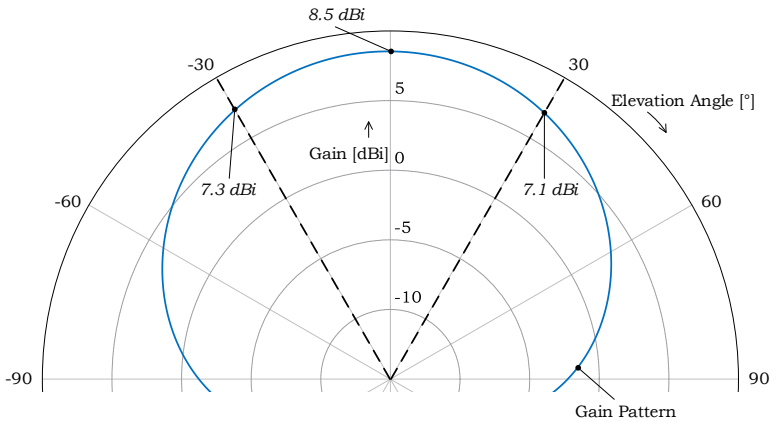

(b)

FIGURE 3.5: Antenna gain pattern (solid lines) and exemplary signal paths (dashed lines): (b) Azimuth plane of the antenna (b) Elevation plane of the antenna

Considering the tag and interrogator antenna gain pattern, the enhanced model equation (3.9) is modified to

$$P_{\text{Rx,tag}} = P_{\text{Tx,int}} \left(\frac{\lambda}{4\pi d_1}\right)^2 \left| \sum_{n=1}^{7} \sqrt{G_{\text{ant,int}}\left(\theta_n, \phi_n\right) G_{\text{ant,tag}}\left(\theta_n, \phi_n\right)} \underline{\Gamma}_n \frac{d_1}{d_n} e^{-jk(d_n - d_1)} \right|^2 \tag{3.20}$$

In the simulation of the enhanced model equation (3.20) (figure 3.6), the fading amplitudes fit the measurement results much better in several ranges of d. However, the locations of the maxima and minima in the simulation are spatially shifted with respect to the measurement in most cases. In the ranges 2.5 m $< d <$ 3.0 m and 3.5 m $< d <$ 4.2 m, also the simulated $P(d)$ amplitudes show a high deviation from the measurement. The spatial shift of the $P(d)$ development over d is most probably caused by inaccurate phase calculations. Thus, in order to further enhance the transmission channel model, the phase patterns of the antennas have to be considered.

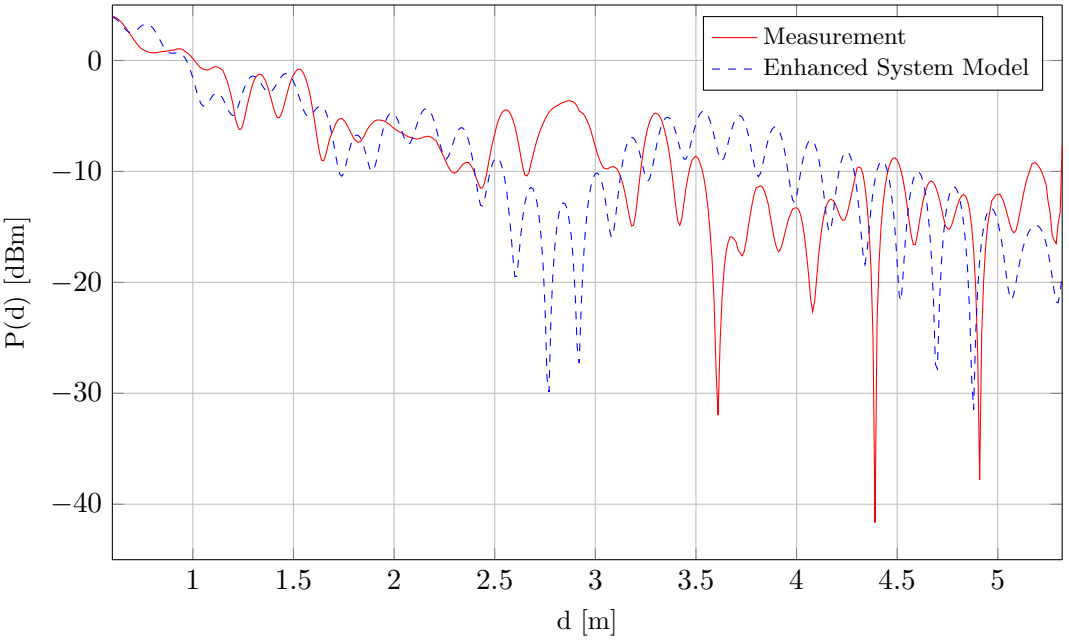

FIGURE 3.6: Comparison of RSS measurement and enhanced transmission channel model ($N = 7$ signal paths, three-dimensional antenna gain pattern)

3.2.4 Three-Dimensional Antenna Phase Pattern

Every antenna has a certain three-dimensional phase pattern (similar to the gain pattern) that depends on the antenna geometry and construction. Each of the N signal paths experiences a certain phase shift at the interrogator antenna, $\Delta\varphi_{\text{int}}(\theta_n, \phi_n)$, and at the tag antenna, $\Delta\varphi_{\text{tag}}(\theta_n, \phi_n)$, depending on the path angle with respect to the antenna.

As a consequence, the channel model equation (3.20) is further modified to consider the antenna phase pattern:

$$P_{\mathrm{Rx,tag}} = P_{\mathrm{Tx,int}} \left(\frac{\lambda}{4\pi d_1}\right)^2 \left| \sum_{n=1}^{7} \sqrt{G_{\mathrm{ant,int}}\left(\theta_n, \phi_n\right) G_{\mathrm{ant,tag}}\left(\theta_n, \phi_n\right)} \cdot \underline{\Gamma}_n \cdot \frac{d_1}{d_n} e^{-j(k(d_n - d_1) + \Delta\varphi_{\mathrm{int}}(\theta_n, \phi_n) + \Delta\varphi_{\mathrm{tag}}(\theta_n, \phi_n))} \right|^2 \tag{3.21}$$

The simulation of the enhanced channel model equation (3.21) shows a close match of the positions and amplitudes of the local maxima and minima with the $P(d)$ measurement (figure 3.7).

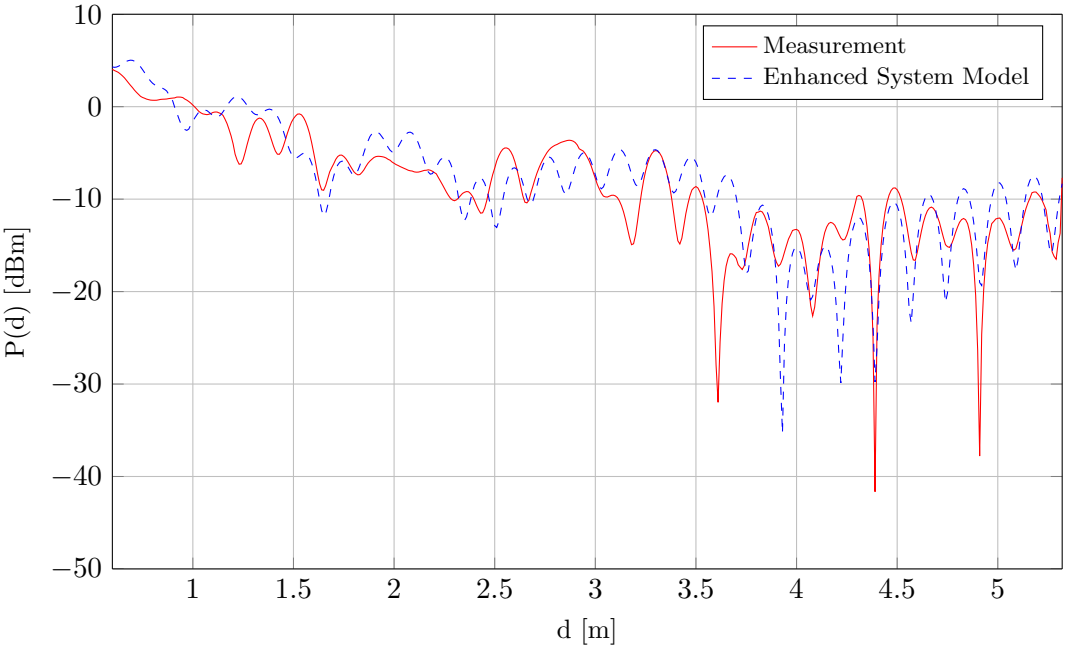

FIGURE 3.7: Comparison of RSS measurement and enhanced transmission channel model ($N = 7$ signal paths, three-dimensional antenna gain and phase pattern)

For the limited application scenario that was considered up to this point, the enhanced transmission channel model delivers a very close approximation of the real-world situation. However, for a simulation of the signal parameters in localization systems, some further enhancements and generalizations are required.

3.3 Enhancement of the Modified Friis-Model for Localization Systems

3.3.1 Circular Polarization

For the typical application scenario in this section, a very basic system setup with linearly polarized antennas is assumed. However, in most cases, commercial passive UHF RFID systems use circularly polarized antennas for the interrogator.

The electric field vector of a circularly polarized transmitter signal rotates around the axis of the propagation direction which changes the reflection coefficient of a surface to [245]

$$\underline{\Gamma}_C = \frac{\underline{\Gamma}_{\parallel} + \underline{\Gamma}_{\perp}}{2}, \tag{3.22}$$

where $\underline{\Gamma}_{\parallel}$ and $\underline{\Gamma}_{\perp}$ are the reflection coefficients for the linear polarizations (see equations (3.12) and (3.13)).

3.3.2 Polarization Mismatch Loss

The enhanced transmission channel model assumes matching polarizations of the interrogator and tag antennas. However, in reality, this is difficult to achieve. In typical application scenarios for passive UHF RFID systems, the orientation of the tags is random and non-predictable. In addition, typical RFID systems use circularly polarized patch antennas for the interrogator and linearly polarized dipole antennas for the tag. Thus, a polarization loss factor L_{pol} has to be considered for non-matching polarizations in the transmission channel model equation (3.21).

For two linearly polarized antennas [246],

$$L_{\mathrm{pol}} = \cos^2 \vartheta, \tag{3.23}$$

where ϑ is the rotation angle between the antennas.

A circularly polarized signal, in principle, consists of two orthogonal, linear electrical field components. In a combination of a linear antenna with a circular antenna, the linear antenna is only able to receive one of the two components which leads to $L_{\mathrm{pol}} = 0.5$.

If two circularly polarized antennas are used, the polarization mismatch loss depends on the axial ratio R of the antennas and is given by [246]:

$$L_{\mathrm{pol}} = \frac{1}{2} + \frac{4R_{\mathrm{s}}R_{\mathrm{r}} + (R_{\mathrm{s}}^2 - 1) \cdot (R_{\mathrm{r}}^2 - 1) \cdot \cos 2\Delta\xi}{2 \cdot (R_{\mathrm{s}}^2 + 1) \cdot (R_{\mathrm{r}}^2 + 1)}, \tag{3.24}$$

where R_s is the axial ratio of the received signal, R_r is the axial ratio of the receiver antenna and $\Delta\xi$ is the relative tilt angle between the major axes of the polarization ellipses of the signal and the receiver antenna.

3.3.3 Antenna Orientation

In the application example that is used for the model simulations and the measurements, the tag antenna and the interrogator are positioned on a straight line and are facing each other. However, in a practical passive UHF RFID system installation, both antennas have arbitrary coordinates (x, y, z) as well as arbitrary, three-dimensional orientations, $\theta_{\mathrm{ant,int}}$, $\phi_{\mathrm{ant,int}}$, and $\theta_{\mathrm{ant,tag}}$, $\phi_{\mathrm{ant,tag}}$. As an example, figure 3.8 (top) depicts a three-dimensional system setup that corresponds to the basic application scenario, but the positions and orientations of the interrogator and the tag are changed. The side view drawing in figure 3.8 (center) and the top view drawing in figure 3.8 (bottom) show the setup and all first-order reflection paths.

As described before, each of the $n = 1...N$ signal paths leaves the interrogator antenna and reaches the tag antenna in certain spatial angles, $\theta_{\mathrm{path,int},n}$, $\phi_{\mathrm{path,int},n}$ and $\theta_{\mathrm{path,tag},n}$, $\phi_{\mathrm{path,tag},n}$. This observation is considered in the enhanced transmission channel model by introducing the three-dimensional antenna gain and phase patterns. However, the definitions of the used path angles θ_n and ϕ_n have to be adapted to include the antenna orientations. For the interrogator, it holds

$$\theta_n = \theta_{\mathrm{path,int},n} + \theta_{\mathrm{ant,int}} \text{ and } \phi_n = \phi_{\mathrm{path,int},n} + \phi_{\mathrm{ant,int}}, \tag{3.25}$$

and for the tag,

$$\theta_n = \theta_{\mathrm{path,tag},n} + \theta_{\mathrm{ant,tag}} \text{ and } \phi_n = \phi_{\mathrm{path,tag},n} + \phi_{\mathrm{ant,tag}}. \tag{3.26}$$

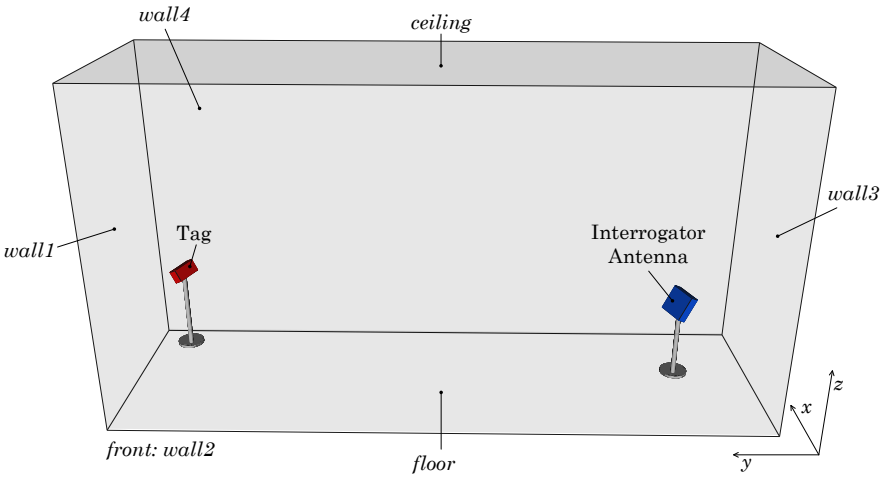

(a)

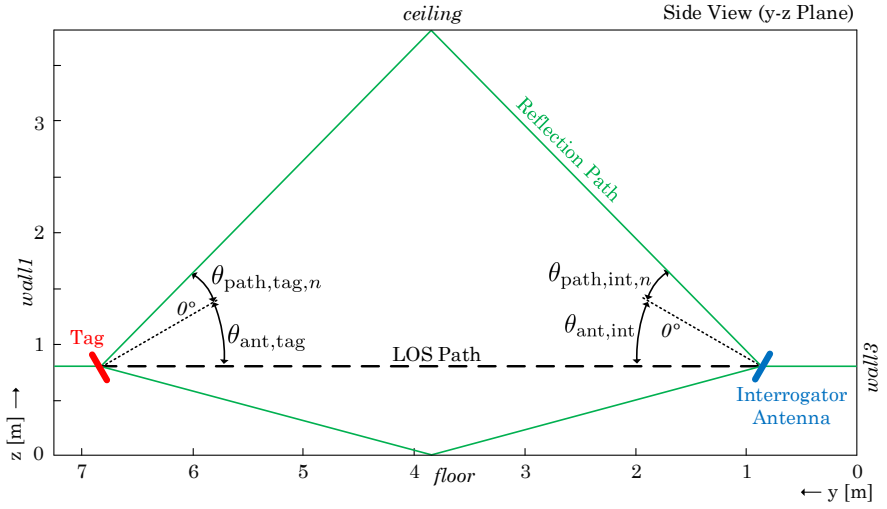

(b)

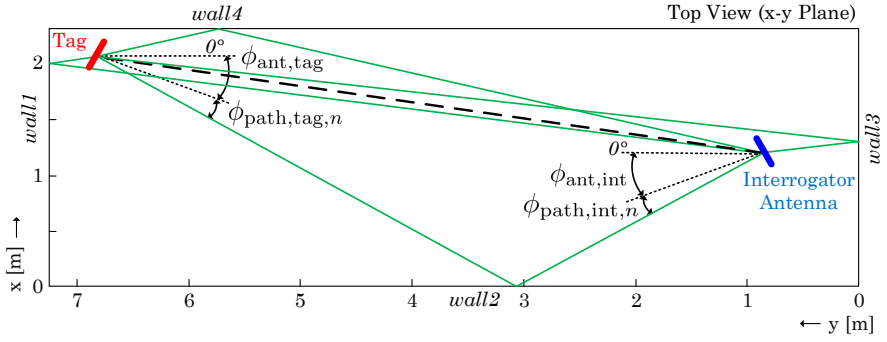

(c)

FIGURE 3.8: Signal paths in an UHF RFID system setup with arbitrary antenna orientations: (a) Three-dimensional view (b) Side View (c) Top view

3.3.4 Downlink Channel Model

Up to this point, only the downlink was considered in the enhanced transmission channel model. However, the model equation (3.21) can also be used for the uplink if the used backscatter principle is considered. Since the tag is not able to reflect the whole amount of signal power, $P_{\mathrm{Rx,tag}}$, it receives from the interrogator, a backscatter loss, L_{BS}, is introduced which is calculated as follows.

If $P_{\mathrm{Rx,tag}}$ is less than or equal to the tag sensitivity (typ. -17 dBm), the backscatter loss is fixed with a value of $L_{\mathrm{BS}} = 0.1$ (-10 dB). For received signal powers that are greater than the tag sensitivity, L_{BS} increases linearly with $P_{\mathrm{Rx,tag}}$ (1 dB increase of L_{BS} per 1 dB increase of $P_{\mathrm{Rx,tag}}$ [190]).

Considering that, the enhanced model equation for the uplink becomes

$$P_{\mathrm{Rx,int}} = P_{\mathrm{Tx,tag}} \left(\frac{\lambda}{4\pi d_1}\right)^2 \cdot \left| \sum_{n=1}^{7} \sqrt{G_{\mathrm{ant,int}}\left(\theta_n, \phi_n\right) G_{\mathrm{ant,tag}}\left(\theta_n, \phi_n\right)} \cdot \underline{\Gamma}_n \cdot \frac{d_1}{d_n} e^{-j\left(k\left(d_n - d_1\right) + \Delta\varphi_{\mathrm{int}}\left(\theta_n, \phi_n\right) + \Delta\varphi_{\mathrm{tag}}\left(\theta_n, \phi_n\right)\right)} \right|^2, \tag{3.27}$$

with

$$P_{\mathrm{Tx,tag}} = P_{\mathrm{Rx,tag}} \cdot L_{\mathrm{BS}}\left(P_{\mathrm{Rx,tag}}\right) \tag{3.28}$$

3.3.5 Received Signal Phase

The simulation of all biparameter-based localization approaches (e.g. receiver or transmitter beamforming) requires an estimation of the signal phase in addition to the signal power.

In a free-space environment, the phase $\varphi_{\mathrm{FS,tag}}$ of the received signal at the tag antenna is proportional to the interrogator-to-tag distance d_1:

$$\varphi_{\mathrm{FS,tag}} = k d_1 + \varphi_0, \text{ with } k = \frac{2\pi f}{c} \tag{3.29}$$

Without loss of generality, the initial phase is assumed as $\varphi_0 = 0°$.

Similarly to equation 3.21, an enhanced transmission channel model equation is introduced for the received signal phase at the tag in the downlink, $\varphi_{\mathrm{Rx,tag}}$, considering a superposition of $N = 7$ signal paths as

$$\varphi_{\mathrm{Rx,tag}} = \arg\left[\left(\sum_{n=1}^{7}\sqrt{G_{\mathrm{ant,int}}\left(\theta_n,\phi_n\right)G_{\mathrm{ant,tag}}\left(\theta_n,\phi_n\right)}\cdot\underline{\Gamma}_n\cdot \frac{d_1}{d_n}e^{-j\left(k\left(d_n-d_1\right)+\Delta\varphi_{\mathrm{int}}\left(\theta_n,\phi_n\right)+\Delta\varphi_{\mathrm{tag}}\left(\theta_n,\phi_n\right)\right)}\right)^2\right], \tag{3.30}$$

where arg() denotes the argument of a complex number.

The received signal phase, $\varphi_{\mathrm{Rx,int}}$, at the interrogator in the uplink is

$$\varphi_{\mathrm{Rx,int}} = \varphi_{\mathrm{Tx,tag}} + \arg\left[\left(\sum_{n=1}^{7}\sqrt{G_{\mathrm{ant,int}}\left(\theta_n,\phi_n\right)G_{\mathrm{ant,tag}}\left(\theta_n,\phi_n\right)}\cdot\underline{\Gamma}_n\cdot \frac{d_1}{d_n}e^{-j\left(k\left(d_n-d_1\right)+\Delta\varphi_{\mathrm{int}}\left(\theta_n,\phi_n\right)+\Delta\varphi_{\mathrm{tag}}\left(\theta_n,\phi_n\right)\right)}\right)^2\right], \tag{3.31}$$

where $\varphi_{\mathrm{Tx,tag}}$ is the initial transmitter (backscatter) phase of the tag which can be calculated using equation (3.30).

The comparison of the multipath phase development (equation (3.30)) in the downlink of the application scenario with the free-space phase development (equation (3.29)) shows that multipath significantly degrades the received signal phase (figure 3.9).

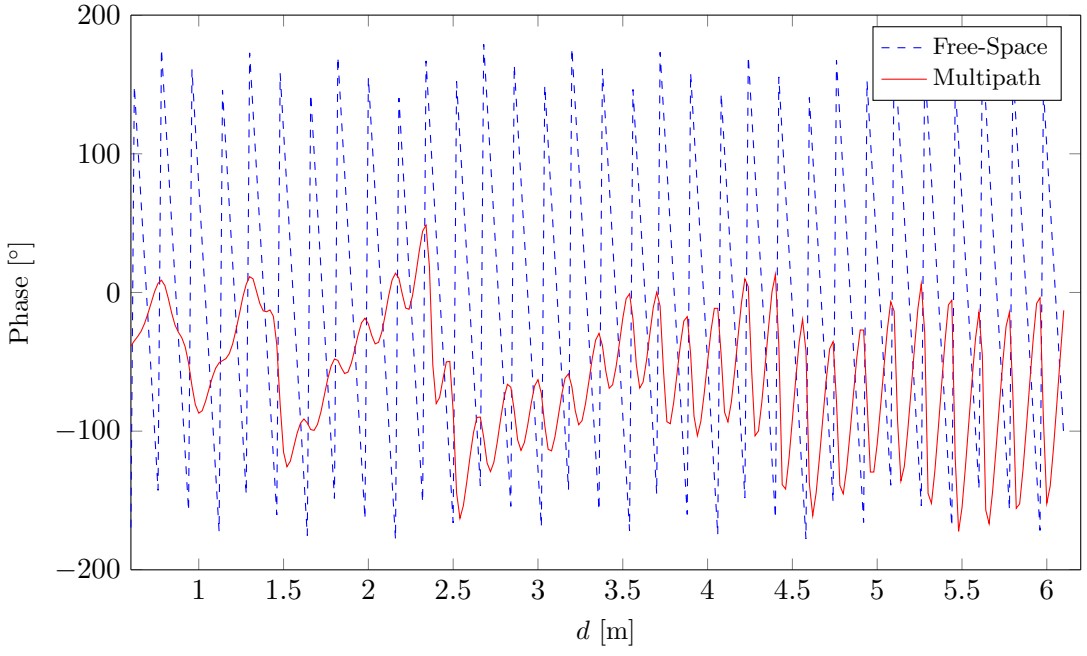

FIGURE 3.9: Phase simulation in the application scenario (free-space and multipath)

3.4 Development of a Simulation Environment

A simulation environment is developed using the software Matlab which implements the equations of the enhanced transmission channel model. In order to enable simulation capabilities for arbitrary localization environments and to provide a high ease of use, the full three-dimensional system setup and the geometry of the surrounding environment is specified in a specially designed Microsoft Excel configuration file. An example file is given in appendix B.2.

Based on the data included in the configuration file, the simulation environment calculates all parameters (e.g. path lengths or complex reflection coefficients) which are needed for the estimation of the received signal power and phase in the specified scenario. For the reflection surfaces, six different materials can be chosen independently (see appendix B.3).

Any type of antenna can be used for the interrogator and the tag because the simulation environment provides a data import of measured or simulated antenna gain and phase pattern as well as the consideration of the three different antenna polarizations.

For an easy interpretable representation of the simulation results (estimated signal power and phase data), the simulation environment is able to generate various plots (one-, two- and three-dimensional). As an example, figure 3.10 shows a two-dimensional power and a phase simulation for the downlink of the basic application scenario from the previous sections. In addition, a three-dimensional drawing of the simulation scenario can be generated which displays all reflection paths and the coordinates of the surface reflection points. Further examples of generated plots and drawings are provided in appendix B.4.

The calculation of one signal amplitude or phase value in the up- or downlink takes around 20 ms on standard PC hardware. The full two-dimensional simulation (amplitudes or phases as in figure 3.10) of the measurement setup that consists of $M = 231 \times 686 = 158.466$ calculation points arranged in a $0.01\,\mathrm{m} \times 0.01\,\mathrm{m}$ grid takes approximately 50 minutes to execute.

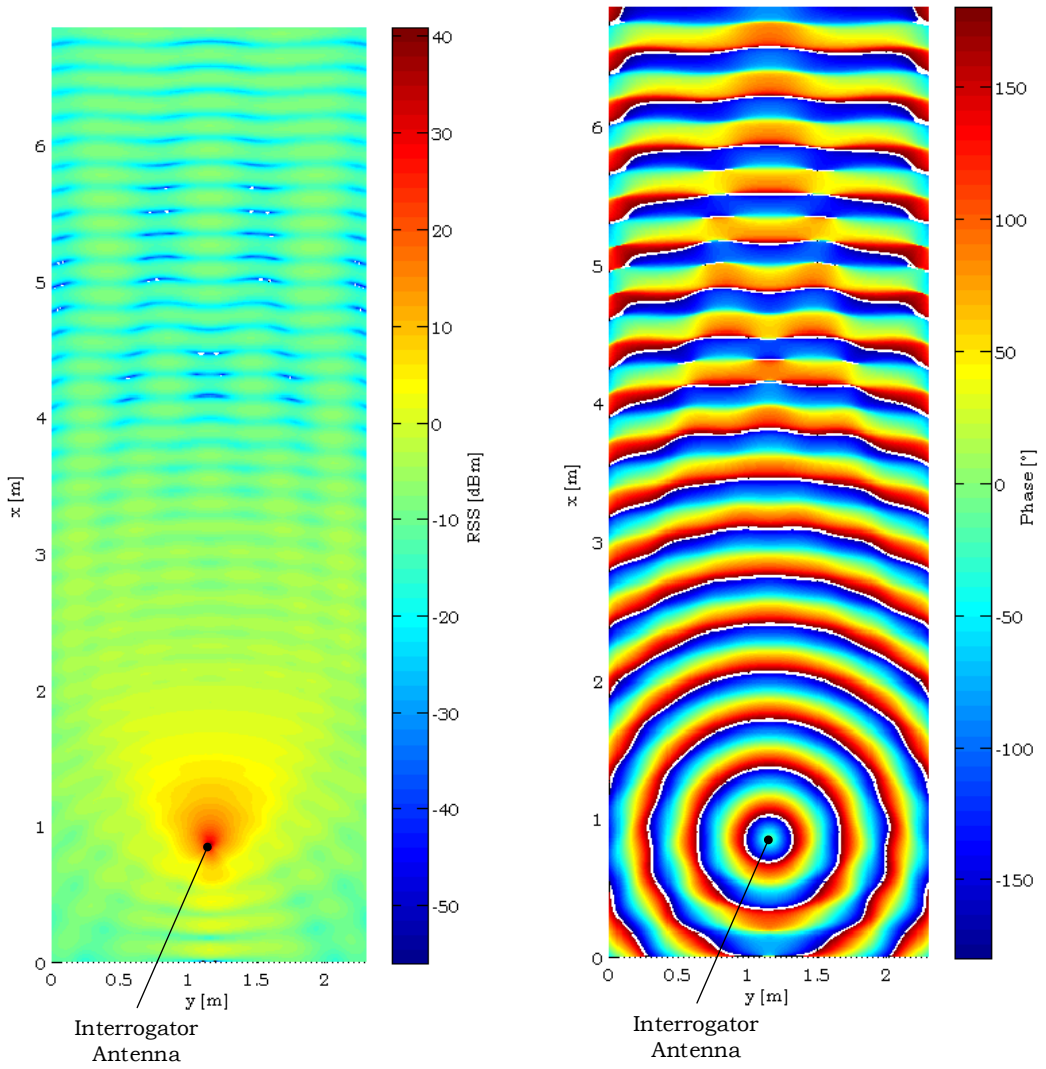

FIGURE 3.10: Two-dimensional RSS simulation (A) and phase simulation (B) of the application scenario

3.5 Tag Readability Estimation

Usually, the basic Friis Transmission Equation is used to calculate the maximum read range of a tag in a certain passive UHF RFID system setup [242, 247, 248]. It is assumed that such systems are always downlink limited, i.e. if the received signal power at the tag in the downlink is high enough to activate the tag, the received signal power at the interrogator will exceed the interrogator sensitivity. Since the Friis equation does not consider multipath, it only allows an estimation of the maximum read range but not an estimation of spatially limited no-read zones.

For simulations and measurements of the tag readability, a 0.3 m × 0.3 m grid of tag positions is placed into three different scenarios:

- An office room of size 7.25 m × 2.30 m × 3.00 m with a line-of-sight between all tag positions and the interrogator antenna (LOS1 scenario)
- An office room of size 7.25 m × 2.30 m × 3.00 m with no line-of-sight for several tag positions (NLOS scenario)
- A seminar room of size 7.10 m × 4.70 m × 3.00 m with a line-of-sight for all tag positions (LOS2 scenario)

A detailed description of the setup and the procedures as well as detailed measurement and simulation results are given in appendix B.5.

Table 3.3 summarizes the results of the tag read region simulations. The readability of tags located at 87% of the measurement points is simulated correctly. From the wrongly estimated 13% of the tag measurement points, only 8% are simulated as readable but are not readable in the measurement. This verifies the reliability of the simulation framework and the enhanced transmission channel model.

From the simulation results in appendix B.5, it can also be concluded that the estimation of the tag readability cannot be based on the downlink alone. Different no-read zones can be found in both links that have to be combined to make a general prediction of the tag readability.

TABLE 3.3: Results of readability simulations based on the enhanced transmission channel model

Scenario	**Measurement Points**	**Simulation Correct**	**Simulation Incorrect**	**False No-Read in Simulation**	**False Read in Simulation**
LOS 1	133	116 (87%)	17 (13%)	9 (7%)	8 (6%)
LOS 2	266	228 (86%)	38 (14%)	6 (2%)	32 (12%)
NLOS	130	114 (88%)	16 (12%)	10 (8%)	6 (4%)
SUM	**529**	**458 (87%)**	**71 (13%)**	**25 (5%)**	**46 (8%)**

3.6 Summary

On the basis of a modified Friis model, an enhanced transmission channel model for passive UHF RFID localization systems has been developed.

The enhanced model equation includes several characteristics of the channel and the channel interface of the interrogator and the tag which allows an accurate estimation of received signal power in both links of a passive UHF RFID localization system: a superposition of the LOS and all first-order reflections, three-dimensional gain and phase patterns of the antennas (individually for each signal path), different antenna polarizations, antenna orientations, complex reflection coefficients of the reflection surfaces (individually for each surface) and the antenna polarization loss.

Simulations of a typical localization scenario have been used to demonstrate the improvements of every extension of the channel model equation.

An additional channel model equation for the received signal phase was presented which considers the same characteristics as the received signal power equation.

The final channel model equations have been used to implement a new simulation environment which is flexible, easy-to-use, easy-to-setup and achieves low computing times (e.g. 50 minutes for the full, high-resolution simulation of a typical application scenario).

The high reliability (87%) of tag readability simulations has verified the estimation accuracy of the enhanced transmission channel model. In addition, the general assumption that the tag readability in passive UHF RFID systems only downlink limited [247] was proven wrong.

Various simulations have confirmed that multipath highly deteriorates any signal parameter measurement in passive UHF RFID localization system. It thus necessary to investigate techniques for a reduction of multipath effects. The new simulation framework is the ideal tool for an efficient analysis of these techniques.

Chapter 4

Minimization of the Effects of Multipath

In chapter 3, an enhanced Friis-based channel model was derived, and it was concluded that the enhanced model that included multiple signal paths (reflected signals) and all channel interface parameters, could be regarded as the general channel model for received signal power and phase estimations in passive UHF RFID localization systems. Based on the general channel model, the influence of multipath interference on the received signal power and phase was investigated by simulation. In this chapter, three solutions are proposed to minimize the effects of multipath interference: a) by varying the channel interface parameters, b) by applying diversity techniques, c) by the installation of UHF absorbers. Each of the three solutions is explained, modelled and simulated. The simulation results are presented which demonstrate the benefits of the proposed solutions.

4.1 Minimization of Multipath Interference

Since the characteristics of the localization environment (e.g. physical dimensions and surface materials etc.) define the wireless channel in the space between the interrogator antenna and the tag antenna, only the channel interface parameters can be modified to alter the behaviour of the channel and, hence the effects of multipath signals. These parameters are included in the enhanced transmission channel model (chapter 3). For convenience, the equations for the received tag signal power, $P_{\mathrm{Rx,int}}$, and the receive tag signal phase, $\varphi_{\mathrm{Rx,int}}$, in the uplink are reproduced here (equations (4.1) and (4.2)):

$$P_{\mathrm{Rx,int}} = P_{\mathrm{Tx,tag}} \left(\frac{\lambda}{4\pi d_1}\right)^2 \cdot \left| \sum_{n=1}^{7} \sqrt{G_{\mathrm{ant,int}}\left(\theta_n, \phi_n\right) G_{\mathrm{ant,tag}}\left(\theta_n, \phi_n\right)} \cdot \underline{\Gamma}_n \cdot \frac{d_1}{d_n} e^{-j\left(k\left(d_n - d_1\right) + \Delta\varphi_{\mathrm{int}}\left(\theta_n, \phi_n\right) + \Delta\varphi_{\mathrm{tag}}\left(\theta_n, \phi_n\right)\right)} \right|^2 \tag{4.1}$$

$$\varphi_{\mathrm{Rx,int}} = \varphi_{\mathrm{Tx,tag}} + \arg\left[\left(\sum_{n=1}^{7} \sqrt{G_{\mathrm{ant,int}}\left(\theta_n, \phi_n\right) G_{\mathrm{ant,tag}}\left(\theta_n, \phi_n\right)} \cdot \underline{\Gamma}_n \cdot \frac{d_1}{d_n} e^{-j\left(k\left(d_n - d_1\right) + \Delta\varphi_{\mathrm{int}}\left(\theta_n, \phi_n\right) + \Delta\varphi_{\mathrm{tag}}\left(\theta_n, \phi_n\right)\right)} \right)^2 \right] \tag{4.2}$$

Since the two links in a passive UHF RFID system are reciprocal, only the uplink (tag $\rightarrow$ interrogator) is considered. In addition to that, all signal measurements in a target tag localization system are conducted at the interrogator in the uplink.

As can be seen from equation (4.2), the received signal phase in the uplink, $\varphi_{\mathrm{Rx,int}}$ is a superposition of the phases of the single signal paths weighted with their relative signal power. Because a reduction of the influence of multipath has the same effect on $\varphi_{\mathrm{Rx,int}}$ as on $P_{\mathrm{Rx,int}}$, the analyses in this chapter focus on the received signal power, $P_{\mathrm{Rx,int}}$, where multipath leads to constructive and destructive interference (power fading).

4.1.1 The Channel Interface Parameters

According to equation (4.1), the following parameters of the channel interface can be manipulated: a) the gain pattern of the interrogator antenna ($G_{\text{ant,int}}(\theta_n, \phi_n)$) and the tag antenna ($G_{\text{ant,tag}}(\theta_n, \phi_n)$) which are defined by the antenna type and the antenna orientation (chapter 3), b) the complex reflection coefficients of the signal paths ($\underline{\Gamma}_n$) which are defined, amongst others (e.g. the signal incidence angle), by the polarization of the tag antenna in the uplink.

A manipulation of the antenna phase pattern, $\Delta\varphi_{\text{int}}(\theta_n, \phi_n)$ and $\Delta\varphi_{\text{tag}}(\theta_n, \phi_n)$, is not feasible because it depends on the unique physical properties and construction of the antenna is not easily predictable.

The tag transmitter power, $P_{\text{Tx,tag}}$, and the tag transmitter phase, $\varphi_{\text{Tx,tag}}$, in the uplink are defined by the received signal power and the received signal phase at the tag in the downlink. They can only be manipulated by changing the interrogator transmitter power and phase. However, a change of the tag transmitter power only causes an equal change of the signal power of all signal paths. The same holds for a phase variation where the phase change of the tag transmitter signal equally effects all signal paths. In essence, this leads to a changed signal power and/or phase of the overall interrogator receiver signal and does not change the effects of multipath. Thus, without loss of generality, a fixed tag transmitter power, $P_{\text{Tx,tag}}$, and a fixed initial tag transmitter phase of $\varphi_{\text{Tx,tag}} = 0°$ are assumed for the following analyses.

4.1.1.1 Antenna Type

The type of the interrogator antenna and the tag antenna directly influences the corresponding gain pattern and thus the individual path gains, $G_{\text{ant,int}}(\theta_n, \phi_n)$ and $G_{\text{ant,tag}}(\theta_n, \phi_n)$, in equation (4.1).

Two different antenna types, in general, can be differentiated: non-directional[1] and directional antennas. If non-directional antennas are used ($G_{\text{ant}}(\theta_n, \phi_n) = G_n =$ const.), the LOS path as well as the reflection paths experience the same gain at the tag and at the interrogator. Thus, the influence of reflections on the overall interrogator receiver signal is high. It can be reduced by applying directional antennas that usually have a high gain in boresight (main lobe direction) and

[1]The principle of a non-directional or an omnidirectional antenna is only theoretical. In practice, every antenna is more or less directional. For example, a dipole radiates omnidirectionally only for one plane (e.g. the azimuth plane for a vertically polarized dipole).

lower gains towards other directions (side lobe and null directions). Signal paths that leave the tag antenna or arrive at the interrogator antenna at directions other than the boresight are attenuated by the lower gain. Although patch antennas help to reduce the influence of certain multipath components, their practical application has limits.

Commercially available passive UHF RFID tags have a dipole antenna that is omnidirectional in one plane (e.g. the azimuth plane for a vertically polarized dipole). Due to the random orientation of tags in typical applications, this omnidirectivity is required to enhance the tag readability. In order to use a patch antenna for the tag, the design of a custom tag is required. In addition, patch antennas are larger than dipoles, not as cost-effective and limit the possible localization target types. At the interrogator, directional antennas have the disadvantage of a limited angular tag read range.

4.1.1.2 Antenna Polarization

The antenna polarization of the transmitter (interrogator) directly influences the reflection coefficient $\underline{\Gamma}_n$ for the reflected signal paths ($n = 2...7$) in equation (4.1) and thus the corresponding signal path power (section 3.2).

There exist two different antenna polarizations: linear and elliptical. A special case of elliptical polarization is circular polarization that is almost exclusively used for commercial UHF RFID interrogator antennas. Dipoles or monopoles are linearly polarized and can be arranged vertically or horizontally. Patch antennas can be designed for linear or circular polarization.

In a multipath environment, the amount of reflected signal power depends on the material of the reflection surface, the incidence angle of the signal, and the signal polarization (see equations (3.15), (3.16) and (3.22)).

Figure 4.1 compares the reflection coefficients for the three different polarizations as a function of the signal incidence angle at a surface, assuming concrete (mean reflection coefficient $\overline{\Gamma} = 0.5$) as the reflection material. Horizontal polarization delivers the highest reflection coefficients, followed by vertical polarization. The lowest mean reflection coefficient is achieved with circular polarization.

In a real-world multipath scenario, the signal distribution is much more complex than in the previous example. Several signal paths with different reflection angles interact depending on the geometric relations for each tag location. Thus, the

influence of the different polarizations on the overall receiver signal should be analysed in further simulations.

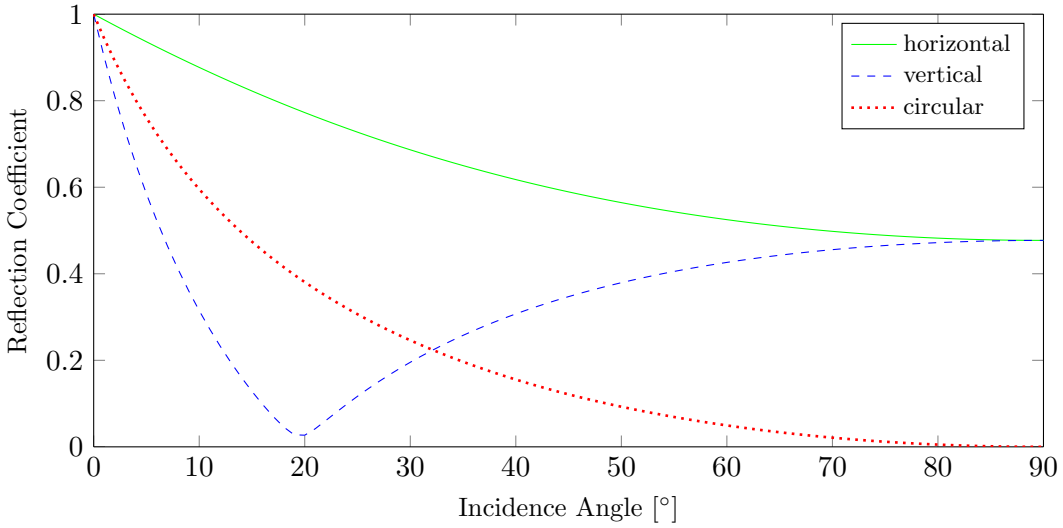

FIGURE 4.1: Reflection coefficients for different polarizations

The use of circularly polarized antennas introduces another interesting effect. Circular polarization can be left-handed (LHCP, left hand circular polarization) or right-handed (RHCP, right hand circular polarization) and circular antennas have a fixed direction. RHCP means that the electric field vector of the circular signal rotates clockwise along the direction of propagation. In LHCP polarization it rotates counter-clockwise. If a left-handed transmitter signal is reflected at a surface, it changes its polarization to right-handed. For this RHCP signal, the axial ratio is $R_\mathrm{s} = -1$ and for the LHCP receiver antenna that is matched with the transmitter antenna $R_\mathrm{r} = 1$. This results in a polarization mismatch loss of $L_\mathrm{pol} \to \infty$ (see equation (3.24) in section 3.3). As a consequence, the power of the received RHCP signal at the LHCP antenna approaches zero.

In practice, non-matching circular polarization directions lead to a signal attenuation in the range between 10 dB and 20 dB [249]. Thus, the signal power level of the reflections is decreased by at least 10 dB compared to the LOS signal which should highly reduce the effects of multipath.

4.1.1.3 Antenna Orientation

The orientation of target tags in a passive UHF RFID localization system is random and cannot be influenced. However, the orientation of the interrogator antenna (azimuth angle $\phi_\mathrm{ant,int}$ and elevation angle $\theta_\mathrm{ant,int}$) directly influences

the individual antenna gain $G_{\text{ant,int}}(\theta_n, \phi_n)$ for each incident signal path because $\theta_n = \theta_{\text{path,int},n} + \theta_{\text{ant,int}}$ and $\phi_n = \phi_{\text{path,int},n} + \phi_{\text{ant,int}}$. According to equation (4.1), this has a different effect on the received signal power of each path and thus influences the overall receiver signal at the interrogator.

For a further analysis, the gain pattern of the antenna used has to be considered that depends on the specific antenna type. Figure 4.2 shows three representative, simulated gain patterns in the azimuth plane: a dipole, a patch antenna and a three-element patch antenna array. If an omnidirectional antenna is used for the interrogator, a change of the antenna orientation does not alter the gain pattern and thus not the fading characteristic (dipole in figure 4.2). For directional antennas, different cases have to be considered.

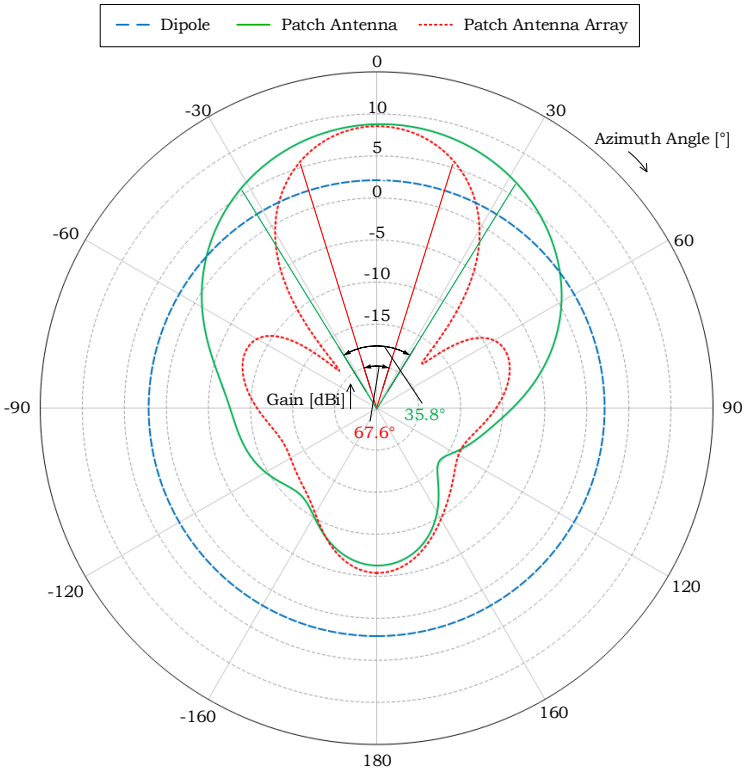

FIGURE 4.2: Three different antenna gain patterns

Directional antenna gain patterns, in general, consist of a main lobe, side lobes, and nulls. A characteristic value is the 3dB-beamdwidth that specifies the width of the main lobe (angular range between the two points where the antenna gain is $G_{\text{3dB}} = G_{\text{max}} - 3$ dB). If the interrogator antenna has a high 3dB-beamwidth (e.g. the patch antenna in figure 4.2), the gain difference for the individual signal paths is only minor and only a minor reduction of multipath effects is achieved. Antennas with small 3dB-beamwidths (e.g. the antenna array in figure 4.2) can

highly reduce the gain experienced by the reflection signal paths and thus reduce their influence on the overall receiver signal. Further investigations have to be conducted to evaluate a practical application in passive UHF RFID localization systems. It must be noted that the discussed effects of the antenna orientation on multipath are identical for the azimuth and the elevation plane of the antenna.

4.1.2 Diversity Combining Techniques

A well-established approach to mitigate the effects of multipath in wireless communication systems is diversity. In a diversity system, two uncorrelated versions of the desired signal are generated by switching between different parameter values of the transmitter channel interface. In an optimum case, the diversity signals experience independent characteristics of the wireless channel and are thus differently affected by multipath. It has been shown, that diversity improves the SNR in wireless communication systems at relatively low cost because it is easily implementable [51]. For example, almost all modern WLAN hardware as well as GSM or UMTS base stations comprise multiple antennas for diversity [250, 251].

If multiple, uncorrelated copies of the same receiver signal are available in a diversity system, they have to be combined in a way that the system performance is optimized.

4.1.2.1 Diversity and Combining Principles

The existing diversity techniques are time diversity, frequency diversity, spatial diversity and polarization diversity. In a time diversity system, the same signal is transmitted at two or more distinct times. However, for the investigations in this work, a static environment and thus a static channel between the interrogator and the tag are assumed. Furthermore, the spatial position of the tag is assumed as static whereby time diversity achieves no effect on multipath. Frequency diversity systems transmit the same signal on different carrier frequencies, whereas spatial diversity involves multiple transmitter or receiver antennas that are spatially separated. Both approaches are applicable to the interrogator in a passive UHF RFID localization system. The application of polarization diversity (e.g. switching between vertical and horizontal polarization) in passive UHF RFID localization systems is rather simple because it requires two differently oriented target tags and two matching interrogator antennas.

For the combination of multiple diversity signals, four combining methods are used: switched combining, selection combining, maximal-ratio combining, and equal gain combining [252]. The choice of the combining method, in general, is independent of the used diversity technique.

In switched combining, the receiver constantly measures the RSS of the currently used diversity signal. If it drops below a predefined threshold, the receiver switches to a different diversity signal. The principle of selection combining is to constantly measure the RSS of all available diversity signals and to select the strongest. Equal gain combining adds together all available receiver diversity signals coherently while maximal-ratio combining weights each diversity signal with its respective SNR value prior to the summation.

All of the described combining techniques, in principle, can be applied to passive UHF RFID systems to improve the SNR and thus the tag readability. However, passive UHF RFID localization systems have special requirements. Since an evaluation of the originally transmitted target tag signal is needed, equal-gain and maximal-ratio combining cannot be used because they rely on a sum signal. Selection and scanning combining can be applied to passive UHF RFID localization systems because they use switching between different diversity signals based on the individual signal strength. For all investigations in this chapter, two diversity signals are used. In this case, both combining methods (selection and scanning) deliver the same result of choosing the strongest signal.

In the next sections, the applicability of the different diversity techniques to passive UHF RFID localization systems is discussed.

4.1.2.2 Frequency Diversity

In equation (4.1), the system frequency f is included in the factor $k = \frac{2\pi f}{c}$. k directly influences the phase of the multipath signals and thus the spatial regions of constructive and destructive interference. By switching between two different frequencies (frequency diversity), fading locations in a specific environment are spatially shifted which should reduce the effects of multipath in a passive UHF RFID localization system. In order to make frequency diversity effective, the available frequency bandwidth in a wireless communication system must be higher than the coherence bandwidth B_c [253]. In passive UHF RFID systems, the available bandwidth is limited by worldwide frequency regulations [18]. Only the US frequency range that applies to ten countries provides a sufficient bandwidth for frequency

diversity. However, since the application scenarios and operational principles of passive UHF RFID systems are very unique amongst wireless communication systems, it is reasonable to further investigate the applicability of frequency diversity.

4.1.2.3 Spatial Diversity

In a spatial diversity system, two or more interrogator receiver antennas with different locations are installed. This results in different path lengths d_n in the considered scenario and different complex reflection coefficients $\underline{\Gamma}_n$. According to equation (4.1), these changes lead to a different fading characteristic for each interrogator antenna location. Thus, spatial diversity combining should reduce the effects of multipath. However, the minimum needed interrogator antenna displacement to achieve a significant reduction of the effects of multipath has to be further investigated.

4.1.2.4 Polarization Diversity

Switching between horizontal and vertical antenna polarization in a polarization diversity system changes the reflection coefficient, $\underline{\Gamma}_n$, for each signal path. As a consequence, the superposition of all signal paths at the interrogator and thus the received signal power, $P_{\mathrm{Rx,int}}$, is different for both polarizations. This should reduce the effects of multipath in a passive UHF RFID localization system. However, the complex interaction of multiple signal paths and the effects of the different polarizations on the interrogator receiver signals must be investigated in further simulations.

4.1.3 Reflection Cancellation

If the localization area is spatially limited and the signal reflection points at the surfaces of the localization environment are known, high-frequency absorbers can be attached to the these reflection points. This leads to very low reflection coefficients $\underline{\Gamma}_n \rightarrow 0$ for the reflection signal paths ($n = 2...7$) and reduces their influence on the overall receiver signal (equation (4.1)). An investigation of how far this this approach is feasible in practice is needed.

4.2 Verification of Multipath Reducing Techniques

In the next sections, the received signal power development, $P(d)$, as a function of the interrogator-to-tag distance, d, is simulated in a typical application scenario to further investigate the practical feasibility of the theoretically analysed techniques for a reduction of multipath effects. For this purpose, the previously introduced simulation environment is used. Each technique is considered individually to avoid interdependencies.

First, a new way to quantify the magnitude of multipath effects in a specific system setup is presented that helps to compare the impact of multipath reducing techniques.

4.2.1 Fading Quantification

The 'fading quantification'FQ is introduced to assess the effects of multipath on the received signal power in a specific scenario. In a free-space situation where no reflections are present, the received signal power $P(d)$ decreases proportional to $\frac{1}{d^2}$ (according to the Friis equation; see section 2.5).

The magnitude of fading maxima and minima in two-dimensional RSS measurements or simulations ($P(d)$ versus d) is quantified using their root mean squared deviation from a Friis-based degradation of the signal amplitude. For this purpose, the M signal power measurement or simulation values $P_0 ... P_{M-1}$ are interpolated in a fitting Friis function $P_\mathrm{F}(d)$ (for this interpolation, the Matlab curve fitting tool can be used). Then, the root mean squared deviation FQ between the interpolation graph and the measurement or simulation graph, respectively, is calculated as

$$FQ = \sqrt{\frac{1}{M} \sum_{m=0}^{M-1} \left(P_m - P_{\mathrm{F},m}\right)^2}. \tag{4.3}$$

The higher the FQ value is, the higher is the magnitude of multipath effects. For example, for the simulation of the RSS measurement setup from the previous chapter (section 3.1, figure 3.7), $FQ = 22.2$ dB[2] and the ideal, free-space case leads to $FQ = 0$ dB.

[2]Note that equation (4.3) delivers linear values that can be converted to logarithmic values in dB

4.2.2 Simulation Scenario

The typical application scenario from the previous chapter (section 3.1) is used as the basic setup for an investigation of multipath reducing techniques. Table 4.1 lists the parameters of the used passive UHF RFID system and the surrounding environment.

TABLE 4.1: System setup of the standard simulation scenario

Parameter	Value
Room Size (Length, Width, Height)	(7.25, 2.30, 3.80) m
Int. Antenna Position (x, y, z)	(1.15, 0.85, 1.50) m
Tag Antenna Position (x, y, z)	(1.15, 1.45...6.95, 1.50) m
Frequency (f)	867.1 MHz ($\lambda = 0.345$ m)
Transmitter Power $(P_{\mathrm{Tx,tag}})$	20 dBm
Num. of Signal Paths (N)	7 (LOS and six reflections: four walls, floor, ceiling)
Int. Antenna Polarization	vertical
Tag Antenna Polarization	vertical
Polarization Loss (L_{pol})	0
Int. Antenna Type	patch
Tag Antenna Type	dipole
Int. Antenna Orientation (θ, ϕ)	$(0, 0)^\circ$
Tag Antenna Orientation (θ, ϕ)	$(0, 180)^\circ$
Antenna Gain Patterns	simulated with FEKO
Antenna Phase Patterns	simulated with FEKO
Reflection Surface Materials	wall 1, wall 4: gypsum board ($\underline{\varepsilon}_2 = 6.2 + j0.69$) wall 2, floor, ceiling: concrete ($\underline{\varepsilon}_2 = 7.9 + j0.89$) wall3: glass ($\varepsilon_2 = 3$)

4.2.3 Antenna Type

Four different combinations of tag and interrogator antenna types (dipole or patch) are simulated to investigate their influence on multipath fading (table 4.2). The simulation of two passive UHF RFID systems with a fixed dipole interrogator antenna and a dipole or a patch tag antenna shows a reduction of multipath effects for the tag patch antenna (figure 4.3). Because patch antennas are directional, single reflections in the setup are highly attenuated. This is confirmed by the simulated fading quantification which is reduced from 28.5 dBm to 22.2 dB (22% improvement; table 4.2).

Due to the attenuation of single signal paths described above, the use of an interrogator patch in antenna in combination with a dipole tag antenna also reduces multipath effects (figure 4.4). However, the lowest FQ value of 15.9 dB is achieved by using a combination two patch antennas (improvement of 44%).

Although standard passive UHF RFID tags use dipole antennas, a replacement with patch antennas is beneficial for localization systems. The disadvantage is that

patch antennas are not as size- and cost-effective as dipoles. In addition, patch antennas do not emit signal energy rearwards which makes an orientation of the tag towards the interrogator antenna necessary. Thus, the use of patch tag antennas is required for an optimum localization accuracy but limits the possible application. However, even the use of a patch antenna for the interrogator in combination with a dipole tag reduces the effects of multipath significantly compared to a dipole antenna system.

TABLE 4.2: Setup parameters and fading quantifications for the antenna type simulations

Setup	**Parameter**	**Value**	*FQ* **[dB]**
1	Int. Antenna Type Tag Antenna Type	Dipole Dipole	28.5
2	Int. Antenna Type Tag Antenna Type	Dipole Patch	22.2
3	Int. Antenna Type Tag Antenna Type	Patch Dipole	22.0
4	Int. Antenna Type Tag Antenna Type	Patch Patch	15.9

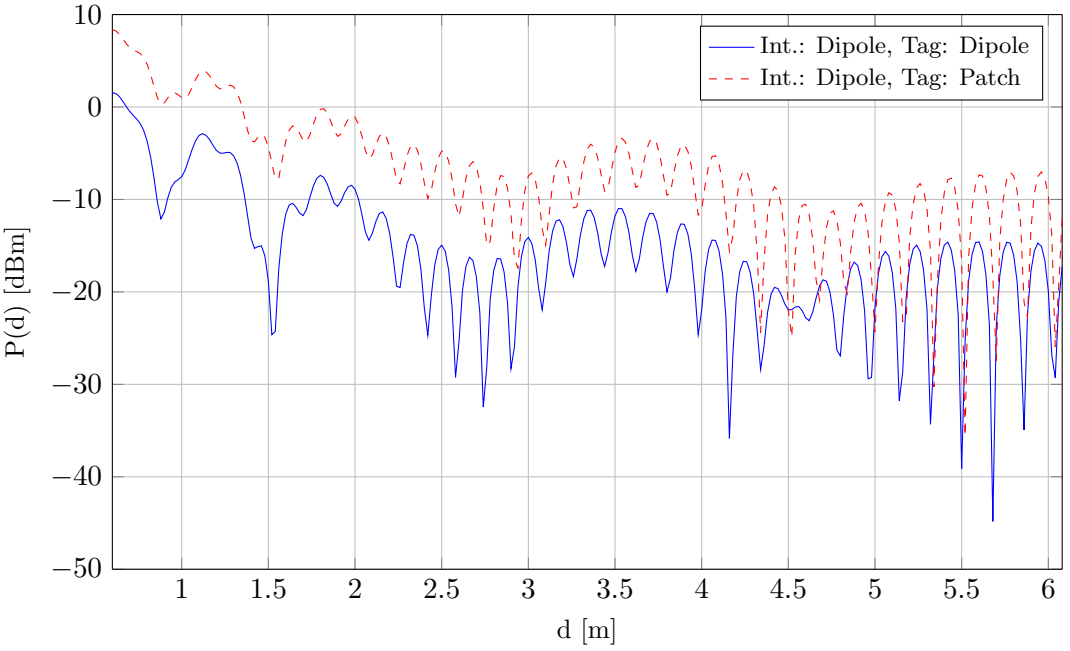

FIGURE 4.3: Simulation of different tag antenna types with a dipole interrogator antenna

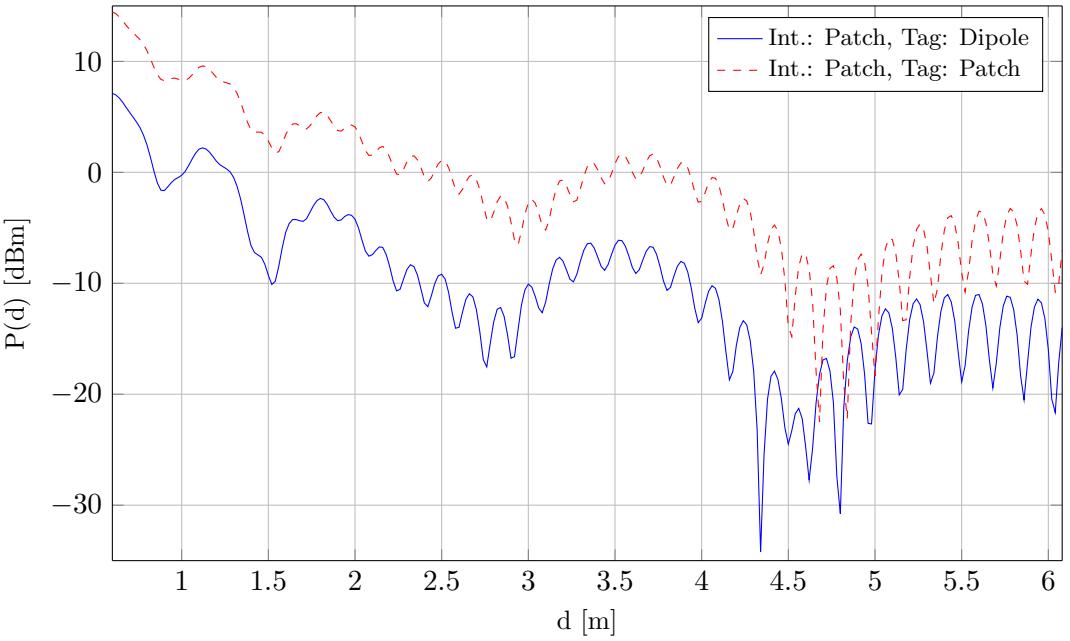

FIGURE 4.4: Simulation of different tag antenna types with a patch interrogator antenna

4.2.4 Antenna Polarization

The three different antenna polarizations used in passive UHF RFID systems (linear vertical, linear horizontal, circular) theoretically allow nine different combinations of tag and interrogator antennas. However, the practical application introduces several limitations.

In the two combinations vertical/horizontal (notation 'interrogator antenna polarization/tag antenna polarization') and horizontal/vertical, no signal energy can be received (signal attenuation is infinite).

In typical localization applications, the orientation of the target tag is random and a vertical or horizontal orientation cannot be guaranteed. Thus, the combinations vertical/vertical and horizontal/horizontal are only theoretical and would limit the possible applications. In the combinations circular/linear and linear/circular, the orientation of the linear antenna is not important. However, both combinations involve a polarization loss of 3 dB which leads to a reduced reading range. A circular/circular system has no polarization loss and equal performance for any antenna orientation.

Seven different antenna polarization combinations for the tag and the interrogator are simulated to further investigate their effects on multipath fading (table 4.3). In all cases, patch antennas are chosen to achieve comparable results.

The simulated fading characteristics (figure 4.5 and table 4.3) show that circular polarization outperforms the two linear cases with a very low FQ of 3 dB (81% improvement compared to linear polarization). The disadvantage is that only patch antennas can be constructed for circular polarization which are significantly larger than dipoles.

The simulations are repeated for different x-coordinates of the tag positions and for different room sizes to change the geometric relations for the signal paths. Although horizontal polarization performs better than vertical polarization in some scenarios and vice versa, circular polarization delivers the lowest fading quantification in all cases.

The simulated FQ values (table 4.3) also show a significant reduction of multipath effects for a combination of a circularly polarized tag antenna with a linearly polarized interrogator antenna (35% improvement). This is due to the fact that this analysis is presented for the uplink where the tag acts as the transmitter and the reflection coefficient is determined by the polarization of the transmitter signal.

In order to achieve a maximum reduction of multipath effects, circularly polarized antennas have to be used for the tag and the interrogator but the required patch antennas limit possible applications.

TABLE 4.3: Setup parameters and fading quantifications for the antenna polarization simulations

Setup	**Interrogator Antenna Polarization**	**Tag Antenna Polarization**	FQ **[dB]**
1	vertical	vertical	15.9
2	horizontal	horizontal	16.6
3	circular	circular	3.0
4	circular	horizontal	16.6
5	circular	vertical	15.9
6	horizontal	circular	10.3
7	vertical	circular	10.3

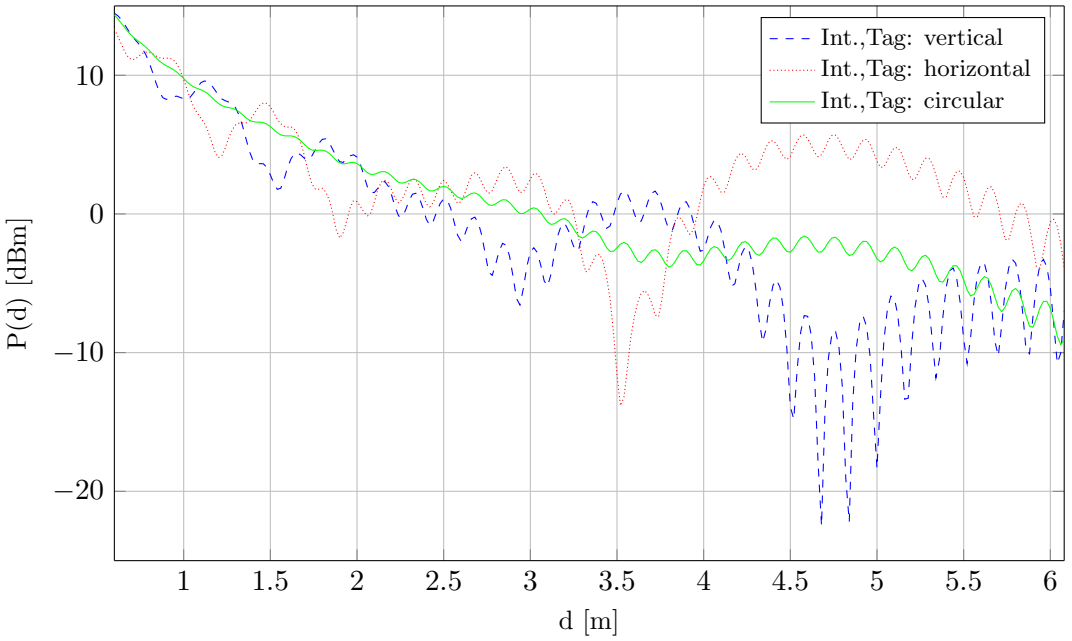

FIGURE 4.5: Simulation of different antenna polarizations (linear and circular polarizations)

4.2.5 Antenna Orientation

From the three representative gain patterns in figure 4.2 (section 4.1), the quasi-omnidirectional dipole is not considered. It has an equal gain in the azimuth plane which makes a change of the antenna orientation effectless. For the other two antenna types (patch and patch array), simulations are conducted for azimuth angles in a range of $\phi = 0°...80°$ (table 4.4) to investigate the influence of the antenna orientation on multipath effects.

The simulated fading characteristics for the interrogator patch antenna (figure 4.6) show that primarily the overall signal amplitude changes with the antenna orientation. However, the FQ value increases with the antenna angle (table 4.4). In the case of $\phi = 0°$, the interrogator antenna is facing the tag antenna and thus the LOS path experiences the maximum gain. With an increasing ϕ, this gain decreases while the gain of the reflection paths increases. As a consequence, the influence of the reflections on the overall receiver signal and thus the FQ values increase.

The simulation of the patch antenna array (higher directivity than the patch antenna) delivers results for the fading characteristics that are comparable to the patch antenna for small angles ($\phi < 40°$, table 4.4). For $\phi \geq 40°$, the patch antenna array gain pattern (figure 4.2) runs from the main lobe into a null and then

into a side lobe. This fact can also be observed in the general power level of the simulated fading characteristics (figure 4.7). The fading quantifications show that the highest FQ value corresponds to an antenna orientation ($\phi = 40°$) where one null in the gain pattern faces towards the tag. In this case, the received signal power of the LOS path is very low while the reflection path incident from the main lobe direction has a high RSS. For azimuth angles with $\phi \geq 60°$, one side lobe of the gain pattern is directed towards the tag which increases the received signal power of the LOS path and decreases the RSS of the reflection paths.

The implementation of a orientation diversity combining system is not feasible because an RSS-based decision process would always choose the same antenna orientation with $\phi = 0°$.

Because the orientation of the interrogator antenna has a certain influence on the effects of multipath, it is reasonable to use this technique in passive UHF RFID localization systems. For lateration or angulation approaches, two or more interrogator antennas are required that can easily be arranged in different orientations.

TABLE 4.4: Setup parameters for the antenna orientation simulations

Parameter	**Value**	FQ **[dB]**
Interrogator antenna orientation for a *patch antenna* (θ, ϕ)	$(0°, 0°)$	22.2
	$(0°, 20°)$	22.6
	$(0°, 40°)$	23.4
	$(0°, 60°)$	27.6
	$(0°, 80°)$	32.5
Interrogator antenna orientation for a *patch antenna array* (θ, ϕ)	$(0°, 0°)$	22.1
	$(0°, 20°)$	23.1
	$(0°, 40°)$	41.8
	$(0°, 60°)$	34.6
	$(0°, 80°)$	30.5

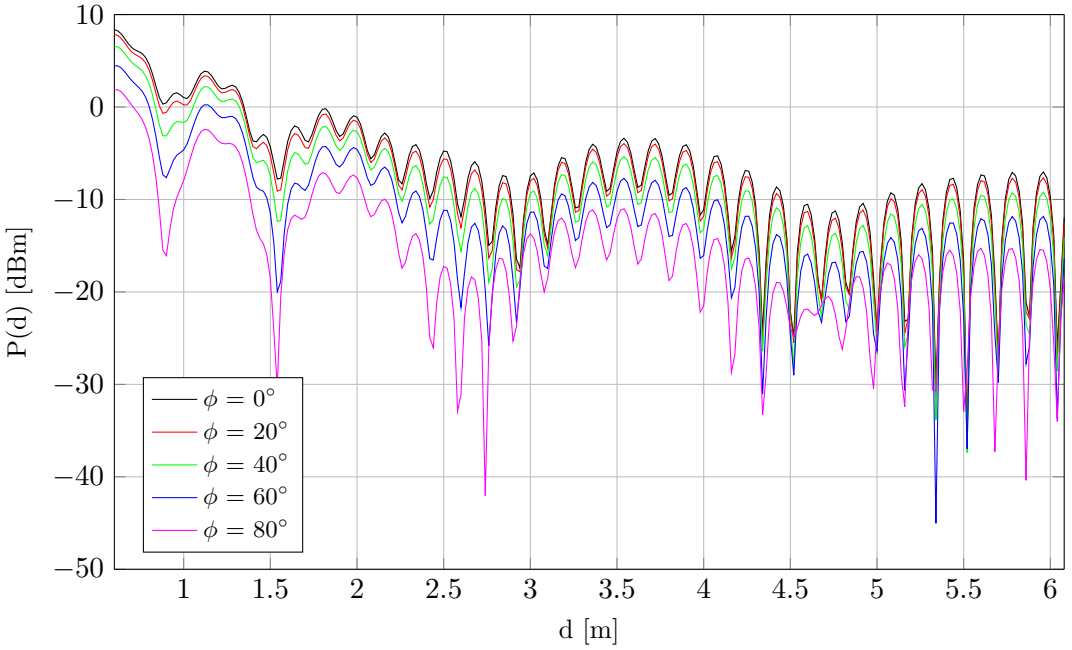

FIGURE 4.6: Simulation of different interrogator antenna azimuth angles for a patch antenna

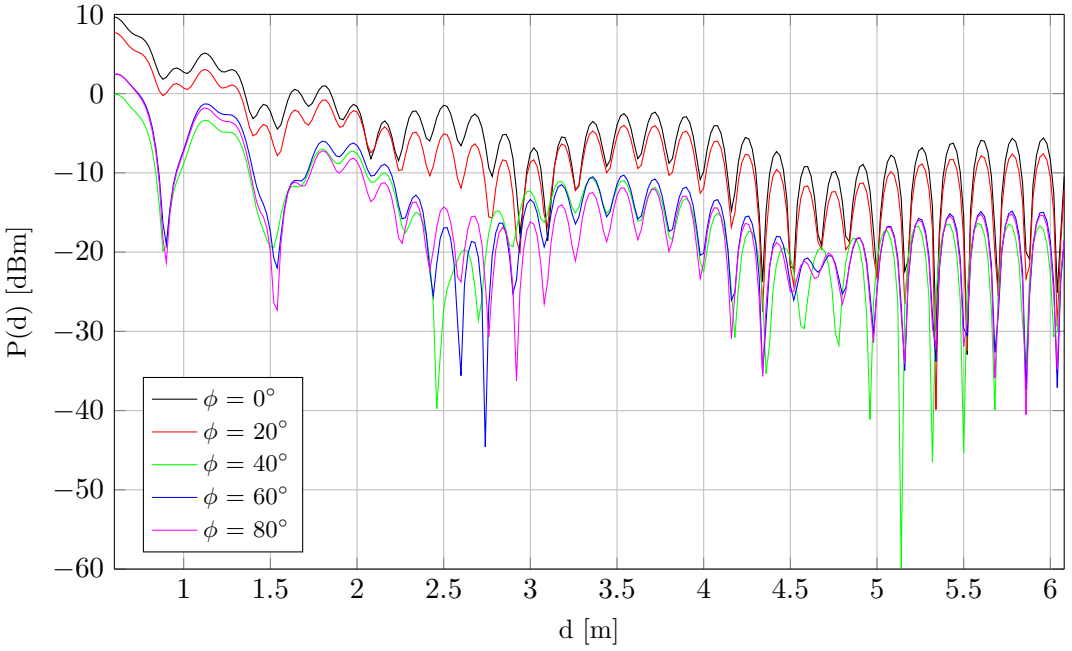

FIGURE 4.7: Simulation of different interrogator antenna azimuth angles for a patch antenna array

4.2.6 Frequency Diversity

A typical indoor application scenario for passive UHF RFID localization systems has a coherence bandwidth of $B_c = 17.6$ MHz (section 1.2). Worldwide frequency regulations limit the available bandwidth of passive UHF RFID systems depending on the specific area where they are operated (table 4.5) In contrast to the European frequency range with the lowest bandwidth of 2 MHz ($\approx 0.1 \cdot B_c$), the US range offers 26 MHz which is approximately $1.5 \cdot B_c$. Passive UHF RFID localization systems must be operable worldwide and are thus limited by the smallest available bandwidth. According to technical specification 102 902 by the European Telecommunications Standards Institute (ETSI), a new European frequency range with $BW = 10$ MHz $\approx 0.6 \cdot B_c$ will be introduced in the future [254].

Table 4.5: Selected EPCglobal Class 1 Generation 2 frequency ranges

Description	**Frequency Range**	**Bandwidth**
Europe	865.6 MHz – 867.6 MHz	2 MHz
USA	902 MHz – 928 MHz	26 MHz
Europe New	915 MHz – 925 MHz	10 MHz

Six different frequencies $f_1 ... f_6$ (table 4.6; limiting values of the respective local ranges) are used to evaluate the influence of the system frequency on multipath fading. Additionally, diversity combining of two frequencies in the respective band is simulated.

Table 4.6: Fading quantifications for the frequency diversity simulations

Setup	FQ **[dB]**
$f_1 = 865.6$ MHz	22.2
$f_2 = 867.6$ MHz	22.3
Diversity f_1, f_2	19.5
$f_3 = 902$ MHz	20.3
$f_4 = 928$ MHz	22.8
Diversity f_3, f_4	6.8
$f_5 = 915$ MHz	19.3
$f_6 = 925$ MHz	20.0
Diversity f_5, f_6	11.4

The simulated $P(d)$ development (figure 4.8) shows that the available European bandwidth is not high enough to achieve a change in the channel fading characteristics. This is confirmed by the simulated fading quantifications (22.2 dB vs. 22.3 dB and 19.5 dB for a diversity system; table 4.6). A frequency diversity system that utilizes the US bandwidth of 26 MHz effectively manipulates the fading characteristic (figure 4.9). The two related fading quantifications for f_3 and f_4 only differ by 2.5 dB (20.3 dB vs. 22.8 dB) but the diversity system has a low FQ of 6.8 dB (an improvement of 67% compared to the single frequencies). The available

bandwidth in the new European range of 10 MHz is also high enough to realize a frequency diversity system that reduces signal fading (figure 4.10). Again, the two fading quantifications lie in the same range (19.3 dB and 20.0 dB) but the diversity system reduces the FQ to 11.4 dB (41% improvement). A further improvement of the fading quantification is achieved in a diversity system which combines the current European band with the future European band and has a bandwidth of 59.4 MHz available.

It can be observed that the fading quantifications change for different frequencies (table 4.6). For example, the lowest value is achieved for $f_5 = 915$ MHz. The reason for that is the geometric relations of the considered scenario that lead to specific fading characteristics for each frequency. Additional simulations are conducted to further investigate this effect, where different values for the fixed x-coordinate of the tag are assumed ($x = 0.1$ m, 0.4 m, ..., 2.2 m). The results show no correlation between the system frequency and the FQ values. However, the combined diversity simulations show the same improvements for higher bandwidths. This is also confirmed by simulations with changed room dimensions.

Due to the current regulations, frequency diversity cannot be used to reduce the effects of multipath in passive UHF RFID localization systems because a global deployment is prevented by the available European bandwidth. However, with the future introduction of the new European band, frequency diversity will become feasible. An important finding is that an available bandwidth of only $0.6 \cdot B_\mathrm{c}$ is sufficient to make frequency diversity effective in typical application scenarios.

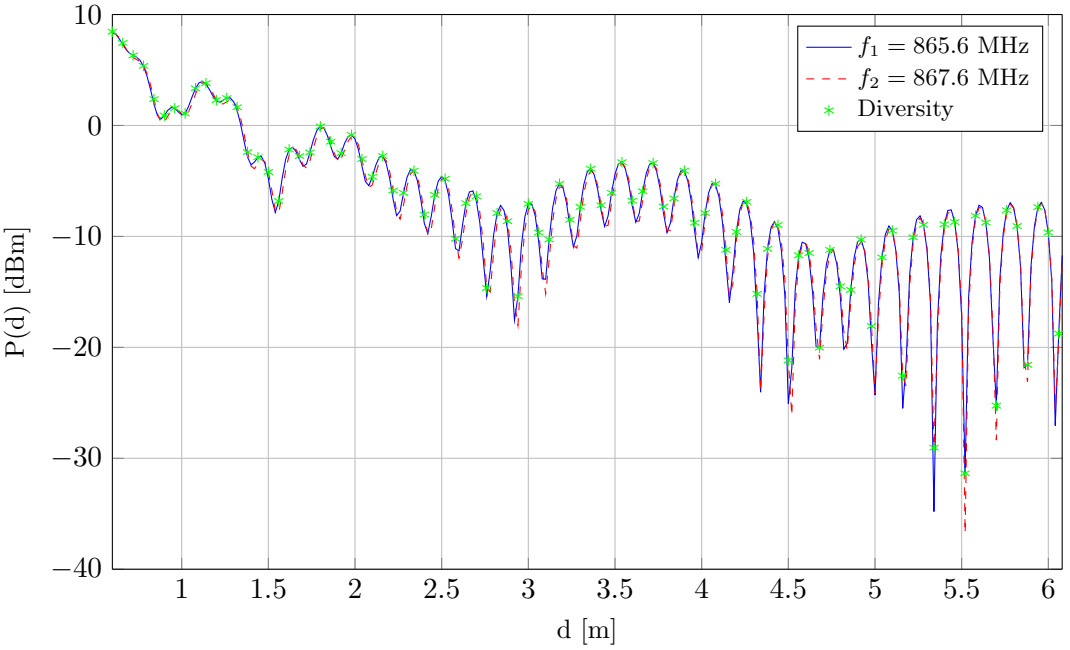

FIGURE 4.8: Simulation of frequency diversity in the European UHF RFID band

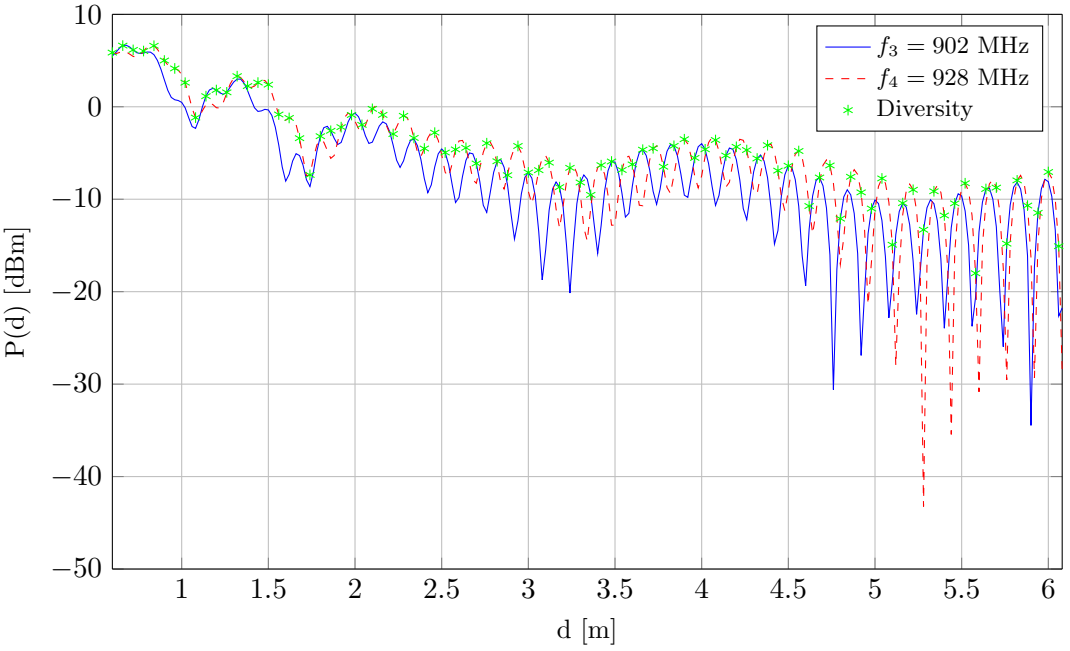

FIGURE 4.9: Simulation of frequency diversity in the US UHF RFID band

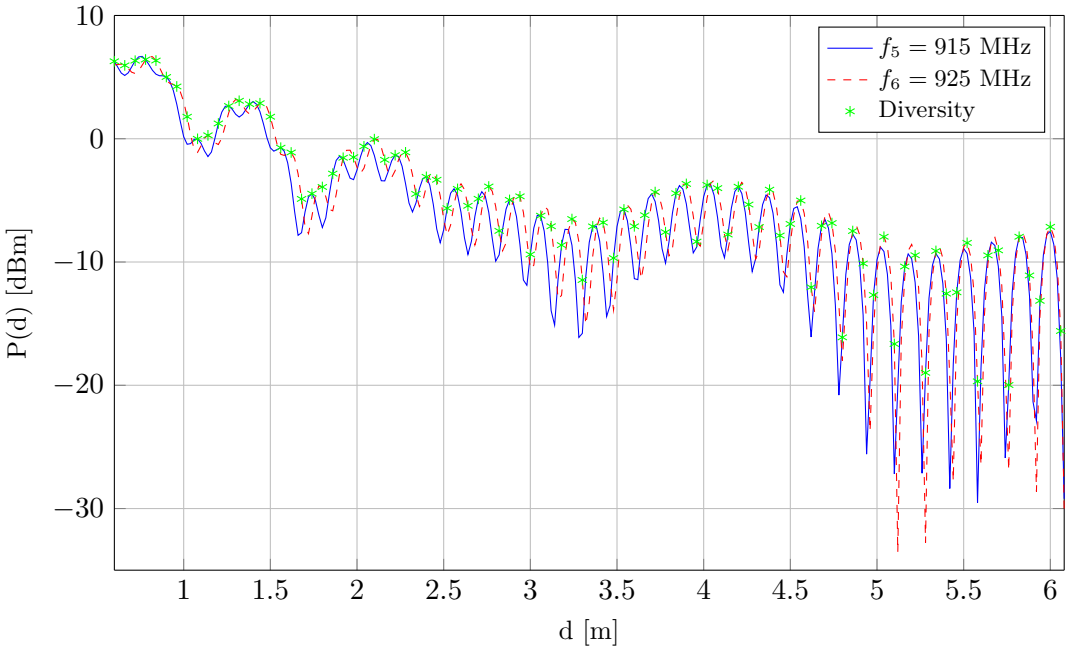

FIGURE 4.10: Simulation of frequency diversity in the new European UHF RFID band

4.2.7 Spatial Diversity

Spatial diversity can be achieved in a system where the receiver signals of different interrogator antenna positions are combined. Four antenna locations $L_{\text{int},1}...L_{\text{int},4}$ (table 4.7) with different x-coordinates in the standard setup are considered for a simulation of spatial diversity. A top view drawing of this scenario is depicted in figure 4.11.

TABLE 4.7: Setup parameters for the spatial diversity simulations

Parameter	Value	Spatial Displacement
Int. Antenna Position (x, y, z)	$L_{\text{int},1} = (1.15, 0.85, 1.50)$ m	-
	$L_{\text{int},2} = (1.25, 0.85, 1.50)$ m	0.1 m $\approx 0.3\lambda$
	$L_{\text{int},3} = (1.3225, 0.85, 1.50)$ m	0.1725 m $= \lambda/2$
	$L_{\text{int},4} = (1.495, 0.85, 1.5)$ m	0.345 m $= \lambda$

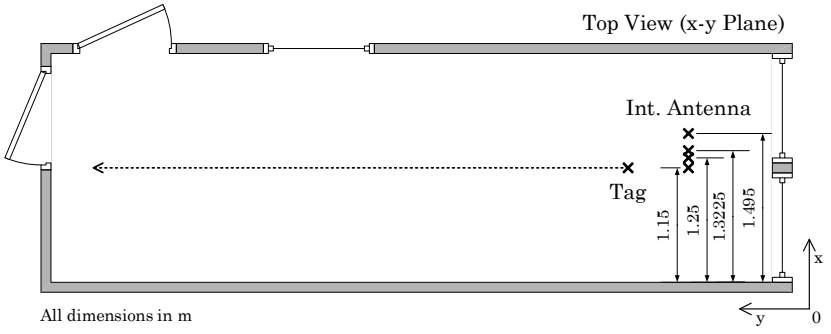

FIGURE 4.11: Simulation scenario for spatial diversity

In the three-dimensional setup, a change of the antenna height (z-coordinate) would result in the same effect as a displacement on the x-axis. The use of two interrogator antennas with different y-coordinates is not feasible in practice because one antenna would be placed in front of the other which blocks the rear antenna.

Figure 4.12 shows the simulation results for a diversity system with the interrogator antenna locations $L_{\text{int},1}$ and $L_{\text{int},2}$. The corresponding fading quantifications are listed in table 4.8. The small spatial antenna shift of 10 cm ($\approx 0.3 \cdot \lambda$) is not high enough to achieve a significant change of the signal fading characteristic. Diversity combining of both locations reduces the fading quantification to 18.9 dB (a reduction of only 6% compared to the single locations). A spatial displacement of $\lambda/2$ reduces the combined fading quantification for $L_{\text{int},1}$ and $L_{\text{int},3}$ to 17.5 dB (21% improvement). The two interrogator antenna locations $L_{\text{int},1}$ and $L_{\text{int},4}$ (displacement of 0.345 m = λ) enables a significant change of the fading characteristic (figure 4.13). Diversity switching between the $L_{\text{int},1}$ and $L_{\text{int},4}$ antennas results in a low FQ of 13.5 dB (31% improvement).

The described effect is well-known from mobile phone systems where a spatial distance of $d > \lambda/2$ is required to achieve sufficient diversity [255]. However, the analysis presented shows that a minimum antenna displacement of λ is required for passive UHF RFID systems in typical indoor environments.

TABLE 4.8: Fading quantifications for spatial diversity

Setup	FQ **[dB]**
$L_{\text{int},1}$	22.2
$L_{\text{int},2}$	20.2
$L_{\text{int},3}$	23.2
$L_{\text{int},4}$	19.6
Diversity $L_{\text{int},1}, L_{\text{int},2}$	18.9
Diversity $L_{\text{int},1}, L_{\text{int},3}$	17.5
Diversity $L_{\text{int},1}, L_{\text{int},4}$	13.5

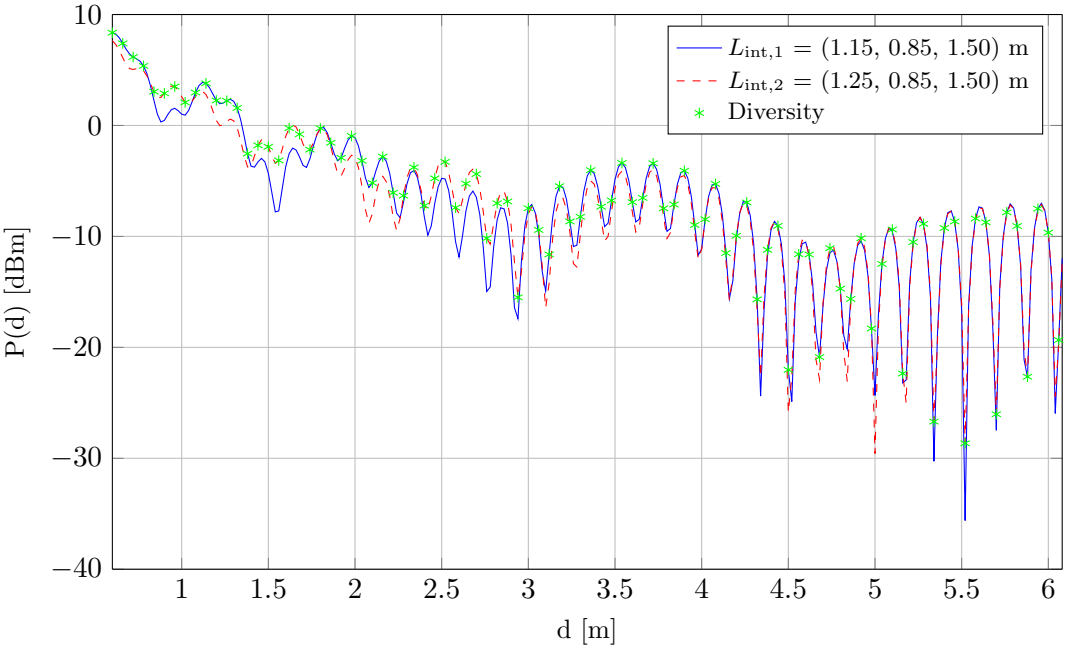

FIGURE 4.12: Simulation of spatial diversity for a position shift of 0.1 m

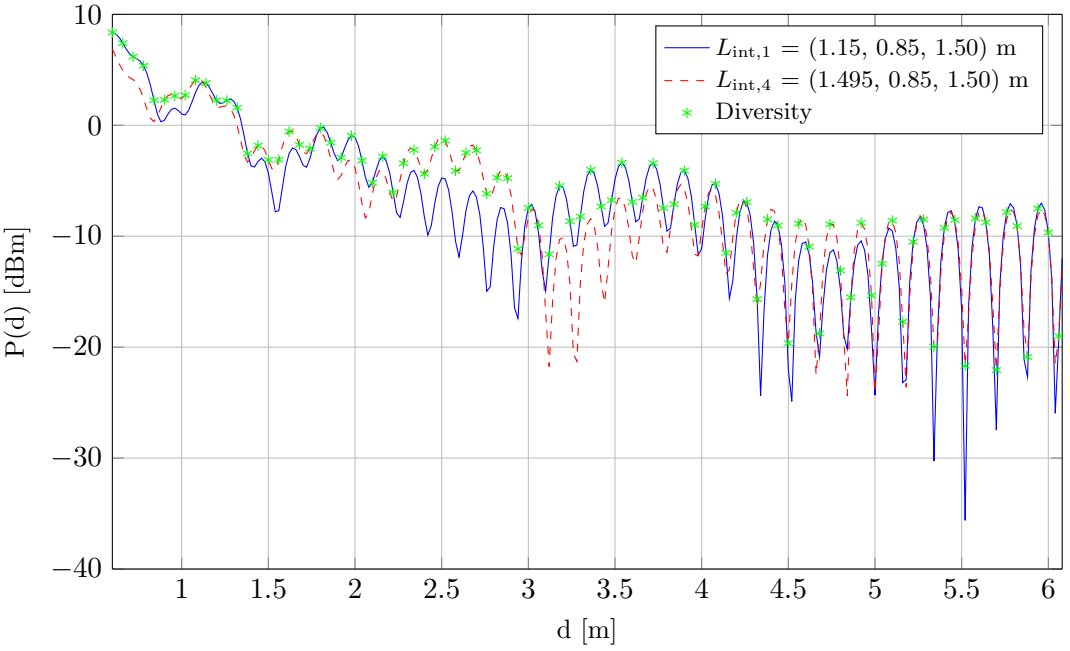

FIGURE 4.13: Simulation of spatial diversity for a position shift of $\lambda = 0.345$ m

4.2.8 Polarization Diversity

A diversity combining system using vertical and horizontal polarization significantly reduces the effects of multipath (figure 4.14). Compared to a single polarization system, the fading quantification is reduced from 15.9 dB to 7.4 dB (53% improvement). However, polarization diversity involves a high system complexity because two tags and two interrogator antennas are required. In a bistatic interrogator setup, the interrogator comprises separate antennas for signal transmission and reception. Thus, four interrogator antennas would be needed to realize polarization diversity.

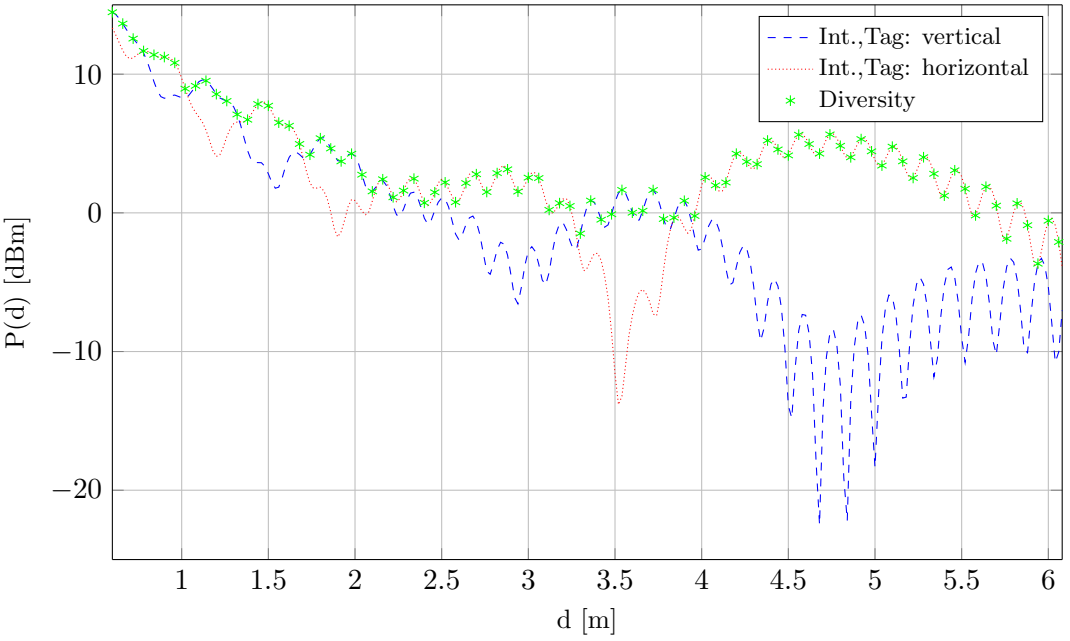

FIGURE 4.14: Simulation of polarization diversity

4.2.9 Reflection Cancellation

Figure 4.15 compares simulations of different setups for the standard scenario where single reflections are cancelled out and the signal power is the superposition of $N = 6$ signal paths. It can be seen that most of the simulations with six signal paths show the same fading characteristic as the standard setup with seven signal paths. This is also confirmed by the simulated fading quantifications (table 4.9). However, the simulation with the lowest FQ of 13.7 dB (improvement of 38%) shows a different fading characteristic than the others. By cancelling out *wall3* reflection (wall behind the interrogator), the small local amplitude maxima and minima from the other simulations are not present.

The practical use of reflection cancellation for passive UHF RFID localization system is limited because most applications demand a movement of the target tag within the full read range of the used interrogators. However, for very particular problems (e.g. a very small localization area), reflection cancellation can significantly reduce the effects of multipath.

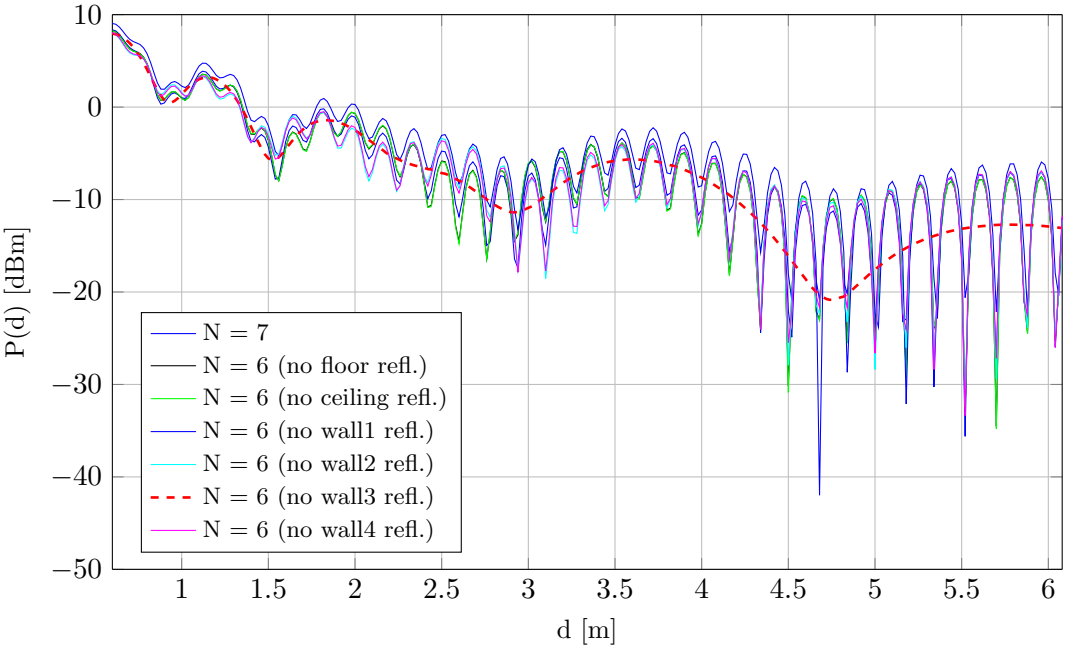

FIGURE 4.15: Simulation of reflection cancellation

TABLE 4.9: Fading quantifications for the reflection cancellation simulations

Setup	FQ **[dB]**
$N = 7$	22.2
$N = 6$ (no floor refl.)	23.8
$N = 6$ (no ceiling refl.)	23.9
$N = 6$ (no wall1 refl.)	22.1
$N = 6$ (no wall2 refl.)	21.6
$N = 6$ (no wall3 refl.)	13.7
$N = 6$ (no wall4 refl.)	21.1

4.3 Summary

Different diversity combing techniques and manipulations of the channel interface have been investigated with respect to their ability to minimize the effects of multipath in a passive UHF RFID localization system.

The fading quantification FQ has been proposed to rate the magnitude of multipath interference in a specific scenario.

Simulations of a standard application scenario have been used to efficiently analyse the complex interactions of multiple signal paths. The following findings have been demonstrated for channel interface parameter variations. Directional antennas help to attenuate or cancel out single reflections but the replacement of the usual tag dipole antennas with patch antennas increases their cost and size. However, in particular practical applications, this approach is reasonable to achieve an optimum localization accuracy. The same is true for circular antenna polarization that requires tags with patch antennas but significantly reduces the effects of multipath. The use of different interrogator antenna orientations can be implemented easily in localization systems and has a certain influence on multipath effects. It highly depends on the type and the corresponding gain pattern of the interrogator antenna. In applications with small localization areas, the installation of high-frequency absorbers to the reflection surfaces helps to cancel out single or multiple reflections.

In the different diversity combining approaches, two parameter values of the RFID setup have been switched and the receiver signals have been combined to reduce the effects of multipath. The comparison by simulations has shown the following results. Current worldwide regulations prevent the use of frequency diversity in passive UHF RFID systems. However, with the future approval of the new European UHF RFID frequency range, frequency diversity can be utilized to significantly reduce the effects of multipath. The application of spatial diversity

reduces multipath fading but only if the spatial distance between the different antenna locations is greater than λ. Polarization diversity significantly reduces the effects of multipath but increases the overall system cost because multiple target tags as well as multiple interrogator antennas are required.

Chapter 5

Receiver Beamforming Localization

The investigations of existing passive UHF RFID localization systems in chapter 2 have identified the receiver beamforming target tag localization approach as one of the most promising directions for further research. Especially the algorithmic (digital) Root MUSIC receiver beamforming technique seems to be ideally suited to provide sufficient localization accuracy in typical application scenarios.

A Root-MUSIC-based approach for passive UHF RFID tag localization is presented where the target tag location is angulated from an estimation of multiple tag directions (angles-of-arrival, AoA).

A typical application scenario and the previously introduced simulation environment (chapter 3) are used to determine the achievable localization performance of the new approach.

Besides the localization accuracy, the localization robustness (i.e. the standard localization error deviation) is an important performance measure for localization systems operated in multipath environments. Since every target tag location experiences a different magnitude of multipath effects, low localization error deviations show the system's robustness against multipath reflections.

Multipath reducing techniques (chapter 4) are transferred to the basic receiver beamforming localization method and the achievable localization performance is simulated and compared. These techniques are frequency diversity, spatial diversity, antenna orientation, patch antennas, circularly polarized antennas and reflection cancellation. As a result, an optimum receiver beamforming localization

system with respect to the accuracy and robustness in typical indoor application scenarios is proposed.

A new multiangulation algorithm is presented which calculates the point in space that has the minimum distance to all directional lines created by the measured AoAs to estimate the tag position.

Finally, a new experimental testbench is designed and used in real-world measurements to analyse the performance of the receiver beamforming localization method.

5.1 Localization Principle

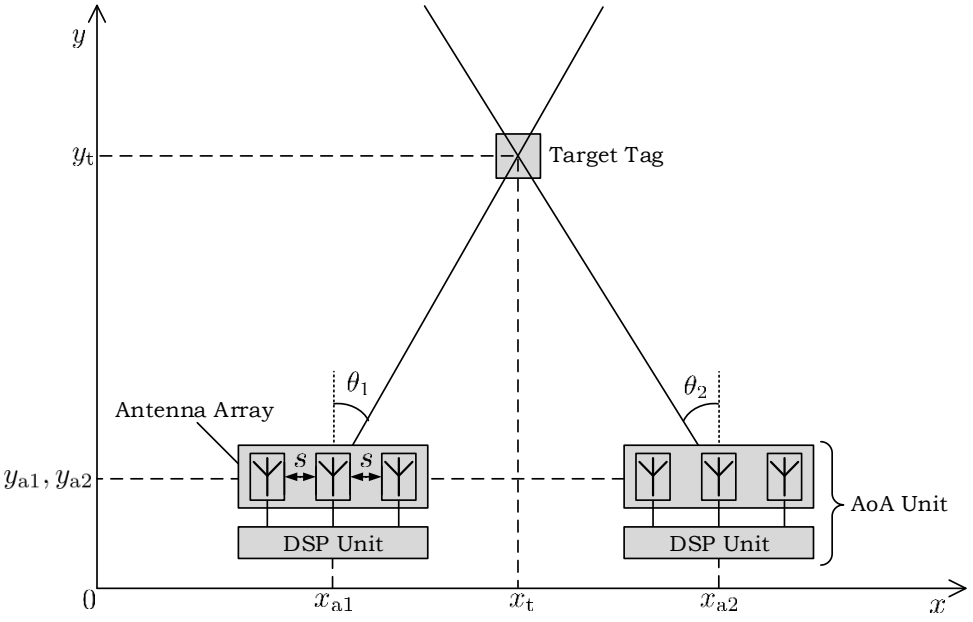

FIGURE 5.1: Principle of the receiver beamforming localization approach (top view)

The main components of the receiver beamforming localization system (figure 5.1) are the two AoA units that consist of a three-element antenna array and a digital signal processing (DSP) unit. The AoA units, in principle, are modified UHF RFID interrogators that use the antenna array as the receiver antenna.

The objective is to estimate the location of the target tag, $L_t = (x_t, y_t)$, in an azimuth plane of the localization environment. The z-coordinate of this plane is determined by the height of the AoA unit's antenna arrays. Usually, the origin of the coordinate system lies in one corner of the localization plane. The two AoA units communicate with the target tag and use the Root MUSIC algorithm

on the received array signals to estimate the two angles-of-arrival, θ_1 and θ_2. Then, straight lines are constructed from the locations of the antenna arrays, $L_{a1} = (x_{a1}, y_{a1})$ and $L_{a2} = (x_{a2}, y_{a2})$, towards the direction of the measured AoAs. The intersect point of these lines gives an estimate for the target tag location (angulation principle).

The derivation of the Root MUSIC AoA equation for the case of $L = 2$ antenna array elements is given in appendix A.2. The final form of this equation is

$$\theta = -\arcsin\left(\frac{\lambda \arg\{z_1\}}{2\pi s}\right) = -\arcsin\left(-\frac{\lambda\phi}{2\pi s}\right) = \arcsin\left(\frac{\lambda\phi}{2\pi s}\right), \tag{5.1}$$

where λ is the system wavelength, s is the inter-element spacing of the antenna array, $z_1 = e^{-j\phi}$ and $\phi = \frac{2\pi s}{\lambda}\sin\theta$.

In this equation, $\phi = \arg\{z_1\}$ is equal to the phase difference, $\Delta\varphi_{1,2}$, between the receiver signals of the two antenna array elements. To prove that, the incidence of the target tag signal wavefront on the two-element interrogator antenna array is considered (figure 5.2).

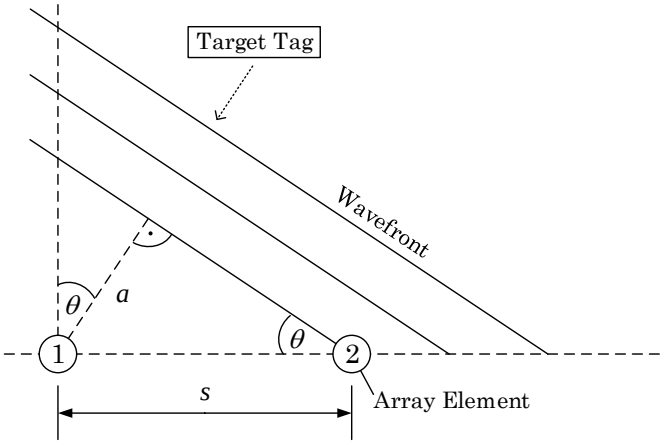

FIGURE 5.2: Signal wavefront impinging on a two-element antenna array

The signal wavefront will first arrive at antenna array element ② and then at element ① which leads to a phase shift between the receiver signals of the two elements.

The distance a between the wavefront and antenna array element ① is

$$a = s \cdot \sin\theta. \tag{5.2}$$

Since the wavefront travels at the speed of light, c, the time delay, τ, of the wavefront arriving at antenna array element ① is

$$\tau = \frac{a}{c} = \frac{s}{c} \sin\theta. \tag{5.3}$$

The resulting phase difference, $\Delta\varphi_{1,2}$, is derived from the the time delay τ using the pulsatance $\omega = 2\pi f$ (where f is the system frequency) as

$$\Delta\varphi_{1,2} = \omega\tau = \frac{2\pi f s}{c} \sin\theta = \frac{2\pi s}{\lambda} \sin\theta, \tag{5.4}$$

which is indeed the same as $\arg\{z_1\} = \phi = \frac{2\pi s}{\lambda} \sin\theta$. Thus, in the AoA equation (5.1), ϕ can be exchanged for $\Delta\varphi_{1,2}$:

$$\theta = \arcsin\left(\frac{\lambda\Delta\varphi_{1,2}}{2\pi s}\right) \tag{5.5}$$

The extension of the basic localization approach with a three-element antenna array has two advantages: a) a narrower 3dB-beamwidth, b) averaging of two phase differences. The 3dB-beamdwidth, in general, decreases with an increasing number of antenna elements [246] and a narrow main lobe helps to attenuate certain signal paths (see section 4.2.3). The averaging of the signal phase differences $\Delta\varphi_{1,2}$, $\Delta\varphi_{2,3}$ between the two pairs of adjacent array elements using

$$\overline{\Delta\varphi} = \frac{\Delta\varphi_{1,2} + \Delta\varphi_{2,3}}{2} \tag{5.6}$$

reduces the influence of measurement errors.

A further increase of the number of antenna array elements is not reasonable because it would increase the overall size of the array. A practical value for the maximum size that is demanded by typical localization applications lies in the range of an A4 paper sheet (210 mm × 297 mm). Furthermore, a high-frequency front-end is required for each antenna array element to evaluate the target tag signal. Thus, the DSP unit's complexity, cost and size increase with additional array elements.

The overall size of the array is also determined by the distance between the antenna elements s which should be chosen as high as possible to maximize decoupling between the element receiver signals. However, it has to be smaller than $\lambda/2$ ($\approx$ 17 cm in the European UHF RFID frequency range) to avoid the occurrence of grating lobes which would lead to ambiguities in the AoA estimation [44, 246].

A monopole antenna array can be realized with very small inter-element spacing s. The elements of a patch array have a certain size that depends on the used signal frequency an increases s (measured between the center points of the elements). For the new localization approach, a three-element antenna array consisting of monopoles with $s = 0.3\lambda$ (≈ 10 cm) is chosen as a first step.

5.2 Simulation of the Localization Performance

The new simulation environment (chapter 3) is extended in a way that the phases and power levels of the received tag signal at each antenna array element are calculated. For this purpose, both links (down- and uplink) are considered.

5.2.1 Simulation Scenario

A standard application scenario is set up to analyze the performance of the receiver beamforming localization approach in terms of accuracy and robustness (figure 5.3). $N = 25$ different tag positions ①...㉕ are defined in a standard university seminar room of size 10.7 m × 7.1 m × 3.0 m. In a square, 3 m × 3 m grid (in the x/y-plane), the tag positions are equally spaced with a distance of 0.50 m to each other (figure 5.4).

The dimensions of the localization grid are chosen for practical reasons: a) The antenna arrays must be positioned outside the grid, b) All tag positions must lie within the read range of the AoA units. The maximum AoA-unit-to-tag distance of 4.2 m (e.g. antenna array position A_1 and tag position ㉕) lies well within the read range of standard UHF RFID interrogators. Furthermore, the number of tag positions is limited to $N = 25$ to allow short measurement times in a real-world scenario. It is also reasonable to choose a distance between the tag positions which is greater than the system's wavelength because for distances which are smaller than the wavelength, the multipath characteristic at the tag position does not change significantly.

For the antenna array positions, any coordinates could be chosen but the tag readability has to be ensured. The investigations in the previous chapter have shown that patch antennas help to minimize the effects of multipath. Since this antenna type has a limited 3dB-beamdwidth ($\approx \pm 60°$), the two array positions $A_1 = (0, 0, 1.5)$ m and $A_2 = (3, 0, 1.5)$ m are located at the corners of the tag

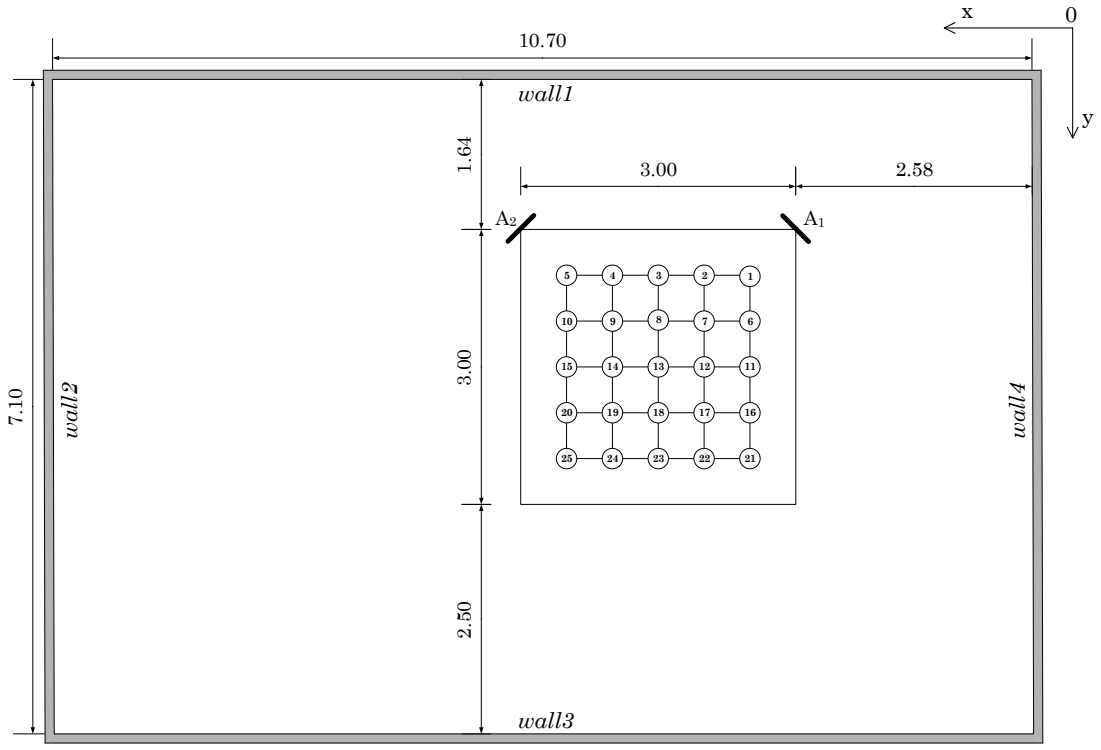

FIGURE 5.3: Receiver beamforming localization setup in a university seminar room (all dimensions in m)

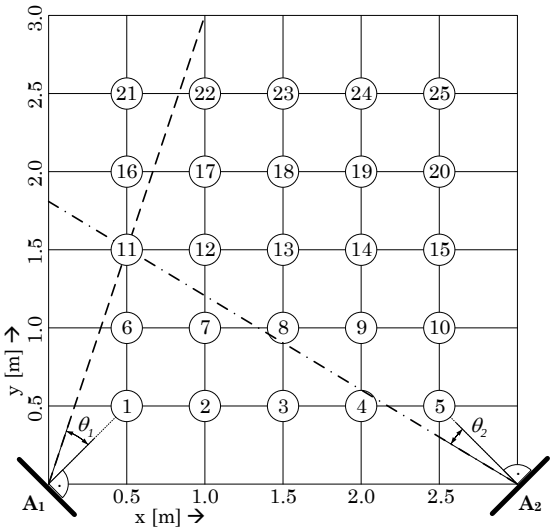

FIGURE 5.4: Grid of tag and antenna array positions in the receiver beamforming setup

grid in an azimuth angle of $\theta_{\text{ant,int}} = 45°$ to guarantee the readability of all 25 tag positions. The antenna array as well as the target tag are arranged vertically in this first simulation.

To minimize mutual coupling between the transmitter antenna and the receiver antenna of the AoA unit, a bistatic design of the DSP unit is realized that allows a spatial separation of both antennas. In the following simulations, the parameters of a commonly used circularly polarized patch antenna are chosen for the AoA unit's transmitter antenna.

Table 5.1 summarizes all system parameters used for the simulations.

TABLE 5.1: Parameters of the basic receiver beamforming localization setup

Parameter	Value
Room Size (Length, Width, Height)	(7.1, 10.7, 3.0) m
Antenna Array Positions (x, y, z)	A_1 = (2.58, 1.64, 1.50) m and A_2 = (5.58, 1.64, 1.50) m
System Frequency	866.5 MHz (center of the European range; $\lambda = 0.345$ m)
Interrogator TX Antenna - Type - Polarization	 Patch Circular
Interrogator RX Antenna - Type - Polarization	 Monopole antenna array (three elements, $s = \lambda/3$) Vertical
Tag Antenna - Type - Polarization	 Dipole Vertical
Antenna Gain Patterns	Simulated with FEKO
Antenna Phase Patterns	Simulated with FEKO
Interrogator TX Power	23.8 dBm
Signal Paths	7 (LOS and first-order reflections)
Reflection Surface Materials	wall 1, wall 2, wall 3: gypsum board ($\underline{\varepsilon}_2 = 6.2 + j0.69$) wall 4: glass ($\varepsilon_2 = 3$) floor, ceiling: concrete ($\underline{\varepsilon}_2 = 7.9 + j0.89$)

5.2.2 Performance Indicators

As performance indicators for the localization accuracy and robustness, different error values are calculated. The angles-of-arrival, $\theta_{1,n}$ and $\theta_{2,n}$ (estimated from the AoA unit locations A_1, A_2) as well as the target tag coordinates, $(x_{\text{t},n}, y_{\text{t},n})$, are calculated as a reference for each of the $n = 1...25$ target tag positions only from the geometry of the localization environment. The simulation environment is used to estimate the AoAs $\hat{\theta}_{1,n}$, $\hat{\theta}_{2,n}$ and the tag position $(\hat{x}_{\text{t},n}, \hat{y}_{\text{t},n})$ based on the application of the Root MUSIC algorithm on the received target tag signals. The following error values are then used to rate the performance of the considered localization system (a is the number of the considered AoA unit and $n = 1...N$ is the number of the considered tag position):

- The AoA estimation errors $\Delta\theta_{a,n}$ for each AoA unit and for each tag position:

$$\Delta\theta_{a,n} = \left|\hat{\theta}_{a,n} - \theta_{a,n}\right| \tag{5.7}$$

- The mean AoA estimation error $\overline{\Delta\theta}_a$ for each AoA unit:

$$\overline{\Delta\theta}_a = \frac{1}{N}\sum_{n=1}^{N}\Delta\theta_{a,n} \tag{5.8}$$

- The localization error (or localization accuracy) Δd_n for each tag position:

$$\Delta d_n = \sqrt{(x_{\mathrm{t},n} - \hat{x}_{\mathrm{t},n})^2 + (y_{\mathrm{t},n} - \hat{y}_{\mathrm{t},n})^2} \tag{5.9}$$

- The mean localization error (or localization accuracy) $\overline{\Delta d}$:

$$\overline{\Delta d} = \frac{1}{N}\sum_{n=1}^{N}\Delta d_n \tag{5.10}$$

- The mean AoA standard error deviation $\sigma_{\Delta\theta_a}$ for each AoA unit:

$$\sigma_{\Delta\theta_a} = \sqrt{\frac{1}{N}\sum_{n=1}^{N}\left(\Delta\theta_{a,n} - \overline{\Delta\theta}_a\right)^2} \tag{5.11}$$

- The mean localization error standard deviation $\sigma_{\Delta d}$:

$$\sigma_{\Delta d} = \sqrt{\frac{1}{N}\sum_{n=1}^{N}\left(\Delta d_n - \overline{\Delta d}_n\right)^2} \tag{5.12}$$

The disadvantage of using mean errors for an evaluation of the simulation data is that single outliers and the range of errors cannot be identified. The empirical cumulative distribution function (ECDF), $\hat{F}(x)$, overcomes these disadvantages because it relates a certain error value x to the probability of its occurrence in a simulation or measurement and is defined as

$$\hat{F}(x) = \hat{P}(X \leq x) = \frac{1}{N}\sum_{n=1}^{N} I\left(x_n \leq x\right), \tag{5.13}$$

where the x_n are the N error values produced in the measurement or simulation and $I()$ is the indicator function with

$$I\left(x_n \leq x\right) = \begin{cases} 1, & \text{when } x_n \leq x \\ 0, & \text{when } x_n > x \end{cases}$$

For the simulated AoA errors, $\hat{P}(\Delta\theta \leq \theta)$ is the cumulated probability of an error value (angle) $\Delta\theta$ being smaller than an angle of θ. The ECDF $\hat{P}(\Delta d \leq d)$ for the localization error is defined accordingly.

5.2.3 The Influence of Multipath on the Localization Performance

The simulation of the ideal free-space situation (only LOS path) delivers the following error values:

$\overline{\Delta\theta}_1 = 0.024°$
$\overline{\Delta\theta}_2 = 0.024°$
$\sigma_{\Delta\theta_1} = 0.026°$
$\sigma_{\Delta\theta_2} = 0.026°$
$\overline{\Delta d} = 0.0013 \text{ m} = 0.13 \text{ cm}$
$\sigma_{\Delta d} = 0.0005 \text{ m} = 0.05 \text{ cm}$

The very low errors verify the functionality of the extended simulation environment and the application of the receiver beamforming technique to a passive UHF RFID localization system.

The residual errors are caused by the assumption of parallel tag signal wavefronts in the Root MUSIC algorithm. The smaller the distance between the tag and the antenna array is, the higher is the curvature of the signal wavefront which leads to errors in the calculation of signal phases and phase differences. In the simulation environment, the path lengths are calculated as the absolute value of the vector between the array element position and the tag position which assumes a circular tag signal wavefront.

The influence of multipath on the localization performance is investigated by adding the first-order reflections to the simulation scenario (number of signal paths $N = 7$). The results show highly increased error values for the estimated AoAs and the estimated target tag locations (table 5.2).

TABLE 5.2: AoA estimation and localization errors (only LOS / LOS and multipath)

Parameter	Only LOS	LOS and Multipath
$\overline{\Delta\theta}_1$	0.024°	2.71°
$\overline{\Delta\theta}_2$	0.024°	2.97°
$\sigma_{\Delta\theta_1}$	0.026°	2.06°
$\sigma_{\Delta\theta_2}$	0.026°	2.32°
$\overline{\Delta d}$	0.13 cm	22 cm
$\sigma_{\Delta d}$	0.05 cm	16 cm

Figure 5.5(a) plots the ECDFs of the 50 AoA errors (25 tag positions per antenna array location) for the LOS-only simulation and the multipath simulation. It can be seen that in the multipath scenario, 60% of the AoA errors lie below $\theta = 3°$

and that the maximum AoA error is $\Delta\theta = 8.2°$. The ECDFs for the localization errors $\hat{P}(\Delta d \leq d)$ for the 25 target tag positions are shown figure 5.5(b).

It must be noted that the localization approach with two antenna array positions includes basic spatial and orientation diversity that influences the achieved values for $\overline{\Delta d}$ and $\sigma_{\Delta d}$. However, the comparison of the AoA estimation errors and standard error deviations is not affected by this interdependency.

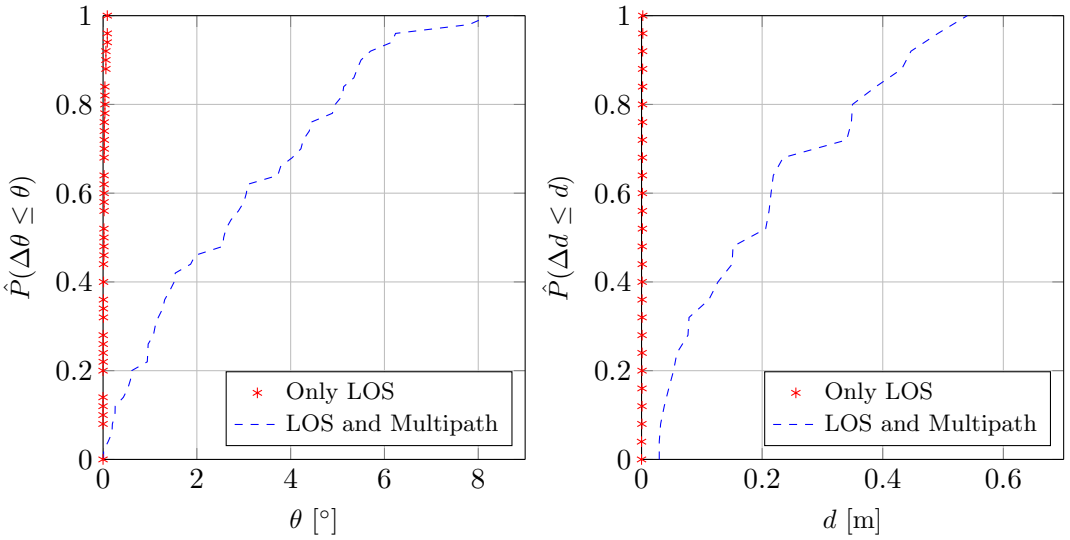

(a) (b)

FIGURE 5.5: Error probabilities for the receiver beamforming localization approach
(a) Tag angle estimation error probabilities,
(b) Tag location estimation error probabilities

5.2.4 Improvement of the Localization Performance

The previous localization simulations have proven that multipath highly deteriorates the localization performance of the receiver beamforming system. In the next sections, the influence of multipath reducing techniques (chapter 4) on the localization performance is investigated. As far as possible, every technique will be investigated individually to prevent interdependencies.

5.2.4.1 Antenna Type

Four possible antenna type (patch or dipole) combinations for the interrogator receiver antenna array and the tag antenna are simulated to investigate their influence on the localization performance. The polarization for all antennas is assumed as vertical.

It must be noted that the orientation of the tag antenna in the considered setup is important for patch antennas because no signal energy is received or transmitted towards the rear of the antenna. Thus, for the simulation, it is rotated towards the x-axis to face the two antenna array locations A_1 and A_2.

The simulation results (table 5.3 and figure 5.6) show that the use of a patch tag antenna increases the mean AoA accuracy as well as the mean localization accuracy. However, since the tag has to face the antenna arrays, the practical application is limited. On the other hand, replacing the interrogator dipole antenna array with a patch antenna array is feasible in practice and improves the mean localization accuracy by 7 cm (32%). The highest localization accuracy is achieved by using patch antennas for the tag and the interrogator (improvement of 11 cm/50%).

TABLE 5.3: AoA estimation and localization errors
(dipole tag antenna/patch tag antenna)

Parameter	**Int.: Dipole Tag: Dipole**	**Int.: Dipole Tag: Patch**	**Int.: Patch Tag: Dipole**	**Int.: Patch Tag: Patch**
$\overline{\Delta\theta_1}$	2.71°	2.18°	1.92°	1.42°
$\overline{\Delta\theta_2}$	2.97°	2.40°	1.93°	1.48°
$\sigma_{\Delta\theta_1}$	2.06°	1.68°	1.33°	1.36°
$\sigma_{\Delta\theta_2}$	2.32°	2.02°	1.46°	1.34°
$\overline{\Delta d}$	22 cm	16 cm	15 cm	11 cm
$\sigma_{\Delta d}$	16 cm	11 cm	10 cm	9 cm

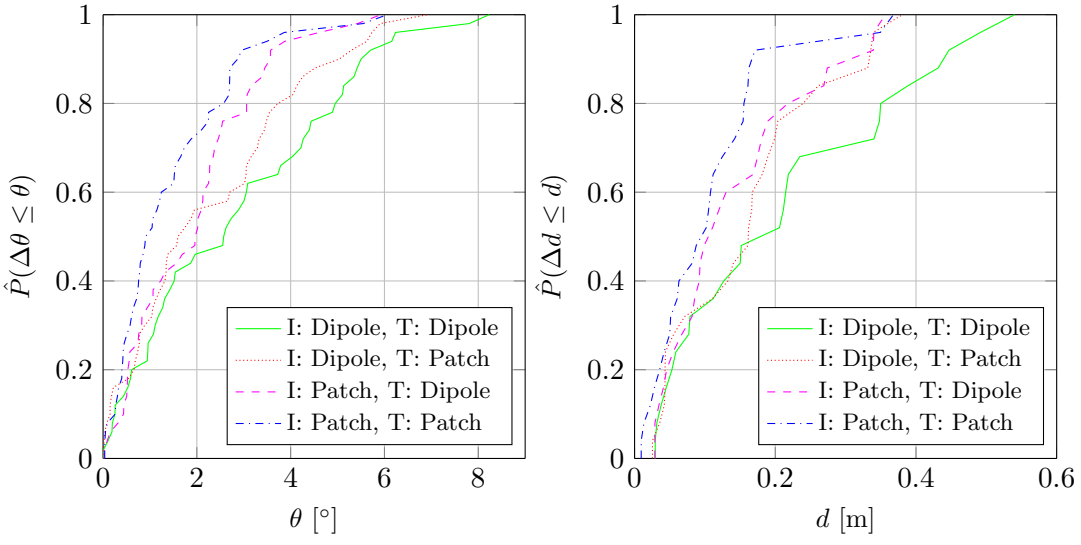

FIGURE 5.6: Error probabilities for different antenna type combinations

5.2.4.2 Antenna Polarization

Three different system setups with matching polarizations (vertical, horizontal, circular) of the tag and the interrogator antenna are simulated to investigate the achievable localization accuracies. Mixed polarizations lead to signal attenuation and perform equally or worse than matching polarizations in the previously discussed fading simulations (chapter 4). Patch antennas are chosen for the interrogator and the tag to achieve comparable results and the tag position is angulated from the two antenna array positions A_1 and A_2.

From the two linear cases, vertical polarization outperforms horizontal polarization with respect to localization accuracy (11 cm vs. 19 cm) as a result of the geometry of the localization environment. Additional simulations show that other cases exist where horizontal polarization performs better than vertical polarization. However, in all scenarios, circular polarization achieves the lowest localization errors and improves the accuracy of the monopole array system by 14 cm (64%) and the mean standard error deviation by 11 cm (69%). The cumulated error density functions (figure 5.7) confirm that circular polarization is required for an optimum localization accuracy.

TABLE 5.4: AoA estimation and localization errors for different antenna polarizations

Parameter	Vertical Polarization	Horizontal Polarization	Circular Polarization
$\overline{\Delta\theta_1}$	1.42°	2.59°	0.97°
$\overline{\Delta\theta_2}$	1.48°	2.71°	1.03°
$\sigma_{\Delta\theta_1}$	1.36°	2.88°	0.80°
$\sigma_{\Delta\theta_2}$	1.34°	3.14°	0.90°
$\overline{\Delta d}$	11 cm	19 cm	8 cm
$\sigma_{\Delta d}$	9 cm	16 cm	5 cm

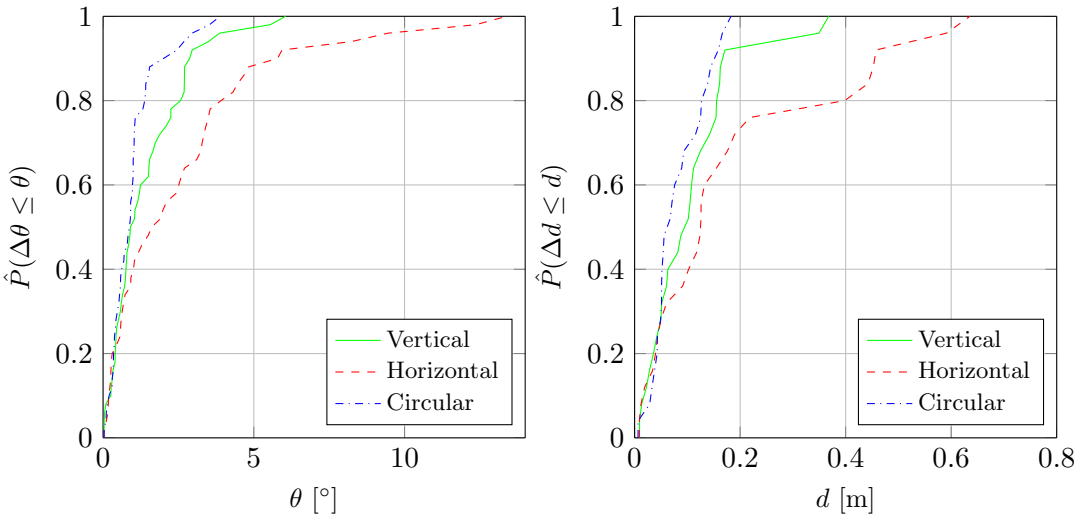

FIGURE 5.7: Error probabilities for different antenna polarizations

5.2.4.3 Reflection Cancellation

For an assessment of the feasibility of reflection cancellation, simulations and a cost-benefit analysis are required. A typical 50 cm × 50 cm pyramidal high-frequency absorber costs around 60 € and has a guaranteed attenuation of -20 dB in the UHF RFID frequency range. Table 5.5 lists the localization performance for the standard localization environment and for an environment where different signal paths are cancelled out. The number of required absorbers and the overall costs are also included in the table. It can be seen, that attaching absorbers to the ceiling increases the localization accuracy by 4 cm (18%) with relatively low costs. Cancelling out all reflections except the floor signal path leads to a 15 cm (68%) localization error reduction but also to high costs.

If circularly polarized patch antennas are used for the interrogator and the tag, this effect is reduced. The reason is the fact that circular polarization attenuates the reflected signal paths and patch antennas concentrate the transmitted energy towards limited angles which also reduces the power level of the reflected signals.

TABLE 5.5: AoA estimation and localization errors for reflection cancellation

Parameter	$N = 7$	$N = 6$					$N = 2$
	All Paths	**All Except Ceiling**	**All Except *wall1***	**All Except *wall2***	**All Except *wall3***	**All Except *wall4***	**Only Floor**
Absorbers	-	4	4	2	5	3	18
Cost [€]	-	240	240	120	300	180	1080
$\overline{\Delta\theta}_1$	2.71°	2.36°	2.32°	2.78°	2.22°	2.49°	0.88°
$\overline{\Delta\theta}_2$	2.97°	2.66°	2.69°	2.67°	2.57°	2.94°	0.92°
$\sigma_{\Delta\theta_1}$	2.06°	1.74°	2.02°	2.09°	1.77°	1.89°	0.81°
$\sigma_{\Delta\theta_2}$	2.32°	1.96°	1.87°	1.85°	1.97°	2.20°	0.79°
$\overline{\Delta d}$	22 cm	18 cm	19 cm	20 cm	18 cm	20 cm	7 cm
$\sigma_{\Delta d}$	16 cm	13 cm	16 cm	15 cm	14 cm	15 cm	5 cm

5.2.4.4 Frequency Diversity

The effects of frequency diversity on the localization performance are investigated in the following bands: a) the European band ($f_1 = 865.6$ MHz, $f_2 = 867.6$ MHz), b) the US band ($f_3 = 902$ MHz, $f_4 = 928$ MHz), c) the new European band ($f_5 = 915$ MHz, $f_6 = 925$ MHz). Table 5.6 lists the results for the AoA and the localization errors in comparison to the standard system with $f = 866.5$ MHz.

As expected from the previous findings (chapter 4), the localization accuracy increases with the available frequency bandwidth (table 5.6). There is no improvement in the European band, an improvement of 5 cm (23%) in the new European

band and an improvement of 9 cm (41%) in the US band. This is also confirmed by the cumulative error distribution functions in figure 5.8. The mean standard error deviations are improved by 5 cm (31%, European band) and 7 cm (44%, US band).

The same simulations are repeated for different room sizes and for different locations of the tag and antenna array grid to exclude an influence on the results. There, the aforementioned effects were confirmed. However, an interesting finding is that in most cases, higher system frequencies lead to lower AoA errors and to higher localization accuracies.

TABLE 5.6: AoA estimation and localization errors for frequency diversity systems

Parameter	Standard System	Frequency Diversity		
		European Band	US Band	New Europ. Band
$\overline{\Delta\theta_1}$	2.71°	2.91°	2.29°	2.84°
$\overline{\Delta\theta_2}$	2.97°	3.03°	1.73°	2.59°
$\sigma_{\Delta\theta_1}$	2.06°	2.26°	1.76°	1.95°
$\sigma_{\Delta\theta_2}$	2.32°	2.23°	1.73°	2.07°
$\overline{\Delta d}$	22 cm	22 cm	13 cm	17 cm
$\sigma_{\Delta d}$	16 cm	17 cm	11 cm	9 cm

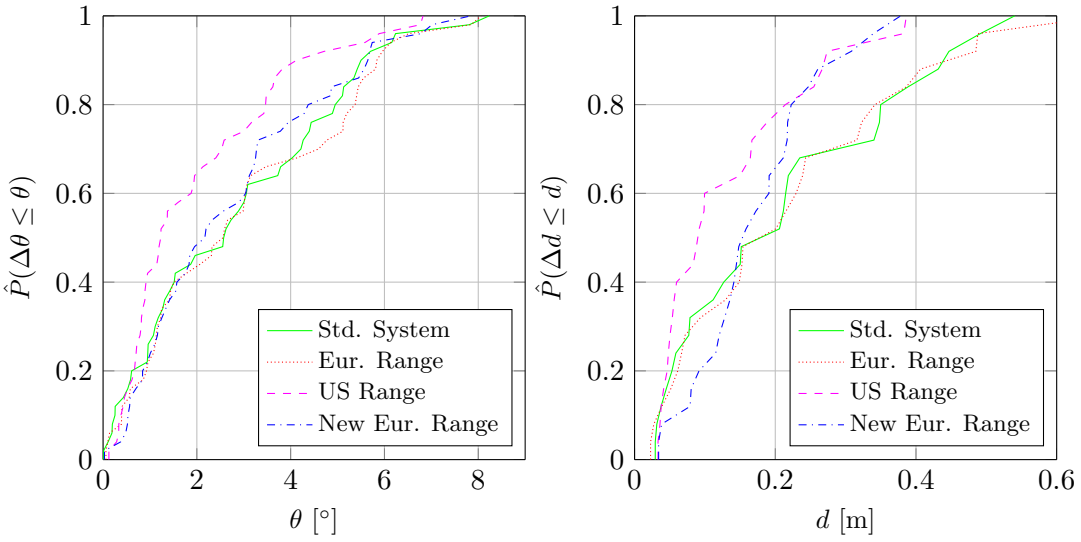

FIGURE 5.8: Error probabilities for frequency diversity localization

5.2.4.5 Spatial Diversity and Antenna Orientation

Two additional antenna array positions are introduced in the measurement grid to investigate the influence of spatial diversity on the localization system performance: $A_3 = (3, 3, 1.5)$ m and $A_4 = (0, 3, 1.5)$ m (figure 5.9). Since the antenna arrays have to be arranged in a 45° angle (section 5.2.1), orientation diversity is applied simultaneously to spatial diversity.

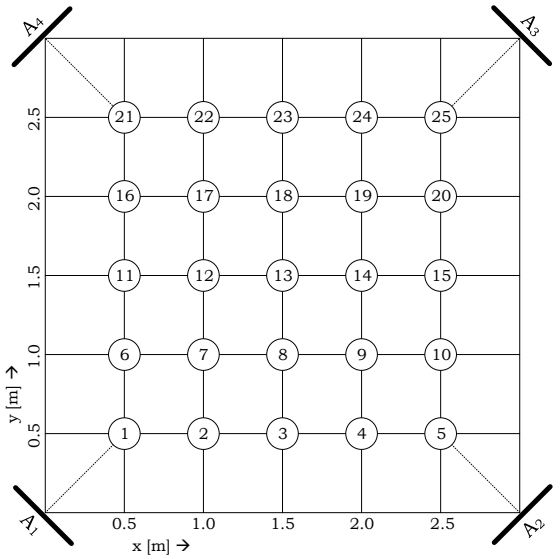

FIGURE 5.9: Localization setup with four antenna array positions

Using two array positions in the localization system, the target tag position is estimated as the intercept point of the estimated angle-of-arrival lines. However, for three or more array positions, more sophisticated methods are required. Due to inaccuracies in the AoA estimation, the AoA lines do not intercept in one single point but in a polygon (e.g. a triangle for three lines). One localization approach is to estimate the tag position as the centroid of this polygon. However, with an increasing number of polygon edges, the complexity increases. In addition, there are cases where an intercept point lies far outside the measurement area which makes the calculation of the centroid difficult and decreases the localization accuracy. In the worst case, two AoA lines are parallel to each other and have no intercept point.

A new multiangulation algorithm is introduced to overcome these limitations and to estimate the target tag location from any number of estimated AoAs. The task of this 'Nearest Point' algorithm is to find the point P_m in the azimuth plane of the antenna arrays which has the minimum Euclidean Distance from all AoA lines. The detailed calculation steps are given in appendix C.2. In addition to the considered two-dimensional case, it can also be used for three-dimensional localization.

In a first spatial diversity simulation, all four AoA unit positions (i.e. four estimated AoAs) are used to angulate the tag position with the nearest point algorithm (table 5.7). The results show that the mean AoA estimation errors are different for the different antenna array positions. The reason is the different geometry of

the localization environment seen from the antenna array position which leads to different multipath characteristics.

The spatial diversity system with four antenna array positions improves the localization accuracy by 10 cm (45%) and the mean localization error standard deviation by 8 cm (50%) compared to the two-AoA system.

A different spatial diversity method is to angulate the tag position from the subset of estimated AoAs belonging to the antenna array positions with the highest target tag RSS (table 5.8). However, the simulation results show no improvement for this approach compared to the four-AoA system. Instead, the localization accuracy increases with an increasing number of considered AoAs. Figure 5.10 shows the error distribution for all spatial diversity systems that confirm the aforementioned findings. The error distribution for the angle estimation is not shown in figure 5.10 because it is identical for all spatial diversity systems.

TABLE 5.7: AoA estimation and localization errors for four antenna array positions

Parameter	**4 AoAs**	**2 AoAs**
$\overline{\Delta\theta}_1$	2.71°	2.71°
$\overline{\Delta\theta}_2$	2.97°	2.97°
$\overline{\Delta\theta}_3$	2.69°	-
$\overline{\Delta\theta}_4$	2.57°	-
$\sigma_{\Delta\theta_1}$	2.06°	2.06°
$\sigma_{\Delta\theta_2}$	2.32°	2.32°
$\sigma_{\Delta\theta_3}$	2.04°	-
$\sigma_{\Delta\theta_4}$	1.91°	-
$\overline{\Delta d}$	12 cm	22 cm
$\sigma_{\Delta d}$	8 cm	16 cm

TABLE 5.8: AoA estimation and localization errors for subsets of four antenna array positions

Parameter	**2 AoAs**	**2 of 4 AoAs**	**3 of 4 AoAs**	**4 AoAs**
$\overline{\Delta d}$	22 cm	17 cm	15 cm	12 cm
$\sigma_{\Delta d}$	16 cm	13 cm	9 cm	8 cm

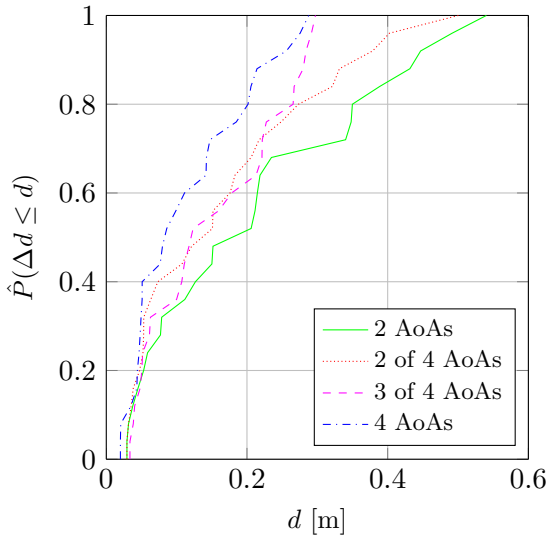

FIGURE 5.10: Error probabilities for spatial diversity

5.2.5 Optimum Localization System

The findings of the previous section are used to set up a receiver beamforming system that achieves optimum localization performance in multipath environments. This system has the following properties:

- Root MUSIC AoA estimation with three-element antenna arrays and averaging of phase-difference measurements
- Multiangulation with the nearest point algorithm
- Spatial and orientation diversity with four antenna array positions
- Patch antennas for the tag and the interrogator
- Circular antenna polarization for the tag and the interrogator

Since the objective is to universally optimize the achievable localization accuracy, reflection cancellation is not considered because it is limited to specific scenarios. Frequency diversity is also not considered because current frequency regulations prevent a global use.

The simulated localization performance of the improved system (table 5.9 and figure 5.11) shows that the mean AoA estimation accuracy for all considered antenna array positions is increased from 2.84° to 0.31° (90% improvement) and the mean standard error deviation from 2.19° to 0.29° (88% improvement). The localization accuracy is improved by 91% (from 22 cm to 2 cm) and the mean localization error standard deviation by 94% (from 16 cm to 1 cm).

It must be noted that the achieved values are ideal because the orientation of the tag antenna is changed for the AoA estimation of each antenna array position in a way that it faces the array. However, the results clearly show that the localization performance of passive UHF RFID receiver beamforming localization systems can be highly improved by using multipath reducing techniques.

TABLE 5.9: AoA estimation and localization errors for the optimized localization system

Parameter	**Basic Approach**	**Improved Approach**
$\overline{\Delta\theta}_1$	2.71°	0.34°
$\overline{\Delta\theta}_2$	2.97°	0.32°
$\overline{\Delta\theta}_3$	-	0.29°
$\overline{\Delta\theta}_4$	-	0.28°
$\sigma_{\Delta\theta_1}$	2.06°	0.31°
$\sigma_{\Delta\theta_2}$	2.32°	0.32°
$\sigma_{\Delta\theta_3}$	-	0.26°
$\sigma_{\Delta\theta_4}$	-	0.25°
$\overline{\Delta d}$	22 cm	2 cm
$\sigma_{\Delta d}$	16 cm	1 cm

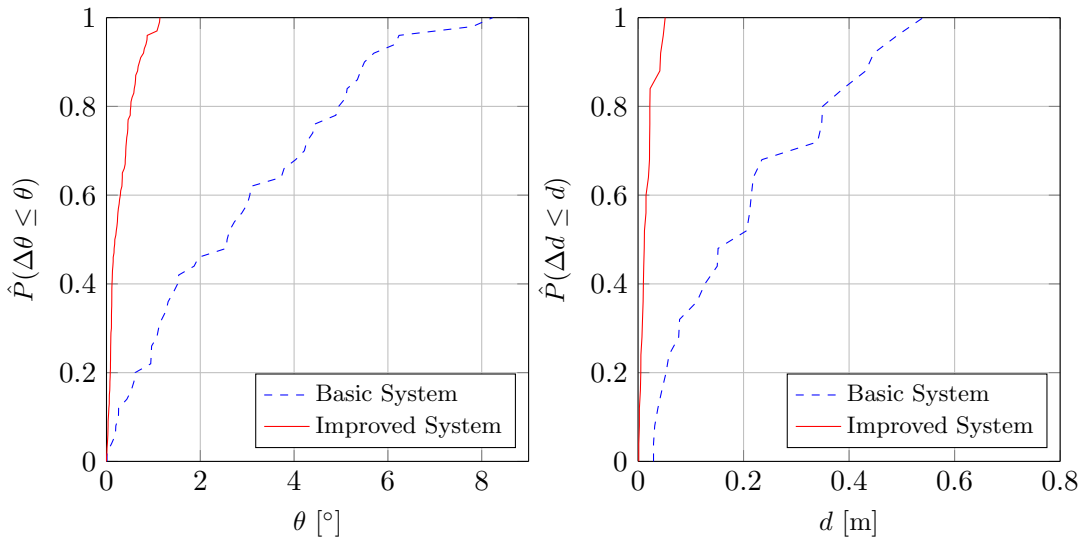

FIGURE 5.11: Error probabilities for the basic and the improved localization systems

5.3 Experimental Verification of the Localization Performance

In order to verify the localization performance of the optimum receiver beamforming localization approach in real-world measurements, the simulation scenario with the grid of 25 tag positions and the four AoA units (figure 5.9) is rebuild in a physical experimental testbed.

5.3.1 Experimental Testbed

The experimental testbed consisted of multiple AoA units which comprised a DSP unit and a three-element antenna array (figure 5.1).

5.3.1.1 DSP Unit

According to the localization principles (section 5.1), a measurement of the phase differences between the receiver signals of adjacent antenna array elements is required to apply the Root MUSIC algorithm. Thus, the DSP unit could be realized by combining three standard UHF RFID interrogators that communicate with the tag and then provide the phase information of the received tag signal. However, there was no commercial product available that provides a phase measurement. Additionally, the three interrogators would need a synchronisation mechanism to achieve an in-phase signal measurement. Thus, the design of a new DSP unit was necessary.

The phase difference, $\Delta\varphi_{1,2}$, between two receiver signals $x_1 = r_1 \cdot e^{j\varphi_1}$ and $x_2 = r_2 \cdot e^{j\varphi_2}$ is the argument of their cross-correlation product

$$\begin{aligned}\Delta\varphi_{1,2} &= \arg\left\{x_1^* x_2\right\} \\ &= \arg\left\{r_1 \cdot e^{-j\varphi_1} \cdot r_2 \cdot e^{j\varphi_2}\right\} \\ &= \arg\left\{r_1 \cdot r_2 \cdot e^{j\varphi_2 - j\varphi_1}\right\}, \\ &= \varphi_2 - \varphi_1\end{aligned}$$

where * denotes the complex conjugate. For a calculation of the cross-correlation product in a signal processing system, a time-discrete sampling of the receiver signal was required. However, since the carrier frequency of the wireless signals in

passive UHF RFID systems lies in a range between 860 MHz and 960 MHz, very complex and expensive analogue-to-digital converters (ADC) would be required.

A different approach that requires only standard, cost-effective ADCs is to sample the I/Q demodulated baseband receiver signals that have a frequency of $f_{\mathrm{BB}} =$ 40 kHz...320 kHz. For a continuous baseband signal, the phase difference between x_1 and x_2 is given as

$$\Delta\varphi_{1,2} = \arg\left\{x_1^* x_2\right\} = \arg\left\{(I_1 - jQ_1)\cdot(I_2 + jQ_2)\right\}. \tag{5.14}$$

If $n = 1...N$ samples of the I/Q components of the two antenna array element receiver signals x_1 and x_2 are available in $I_1[n], I_2[n]$ and $Q_1[n], Q_2[n]$, respectively, $\Delta\varphi_{1,2}$ can be calculated as

$$\Delta\varphi_{1,2} = \arctan\left(\frac{\sum_{n=1}^{N} I_2[n]Q_1[n] - I_1[n]Q_2[n]}{\sum_{n=1}^{N} I_1[n]I_2[n] + Q_1[n]Q_2[n]}\right) \tag{5.15}$$

The advantage of the correlation method is that it uses all of the acquired samples to calculate the correlation product for every single pair of I and Q samples. This averages and reduces the signal noise.

The main components of the new DSP unit are three radio-frequency (RF) front-ends that amplify and demodulate the receiver signals of the antenna array elements to provide their analogue I and Q components which are then sampled. A microcontroller calculates angle-of-arrival from the averaged phase difference $\Delta\varphi_{\mathrm{mean}}$ (equation (5.5)) using the cross-correlation of the I and Q samples (equation (5.15)). Synchronization among the RF front-ends is achieved by means of a common in-phase local oscillator signal. A detailed block diagram and a picture of the DSP unit are included in appendix C.3.1.

5.3.1.2 Three-Element Antenna Array

The analyses in the previous sections have shown that the optimum localization performance is achieved by using a circularly polarized patch antenna array for the AoA unit. However, designs for this type of array could not be found in the literature or in commercial products which required the development of a novel design. For clarity reasons, the following text describes all design steps for a

transmitter antenna array. Since all antenna characteristics are reciprocal, its performance is equal for transmitting and receiving signals.

As described before, the new antenna array should consist of $N = 3$ elements and its overall size should not exceed the size of an A4 paper sheet (210 mm × 297 mm). Furthermore, it was beneficial if it could be built in an industrial process on FR4 (Flame Retardant 4, composite material for printed circuit boards) board which allows a lightweight and low-cost design. With respect to these requirements, a linearly polarized microstrip patch antenna (figure 5.12) was chosen as the basis for the new design. A substrate material (e.g. FR4) of size $W_{\text{sub}} \times L_{\text{sub}} \times H_{\text{sub}}$ separated the microstrip antenna element of size $W_{\text{patch}} \times L_{\text{patch}} \times H_{\text{patch}}$ from a ground plane that had the same size as the substrate. Since the typical thickness of the copper layers for the ground plane and the antenna element was only 35 μm, it was not considered in the following calculation of the antenna dimensions.

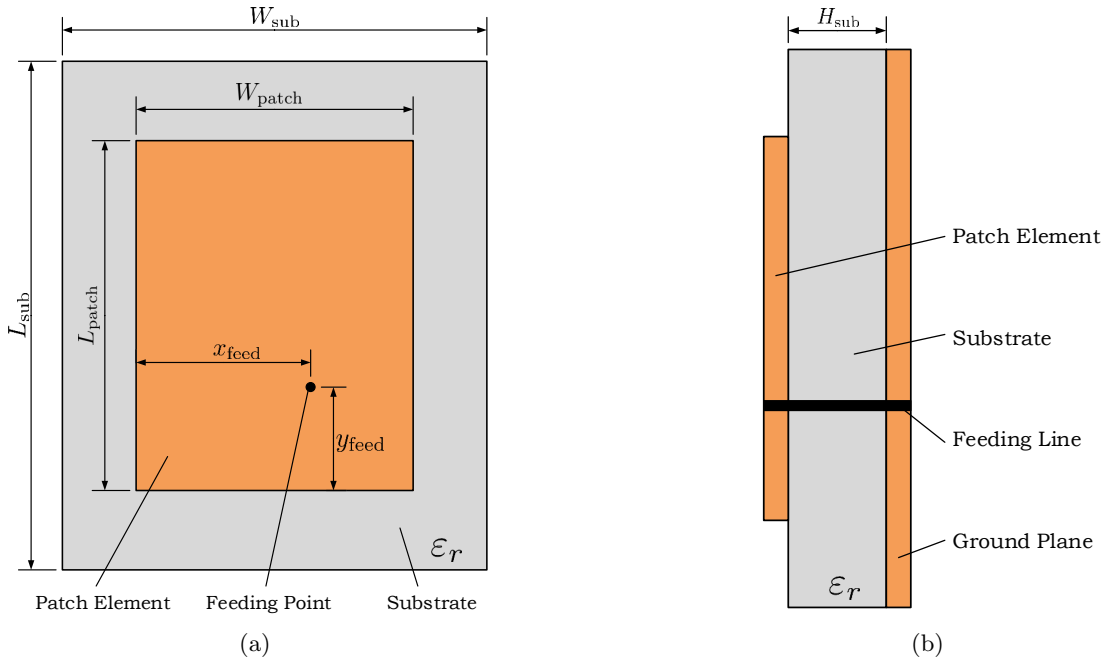

FIGURE 5.12: Structure of a microstrip patch antenna: (A) Top view, (B) Side view

For the excitation, a coaxial pin feed was chosen because it allows an easier and more robust assembly of the antenna compared to a microstrip line (a copper line that leads from the edge of the substrate to the edge of the patch element) feed. In addition, the feeding point could be placed at any location of the patch element in order to influence the input impedance. Furthermore, the coaxial feed had lower spurious radiation than a microstrip.

The geometry of the patch element and the substrate depended on the dielectric constant of the substrate, ε_r, the height of the substrate, H_{sub}, and the desired operating frequency, f_0.

After designing a single linearly polarized patch antenna for the UHF RFID frequency range, it could be adapted for circular polarization and then extended with further elements to form a linear uniform array.

The bandwidth of the worldwide UHF RFID frequency regulations is $BW_{\text{RFID}} = 100$ MHz (860 MHz to 960 MHz). Since the bandwidth BW_{MS} of a microstrip patch antenna is limited to around $0.02 \cdot f_0 \leq BW_{\text{MS}} \leq 0.05 \cdot f_0$ [256] (18 MHz $\leq BW_{\text{MS}} \leq$ 46 MHz for the global center frequency $f_0 = 910$ MHz), it can only support one of the global bands. Thus, the target frequency for the new design was assumed to be the center frequency of the European UHF RFID range ($f_0 = 866.6$ MHz). Standard values for FR4 substrate were $\varepsilon_r = 4.3$ and $H_{\text{sub}} = 1.5$ mm.

Using the equations given in [257], the width of the patch element was calculated as

$$W_{\text{patch}} = \frac{c}{2f_0\sqrt{\frac{\varepsilon_r+1}{2}}} = 106.30 \text{ mm}. \tag{5.16}$$

The length L_{patch} was derived from the effective dielectric constant for the width of the antenna $\varepsilon_{\text{eff},W}$ with

$$\varepsilon_{\text{eff},W} = \frac{\varepsilon_r + 1}{2} + \frac{\varepsilon_r - 1}{2} \cdot \frac{1}{\sqrt{1 + 12\frac{H_{\text{sub}}}{W_{\text{patch}}}}} = 4.04 \tag{5.17}$$

as

$$L_{\text{patch}} = \frac{c}{2f_0\sqrt{\varepsilon_{\text{eff},W}}} - 0.824H_{\text{sub}} \cdot \frac{(\varepsilon_{\text{eff},W} + 0.3)\left(\frac{W_{\text{patch}}}{H_{\text{sub}}} + 0.264\right)}{(\varepsilon_{\text{eff},W} - 0.258)\left(\frac{W_{\text{patch}}}{H_{\text{sub}}} + 0.8\right)} = 83.25 \text{ mm} \tag{5.18}$$

The width W_{sub} and the length L_{sub} of the substrate should exceed the dimensions of the patch element by at least $6 \cdot H_{\text{sub}}$:

$$W_{\text{sub}} = 6H_{\text{sub}} + W_{\text{patch}} = 115.3 \text{ mm} \tag{5.19}$$

$$L_{\text{sub}} = 6H_{\text{sub}} + L_{\text{patch}} = 92.25 \text{ mm} \tag{5.20}$$

For the location of the feeding point, $x_{\text{feed}} = W_{\text{patch}}/2 = 53.15$ mm should be chosen [257] and y_{feed} was derived from the effective dielectric constant $\varepsilon_{\text{eff},L}$ for

the length of the antenna

$$\varepsilon_{\text{eff},L} = \frac{\varepsilon_r + 1}{2} + \frac{\varepsilon_r - 1}{2} \cdot \frac{1}{\sqrt{1 + 12\frac{H_{\text{sub}}}{L_{\text{patch}}}}} = 4.64 \tag{5.21}$$

as

$$y_{\text{feed}} = \frac{L_{\text{patch}}}{2\sqrt{\varepsilon_{\text{eff},L}}} = 19.33 \text{ mm}. \tag{5.22}$$

The performance of the antenna design that was derived from the universal equations was investigated by means of simulations. For this purpose, the software FEKO[1] was used which is a three-dimensional electromagnetic simulation tool that is based on the Method of Moments (MoM) integral formulation of the Maxwell Equations. It consists of three programs called CADFEKO, FEKO Solver and POSTFEKO. In CADFEKO, a three-dimensional CAD model of the antenna is drawn and all material properties (e.g. the dielectric constant of the substrate) are defined. Then, the desired simulation result (e.g. three-dimensional gain pattern) is specified and the FEKO Solver is started which applies the MoM method to execute the simulation. Following the simulation phase, POSTFEKO provides different types of plots (e.g. Cartesian or polar) to visualize the simulation results. Pictures of CADFEKO and POSTFEKO for the design of the microstrip patch antenna are provided in appendix C.1.

At this first stage of the antenna design process, the most important performance criterion was the reflection coefficient (or return loss) S_{11}. In units of dB, it is defined as

$$S_{11} = 10 \log_{10} \frac{P_{\text{incident}}}{P_{\text{reflected}}} \text{ dB}, \tag{5.23}$$

where P_{incident} is the signal power generated from the signal source that is feeding the antenna and $P_{\text{reflected}}$ is the signal power that is reflected back from the antenna to the signal source. The radiated power of the antenna is

$$P_{\text{radiated}} = P_{\text{incident}} - P_{\text{reflected}}. \tag{5.24}$$

The amounts of incident and reflected power depend on the impedances $\underline{Z}_{\text{S}}$ and $\underline{Z}_{\text{ant}}$ of the source and the antenna, respectively. Thus, the reflection coefficient can also be expressed as

$$S_{11} = -20 \log_{10} \left| \frac{\underline{Z}_{\text{ant}} - \underline{Z}_{\text{S}}^*}{\underline{Z}_{\text{ant}} + \underline{Z}_{\text{S}}} \right| \tag{5.25}$$

[1] **Fe**ldberechnung für **K**örper mit beliebiger **O**berfläche (German for 'field calculations involving bodies of arbitrary shape')

If the impedances of the source and the antenna are matched ($\underline{Z}_{\text{ant}} = \underline{Z}_{\text{S}}^{*}$), all incident signal power is radiated by the antenna ($P_{\text{radiated}} = P_{\text{incident}}$ and $P_{\text{reflected}} = 0$ W) and the return loss will approach zero. However, in reality, it is not possible to realize perfect matching. As a rule of thumb, $S_{11} \leq -10$ dB is sufficient as a design target because it means that 90% of the input signal energy is radiated by the antenna [140]. The typical source impedance in wireless communication systems is $Z_{\text{S}} = 50\ \Omega$. Thus, the objective of the antenna design was to achieve close approximation of $Z_{\text{ant}} = 50\ \Omega$.

The simulation of the newly designed patch antenna delivered an input impedance of $\underline{Z}_{\text{ant}} = (25.7 - j1.6)\,\Omega$ and a reflection coefficient of $S_{11} = -10$ dB for $f_0 = 866.6$ MHz which was equal to the target S_{11}. However, the minimum value of S_{11} lay at $f = 861.7$ MHz. The parameters of the antenna geometry can be adapted to shift the minimum S_{11} value to the target frequency so that it radiates the maximum possible signal power at this frequency. The software FEKO allows an automatic optimization of the geometry parameters W_{patch}, x_{feed} and y_{feed} to achieve a minimum S_{11} at the target frequency. After setting a desired range for the respective parameter (e.g. $x_{\text{feed}} = 0...W_{\text{patch}}$) and a desired target parameter value (e.g. S_{11} minimal at $f_0 = 866.6$ MHz), FEKO simulated all possible parameter values and identified the optimum. It is also possible to define multiple variable parameters and optimization goals.

The results of the design optimization process were as follows: $W_{\text{patch}} = 105.6$ mm, $L_{\text{patch}} = 82.703$ mm, $x_{\text{feed}} = 18.515$ mm, $y_{\text{feed}} = 15.438$ mm, $W_{\text{sub}} = 114.6$ mm, $L_{\text{sub}} = 91.703$ mm. The simulated S_{11} for this design showed that the minimum ($S_{11} = -23.1$ dB) now corresponded to the target frequency and that the input impedance for $f_0 = 866.6$ MHz was now $\underline{Z}_{\text{ant}} = (43.8 + j4.26)\ \Omega$. The simulated bandwidth of the antenna (all frequencies with $S_{11} < -10$ dB) was 12.1 MHz, corresponding to a frequency range of 860.8 MHz to 872.9 MHz which covered the full European UHF RFID range.

As a next step, the maximum gain of the antenna was simulated and investigated. The gain, in general, is expressed in units of dBi and defines the factor between the power radiated by the considered antenna compared to a lossless isotropic antenna if both antennas are fed with the same signal power. Typical interrogators for passive UHF RFID systems generate an output power of 500 mW (27 dBm). Thus, a maximum antenna gain of 3 dBi is sufficient to reach the allowed interrogator transmitter power of 30 dBm EIRP (Equivalent Isotropically Radiated Power). The simulation of the revised patch antenna showed a maximum gain of only

$G_{\max} = -3.62$ dBi which was most probably caused by losses in the FR4 substrate. Thus, a thicker substrate and/or a substrate with a lower ε_r had to be used to increase the gain of the antenna [257]. The maximum available thickness of double sided copper coated FR4 material was 3.2 mm. Using this substrate, a maximum gain of $G_{\max} = 0.47$ dBi was achieved which is still too low for a passive UHF RFID localization system.

For a further gain improvement, it was necessary to use a different substrate material. Air has the lowest possible dielectric constant of $\varepsilon_r \approx 1$ and can be used as a substrate if the antenna element is separated from the ground plane by an air gap. The patch element and the ground plane could then be realized on two separate FR4 boards. The height of the air gap was chosen as $H_{\text{sub}} = 5$ mm to achieve a low overall thickness of the antenna. This design delivered a maximum simulated gain of $G_{\max} = 6$ dBi which was more than sufficient for the target application. However, the practical assembly of an air gap antenna was difficult and the antenna had a limited stability against mechanical forces. Thus, it was reasonable to apply a robust substrate material that has a lower ε_r than FR4 material. A 5 mm polyvinyl chloride (PVC) board was inexpensive, very robust and had a dielectric constant of $\varepsilon_r = 2.9$. After replacing the air gap with a PVC substrate material, the patch antenna achieved a maximum simulated gain of $G_{\max} = 4.5$ dBi.

The two existing techniques to achieve circular polarization are the dual feed method and the single feed method (figure 5.13). Both methods utilize a rectangular patch antenna element of size $L_{\text{patch}} \times L_{\text{patch}}$. The dual feed technique applies two excitation points F_1, F_2 that have to be fed with 90° phase shifted versions of the source signal signal. This would require an external power divider to generate the phase shifted signals from a single feeding source which increases the complexity and cost of the antenna. The single feed method only needs a single excitation point F and two edges of the patch element have to be cut which was easy to realize using the described FR4 and PVC based solution.

The software FEKO was thus used to adapt the design of the linearly polarized microstrip patch antenna to a single feed circularly polarized antenna. Different optimisation processes were executed to maintain the high gain and the low reflection coefficient for the target frequency.

The most important performance parameter of a circularly polarized antenna is the axial ratio R that defines the ratio of the two orthogonal components of the radiated electrical field. For perfect circular polarization, both components have

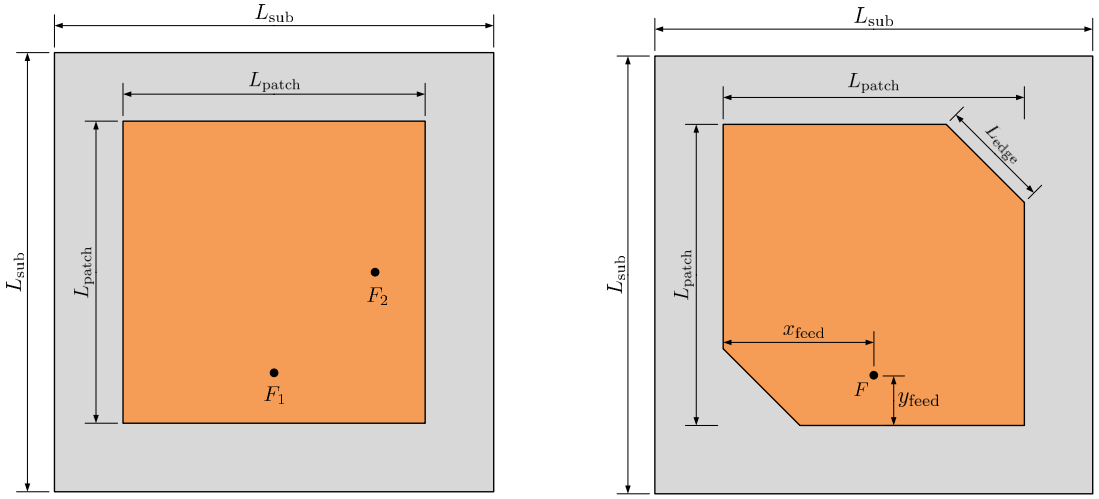

FIGURE 5.13: Excitations for circularly polarized microstrip patch antennas: (A) Dual feed, (B) Single feed

to be identical, i.e. the axial ratio is $R = 1 = 0$ dB. This parameter was also taken into account in the optimization process.

The final design of the single circularly polarized microstrip patch was as follows: $L_{\text{patch}} = 92$ mm, $L_{\text{sub}} = 131$ mm, $H_{\text{sub}} = 5$ mm, $x_{\text{feed}} = 46$ mm, $y_{\text{feed}} = 21$ mm. This design delivers the following simulation results for $f_0 = 866.6$ MHz: $G_{\max} = 4.7$ dBi, $S_{11} = -11.3$ dB, $R = 1.14 = 0.56$ dB.

Three single microstrip patch antenna elements were combined to form a linear uniform antenna array with the inter-element spacing s. As previously described, s had to be smaller than $\lambda/2$ ($\lambda/2 = 173$ mm for $f = 866.6$ MHz) but had to be high enough to minimize mutual coupling between the elements. Simulations of the S_{21} parameter (i.e. the ratio between the transmitted signal power of element 2 and the part of the transmitted power that couples into element 1) using the new three-element design showed that the S_{21} did not significantly increase for an inter-element spacing larger than $s = 160$ mm which was smaller than $\lambda/2$ and thus an optimum value. Figure 5.14 depicts the final design of the new antenna array. The sizes of ground plane and the substrate were increased to achieve a symmetrical look and an overall dimension of 480 mm $\times$ 160 mm. Although the width of the antenna array exceeded the width of an A4 paper sheet, the length was smaller and the overall area was close to the area of an A4 paper (624 cm^2 for an A4 paper sheet and 768 cm^2 for the array). Figure 5.15 shows a picture of the assembled array that was constructed according to the simulation results.

Table 5.10 compares the simulated and the measured antenna parameters as mean values over the full European UHF RFID range.

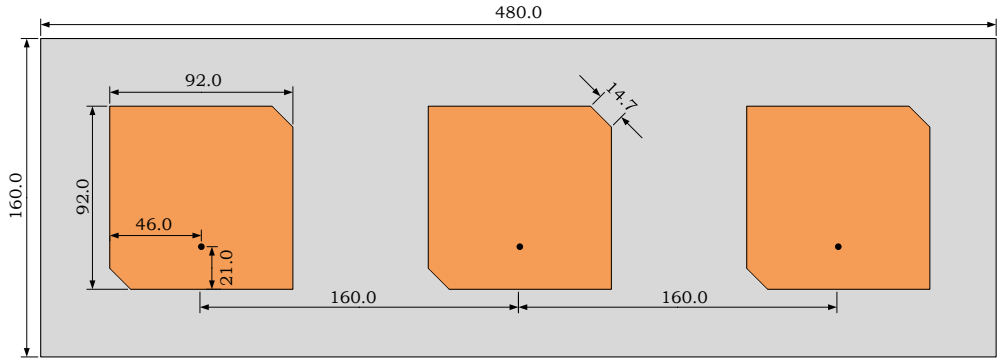

FIGURE 5.14: Final design of the circularly polarized patch antenna array (all dimensions in mm)

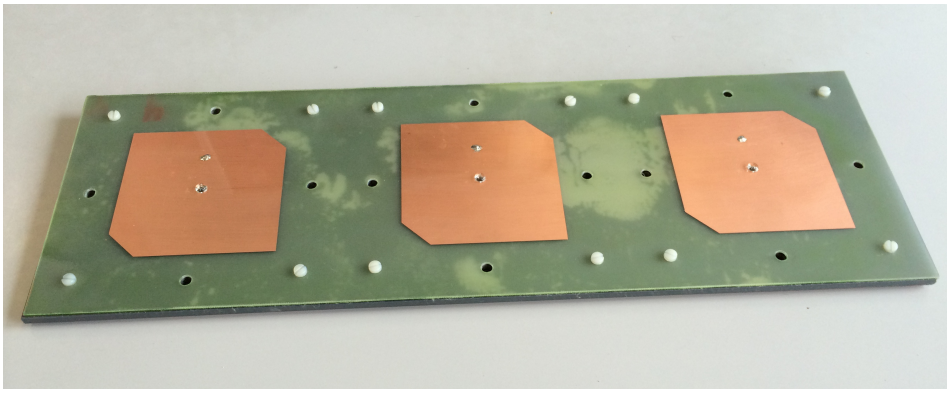

FIGURE 5.15: Picture of the circularly polarized patch antenna array

TABLE 5.10: Simulation and measurement results for the new circularly polarized microstrip patch antenna array

	Single Elements		**Full Array**				
	S_{11} **[dB]**	$\underline{Z}_{\text{ant}}$ [Ω]	$G_{\max}$ **[dBi]**	BW **[MHz]**	R **[dB]**	S_{21} **[dB]**	S_{31} **[dB]**
Simulation	-10.3	55.2+j29	8.5	66 (854-920)	1.8	-20.9	-24.3
Measurement	-15.4	41.9-j15.7	8.2	70 (812-882)	1.3	-18.5	-25.2

The antenna array was connected to the DSP unit by means of cables. Since very small length differences of the cables led to high phase shifts of the received tag signal at the input of the DSP unit, the phase shifts of the cables were determined in measurements (e.g. using a network analyzer) and equalized in the AoA calculation.

Since there were no constraints on the size of the transmitter antenna for the AoA unit, a circularly polarized patch antenna with a higher gain was used. Details of this antenna are given in appendix C.3.2.

All components of the AoA unit (receiver antenna array, DSP unit, transmitter antenna) were mounted onto a wooden stand that did not generate additional reflections in the measurement setup. The receiver antenna array was arranged at a height of 1.5 m. Measurements of the mutual coupling between the transmitter antenna and the receiver antenna array showed that a minimum spatial separation of 0.5 m between the antennas was required to guarantee an optimum functionality of the AoA unit. A picture of the full AoA unit is provided in appendix C.3.3.

5.3.1.3 Target Tags

For the localization experiments, two different types of passive UHF RFID target tags were used: 1) the UPM RaflaTac DogBone, being the most commonly used commercially available label tag and consisting of a tag IC and a linearly polarized folded dipole antenna, 2) the optimum localization system required the use of a circularly polarized target tag. However, since there are no commercial circularly polarized tags available, a standard tag IC was matched to a 50 Ω load by means of a transmission line transformation on FR4 board. Then, the same circularly polarized patch antenna that was used as the AoA unit's transmitter antenna was connected to the custom tag.

Details of the two tags are given in appendix C.3.4.

For localization measurements, the target tag was mounted onto a wooden stand at a height of 1.5 m.

5.3.2 AoA and Localization Measurements

Different measurements were conducted in five real-world scenarios at Cologne University of Applied Sciences to verify the performance of the new receiver beamforming localization method and the new AoA units:

- Scenario S1: The anechoic chamber (AoA measurements)
- Scenario S2: An outdoor balcony (AoA measurements)
- Scenario S3: A standard seminar room (same as for the simulations in this chapter; AoA and localization measurements)
- Scenario S4: A machine hall (AoA and localization measurements)
- Scenario S5: A machine hall with an additional scatterer in measurement zone (AoA and localization measurements)

The different scenarios were chosen to represent typical indoor application environments with differing influences of multipath reflections (no reflections in the anechoic chamber, only floor reflection on the outdoor balcony, all reflections in the other scenarios). In the machine hall, the measurement grid was surrounded with metallic objects such as machines or closets which created additional reflections towards different directions. The additional scatterer (a metallic cylinder with a diameter of 0.55 m and a height of 0.6 m) in scenario S5 that was placed at tag position ⑬ (center of the measurement grid) blocked the LOS path to different AoA unit positions and led to new reflections that originated within the measurement grid and thus had short path lengths and high signal powers. Pictures of the different setups and localization environments are given in appendix C.4.

Target tag angle-of-arrival measurements with one AoA unit were conducted in scenarios S1 and S2. In the anechoic chamber (S1), the antenna array was mounted onto a movable antenna positioner that rotated the array in 5° steps in a range of $-45° \leq \theta \leq 45°$ (figure 5.16). A UPM Raflatac DogBone tag was fixed to a center position at a distance of 3.00 m from the array.

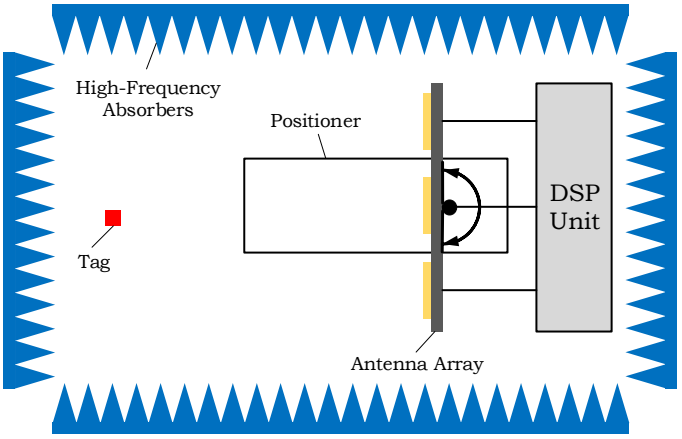

FIGURE 5.16: Drawing of the setup for the AoA measurements in the anechoic chamber (scenario S1, top view)

Figure 5.17 compares the measured AoAs for all $N = 26$ antenna array angles with the actual tag angles. The mean AoA estimation error $\overline{\Delta\theta}$ and the mean standard error deviation $\sigma_{\Delta\theta}$ are calculated according to equations (5.7) and (5.10), respectively. For the AoA measurement in the anechoic chamber (S1), the mean error was $\overline{\Delta\theta}_{\mathrm{S1}} = 1.41°$ and the mean standard error deviation $\sigma_{\Delta\theta,\mathrm{S1}} = 1.20°$.

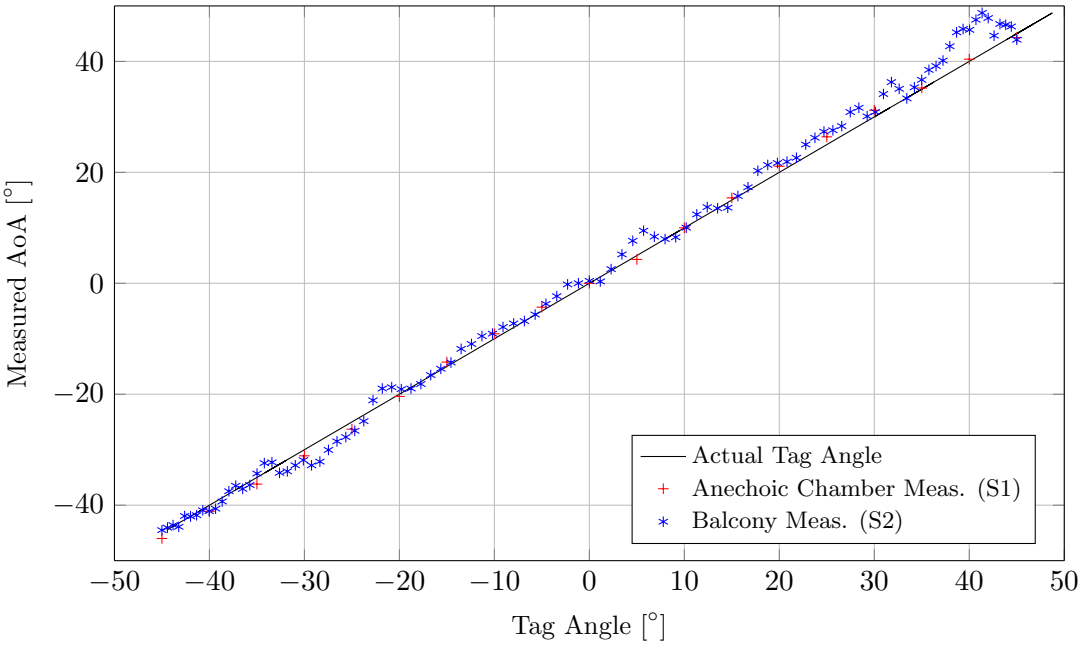

FIGURE 5.17: Results of the AoA measurements for scenarios S1 and S2

In scenario S2 (outdoor balcony), the tag was moved on a straight line in front of the AoA unit's antenna array in a range of $-45° < \theta < 45°$ by means of a nylon cord (figure 5.18). An AoA measurement was performed for $N = 100$ equally spaced tag positions (figure 5.17). The achieved mean AoA error was $\overline{\Delta\theta}_{S2} = 2.61°$ and the mean error standard deviation $\sigma_{\Delta\theta,S2} = 2.21°$. The reason for the high AoA errors for $\theta > 38°$ was the presence of a metallic object in the measurement environment.

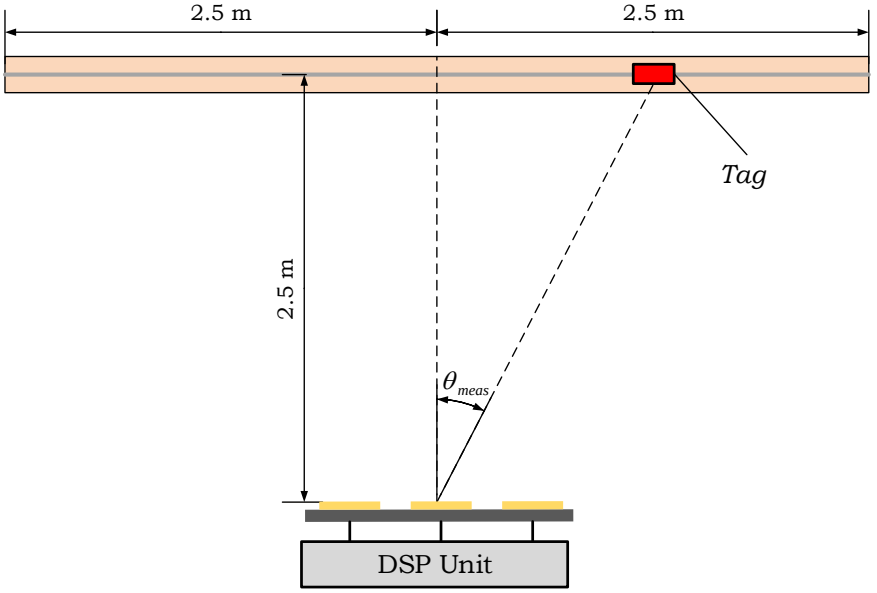

FIGURE 5.18: Drawing of the setup for the AoA measurements on the university balcony (scenario S2, top view)

The ECDFs for the two AoA measurements (figure 5.19) show that all AoA errors in the anechoic chamber lie below 4°. In the balcony measurement, 75% of the errors lie below 4° and 90% below 6°. This confirms the influence of multipath on the localization performance.

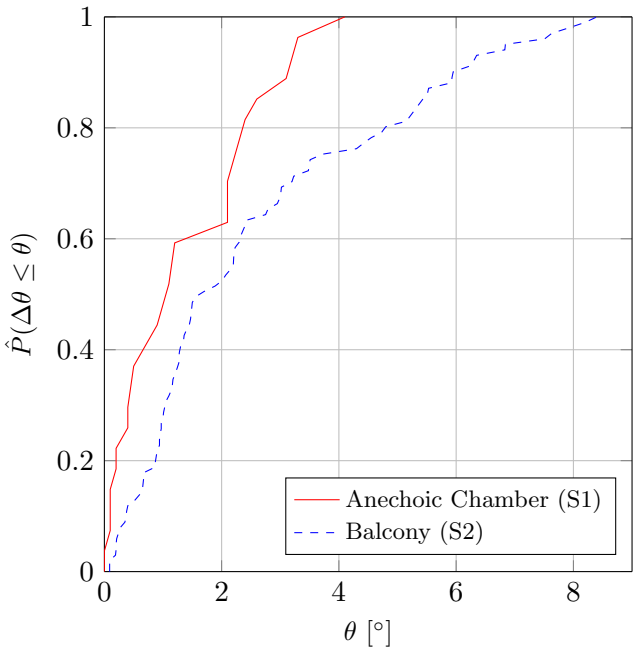

FIGURE 5.19: Error probabilities of the AoA measurements for scenarios S1 and S2

For further measurements, four AoA units were set up in scenarios S3, S4 and S5 together with the tag position grid as depicted in figure 5.9. The tag location was angulated using the four estimated angles-of-arrival and the nearest point algorithm. Table 5.11 lists the achieved mean AoA error (mean value for all four antenna array positions) and the achieved localization accuracies. For the sake of completeness, additional measurements were conducted in the seminar room (S3) and the machine hall (S4) using a circularly polarized patch antenna for the tag (scenarios S3circ and S4circ).

The measurement results show that the AoA estimation and localization accuracies decreased and the standard error deviations increased with an increasing influence of multipath reflections on the receiver signals. Due to the same number of reflection paths in the seminar room and the machine hall, the error values lie in the same range. The most probable reason for the slightly lower error values in the machine hall is that the metallic objects in the localization environment scatter the reflected signal power away from the measurement grid.

An interesting finding is that a relatively high localization performance ($\overline{\Delta d}_{S5}$ = 35 cm) was achieved in the machine hall with the additional scatterer where the influence of multipath was very high and the line-of-sight of several target tag positions was blocked.

The circularly polarized tag antenna improved the localization performance in scenarios S3 and S4. The mean AoA errors were decreased by around 40% and the mean error standard deviation by around 50%. For the localization results, improvements of 50% and 60%, respectively were achieved. From all conducted measurements, the highest localization accuracy (10 cm) and the lowest standard error deviation (5 cm) were achieved with circularly polarized antennas in the machine hall scenario. Up to date, better localization results have not been reported in the literature considering environments with similar multipath characteristics. Figure 5.20 compares the error probabilities for the three basic scenarios S3, S4 and S5. The comparison of the localization performance for a linear tag and a circular tag in S3 and S4 is depicted in figure 5.21.

In the measurements, a low mean processing time of 80 ms for the estimation of one angle-of-arrival was achieved. Consequently, the full localization processing time for acquiring four AoAs and angulating the target tag position was around 400 ms which corresponded to an update rate of 2.5 Hz.

TABLE 5.11: AoA and localization measurement results for all scenarios

Scenario	**Environment**	$\overline{\Delta\theta}$ [°]	$\sigma_{\Delta\theta}$ [°]	$\overline{\Delta d}$ **[cm]**	$\sigma_{\Delta d}$ **[cm]**
S1	Anechoic Chamber	1.41	1.20	-	-
S2	Balcony	2.61	1.48	-	-
S3	Seminar Room	4.42	3.97	24	17
S4	Machine Hall	4.26	3.63	21	14
S5	Machine Hall with Scatterer	6.52	6.03	35	29
S3circ	Seminar Room (Circular Tag)	2.58	1.82	11	7
S4circ	Machine Hall (Circular Tag)	2.64	1.77	10	5

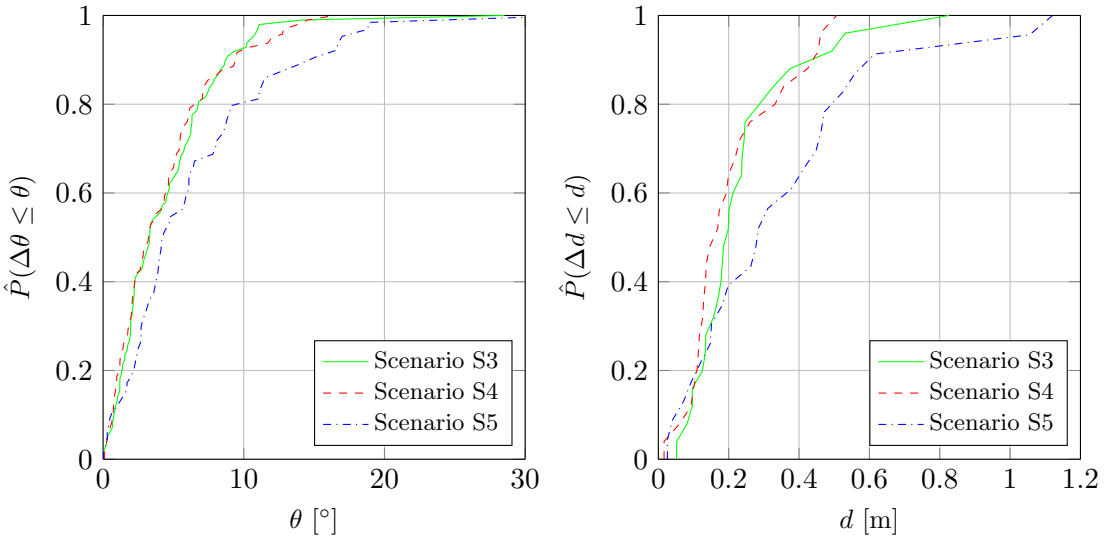

FIGURE 5.20: Error probabilities for the localization scenarios S3, S4, S5

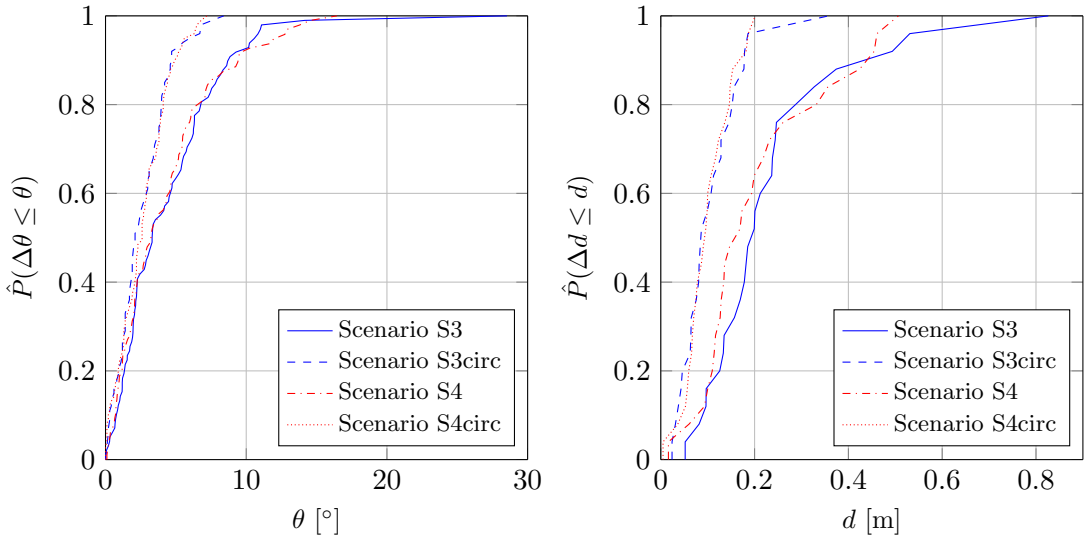

FIGURE 5.21: Error probabilities for the linear and the circular tag in scenarios S3 and S4

5.4 Summary

A receiver beamforming technique for target tag localization in passive UHF RFID systems has been presented which uses the Root MUSIC algorithm to estimate the angle-of-arrival of a target tag signal.

In a standard simulation scenario (university seminar room), the basic localization approach has been analysed and the degradation of the achieved localization performance through multipath has been demonstrated.

Multipath reducing techniques have been used to improve the achievable localization performance. The following improvements have been achieved with respect to the localization accuracy (the improvements in the mean standard error deviations have been shown to be similar):

- Frequency diversity in the new EU band: 23%
- Spatial and orientation diversity: 45%
- Antenna types: 32% (dipole tag) and 50% (patch tag)
- Antenna polarization: 64% (circular system)

Reflection cancellation reduces the simulated localization error by up to 68% but its practical feasibility is limited. The same is true for a circularly polarized tag antenna.

The findings of the improvement analysis have been used to set up an optimum receiver beamforming system that has been able to localize the target tag with a mean simulated accuracy of 2 cm in typical multipath environments (improvement of 91% compared to the basic approach).

A new multiangulation method (nearest point algorithm) has been proposed and has been used for the spatial diversity approach where more than two angles-of-arrival had to be processed.

Based on the theoretical principles of the receiver beamforming approach, a novel experimental testbed has been designed and build which utilizes signal correlation for the Root MUSIC phase-difference measurements. The performance of the new receiver beamforming localization system has been demonstrated in multiple real-world measurements. In a standard system setup with a linearly polarized tag, a high mean localization accuracy of 21 cm and a low mean standard error deviation of 14 cm have been achieved in a typical multipath environment. Even in harsh multipath environments, the localization accuracy and reliability have shown to remain high. The optimum performance has been achieved in a system with a circularly polarized tag (localization accuracy of 10 cm and standard error deviation of 5 cm). A comparable performance has never been achieved under equal multipath conditions.

Chapter 6

Transmitter Beamforming Localization

The investigations of existing beamforming techniques in chapter 2 have led to the belief that digital transmitter beamforming is ideally suited for the realization of a passive UHF RFID localization system which achieves sufficient localization accuracy in typical application scenarios.

Transmitter beamforming can be utilized to estimate the target tag direction in an angulation system where antenna arrays are used as the interrogator's transmitter antenna. The simplest approach is to measure the RSS of the backscattered tag signal while pivoting the antenna array's main lobe in the azimuth plane. The main lobe angle that corresponds to the maximum RSS is then identified as the target tag angle. It is shown that multipath highly deteriorates the achievable angle estimation accuracy of this technique.

In order to improve this accuracy, a novel angle estimation technique is introduced that does not rely on signal power measurements but utilizes the precisely defined response threshold (i.e. the sensitivity) of passive UHF RFID tags. It is called 'angle-of-activation' (AoAct) because the angle estimation process is only based on the readability of the target tag (i.e. its activation). In contrast to the receiver beamforming AoA technique, it has two advantages: 1) the main lobe pivoting process distributes the interrogator transmitter power towards different directions thereby changing the multipath characteristics of the wireless channel (see antenna orientation in section 4.2.5), 2) only a minimum transmitter power is used which guarantees that the tag is not activated by reflections.

Simulations of the basic AoAct algorithm reveal the potential to achieve improved angle estimation accuracy and improved processing time. Thus, the basic algorithm is optimized accordingly and every step in the optimization process is verified by simulations.

For an experimental verification of the AoAct localization performance, a testbed is designed on the principles of digital transmitter beamforming. It is used for measurements in typical indoor application scenarios and the results are compared to the receiver beamforming system. It is shown that the new AoAct method needs higher processing times than the AoA method but it outperforms AoA with respect to the localization accuracy and robustness.

6.1 Localization Principle

The basic transmitter beamforming AoAct localization system is identical to the receiver beamforming AoA system that was introduced in section 5.1 (figure 5.1).

A number of $N \geq 2$ AoAct units that consist of an antenna array and a DSP unit are used to estimate the angles $\theta_{\mathrm{tag},n} = \theta_{\mathrm{tag},1}...\theta_{\mathrm{tag},N}$ between the antenna array and the target tag from different locations. After estimating all angles, the location of the tag is calculated using a multiangulation method (e.g. the nearest point algorithm).

The AoAct units are, in principle, modified UHF RFID interrogators that use an antenna array as their transmitter antenna. The objective of the localization system is to estimate the position of the target tag $L_{\mathrm{t}} = (x_{\mathrm{t}}, y_{\mathrm{t}})$ in an azimuth plane of the localization environment (section 5.1). The z-coordinate of this plane is determined by the height in which the AoAct unit's antenna arrays are arranged.

The transmitter beamforming technique (section 2.4) is utilized to determine the tag angles $\theta_{\mathrm{tag},n}$ as described in the following.

The beam pattern of a uniform linear antenna array with $l = 0...L-1$ elements is manipulated by changing the complex weights w_l in the feeding lines of the array elements which are defined as

$$w_l = A_l e^{j\varphi_l}, \tag{6.1}$$

where A_l and φ_l are the absolute value and the phase of the lth weight, respectively.

The resulting beam pattern $B(\theta)$ in the azimuth plane of the array is calculated as [200]

$$B(\theta) = e^{-j\left(\frac{L-1}{2}\right)\phi} \sum_{l=0}^{L-1} w_l^* e^{jl\phi}, \tag{6.2}$$

with $\phi = \frac{2\pi s}{\lambda} \cos\theta$. s is the inter-element spacing of the antenna array and θ is the the azimuth angle of the antenna array with respect to the normal of the straight line in which the antenna elements are arranged. Examples of beam patterns that are generated by applying different weights w_l are depicted in figure 6.1.

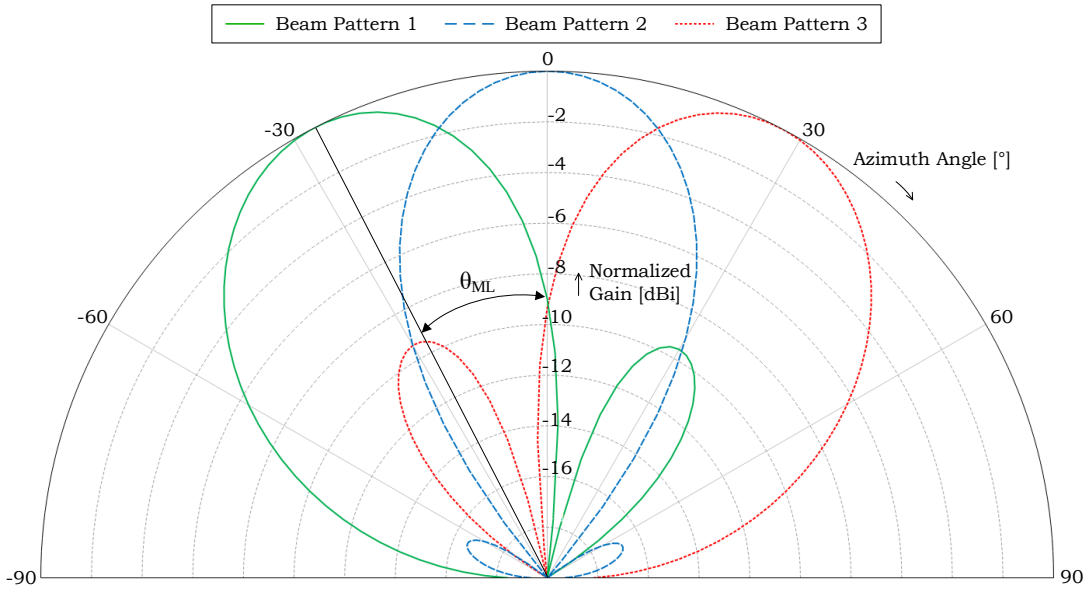

FIGURE 6.1: Examples of transmitter beamforming beam patterns

If a constant absolute weight value of $A_l = 1$ is assumed and the phase shift $\Delta\varphi$ between the weights of two adjacent antenna array elements is constant ($\Delta\varphi = \varphi_{l+1} - \varphi_l = \text{const}$ for all $l = 0...L-1$, where φ_l is the phase of the weight w_l), the main lobe angle θ_{ML} with respect to the normal of the array is [258]

$$\theta_{\text{ML}} = \arcsin\left(\frac{\Delta\varphi}{ks}\right), \tag{6.3}$$

with $k = \frac{2\pi}{\lambda}$.

For the same reasons that were mentioned for the receiver beamforming method (size, hardware complexity, cost, etc.; section 5.1), a three-element antenna array ($L = 3$) was chosen here for the transmitter beamforming approach.

A constant phase shift $\Delta\varphi$ between the weights of two adjacent array elements can be achieved by setting the three weight phases to $\varphi_0 = \varphi, \varphi_1 = 0, \varphi_2 = -\varphi$ (e.g. $\varphi_0 = 45°, \varphi_1 = 0, \varphi_2 = -45°$).

The minimum and maximum possible φ values for fixed values of λ and s can be found by setting the argument of the arcsin function in equation (6.3) to one and solving the argument function for $\Delta\varphi$. For $\lambda = 0.345$ m (according to the centre frequency of the European UHF RFID range) and $s = 0.16$ m (according to the patch antenna array presented in the previous chapter), the usable φ range is

$$\varphi = \varphi_{\min} ... \varphi_{\max} = -167° ... 167°.$$

This corresponds to a maximum pivoting range for the main lobe direction θ_{ML} of

$$\theta_{\mathrm{ML}} = \theta_{\mathrm{ML,min}} ... \theta_{\mathrm{ML,max}} = -90° ... 90°.$$

6.2 Simulation of the Localization Performance

Simulations of the localization performance were conducted using the simulation environment introduced in chapter 3 and the same typical application scenario as for the receiver beamforming localization (university seminar room with 25 target tag locations; figure 5.3 in section 5.1). The simulation environment was extended in a way that variable beam patterns for the interrogator transmitter antenna array were calculated based on the beamforming equation (6.2). The array was a circularly polarized patch antenna array with $L = 3$ and $s = 0.16$ m and the tag comprised a linearly polarized dipole antenna.

6.2.1 RSS-Based Tag Angle Estimation

The simplest approach to use transmitter beamforming for a target tag angle estimation is as follows. The main lobe direction θ_{ML} is pivoted from $\theta_{\mathrm{ML,min}}$ to $\theta_{\mathrm{ML,max}}$ in angular steps of $\Delta\theta_{\mathrm{step}}$ by varying the phase of the weights φ from $\varphi_{\min}$ to $\varphi_{\max}$ in steps of $\Delta\varphi_{\mathrm{step}}$. Simultaneously, the received signal power $P_{\mathrm{Rx,BF}}$ of the backscattered tag signal at the interrogator is measured. Then, the main lobe angle that corresponds to the maximum $P_{\mathrm{Rx,BF}}$ value is used as an estimate for the target tag angle θ_{tag}.

For the simulation of this approach, antenna array location A_1 was chosen and no reflections were assumed (i.e. only the LOS signal was present). In this simulation, a mean tag angle estimation error for the 25 tag locations of $\overline{\Delta\theta}_{\mathrm{LOS}} = 0.28°$ was achieved with a mean error standard deviation of $\sigma_{\Delta\theta,\mathrm{LOS}} = 0.16°$.

After adding multipath (i.e. all first-order reflections; number of signal paths $N = 7$) to the simulation, the error values were $\overline{\Delta\theta}_{\mathrm{MP}} = 2.45°$ and $\sigma_{\Delta\theta,\mathrm{MP}} = 2.29°$.

The ECDFs of the LOS-only and the multipath simulations (figure 6.2) show that the influence of multipath reflections highly increases the error of the angle estimation process which was caused by a false identification of the maximum $P_{\mathrm{Rx,BF}}$ due to constructive and destructive interference. The maximum angle estimation error for one target tag location in the multipath scenario was very high (10°).

The residual angle estimation error of 0.28° for the LOS-only simulation is explainable by the resolution $\Delta\theta_{\mathrm{step}}$ of the main lobe pivoting process. In the simulations, the phase φ of the beamformer weights was increased stepwise by $\Delta\varphi_{\mathrm{step}} = 1°$ which corresponds to an angular main lobe shift of $\Delta\theta_{\mathrm{step}} = 0.34°$. Thus, the mean angle estimation error of the LOS-only simulation must lie in the same range.

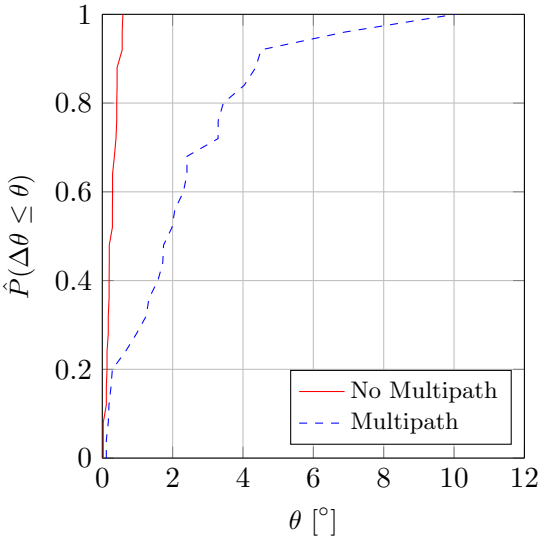

FIGURE 6.2: Error probabilites for RSS-based transmitter beamforming tag angle estimation

For a better visual comparison, all simulated angle estimation accuracies and the mean standard error deviations for the RSS-based transmitter beamforming method are listed in table 6.1.

TABLE 6.1: Simulated tag angle estimation errors for the RSS-based transmitter beamforming localization method

Simulation Scenario	$\overline{\Delta\theta}$ [°]	$\sigma_{\Delta\theta}$ [°]
TxBf, no multipath	0.28	0.16
TxBf, multipath	2.45	2.29
TxBf, multipath and circularly polarized tag	0.83	0.63
TxBf, multipath and spatial/orientation diversity	1.62	1.35
RxBf, multipath and spatial/orientation diversity	1.76	1.29

The use of a circularly polarized antenna for the tag in the multipath scenario reduced the angle estimation error by 66% because the influence of reflections on the antenna array receiver signals was highly reduced. However, compared to the LOS-only case, the error was still high.

If all four antenna array locations $A_1 ... A_4$ (figure 5.3, section 5.1) were used in a diversity approach (spatial and orientation diversity), the mean tag angle estimation error for the multipath scenario was reduced by 34%. Although this error and standard error deviation lay in same range as for the receiver beamforming approach, the aim of the research in this chapter is to further optimize the angle estimation process in multipath environments. For this purpose, the new AoAct target tag angle estimation approach is introduced which does not rely on RSS measurements.

6.2.2 AoAct-Based Tag Angle Estimation

The response threshold of passive UHF RFID tags is defined as the minimum received signal power that is required to activate the tag (i.e. the sensitivity of the tag $P_{\text{sens,tag}}$). It is reported in the literature that $P_{\text{sens,tag}}$ is a precisely defined threshold, i.e. if the received signal power $P_{\text{RX,tag}}$ is minimal lower than $P_{\text{sens,tag}}$ (typically only 0.1 dB lower), the tag is not activated [259, 260]. As soon as $P_{\text{Rx,tag}}$ is equal to or minimally higher than $P_{\text{sens,tag}}$, the tag is activated and responds to interrogator queries. This unique property of passive UHF RFID tags is utilized in the new AoAct localization approach.

Figure 6.3 shows a principle drawing of the AoAct estimation process. For clarity reasons, only the main lobes of idealized beam patterns are displayed. The target tag is positioned to an angle of $\theta_{tag} = 0°$ and the typical sensitivity of a passive UHF RFID tag (-17 dBm, dashed line). First in the AoAct estimation process, beam pattern 1 with a main lobe angle of $\theta_{\text{ML}} = \theta_{\text{ML,min}}$ is set. After that, the main lobe direction is pivoted stepwise with the step-size $\Delta\theta_{\text{step}}$ towards the maximum possible main lobe direction $\theta_{\text{ML,max}}$. For each beam pattern in this process, the tag readability is tested. The two main lobe directions are saved where the tag is activated and then deactivated ($\theta_{\text{ML}} = \theta_{\text{act}}$ for beam pattern 5 and $\theta_{\text{ML}} = \theta_{\text{deact}}$ for beam pattern 6).

For the displayed example, the tag activation angle is θ_{act} = -8° and the tag deactivation angle is θ_{deact} = 8°. The tag angle θ_{tag} with respect to the antenna array is calculated as

$$\theta_{\text{tag}} = \frac{\theta_{\text{act}} + \theta_{\text{deact}}}{2}. \tag{6.4}$$

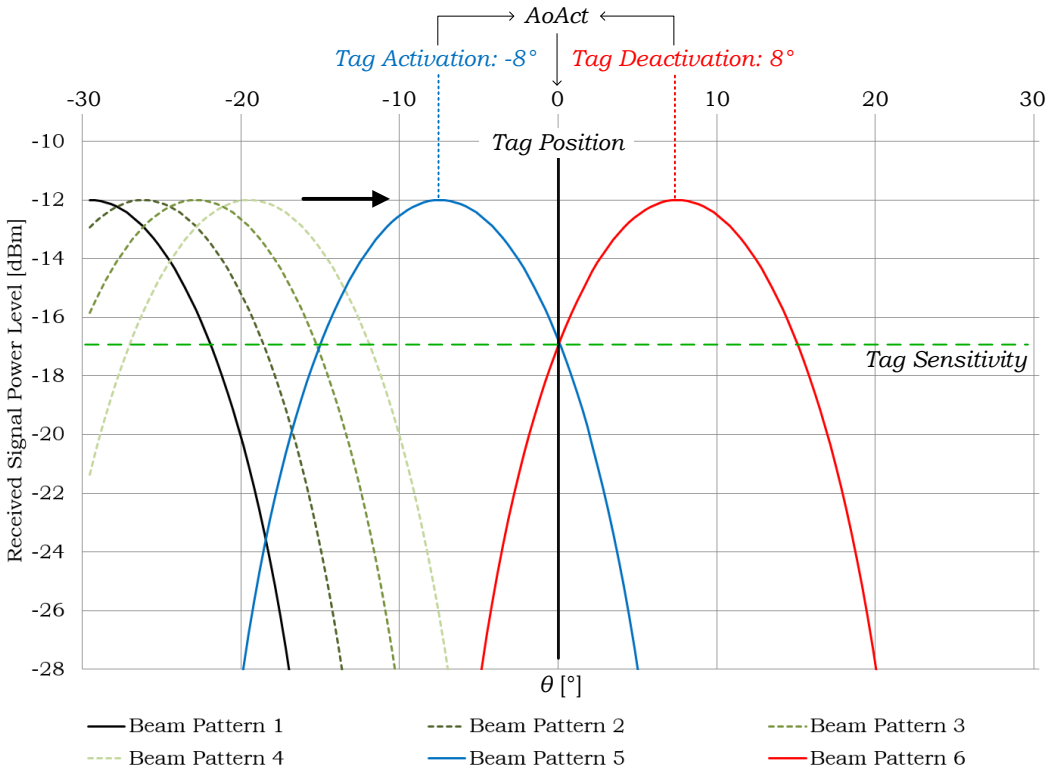

FIGURE 6.3: AoAct estimation procedure

In the previously introduced RSS-based tag angle estimation process, the transmitter power P_{Tx} of the antenna array is not considered because the identification of the maximum backscattered tag signal power is independent of P_{Tx} as long as it is high enough to activate the tag. However, in order to successfully execute the AoAct estimation algorithm, an appropriate P_{Tx} value has to be found. If this level is too low, the tag will not respond during the AoAct estimation process. If P_{Tx} is too high, the tag will respond in a wide angular range of the pivoting process which makes a detection of high θ_{tag} impossible (due to the limited angular range of θ_{ML}). In addition, if a minimum needed P_{Tx} is chosen, it is guaranteed that the activation of the tag is only caused by the direct LOS signal and not by reflections. Thus, the process of estimating the target tag angle is divided into two steps: 1) finding of an appropriate interrogator transmitter power P_{Tx}, and 2) estimating the target tag AoAct.

The overall transmitter power of the beamformer P_{Tx} is the sum of the antenna array element transmitter powers. P_{Tx} is increased by increasing the absolute values of the beamformer weights A_l and decreased accordingly. In order to preserve the shape of the beam pattern, all A_l have to be changed equally.

In a first step to formulate an algorithm for an appropriate P_{Tx} finding, the objective is to find the minimum P_{Tx} that activates the target tag. This process is displayed in figure 6.4. First, P_{Tx} is set to the minimum value $P_{\mathrm{Tx,min}}$ and the main lobe is pivoted in the full angular range in coarse steps while recording the tag readability. A fine resolution of the main lobe angle step size is not needed and would lead to longer execution times. If the target tag does not respond during the first main lobe pivoting, P_{Tx} is increased by ΔP_{step} and the pivoting process is repeated. The first P_{Tx} value that activates the tag is then used for the following AoAct estimation algorithm that is depicted in figure 6.5.

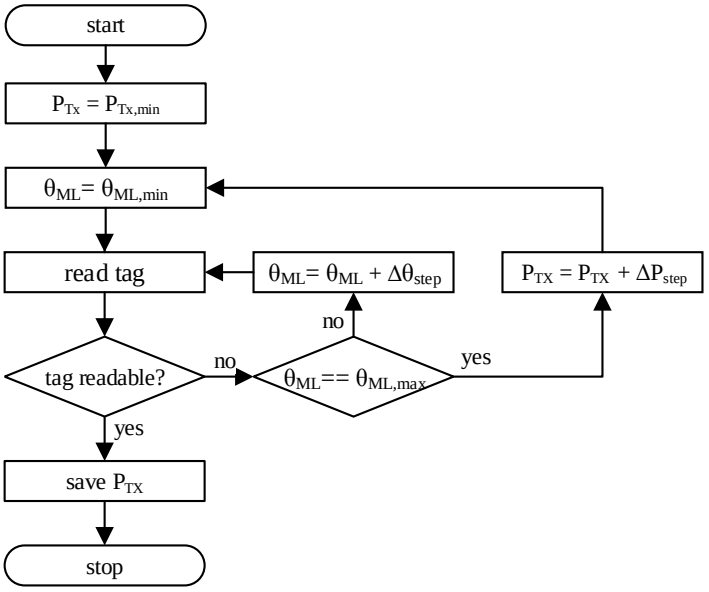

FIGURE 6.4: Flow diagram of the P_{Tx} finding algorithm

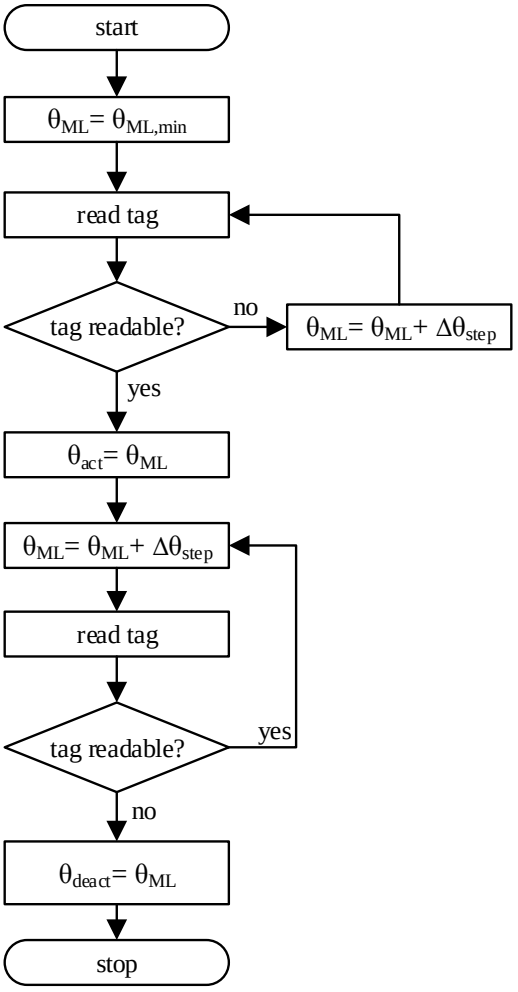

FIGURE 6.5: Flow diagram of the AoAct algorithm

The full AoAct algorithm (i.e. P_{Tx} finding and AoAct estimation) was simulated using the same scenario as for the RSS-based approach. The used step sizes for the transmitter power and the weight phase were $\Delta P_{\mathrm{step}} = 1$ dB and $\Delta\varphi_{\mathrm{step}} = 1°$. In the LOS-only case, a mean AoAct error of $\overline{\Delta\theta}_{\mathrm{LOS}} = 0.46°$ and a mean AoAct error standard deviation of $\sigma_{\Delta\theta,\mathrm{LOS}} = 0.35°$ were simulated (for comparison, the RSS-based approach achieved $\overline{\Delta\theta}_{\mathrm{LOS}} = 0.28°$ and $\sigma_{\Delta\theta,\mathrm{LOS}} = 0.16°$).

In the presence of multipath, the AoAct error was $\overline{\Delta\theta}_{\mathrm{MP}} = 0.78°$ and the error standard deviation $\sigma_{\Delta\theta,\mathrm{MP}} = 0.57°$ (the RSS-based approach achieved $\overline{\Delta\theta}_{\mathrm{MP}} = 2.45°$ and $\sigma_{\Delta\theta,\mathrm{MP}} = 2.29°$). These results show that the performance of the AoAct method is better than the performance of the RSS-based method, especially in the presence of multipath (improvement of 68% in the AoAct accuracy).

6.2.3 Improvement of the AoAct Algorithm Performance

As described for the RSS-based approach, the resolution of the main lobe pivoting process determines the accuracy of the AoAct estimation. However, the increased error values of the AoAct method compared to the RSS-based method in the LOS-only simulation are most probably caused by unbalanced beam pattern.

As an example, figure 6.6 shows the AoAct estimation for a tag angle of $\theta_{\text{tag}} = 0°$ (solid line). In this case, the tag angle is perfectly estimated because the main lobes of the two beam pattern that correspond to θ_{act} and θ_{deact} are symmetrical. Figure 6.7 shows the AoAct estimation for $\theta_{\text{tag}} = -33.7°$, where the main lobes are not symmetrical any more.

In beam pattern 1, the width of the main lobe is different to the left and to the right of the main lobe center. This leads to an angular shift of the estimated AoAct which is calculated as the mean value of the main lobe angles of the two beam pattern.

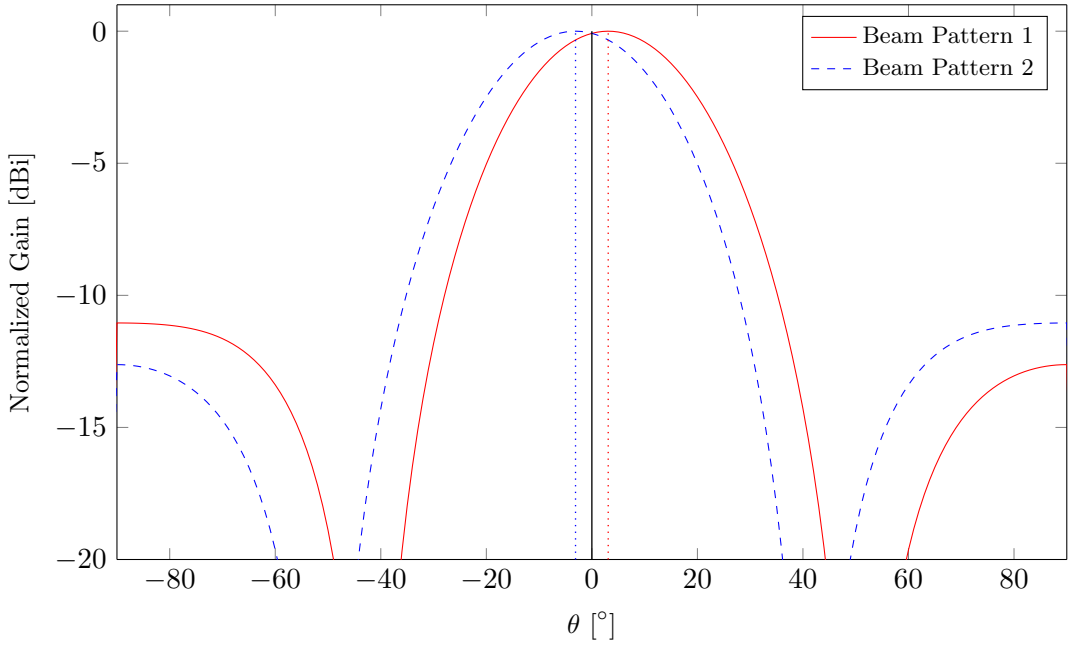

FIGURE 6.6: AoAct estimation for $\theta_{\text{tag}} = 0°$

One possibility to minimize this error is to set the transmitter power of the antenna array minimally higher than needed to activate the tag (e.g. 0.1 dB). This would guarantee that only a very small range to the left and to the right of the main lobe direction activates the tag where the main lobes of all beam patterns are almost symmetrical. In the previous simulations, the P_{Tx} finding process was conducted in steps of $\Delta P_{\text{step}} = 1$ dB. In a worst case, the determined power level is around

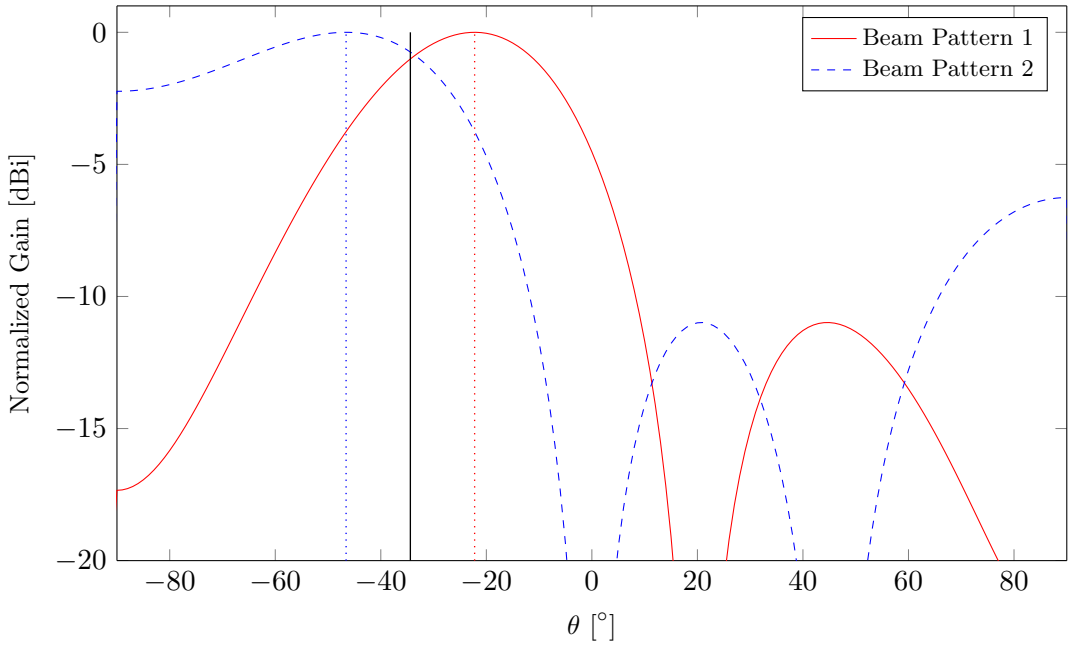

FIGURE 6.7: AoAct estimation for $\theta_{\text{tag}} = -33.7°$

1 dB higher than it would be needed to activate the tag. Consequently, the AoAct estimation is done using the unsymmetrical part of the main lobe.

In a simulation where the step size was decreased to $\Delta P_{\text{Tx}} = 0.1$ dB, the AoAct estimation error was reduced by 43%. However, there are two major disadvantages involved with this method: 1) the execution time for the P_{Tx} finding process is increased by a factor of ten, 2) in a hardware implementation of the transmitter beamforming system, various effects can lead to small fluctuations of P_{Tx} (e.g. temperature drifts). This can result in a case where the determined P_{Tx} is not high enough to activate the tag in the following AoAct estimation process.

A different method to cope with the unbalanced beam pattern is the use of weighting factors for each beam pattern that are determined as follows.

Corresponding to the step-size of the P_{Tx} finding process $\Delta P_{\text{step}} = 1$ dB, the 1 dB beamwidth BW_{1dB} of the main lobe is calculated. In a symmetrical beam pattern, the main lobe angle θ_{ML} lies exactly in the center of BW_{1dB} and the absolute values of the distances from θ_{ML} to the left and to the right BW_{1dB} points of the main lobe are exactly $\Delta\theta_{\text{ML,left}} = \Delta\theta_{\text{ML,right}} = \frac{BW_{\text{1dB}}}{2}$. In unsymmetrical beam pattern, these distances are not equal. Thus, for each of the p beam patterns used in the AoAct method, the weighting factors $b_{p,l}$ and $b_{p,r}$ are calculated as

$$b_{p,l} = \frac{\Delta\theta_{\text{ML,left}}}{0.5 \cdot BW_{\text{1dB}}} \tag{6.5}$$

and

$$b_{p,r} = \frac{\Delta\theta_{\mathrm{ML,right}}}{0.5 \cdot BW_{\mathrm{1dB}}}. \tag{6.6}$$

For example, for beam pattern 1 in figure 6.6, $b_{1,l} = 0.9962$ and $b_{1,r} = 0.9970$ which shows that it is almost symmetrical. For the unsymmetrical beam pattern 1 in figure 6.7, the weights are $b_{1,l} = 1.0292$ and $b_{1,r} = 0.8925$.

In an improved AoAct estimation approach, the tag angle is calculated as

$$\theta_{\mathrm{tag}} = \frac{b_{p,l}\theta_{\mathrm{act}} + b_{p+1,r}\theta_{\mathrm{deact}}}{2}. \tag{6.7}$$

The choice of the left weight $b_{p,l}$ or the right weight $b_{p,r}$ of the beam pattern is determined by the pivoting direction of the main lobe. The given equation assumes a pivoting from the right (positive θ_{ML}) to the left (negative θ_{ML}), where beam pattern 1 activates the tag and beam pattern 2 deactivates the tag.

In the LOS-only simulation, the use of the beam pattern weights reduced the AoAct estimation error by 28% compared to the first AoAct algorithm and in the presence of multipath, the improvement was 58%.

The main disadvantage of the presented AoAct approach in comparison to the AoA receiver beamforming method is the high execution time. For the estimation of one tag angle, the AoA receiver beamforming technique needed a mean simulation time (LOS-only simulation) of 0.11 s. The P_{TX} finding procedure of the AoAct method required a full main lobe pivoting run after each transmitter power change. For $\Delta\varphi_{\mathrm{step}} = 5°$ and $\Delta P_{\mathrm{step}} = 1$ dB (in a range of -20 dBm $\leq P_{\mathrm{Tx}} \leq 25$ dBm), the mean simulation time for one tag position was 9 s. During this process, the beam pattern had to be calculated for each ΔP_{step} and for each $\Delta\varphi_{\mathrm{step}}$. Furthermore, for each beam pattern, the received signal power at the tag location had to be calculated (assuming that the tag was readable in the uplink if it was activated in the downlink). The calculation of the AoAct only needed one full pivot of the main lobe which took a mean simulation time of 1.3 s. Thus, the overall time factor between the AoAct and the AoA simulation was approximately ten.

In order to decrease the execution time of the AoAct method, the P_{TX} finding procedure had to be optimized. The transmitter power range for this process was chosen as -25 dBm $\leq P_{\mathrm{Tx}} \leq 20$ dBm because it corresponds to the dynamic range of commonly used UHF RFID interrogators. Furthermore, the P_{Tx} finding started with the minimum possible P_{Tx}. However, using the Friis Transmission Equation, the minimum transmitter power that was needed for the activation of the

25 tag locations in the considered application scenario was approximately 0 dBm (corresponding to a minimum AoAct-unit-to-tag distance of $d = 0.71$ m). This is also the case for any other practical localization setup because the minimum distance between the tag location and the interrogator should lie in the far-field region of the antenna array ($d >> \lambda$, with $\lambda \approx 0.345$ m in the European UHF RFID frequency range). Thus, it was reasonable to start the P_{Tx} finding process with the maximum possible power level and then reduce it stepwise until the tag was not readable and more. This approach improved the mean simulation time to 4.5 s.

A further optimization can be achieved by dynamically reducing the main lobe pivoting range $\theta_{\mathrm{ML,min}}...\theta_{\mathrm{ML,max}}$. Each pivoting process with a certain P_{Tx} can be stopped as soon as the tag is readable. Then, it suffices to start the next P_{Tx} step at the same θ_{ML}, where the last step was stopped, reduced by one main lobe step $\Delta\theta_{\mathrm{step}}$. This optimization improves the mean execution time of the P_{Tx} finding to 0.4 s. A flow diagram of the optimized process is displayed in figure 6.8.

During this process, the last θ_{ML} that activated the tag, corresponded to the tag activation angle θ_{act} for the AoAct estimation. This information was utilized to optimize the AoAct procedure whose only objective now was to determine the tag deactivation angle θ_{deact}. In addition, the used pivoting process could start at a main lobe angle of $\theta_{\mathrm{ML}} = \theta_{\mathrm{act}}$ which reduced the pivoting time. Figure 6.9 shows a flow diagram of the optimized AoAct estimation. The combination of both optimized algorithms reduced the mean simulation time for one full AoAct procedure to 1.7 s (compared to 10.3 s for the first full AoAct algorithm).

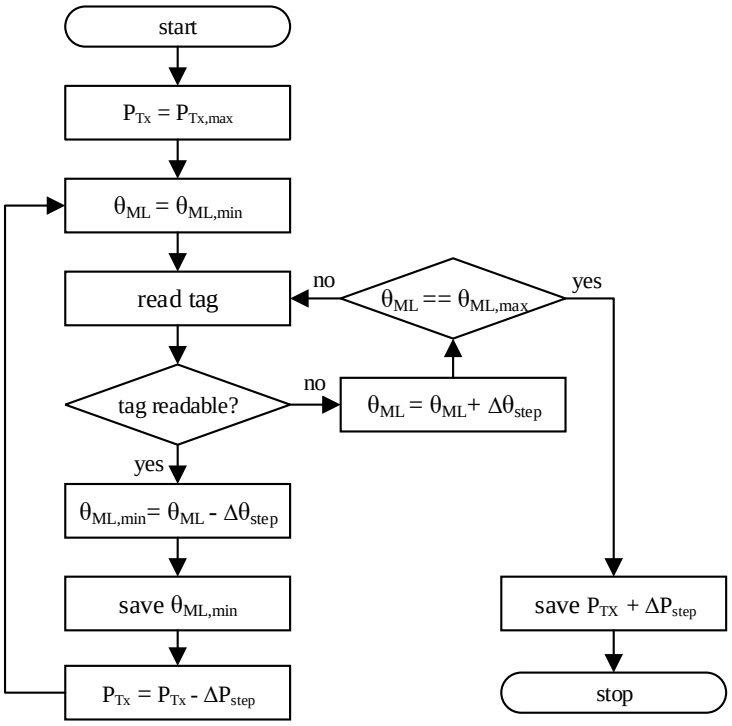

FIGURE 6.8: Flow diagram of the optimized P_{Tx} finding algorithm

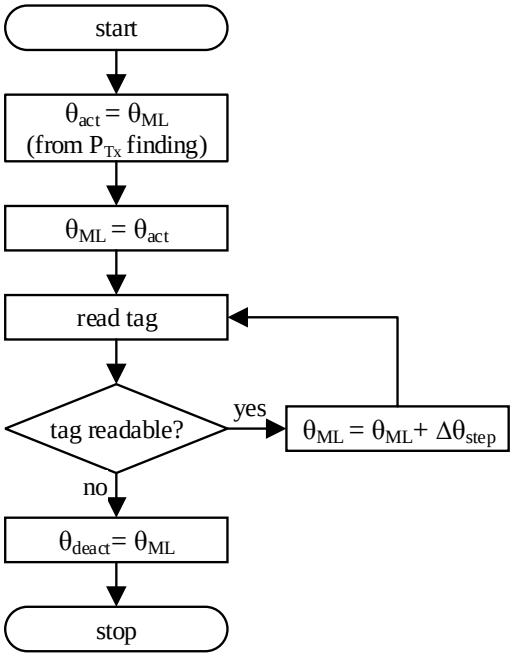

FIGURE 6.9: Flow diagram of the optimized AoAct algorithm

6.3 Experimental Verification of the Localization Performance

The design of experiments for a verification of the AoAct transmitter beamforming localization method was very similar to the receiver beamforming method (section 5.3.1). The objective was to recreate the simulation scenario with four AoAct units and 25 tag locations for real-world AoAct localization measurements.

6.3.1 Experimental Testbed

The experimental testbed consisted of multiple AoAct units which comprise a DSP unit and a three-element antenna array.

6.3.2 DSP Unit

In the DSP unit, the single transmitter signal $x(t)$ was distributed to the $l = 0...L-1$ branches of the transmitter antenna array and then multiplied with the element weights w_l^*. Mathematically, this process can be expressed as follows.

The transmitter signal $x(t)$ is

$$x(t) = \mathrm{Re}\left\{A_x(t)e^{j2\pi f_0 t+\varphi_0} = A_x(t)e^{j\varphi_x(t)}\right\}, \tag{6.8}$$

where $A_x(t)$ is the time-dependent binary signal amplitude that represents the information transmitted by the AoAct unit and f_0 is the carrier frequency. Without loss of generality, the initial phase is assumed as $\varphi_0 = 0$.

After separating $x(t)$ into L branch signals $x_l(t)$ and multiplying with $w_l^* = A_{w_l}e^{-\varphi_{w_l}}$:

$$\begin{aligned} x_l(t) &= x(t) \cdot w_l^* \\ &= \mathrm{Re}\left\{A_x(t)e^{j\varphi_x(t)} \cdot A_{w_l}e^{-\varphi_{w_l}}\right\} \\ &= \mathrm{Re}\left\{A_x(t)A_{w_l}e^{j\varphi_x(t)-\varphi_{w_l}}\right\} \\ &= \mathrm{Re}\left\{A_l(t)e^{j\varphi_l}\right\}. \end{aligned} \tag{6.9}$$

It can be seen that the branch signals $x_l(t)$ are phase-shifted versions of the original transmitter signal $x(t)$ with an amplitude of $A_l(t) = A_x(t)A_{w_l}$ and a phase of $\varphi_l = \varphi_x(t) - \varphi_{w_l}$.

Instead of multiplying the branch transmitter signals with complex weighting factors, digital transmitter beamforming directly generates the L amplitude- and phase-independent branch signals. This is achieved by manipulating the the digital I/Q baseband data signals which are then quadrature modulated onto the high-frequency carrier. Of course, the generation of the branch signals must be based on the same baseband data and on the same reference phase.

In principle, L UHF RFID interrogators could be used to realize a DSP unit that follows the digital transmitter beamforming principle. However, a phase synchronisation would be needed and a mechanism that synchronises the baseband data of all interrogators. In addition, the phases of the interrogator's output signals have to be variable. Since there are no commercial products available that fulfil these demands, the design of a new DSP unit is required.

In this DSP unit, a microcontroller uses a multi-channel digital-to-analogue converter with simultaneous output capability to generate the I and Q components $I_l(t)$ and $Q_l(t)$ for the antenna array branch signals. A newly designed RF front-end comprises a high-frequency modulator that generates a single high-frequency branch signals $x_l(t)$ from the I/Q components. An in-phase local oscillator signal is supplied to all L RF front-ends to supply an equal reference phase for all branch signals. The full EPCglobal protocol stack is implemented on the microcontroller to generate EPCglobal compliant baseband signals that can be modulated and transmitted as well as decoded by the tag.

In order to receive and process the backscattered tag signal, a high-frequency demodulator was embedded into one of the L RF front-ends and connected to a separate receiver antenna. The demodulated I and Q components of the receiver signal are sampled by ADCs and then decoded. The AoAct unit ran a full EPCglobal communication cycle (see section 2.2) to determine the readability of the tag during the AoAct estimation process. The tag was marked as readable if the EPC was successfully decoded by the AoAct unit.

6.3.3 Antenna Configuration and Target Tags

The antenna configuration of the AoAct unit was identical to the configuration of the AoA unit (section 5.3.1), i.e. the circularly polarized three-element patch antenna array was used as the AoAct units' transmitter antenna and the circularly polarized patch antenna (appendix C.3.2) as the receiver antenna.

For the target tag, the commercial UPM Raflatac DogBone and the circularly polarized tag that were introduced for the AoA localization system (section 5.3.1) were used.

A detailed description, a block diagram and pictures of the DSP unit are given in appendix D.1.

6.3.4 AoAct and Localization Measurements

In a first measurement campaign, the beamforming capabilities of the new AoAct unit were investigated. The results showed that the maximum phase resolution was $\Delta\varphi_{\text{step}} = 0.06°$ which corresponded to a maximum angular main lobe direction resolution of $\Delta\theta_{\text{step}} = 0.02°$. The overall beamformer transmitter power level P_{Tx} could be set in a range between -20 dBm and 27 dBm with a maximum resolution of $\Delta P_{\text{step}} = 0.001$ dB. The maximum main lobe directions θ_{ML} were measured as $\pm 52°$.

From the measurements, it was also derived that several hardware-related correction factors had to be considered in the generation of the I/Q baseband signals. The length difference of the cables that connect the DSP unit to the antenna array elements as well as the I/Q imbalance of the modulators had to be compensated. In addition, a variable power amplifier was required in the output of each RF front-end to guarantee a constant output power level of the modulated high-frequency signal. During the AoAct estimation process, this level had to be measured constantly by means of an on-board power detector and the gain of the variable amplifier had to be regulated to compensate output power level variations.

Before conducting AoAct estimation measurements, the quality of the generated beam patterns for the pivoting processes had to be tested. All simulations in the last sections were based on the mathematical beamforming theory (especially equation (6.2)) that assumes ideal point sources as the antenna array elements. However, the physical properties (e.g. dimensions and materials) of the patch antenna array influenced the generated beam pattern.

Figure 6.10 shows a measurement setup in the anechoic chamber that used the AoAct unit to record the generated antenna array beam pattern. As described in the previous section, the amplitudes A_l of the weights for all beam patterns were fixed and set to one. For the measurement, a set of weight phases $\varphi, 0, -\varphi$ for the three antenna array elements was chosen to achieve a fixed beam pattern

and a continuous-wave signal was used as the AoAct unit's transmitter signal. A spectrum analyser that was connected to the receiver horn antenna of the anechoic chamber recorded the received signal power level while automatically turning the antenna array from $\theta = -90°$ to $\theta = 90°$. The normalized RSS measurement was identical to the normalized beam pattern of the array.

The comparison of measured beam patterns with theoretical beam patterns resulting from equation (6.2) for $\varphi = 0°$ and $\varphi = 90°$ (figures 6.11 and 6.12) shows that for $\varphi = 0°$, both patterns have identical main lobe angles but the widths of the main lobes become different with increasing $|\theta|$. Furthermore, the deviation between the theoretical and the measured beam pattern increases with an increasing φ (6.12).

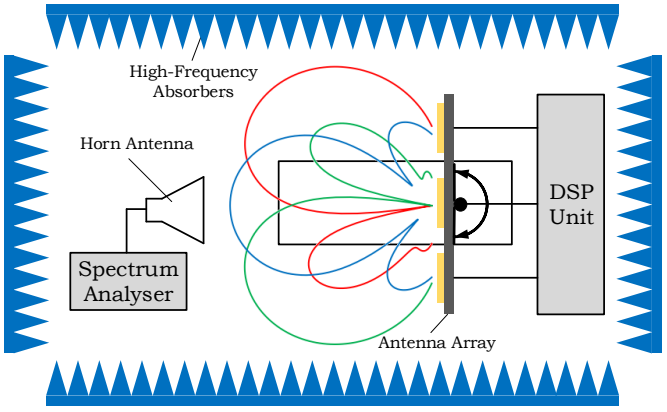

FIGURE 6.10: Setup for beam pattern measurements in the anechoic chamber

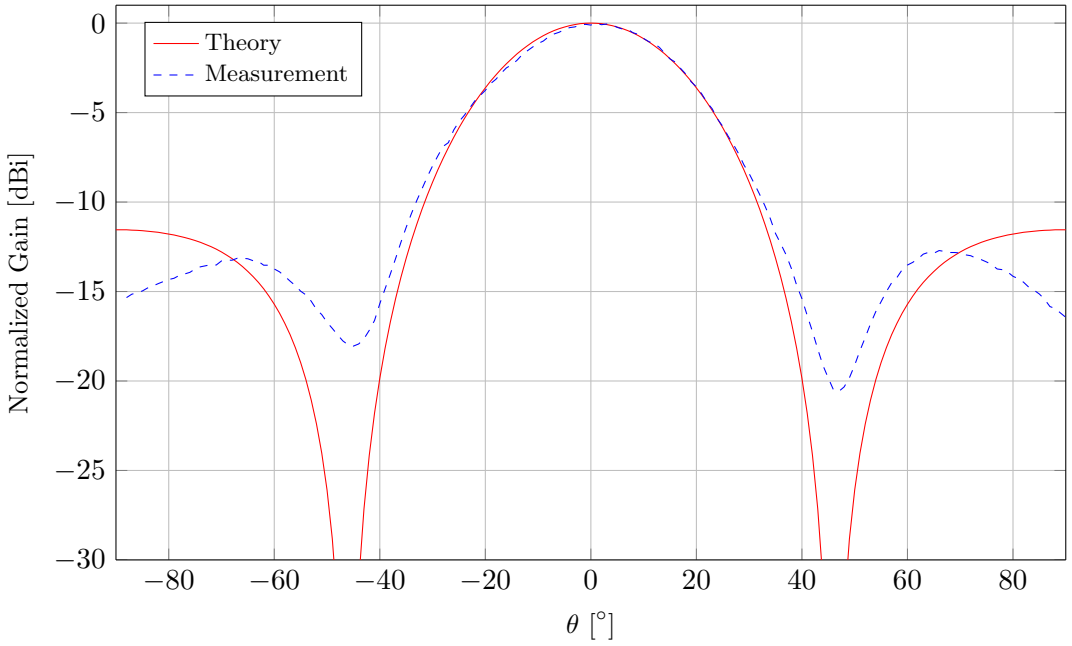

FIGURE 6.11: Comparison of theoretical and measured beam patterns for $\varphi = 0°$

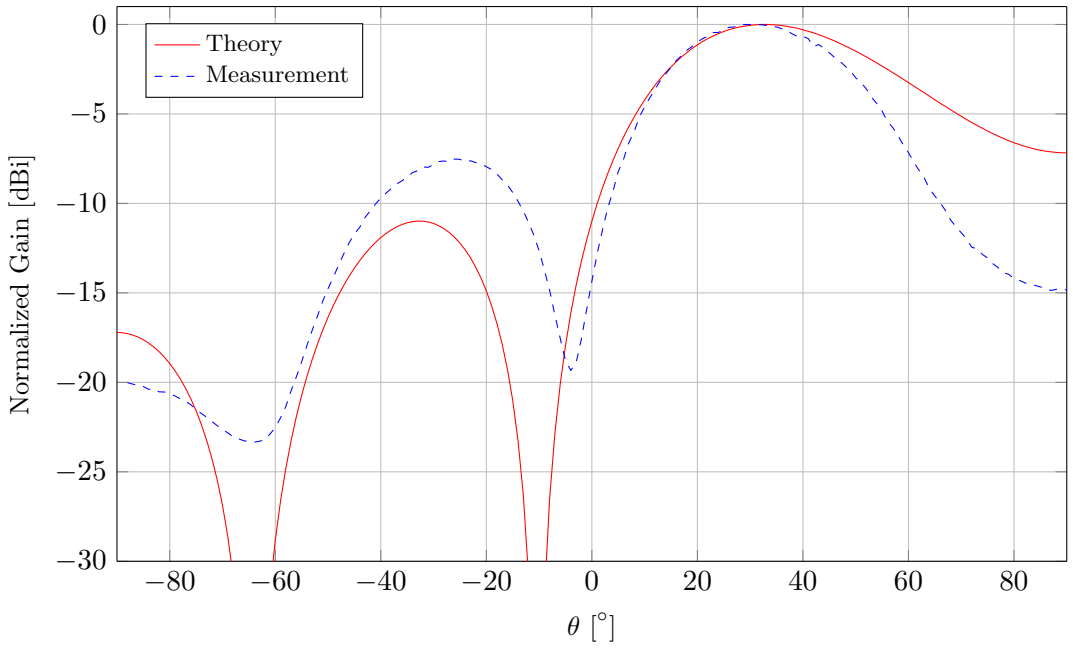

FIGURE 6.12: Comparison of theoretical and measured beam patterns for $\varphi = 90°$

In order to test if the described beam pattern deviations were caused by a malfunction of the DSP unit and not by the physical properties of the antenna array, FEKO simulations of the gain pattern were conducted. As an example, figure 6.13 compares the FEKO simulated beam pattern with the measured beam pattern for $\varphi = 90°$. It can be seen that both patterns match better than in the previous comparison. Additional FEKO simulations for other values of φ verify that. Thus, the deviation between the measured beam pattern and the theoretical beam pattern was caused by the physical properties of the patch antenna array.

For an AoAct estimation with a high accuracy, it is important to derive the main lobe angles and the main lobe widths from the measured beam patterns and to consider them in the AoAct algorithm. Appendix D.2 includes the results of beam pattern measurements for $\varphi = -160°, -150°, ..., 160°$.

The different steps in the optimization of the AoAct and the P_{Tx} finding algorithms that were described in the previous section were reproduced using the hardware AoAct unit and real-world multipath measurements. It was verified that the final algorithm version that resulted from the simulations also delivered the optimum performance in the measurements. There, the first algorithm version needed a mean execution time of 17.4 s and the optimized version only 1.7 s for the estimation of a single AoAct.

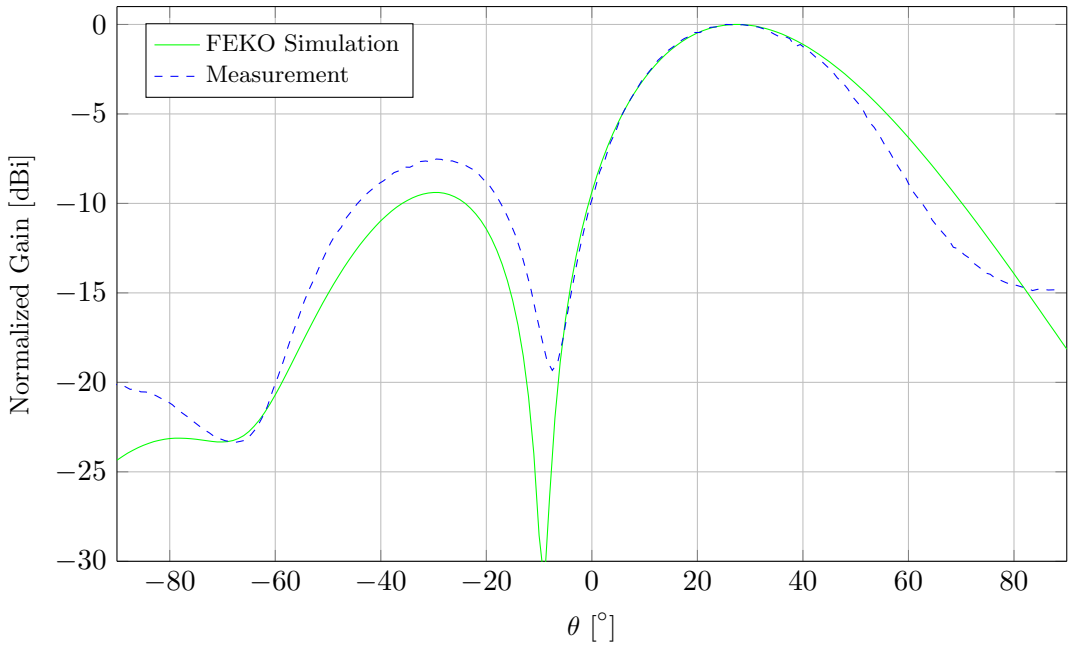

FIGURE 6.13: Comparison of FEKO simulated and measured beam pattern for $\varphi = 90°$

The performance of the new transmitter beamforming AoAct localization method was tested in the same five real-world scenarios that were used for the receiver beamforming approach (section 5.3.2). For clarity reasons, the list of measurement scenarios is repeated:

- Scenario S1: The anechoic chamber (AoAct measurements)
- Scenario S2: An outdoor balcony (AoAct measurements)
- Scenario S3: A standard seminar room (same as for the simulations in this chapter; AoAct and localization measurements)
- Scenario S4: A machine hall (AoAct and localization measurements)
- Scenario S5: A machine hall with an additional scatterer in measurement zone (AoAct and localization measurements)
- Scenario S3circ: The same scenario as S3 but using a circularly polarized patch antenna for the tag (AoAct and localization measurements)
- Scenario S4circ: The same scenario as S4 but using a circularly polarized patch antenna for the tag (AoAct and localization measurements)

In the anechoic chamber (S1), an AoAct measurement was conducted for $N = 47$ tag angles, equally spaced in 2° steps from −46° to 46° (figure 6.14). The mean measured AoAct accuracy over the full angular range was $\overline{\Delta\theta}_{\mathrm{S1}} = 1.22°$ with a mean standard error deviation of $\sigma_{\Delta\theta,\mathrm{S1}} = 0.95°$.

In the outdoor balcony setup (S2), an AoAct estimation was performed for $N = 51$ equally spaced positions along the straight line on which the tag was moved. There, a mean accuracy of $\overline{\Delta\theta}_{S2} = 2.40°$ with a mean standard error deviation of $\sigma_{\Delta\theta,S2} = 1.76°$ was achieved. A high AoAct error was measured in the range between 38° and 45° (6.14). If the measurement range was limited to $-45°...38°$, the mean AoAct estimation error was reduced to $\overline{\Delta\theta}_{S2} = 1.98°$ and the mean error standard deviation to $\sigma_{\Delta\theta,S2} = 1.25°$. The main reason for the high error on one side of the setup was reflections from a metallic object.

Figure 6.15 shows the AoAct error probabilities for scenarios S1 and S2 in comparison to the receiver beamforming AoA measurements in the same scenarios. In both cases, the AoAct method outperforms the AoA method.

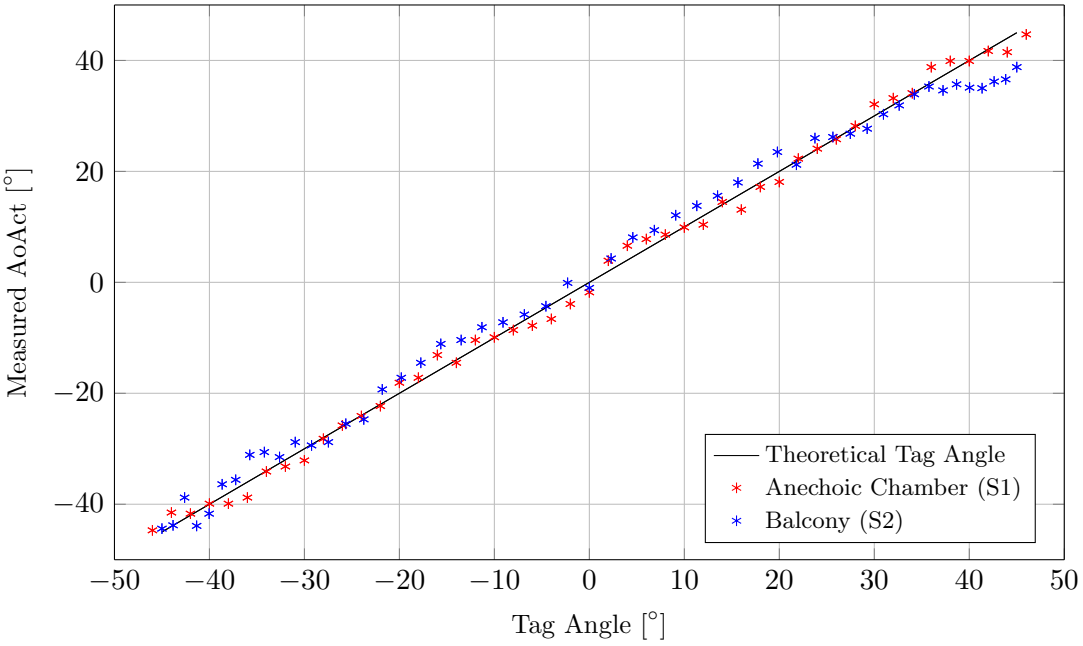

FIGURE 6.14: Results of the AoAct measurements

In scenarios S3, S4 and S5, the AoAct and the location of the target tag were estimated for all 25 tag positions in the measurement grid. For the angulation process, the four AoAct unit positions $A_1...A_4$ and the nearest point algorithm were used.

Table 6.2 compares the mean AoAct accuracies $\overline{\Delta\theta}$, the mean AoAct error standard deviations $\sigma_{\Delta\theta}$, the mean localization accuracies $\overline{\Delta d}$ and the mean localization error standard deviations $\sigma_{\Delta d}$ for all localization measurements using the AoAct method (denoted as 'Tx') and the AoA method (denoted as 'Rx'). In addition, the achieved improvements of the AoAct method compared to the AoA method are listed for each scenario (denoted as 'Imp.').

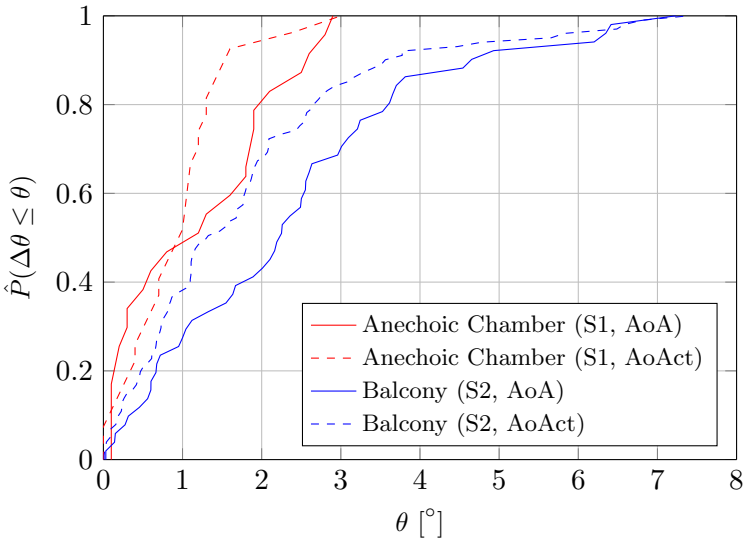

FIGURE 6.15: Error distribution for the AoA and AoAct measurements in scenarios S1 and S2

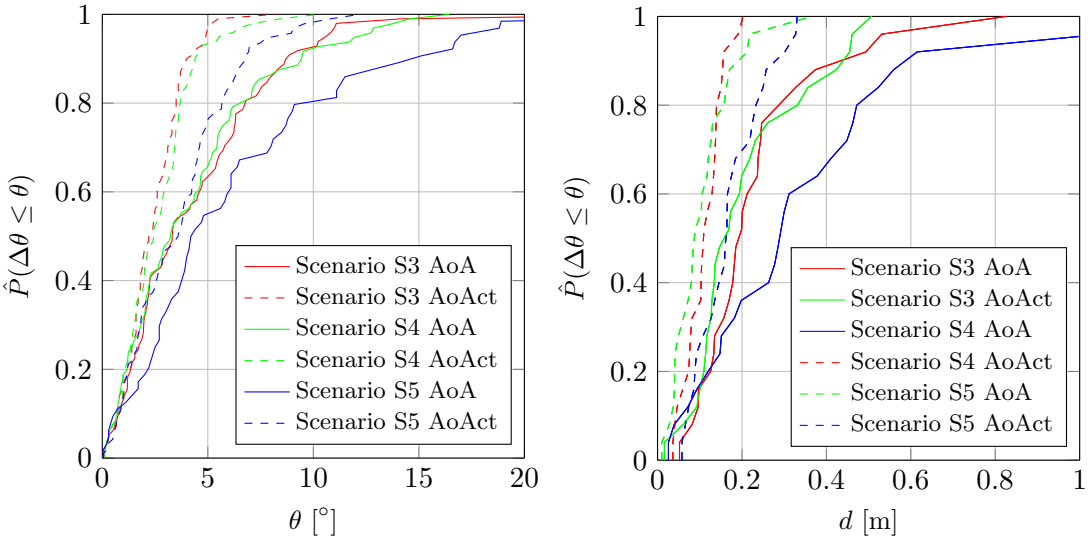

FIGURE 6.16: Error probabilities for the AoA and the AoAct localization in scenarios S3, S4 and S5

TABLE 6.2: Results of all AoA and AoAct measurements

Scenario	$\overline{\Delta\theta}$ [°]			$\sigma_{\Delta\theta}$ [°]			$\overline{\Delta d}$ [cm]			$\sigma_{\Delta d}$ [cm]		
	Rx	Tx	Imp.	Rx	Tx	Imp.	Rx	Tx	Imp.	Rx	Tx	Imp.
S1	1.41	1.22	13%	1.20	0.95	21%	-	-	-	-	-	-
S2	2.61	2.40	8%	1.48	1.76	-19%	-	-	-	-	-	-
S3	4.42	2.42	45%	3.97	1.40	64%	24	11	54%	17	4	76%
S4	4.26	2.65	38%	3.63	1.78	51%	21	11	48%	14	8	43%
S5	6.52	3.66	44%	6.03	2.51	58%	35	18	49%	29	10	66%
S3circ	2.58	2.24	13%	1.82	1.55	15%	11	10	9%	7	4	43%
S4circ	2.64	2.58	2%	1.77	1.36	23%	10	11	-10%	5	5	0%
Mean	**3.49**	**2.45**	**30%**	**2.84**	**1.62**	**43%**	**20**	**12**	**40%**	**14**	**6**	**57%**

In 22 of the overall 24 measurement, the AoAct method outperformed the AoA approach. For the commercial, linearly polarized tag, the improvements of AoAct (localization accuracy as well as standard error deviation) in scenarios S3, S4 and S5 lay in a range between 43% and 76%. The ECDFs for these scenarios clearly confirm this (figure 6.16).

Using the circularly polarized tag, the improvements were much lower which is explainable by the multipath reducing effects of circular polarized antennas. Although the maximum achieved localization accuracy of AoAct was equal to the AoA localization system (10 cm), the standard error deviation and thus, the robustness of the AoAct system showed an improvement of 43% (10 cm vs. 4 cm). Also, the mean accuracy and error values over all measurements (last row in table 6.2) confirmed the improvements of the AoAct system compared to the AoA system.

6.4 Summary

A novel transmitter beamforming method for target tag localization in passive UHF RFID systems has been presented which is based on the pivoting of an antenna array's main lobe.

The RSS-based transmitter beamforming tag angle estimation method has been shown to be highly degraded to multipath. To cope with that, the new AoAct technique has been introduced which utilizes the precisely defined activation threshold of passive UHF RFID tags. The presented AoAct estimation algorithm has been separated into two phases: 1) finding an appropriate beamformer transmitter power level, 2) estimating the target tag AoAct.

It has been shown that the basic approach significantly outperforms the RSS-based transmitter beamforming technique in the presence of multipath. However, also the potential for improved processing times and an improved tag angle estimation accuracy has been demonstrated. By introducing beam pattern weighting factors to account for unbalanced beam patterns, the AoAct estimation accuracy has been increased. By starting the P_{Tx} finding phase with the maximum possible transmitter power, dynamically reducing the main lobe pivoting process and using the information of the P_{Tx} finding phase for the AoAct estimation phase, the overall processing time of the AoAct estimation has been significantly improved.

A new experimental testbed has been designed and built which comprises AoAct units that have been developed based on the principles of digital transmitter beamforming. The very high angular accuracy of this technique has been demonstrated by measurements. A very high main lobe direction resolution of 0.02° and a very high main lobe steering range of ±52° have been achieved using a three-element antenna array.

Localization measurements in different real-world scenarios have shown that the new AoAct technique outperforms the receiver beamforming AoA system in all cases and, especially, in the presence of multipath. The mean localisation accuracy has been improved by 40% and the mean standard localization error by 57% compared to the AoA system.

Chapter 7

Conclusions and Recommendations for Future Work

In this chapter, the achievements and contributions of the research presented in this work are summarized and directions for future work are discussed.

7.1 Conclusions

The demands to realize low-cost indoor localization systems with sufficient accuracy and reliability are not only driven by industrial applications like IoT or Industry 4.0 but also by specialized areas like healthcare that affect everyone's private life. In order to address these demands, wireless technologies are required that are very cost-effective with respect to the used devices but also with respect to installation and maintenance effort. Furthermore, the localization capabilities for various types and high numbers of objects in the same localization area are required. Passive UHF RFID technology seems to be the ideal solution to the above technological requirements. Especially the use of passive UHF RFID tags as the localization target supports this impression because they are very cost-effective, very small, extremely light, need no on-board power supply and be attached to almost any type of object. However, existing passive UHF RFID localization systems clearly reveal two major limitations of this technology: the small signal bandwidth and the small frequency bandwidth. These limitations theoretically contradict the use of passive UHF RFID technology for localization because they

reduce the achievable localization accuracy and robustness in multipath environments to a level which is not sufficient for typical application scenarios. The main goal of this research has been to develop new techniques which improve the performance of passive UHF RFID localization systems in typical multipath application scenarios and to achieve sufficient accuracy and robustness.

For a close estimation of the real-world situation in passive UHF RFID localization systems, a very accurate estimation of the channel behaviour to multipath is required. Existing Friis-based transmission channel models have been compared by simulations and it has been shown that they provide low complexity and thus fast computing times (chapter 3). However, they only give a coarse approximation of the real-world situation due to a limited consideration of the channel parameters and the channel interface parameters. Several enhancements of the modified Friis model have been proposed to achieve an improved estimation quality of the actual signal parameters: an increased number of signal paths (LOS path and first-order reflections), complex reflection coefficients for each individual signal path, three-dimensional antenna gain and antenna phase pattern, the antenna polarization (linear and circular), the polarization mismatch loss, tag and interrogator antenna orientations and the tag's backscatter loss in the uplink. Furthermore, a channel model equation for the received signal phase has been presented. Each single enhancement of the modified Friis model has been verified by simulations and comparison with a real-world measurement in a typical application scenario. It has been shown that each extension of the model improved the estimation quality and that the final channel model equation provides a close approximation of the real-world multipath situation. Despite these improvements, a low computational complexity of the enhanced model has been achieved which has allowed low computing times in all simulations. Based on the enhanced transmission channel model equations, a new simulation environment has been developed. It is easily configurable for any system setup and any localization scenario and thus generally applicable. The simulation environment has been used to predict the tag readability in different multipath environments and a very high prediction reliability of 87% has been demonstrated by comparison with real-world measurements. Furthermore, the widespread assumption that the read range in passive UHF RFID systems is always downlink limited has been proven wrong. It has also been confirmed by simulations that multipath interference highly deteriorates any signal parameter measurement in a localization system.

In order to address the previously mentioned reduction of the achievable localization accuracy caused by multipath, methods had to be found to minimize multipath interference. First, in order to rate the magnitude of multipath interference in a specific scenario, fading quantification has been proposed (chapter 4). It has been used as reliable tool for the analysis of three proposed solutions for a minimization of multipath interference: a) by varying the channel interface parameters, b) by applying diversity techniques, c) by installation of UHF absorbers. Simulations of the respective techniques in a typical application scenario have demonstrated the following results. The orientation of the interrogator antenna influences the fading characteristic of the channel but does not generally reduce the effects of multipath interference. The use of directional patch antennas for the tag and the interrogator reduces the multipath interference but tag patch antennas limit possible applications. However, even a system with a patch antenna for the interrogator and a dipole antenna for the tag achieves a significant multipath interference reduction. Using circularly polarized antennas for the interrogator and the tag highly reduces multipath interference (81%) but requires a patch antenna for the tag. However, the combination of a linearly polarized tag with a circularly polarized interrogator antenna still reduces multipath interference by 35%. The application of frequency diversity is also effective but requires an available frequency bandwidth BW of $BW \geq 0.6 \cdot B_c$ (B_c is the coherence bandwidth of the considered scenario). Due to current frequency regulations, a worldwide operable frequency diversity system can only be realized with the future introduction of the new European frequency range. Spatial diversity requires a displacement of multiple interrogator antennas by at least a wavelength-distance to be effective. The installation of UHF absorbers reduces multipath interference by up to 38% but is only applicable to scenarios with small localization areas.

A digital receiver beamforming localization approach (AoA) has been presented which is based on the Root MUSIC algorithm (chapter 5). Simulations of the basic AoA approach using the new simulation environment and a typical application scenario with 25 target tag positions have confirmed that multipath highly reduces the achievable localization accuracy in typical application scenarios. The three techniques for a minimization of multipath interference have been successfully applied and simulations have demonstrated a significant improvement of the mean localization accuracy between 18% and 69%. As a result, an optimum receiver beamforming localization system has been proposed which utilizes spatial diversity, orientation diversity, patch antennas and circular polarization. Simulations have demonstrated a very high mean localization accuracy of 2 cm for the optimum

approach (improvement of 90% compared to the basic approach). For the implementation of spatial diversity with multiple interrogator antenna locations, a new multiangulation algorithm has been proposed. It is applicable to any number of available AoAs and even works in difficult situations (e.g. two parallel directional lines). A novel experimental testbed has been introduced that comprises multiple AoA units which have been developed on the basis of the optimum localization system. The new DSP unit uses the cross-correlation of receiver signals for phase difference measurements which reduces noise and allows a signal sampling in the baseband. It has been designed from cost-effective off-the shelf components and uses a bistatic transceiver configuration to minimize mutual coupling. A newly designed, circularly polarized three-element patch antenna array has allowed the averaging of two phase-difference measurements. It fulfils all demands for a practical application with respect to size, gain, axial ratio, input impedance and ease of construction. Real-world localization measurements have been conducted in typical application scenarios with a different magnitude of multipath interference. In a scenario with significant multipath interference, a mean localization accuracy of 21 cm and a mean standard error deviation of 14 cm have been achieved. A further improvement of these values to 10 cm and 5 cm, respectively, has been demonstrated with the use of circularly polarized tag antennas. Higher localization accuracies in comparable multipath environments have never been reported for passive UHF RFID localization systems. The overall system processing time for one target tag location has been measured as 400 ms which corresponds to an update rate of 2.5 Hz.

The performance of digital transmitter beamforming techniques for target tag localization in passive UHF RFID systems have been investigated (chapter 6). It has been shown that an RSS-based localization approach is highly deteriorated by multipath and did not perform better than the receiver beamforming AoA method. Therefore, the new AoAct angulation technique has been proposed which is based only on the target tag readability and utilizes the precisely defined response threshold of passive UHF RFID tags. The new localization process has been split into two phases: 1) finding of an appropriate transmitter power level, 2) estimation of the target tag direction. The proposed power finding algorithm has been the result of different optimization steps and was shown to efficiently determine the minimum power level that activates the target tag. It guarantees that the tag is activated only by the line-of-sight interrogator downlink signal and not by reflections. The tag direction estimation phase has been enhanced with

respect to angular accuracy by introducing weighting factors for the beam pattern. Its processing time has been improved by using angle information from the power level finding phase. The processing time of both phases has been further improved by dynamically reducing the angular range of the main lobe pivoting process. It has been demonstrated that the final formulations of the power level finding and AoAct estimation algorithms improve the overall processing time by 83% compared to the basic AoAct approach. A novel experimental testbed has been developed which consists of multiple AoAct units. The newly designed DSP unit manipulates the baseband interrogator transmitter signals to achieve beamforming capabilies which allows a cost-effective design with low complexity. The advantages of the digital transmitter beamforming technique compared to the analogue technique have been demonstrated. The signal phase generation resolution of the new AoAct unit has been measured as 0.06° which corresponds to a very high main lobe direction resolution of 0.02°. In addition, a very wide angular main lobe range of ±52° has been measured. A passive UHF RFID transmitter beamforming system with such high resolution has never been realized before. The repetition of the same localization measurements that were used for the receiver beamforming system has shown that AoAct performs better than AoA in all considered multipath scenarios. With respect to the localization accuracy, a mean improvement of the AoAct method compared to AoA of 40% has been achieved. Although the maximum achieved localization accuracy of 10 cm has been identical to the receiver beamforming system, the mean localization error deviation has been improved to 4 cm.

Referring to the initial research question, it can be concluded that the application of digital receiver beamforming or digital transmitter beamforming in combination with multipath reducing techniques has enabled the realization of passive UHF RFID localization systems with sufficient accuracy for typical application scenarios. The choice of the respective beamforming technique depends on the application requirements. The AoA receiver beamforming system delivers higher update rates while the transmitter beamforming system achieves higher localization accuracy.

7.2 Recommendations for Future Research

A number of directions are recommended to further enhance the performance of localization systems and to enable new application areas:

1. **Dynamic Environments and Additional Signal Distribution Effects**
   Several simplifications have been made in this work for the development of the enhanced transmission channel model and the investigations of the new localization approaches. Additional signal distribution effects like diffraction or scattering at objects in the environment can be considered in the enhanced model to enable the simulation of more complex scenarios (e.g. an office room with furniture). An extension of the simulation environment with additional moving objects in the area of interest would allow the simulation of dynamic environments. These extensions of the simulation environment can be used to investigate the tag readability as well as the performance of localization approaches in complex dynamic environments.

2. **Enhanced Transmission Channel Model for RSS-Based Lateration**
   Several existing RSS-based passive UHF RFID localization systems estimate the target distance by using the classical Friis Transmission Equation and are thus highly prone to multipath. Since the enhanced channel model considers multipath reflections, it may be used for an improved target distance estimation.

3. **Digital Receiver Beamforming Localization System**
   Due to practical limitations, the evaluation of three target tag receiver signals for localization was used in this work. According to the receiver beamforming theory, a higher number of available receiver signals for the AoA estimation leads to a higher angular accuracy and thus to a higher localization accuracy. There may be specific application scenarios where a very high localization accuracy is essential and the size, complexity and cost of the AoA unit are only of secondary importance.

4. **Digital Transmitter Beamforming Localization System**
   An extension of transmitter beamforming localization system with more than three antenna array elements would result in a narrower main lobe beamwidth. This effect could be used to achieve an improved AoAct estimation accuracy and a wider angular localization range. As described for the receiver beamforming localization system, there might be specific application

areas where the increased size, complexity and cost are not as important as the localization accuracy.

In order to enhance the AoAct estimation accuracy using the three-element antenna array, the AoAct process could be changed in a way that not the main lobe but the very sharp nulls of the beam pattern spatially shifted. In this case, the target tag would stay deactivated if a null is steered towards its direction, independent of the AoAct unit's transmitter power level. Thus, the transmitter power finding phase would not be required and the processing time could be increased. In addition, the narrower angular width of the nulls compared to the main lobe should increase the AoAct estimation accuracy.

In the AoAct estimation process, a high number of tag readability tests are conducted which involve the execution of a full EPCglobal communication cycle. In the transmitter beamforming localization system, the received target tag signals are only decoded to evaluate the tag readability. However, if an additional antenna array is used as the AoAct units receiver antenna, the received target tag signals could also be evaluated using the Root MUSIC algorithm. This would allow averaging of one AoAct and multiple AoA measurements. This possibility of future extension was already taken into account in the design of the AoAct unit but experiments have not been conducted, yet.

5. **Frequency Diversity**
   With the future approval of the new European UHF RFID frequency range, the possibilities of frequency diversity for an enhanced localization accuracy should be investigated.

6. **Three-Dimensional Localization, Positioning and Tracking**
   The presented localization approaches in this work were limited to a two-dimensional target tag position estimation but many applications demand a three-dimensional localization. It was explained in this work that, theoretically, the sequential localization for the azimuth plane and for the elevation plane using perpendicularly arranged antenna arrays allows a three-dimensional localization. This should be verified in practical experiments.

   An extension of localization systems which is also highly demanded by industry is positioning. There, the goal is to move an object from an initial position to a desired position. This can be achieved by a periodic localization of the object (tracking) while moving the object stepwise towards the desired

position and adjusting its course. For this purpose, sophisticated tracking algorithms are required that are able to handle inaccuracies in the localization process by using filter algorithms and auxiliary information.

Appendix A

Receiver and Transmitter Beamforming

A.1 Receiver Beamforming

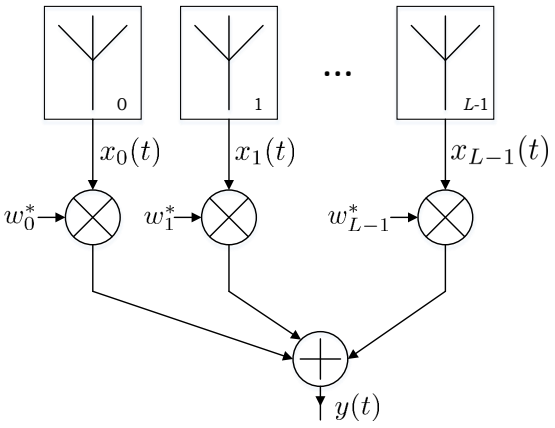

FIGURE A.1: Receiver beamforming principle

Figure A.1 shows the principle drawing of a receiver beamforming system. The received signals $x_0(t), x_1(t), ..., x_{L-1}(t)$ of an L-element ULA are multiplied with complex weighting factors $w_0, w_1, ..., w_{L-1}$ and added together to achieve the signal $y(t)$:

$$y(t) = \sum_{l=0}^{L-1} w_l^* x_l(t) = \mathbf{w}^H \mathbf{x}(t), \tag{A.1}$$

where * denotes the complex conjugate, $\mathbf{w}^H$ is the complex, Hermitian (i.e. conjugate transpose of $\mathbf{w}$) $1 \times L$ vector containing the weights w_l^* for $l = 0...L-1$ and $\mathbf{x}(t)$ is the $L \times 1$ vector containing the antenna array's receive signals $x_l(t)$ for

$l = 0...L-1$. The resulting beam pattern $W(\theta)$ of a ULA can be expressed as [44]

$$W(\theta) = \frac{1}{L}\sum_{l=0}^{L-1} w_l^* e^{-jl\phi} = \mathbf{w}^H \mathbf{a}(\theta), \text{ with } \phi = \frac{2\pi s}{\lambda}\sin\theta, \tag{A.2}$$

where $\mathbf{a}(\theta)$ is the steering vector defined as

$$\mathbf{a}(\theta) = \begin{bmatrix} 1 & e^{-j\phi} & e^{-j2\phi} & ... & e^{-j(L-1)\phi} \end{bmatrix}^T. \tag{A.3}$$

θ is the azimuth angle of the antenna array with respect to the normal of the straight line in which the elements are arranged, s is the inter-element spacing and λ is the signal wavelength.

The average power $P(\mathbf{w})$ of the beamformer output signal $y(t)$ over N time samples of $y(t)$ as a function of the weighting coefficients w_l^* is given by [214]

$$P(\mathbf{w}) = \frac{1}{N}\sum_{t=1}^{N} |y(t)|^2 = \frac{1}{N}\sum_{t=1}^{N} \mathbf{w}^H \mathbf{x}(t)\mathbf{x}^H(t)\mathbf{w} = \mathbf{w}^H \hat{\mathbf{R}} \mathbf{w}, \tag{A.4}$$

where $\hat{\mathbf{R}}$ is an estimate of the covariance matrix of the receive signal vector $\mathbf{x}(t)$ using N time samples of $\mathbf{x}(t)$:

$$\hat{\mathbf{R}} = \frac{1}{N}\sum_{t=1}^{N} \mathbf{x}(t)\mathbf{x}^H(t) \tag{A.5}$$

All receiver beamforming techniques are based on the assumption that the maximum output power $P(\mathbf{w})$ corresponds to the incident angle θ_0 of the desired receiver signal. Equation (A.2) relates the weights $\mathbf{w}$ to the beam pattern $W(\theta)$ of the antenna array. The difference between the existing beamforming methods is the choice of the weighting vector $\mathbf{w}$.

Under the assumption that the noise present in all element receiver signals has a common variance and is uncorrelated among all elements ('spatially white noise'), the conventional beamformer [215] (also referred to as delay-and-sum method or Barlett method) formulates the problem of maximising the beamformer output power:

$$\max_{\mathbf{w}} E\left\{\mathbf{w}^H \mathbf{x}(t)\mathbf{x}^H(t)\mathbf{w}\right\} = \max_{\mathbf{w}} \mathbf{w}^H E\left\{\mathbf{x}(t)\mathbf{x}^H(t)\right\}\mathbf{w} \tag{A.6}$$

Under the constraint that $|\mathbf{w}| = 1$, the weight vector has the optimum solution

$$\mathbf{w}_{\text{conv}} = \frac{\mathbf{a}(\theta)}{|\mathbf{a}(\theta)|} = \frac{\mathbf{a}(\theta)}{\sqrt{\mathbf{a}^H(\theta)\mathbf{a}(\theta)}}, \tag{A.7}$$

which leads to a beamformer output power

$$P_{\text{conv}}(\theta) = \frac{\mathbf{a}(\theta)^H \hat{\mathbf{R}} \mathbf{a}(\theta)}{\mathbf{a}^H(\theta)\mathbf{a}(\theta)} \tag{A.8}$$

$P_{\text{conv}}(\theta)$ is also denoted as the 'spatial spectrum'. All information of the effective incident signal(s) is contained in the correlation matrix $\hat{\mathbf{R}}$. Computing $P_{\text{conv}}(\theta)$ as a function of all possible steering vectors $\mathbf{a}(\theta)$ will result in a maximum value if the steering vector coincides with the incidence angle of an incoming signal. Thus, the peaks of this function will show the direction of incident signal(s). Unfortunately, the angular resolution of a uniform linear array is limited to $\phi_B = \frac{2\pi}{L}$ [214] (e.g. $\phi_B = 180°$ for a two-element array or $\phi_B = 120°$ for a three-element array). This resolution is the minimum angular distance which can be resolved by the beamformer, i.e. two signals that are incident from a segment smaller than ϕ_B cannot be distinguished.

The MVDR method [216] (also known as Capon beamformer) defines the linear power constraint

$$\sum_{l=0}^{L-1} w_l^* e^{-jl\theta_0} = 1 \tag{A.9}$$

which sets the power incident from the direction of the desired signal θ_0 to one. Optimizing the power output of the beamformer to achieve a maximum value under this constraint is equivalent to minimising the total received power of all directions but the desired one. Thus, the average interference is minimized. The solution to this optimisation problem is given by [44]

$$\mathbf{w}_{\text{MVDR}} = \frac{\hat{\mathbf{R}}^{-1}\mathbf{a}(\theta)}{\mathbf{a}^H(\theta)\hat{\mathbf{R}}^{-1}\mathbf{a}(\theta)}. \tag{A.10}$$

The spatial spectrum of the MVDR beamformer is then

$$P_{\text{MVDR}}(\theta) = \frac{1}{\mathbf{a}(\theta)\hat{\mathbf{R}}^{-1}\mathbf{a}^H(\theta)}. \tag{A.11}$$

The angle θ that corresponds to the maximum value of $P_{\text{MVDR}}(\theta)$ gives an estimate for the desired signal incidence angle. However, the resolution capability is still dependent on the array aperture (given by L) and the SNR [214]. Another disadvantage is that the computation of an inverse matrix is needed which may become ill-conditioned if the incident signals are highly correlated [44].

The two subspace-based methods (also known as super-resolution methods) Multiple Signal Classification Algorithm (MUSIC) and Estimation of Signal Parameter via Rotational Invariance Techniques (ESPRIT) were introduced to achieve a higher spatial resolution than the classical beamforming approaches. MUSIC [261] uses the observation that the steering vectors $\mathbf{a}(\theta)$ of incident signals lie in the signal subspace which is orthogonal to the noise subspace. The basic approach is to find the steering vectors that are orthogonal to the noise subspace while searching through all possible steering vectors. Assuming that the signals $s_m(t)$ from $m = 0...M-1$ sources impinge on an L-element antenna array ($M < L$ must hold to be able to distinguish the signals [214]) from the directions θ_m and further assuming that only additive white Gaussian noise (AWGN) distorts the receiver signal (reflections can be included into the M source signals), the receiver signal of the array is

$$\mathbf{x}(t) = \sum_{m=0}^{M-1} \mathbf{a}(\theta_m) s_m(t) + \mathbf{n}(t), \tag{A.12}$$

where $\mathbf{x}(t)$ is the L component receiver signal vector at time t and $\mathbf{a}(\theta_m)$ is the steering vector (see equation (A.3)). In matrix notation, equation (A.12) becomes

$$\mathbf{x}(t) = \mathbf{A}(\theta)\mathbf{s}(t) + \mathbf{n}(t), \tag{A.13}$$

where $\mathbf{x}(t)$ is an $L \times 1$ vector, $\mathbf{A}(\theta) = [\mathbf{a}(\theta_0), \mathbf{a}(\theta_1), ..., \mathbf{a}(\theta_{M-1})]$ is an $L \times M$ matrix, $\mathbf{s}(t)$ is an $M \times 1$ vector of one sample of each source and $\mathbf{n}(t)$ is an $L \times 1$ vector. θ denotes the vector that contains the directions of the M signal sources. Assuming no noise, $\mathbf{x}(t)$ must be a point in the signal subspace. Changing θ through its complete range, the steering vector will intersect with the signal subspace for certain values θ_i. These values define the directions from which the source signals impinge on the antenna array. To estimate the AoA of a signal, an estimate $\hat{\mathbf{R}}$ of the covariance matrix has to be constructed. Then, the eigenvectors of $\hat{\mathbf{R}}$ are separated into signal and noise subspace. Assuming uncorrelated noise, the diagonal covariance matrix can be derived as follows [44]:

$$\begin{aligned}
\hat{\mathbf{R}} &= E\{\mathbf{x}(t)\mathbf{x}^H(t)\} \\
&= \mathbf{A}(\theta)E\{\mathbf{s}(t)\mathbf{s}^H(t)\}\mathbf{A}^H(\theta) + E\{\mathbf{n}(t)\mathbf{n}^H(t)\} \\
&= \mathbf{A}(\theta)\mathbf{S}\mathbf{A}(\theta)^H + \sigma^2\mathbf{I} \\
&= \mathbf{U}_s\mathbf{\Lambda}_s\mathbf{U}_s^H + \mathbf{U}_n\mathbf{\Lambda}_n\mathbf{U}_n^H,
\end{aligned} \tag{A.14}$$

where $\mathbf{U}_s$ and $\mathbf{U}_n$ are the matrices of the signal and noise eigenvectors, respectively. $\mathbf{\Lambda}_s$ and $\mathbf{\Lambda}_n$ are diagonal matrices of the signal and noise eigenvalues

$\mathbf{\Lambda} = \text{diag}\{\lambda_1, \lambda_2, ..., \lambda_L\}$ which are ordered in a way that $\lambda_1 \geq \lambda_2 \geq ... \geq \lambda_L > 0$. The source covariance matrix $\mathbf{S} = E\{\mathbf{s}(t)\mathbf{s}^H(t)\}$ is assumed to be non-singular. σ^2 is the variance of the noise and $\mathbf{I}$ is an $M \times M$ identity matrix. The MUSIC algorithm uses the fact that the noise eigenvectors in $\mathbf{U}_n$ are orthogonal to each steering vector $\mathbf{a}(\theta)$ in the matrix $\mathbf{A}$:

$$\mathbf{U}_n^H \mathbf{a}(\theta) = 0, \text{ with } \theta \in \{\theta_1, ..., \theta_M\} \tag{A.15}$$

The MUSIC spatial spectrum is then defined as

$$P_{\text{MUSIC}}(\theta) = \frac{\mathbf{a}^H(\theta)\mathbf{a}(\theta)}{\mathbf{a}^H(\theta)\mathbf{U}_n\mathbf{U}_n^H\mathbf{a}(\theta)}, \tag{A.16}$$

$P_{\text{MUSIC}}(\theta)$ approaches infinity if the denominator approaches zero which is the case if equation (A.14) is satisfied. Thus, high peaks in $P_{\text{MUSIC}}(\theta)$ result whenever θ points to the direction of an incident signal. Although the MUSIC algorithm delivers a high angular resolution, it has a high computational complexity because it involves a search for peaks over the spatial spectrum $P_{\text{MUSIC}}(\theta)$. In the presence of highly correlated interferers (e.g. reflections of the desired signal), the precondition for the derivation of the signal covariance matrix in equation (A.14) is violated and $\hat{\mathbf{R}}$ may become ill-conditioned. For example, assuming the source signal vector $\mathbf{s}(t) = [s_1(t), as_1(t)]^T$, the source covariance matrix $\mathbf{S}$ in equation (A.14) becomes

$$\mathbf{S} = E\{\mathbf{s}(t)\mathbf{s}^H(t)\} = \begin{bmatrix} \sigma_1^2 & a\sigma_1^2 \\ a\sigma_1^2 & a^2\sigma_1^2 \end{bmatrix}, \tag{A.17}$$

which has a rank of one because the second row corresponds to the first row multiplied by a. Then, the rank of $\mathbf{A}(\theta)\mathbf{S}\mathbf{A}(\theta)^H$ will be less than the number of signal sources M and the signal subspace has a dimension less than M. This leads to less than M peaks in the spatial spectrum P_{MUSIC} which is not true because M incident signals are present. To overcome this problem, spatial smoothing is proposed in the literature [199]. There, the array is divided into smaller subarrays and the covariance matrix for each subarray is averaged. All subarray covariance matrices are then used to form a single, spatially smoothed covariance matrix. Although this technique may improve the performance of MUSIC in the presence of multipath, it is obvious that it has an even higher computational complexity.

Simulations of two different scenarios are conducted to compare the signal incidence angle estimation performance of the hitherto introduced receiver beamforming methods. Figure A.2 shows the spatial spectra for the conventional, the Capon

and the MUSIC beamformer in a scenario where one signal source at $\theta_1 = 10°$ is present. The system frequency is set to $f = 868$ MHz, the SNR to SNR $= 10$ and $t = 1000$ snapshots of the receiver signal are processed. A three-element antenna array with an inter-element spacing of $s = 0.13$ m is assumed. The simulation results show that the MUSIC method delivers the smallest and highest peak in the spatial spectrum. Thus, its angular resolution is highly superior to the other methods. A second scenario uses the same simulation parameters as the first scenario but assumes two signal sources at $\theta_1 = 10°, \theta_2 = 40°$, respectively. The simulated spatial spectra in figure A.3 show that only the MUSIC beamformer is able to distinguish and clearly identify the incidence angles of the two signals.

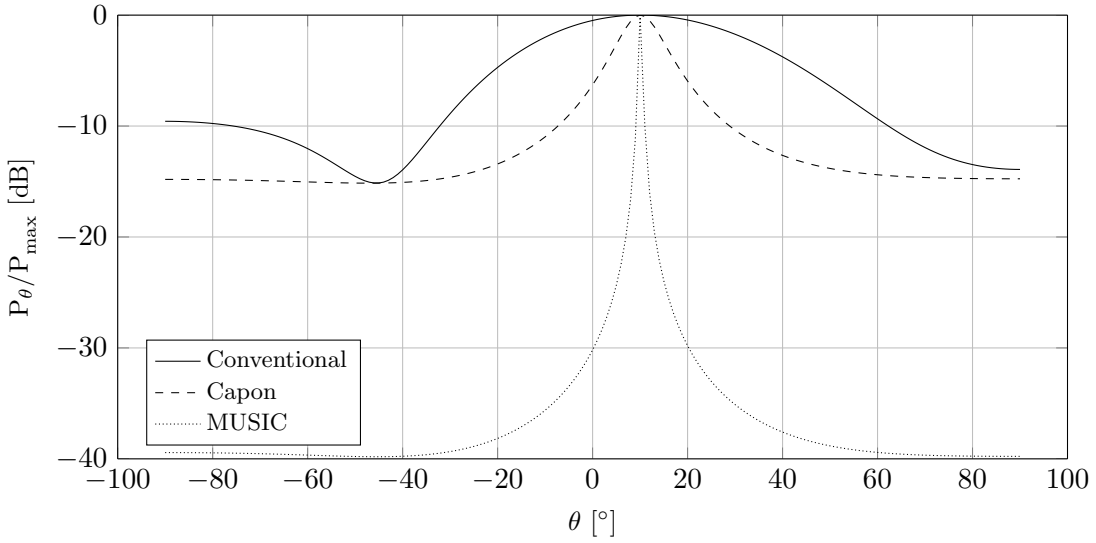

FIGURE A.2: Receiver beamforming simulation for one source ($\theta_1 = 10°$)

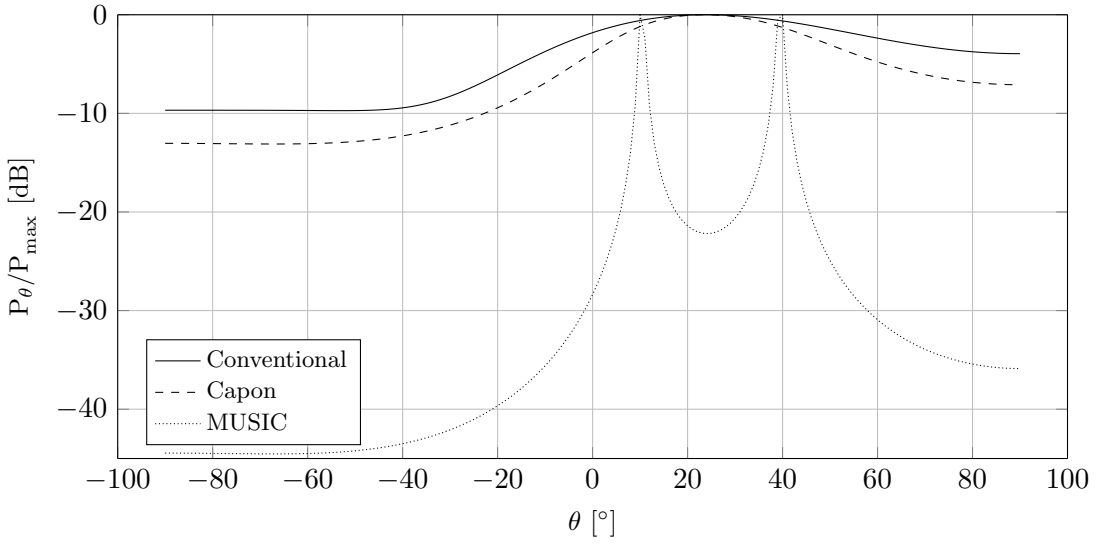

FIGURE A.3: Receiver beamforming simulation for two sources ($\theta_1 = 10°, \theta_2 = 40°$)

The ESPRIT subspace method [218] is very similar to MUSIC because it also involves an eigendecomposition of the covariance matrix $\hat{\mathbf{R}}$. Based on the rotational invariance property of the signal space, it is able to directly calculate the incidence angle of the desired signal. The principle algorithm is as follows [44, 218]:

1. Calculate $\hat{\mathbf{R}}$ from observations of $\mathbf{x}(t)$
2. Estimate the number of signal sources M
3. Select eigenvectors corresponding to the M largest eigenvalues of $\hat{\mathbf{R}}$ to construct a matrix $\mathbf{\Lambda}$
4. Partition $\mathbf{\Lambda}$ into $M \times M$ submatrices: $\begin{bmatrix}\mathbf{\Lambda}_{11}\mathbf{\Lambda}_{12}\\ \mathbf{\Lambda}_{21}\mathbf{\Lambda}_{22}\end{bmatrix}$
5. Find the eigenvalues $\{\lambda_i\}_{i=1}^{M}$ of $-\mathbf{\Lambda}_{12}\mathbf{\Lambda}_{22}^{-1}$
6. Calculate the signal incidence angles as $\theta_i = \arcsin\left(\arctan\frac{\lambda_i}{\pi M}\right)$, with $i = 1, 2, ..., M$

The computational complexity of ESPRIT is lower than in the MUSIC method because it does not need a search for maxima in the pseudo spectrum. However, it still relies on a computation of the signal covariance matrix and its eigenvalues. It is shown that it achieves an almost identical performance as MUSIC for unmodulated sine signals and is less sensitive to noise [219].

Like ESPRIT, the Root MUSIC method [217] is only valid for uniform linear arrays and avoids the search for maxima in the spatial spectrum. It provides a direct calculation of the desired signal incidence angle by finding the roots of a polynomial. Its performance is asymptotically equal to that of the MUSIC algorithm but outperforms it for smaller signal sample numbers [214]. The objective of the original MUSIC algorithm is to find maxima in the pseudo spectrum where the denominator of $P_{\text{MUSIC}}(\theta)$ (see equation (A.16)) approaches zero. The idea of the Root MUSIC method is to construct a polynomial $J(z)$ such that [222]

$$J(z) = \mathbf{p}^H(z)\mathbf{U}_n\mathbf{U}_n^H\mathbf{p}(z) = 0, \tag{A.18}$$

with

$$\mathbf{p}(z) = \begin{bmatrix}1 & z & z^2 & ... & z^{(L-1)}\end{bmatrix}^T, \tag{A.19}$$

where

$$z = e^{-j\frac{2\pi s}{\lambda}\sin(\theta)}. \tag{A.20}$$

Due to the term $\mathbf{p}^H(z)$, there exist powers in z^* which makes it difficult to find a solution. However, since only zeros on the unit circle in the complex plane are of interest, the modified polynomial

$$J(z) = z^{L-1}\mathbf{p}^T(z^{-1})\hat{\mathbf{U}}_n\hat{\mathbf{U}}_n^H\mathbf{p}(z) = 0 \tag{A.21}$$

can be considered instead. In the absence of noise, the roots of $J(z)$ would lie on the unit circle in the complex plane. However, this is not the case in the presence of noise. There, the M closest roots to the unit circle correspond to the $m = 0...(M-1)$ incoming signals. For each of these roots, the signal incidence angles θ_m are found by solving

$$\theta_m = -\arcsin\left(\frac{\lambda \arg\{z_m\}}{2\pi s}\right). \tag{A.22}$$

Because there is no a-priori knowledge of the signal's incidence angles available, the signal correlation matrix has to be estimated only from the antenna array's receiver signals.

A.2 Derivation of the AoA Equation for Root MUSIC

The principles and equations of the Root MUSIC algorithm are introduced in detail in the previous section. As a simplification, $L = 2$ antenna array elements and $M = 1$ signal incident from the angle θ are assumed to derive the Root MUSIC angle-of-arrival equation that is utilized in the receiver beamforming localization approach.

According to equation (A.14), the covariance matrix of the array receiver signals is

$$\begin{aligned}
\hat{\mathbf{R}} &= E\{\mathbf{x}(t)\mathbf{x}^H(t)\} \\
&= \mathbf{A}(\theta)\mathbf{S}\mathbf{A}(\theta)^H + \sigma^2\mathbf{I} \\
&= \sigma_s^2\mathbf{a}(\theta)\,\mathbf{a}(\theta)^H + \sigma_n^2\mathbf{I} \\
&= \sigma_s^2\begin{pmatrix} 1 & e^{j\phi} \\ e^{-j\phi} & 1 \end{pmatrix} + \sigma_n^2\mathbf{I} \\
&= \begin{pmatrix} \sigma_s^2+\sigma_n^2 & \sigma_s^2 e^{j\phi} \\ \sigma_s^2 e^{-j\phi} & \sigma_s^2+\sigma_n^2 \end{pmatrix}
\end{aligned}$$

with $\phi = \frac{2\pi s}{\lambda} \sin\theta$. Now, the eigenvalues of $\hat{\mathbf{R}}$ have to be computed by setting its determinant equal to zero and finding the non-trivial solutions:

$$\begin{aligned}
\begin{vmatrix} \sigma_s^2 + \sigma_n^2 - \lambda & \sigma_s^2 e^{jp} \\ \sigma_s^2 e^{-jp} & \sigma_s^2 + \sigma_n^2 - \lambda \end{vmatrix} &= 0 \\
(\sigma_s^2 + \sigma_n^2 - \lambda)^2 - \sigma_s^4 &= 0 \\
\sigma_s^2 + \sigma_n^2 - \lambda &= \pm\sigma_s^2
\end{aligned}$$

The solutions of this equation i.e. the eigenvalues of $\hat{\mathbf{R}}$ are $\lambda_1 = \sigma_n^2$ and $\lambda_2 = 2\sigma_s^2 + \sigma_n^2$. The smaller eigenvalue λ_1 belongs to the noise subspace. The corresponding eigenvector $\mathbf{u}_1$ is calculated by solving

$$\begin{aligned}
\left(\hat{\mathbf{R}} - \lambda_1 \mathbf{I}\right) \mathbf{u}_1 &= 0 \\
\begin{pmatrix} \sigma_s^2 & \sigma_s^2 e^{j\phi} \\ \sigma_s^2 e^{-j\phi} & \sigma_s^2 \end{pmatrix} \begin{pmatrix} u_{11} \\ u_{12} \end{pmatrix} &= \begin{pmatrix} 0 \\ 0 \end{pmatrix} \\
\Leftrightarrow \mathbf{u}_1 &= \begin{pmatrix} 1 \\ -e^{-j\phi} \end{pmatrix}
\end{aligned} \tag{A.23}$$

Now, the Root MUSIC polynomial (see equation (A.21)) has to be solved:

$$\begin{aligned}
J(z) = z^{L-1} \mathbf{p}^T(z^{-1}) \hat{\mathbf{U}}_n \hat{\mathbf{U}}_n^H \mathbf{p}(z) &= 0 \\
z(1, z^{-1}) \begin{pmatrix} 1 \\ -e^{-j\phi} \end{pmatrix} (1, -e^{j\phi}) \begin{pmatrix} 1 \\ z \end{pmatrix} &= 0 \\
z - e^{-j\phi} - z^2 e^{j\phi} + z &= 0 \\
z^2 - 2e^{-j\phi} z + e^{-2j\phi} &= 0 \\
\Rightarrow z_1, z_2 &= e^{-j\phi}
\end{aligned} \tag{A.24}$$

For the root z_1 of the polynomial, the AoA θ can be found by calculating (see equation (A.22)

$$\theta = -\arcsin\left(\frac{\lambda \arg\{z_1\}}{2\pi s}\right) = -\arcsin\left(-\frac{\lambda\phi}{2\pi s}\right) = \arcsin\left(\frac{\lambda\phi}{2\pi s}\right) \tag{A.25}$$

A.3 Transmitter Beamforming

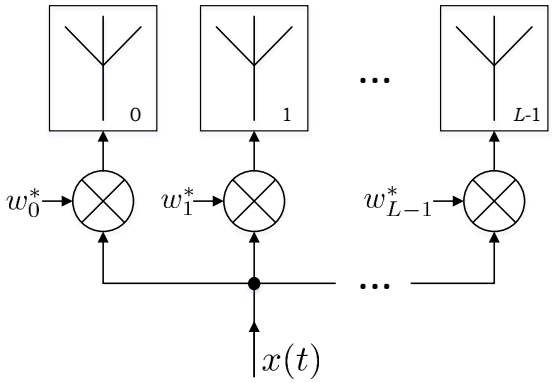

FIGURE A.4: Transmitter beamforming principle

Figure A.4 shows the principle model of a transmitter beamforming system. The transmitter signal $x(t)$ is distributed to the L feeding lines of an L-element antenna array. Each of the branches is multiplied with an individual complex weight factor w_n^* to manipulate the phase and amplitude of the respective signal. At the antenna array output, the L transmitter signals are superposed which generates a specific radiation pattern.

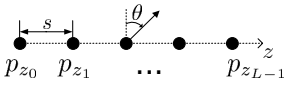

FIGURE A.5: Uniform linear array with L point source elements

Assuming a uniform linear array with L point source elements arranged along the z-axis with a constant element spacing s (see figure A.5), the coordinates of the elements are $p_{x_l} = p_{y_l} = 0$ and

$$p_{z_l} = \left(l - \frac{L-1}{2}\right) s \quad \text{with} \quad l = 0, 1, ..., L-1$$

The geometry of the ULA is included in the array manifold vector $\mathbf{v}_\psi(\psi)$ (similar to the receiver beamforming steering vector $\mathbf{a}(\theta)$) which is defined in the ψ-space [200]:

$$\begin{aligned} \mathbf{v}_\psi(\psi) &= \begin{bmatrix} v_0 & v_1 & \cdots & v_{L-2} & v_{L-1} \end{bmatrix}^T \\ &= \begin{bmatrix} e^{-j\left(\frac{L-1}{2}\right)\psi} & e^{-j\left(\frac{L-3}{2}\right)\psi} & \cdots & e^{j\left(\frac{L-3}{2}\right)\psi} & e^{j\left(\frac{L-1}{2}\right)\psi} \end{bmatrix}^T, \end{aligned} \tag{A.26}$$

where $\psi = -k_z s$. k_z is the wavenumber for the z-dimension for plane waves propagating in a locally homogeneous medium with $k_z = -\frac{2\pi}{\lambda} cos\theta$. λ is the system wavelength and θ is the azimuth angle of the array with respect to the z-axis (see figure A.5). The input signal of the beamforming system $x(t)$ is distributed to L branches and multiplied with the complex weights

$$\mathbf{w}^H = \begin{bmatrix} w_0^* & w_1^* & \cdots & w_{L-1}^* \end{bmatrix}. \tag{A.27}$$

The output signal of the antenna array is a superposition of the weighted element signals. The antenna array beam pattern $B_\psi(\psi)$ (identical to the receiver beamforming beam pattern $W(\theta)$ but defined in ψ-space) for a given weight vector $\mathbf{w}$ and a given array manifold vector $\mathbf{v}_\psi(\psi)$ is calculated as [200]

$$B_\psi(\psi) = \mathbf{w}^H \mathbf{v}_\psi(\psi) = e^{-j\left(\frac{L-1}{2}\right)\psi} \sum_{l=0}^{L-1} w_n^* e^{jl\psi}. \tag{A.28}$$

$B_\psi(\psi)$ is theoretically defined from $-\infty$ to ∞. However, only for a range of $-\frac{2\pi s}{\lambda} \leq \psi \leq \frac{2\pi s}{\lambda}$ it delivers distinct values ('visible region'). With respect to the azimuth angle θ of the ULA, the beam pattern $B_\theta(\theta)$ is defined as

$$B_\theta(\theta) = e^{-j\left(\frac{L-1}{2}\right)\phi} \sum_{l=0}^{L-1} w_l^* e^{jl\phi}. \tag{A.29}$$

To set a specific beam pattern, L values of $B_\theta(\theta)$ are fixed and equation (A.29) is solved for $\mathbf{w}$ to get the corresponding weights. The full derivation of the transmitter beamforming theory can be found in [200].

As an example, figure A.6 shows the simulation results for three different beam pattern $B(\theta)$ of a three-element antenna array with $s = 0.16$ m and $f = 868$ MHz. It can be seen that all pattern have one main lobe, two side lobes and two nulls but at different angles with respect to the antenna array orientation. Table A.1 lists the parameters of the beam pattern. In the simulation, the angular locations of the two nulls and the main lobe are fixed (e.g. $B(-45°) = B(45°) = 0$ and $B(0°) = 1$ for beampattern BP1) and the corresponding weights (w_1, w_2, w_3) are calculated. Then, equation (A.28) is used to plot the resulting beam pattern.

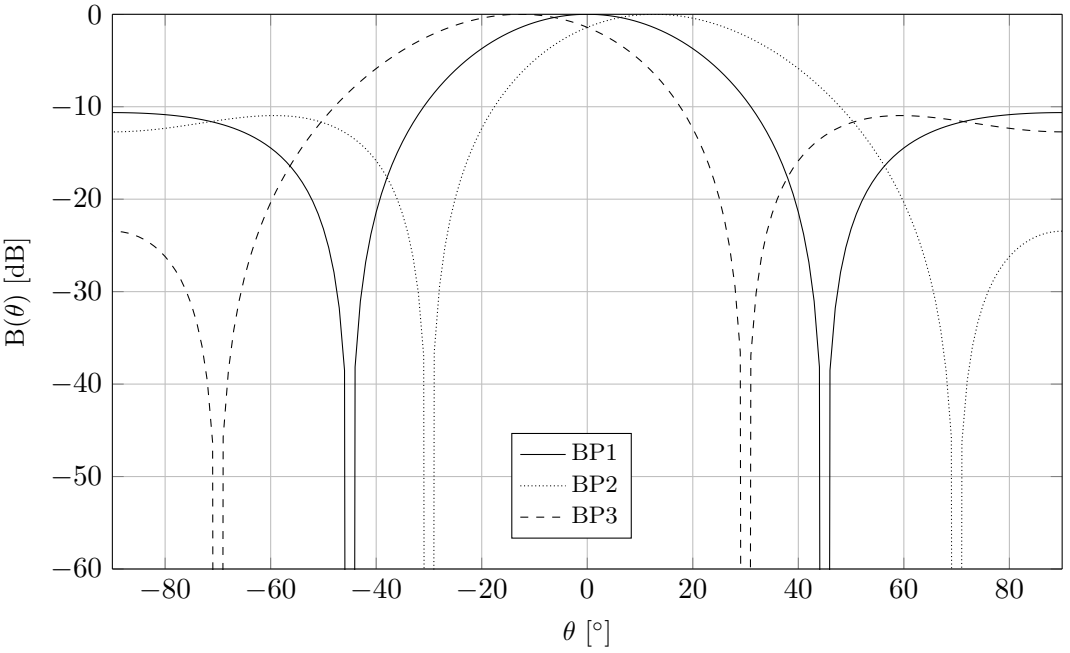

FIGURE A.6: Transmitter beamforming simulation for three different weight vectors

TABLE A.1: Parameters of the simulated beam pattern

Beampattern	**Characteristic Values**			**Weights**		
	First Null	**Second Null**	**Main Lobe**	w_1	w_2	w_3
BP1	$-45°$	$45°$	$0°$	0.34	0.32	0.34
BP2	$-30°$	$70°$	$10°$	$0.34e^{j0.64°}$	0.33	$0.34e^{-j0.64°}$
BP3	$-70°$	$30°$	$-10°$	$0.34e^{-j0.64°}$	0.33	$0.34e^{j0.64°}$

Appendix B

Enhanced Transmission Channel Model

B.1 RSS Measurement Testbench

Two antennas simulate the tag and the interrogator to measure the received signal power in a passive UHF RFID system. It is possible to use any antenna type which is matched to a $50\,\Omega$ load to measure both, the uplink, and the downlink. Figure B.1 depicts a top view drawing of a typical setup for the received signal power measurements. As the picture in figure B.2 shows, the transmitter antenna (Tx) is fixed on a wooden stand and the receiver antenna (Rx) is mounted onto a computer controlled cart. The cart can be moved from a distance $d_{\min}$ to the transmitter antenna to a distance of $d = d_{\min} + 4.7$ m on straight rails. For the minimum distance, $d_{\min} \gg \lambda$ should be chosen to avoid measurements in the near-field region of the transmitter antenna. While moving from the start to the end position, a spectrum analyzer on the cart that is connected to the receiver antenna measures the received signal power $P(d)$. The transmitter signal is a continuous sine wave, generated by a standard signal generator. An additional amplifier can be used to reach the desired transmitter signal power.

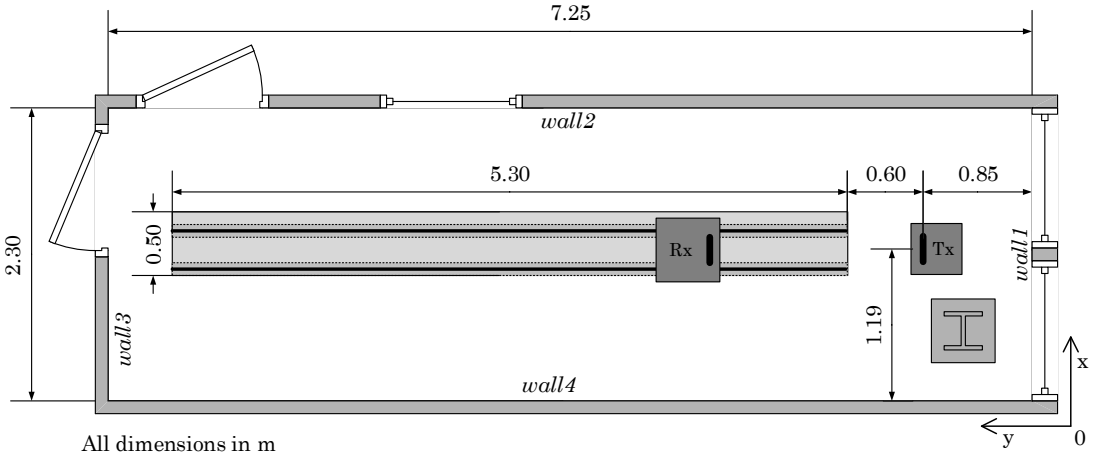

FIGURE B.1: Experimental testbench for the RSS measurements (top view)

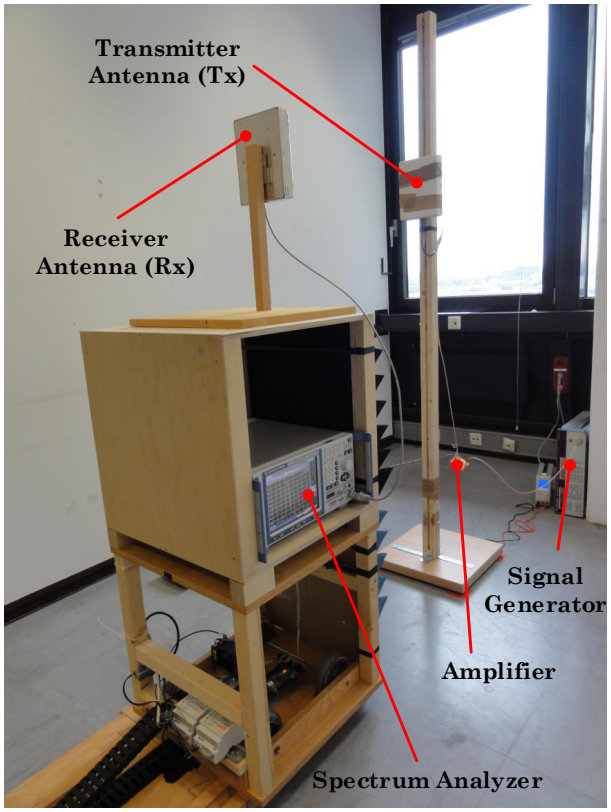

FIGURE B.2: Picture of the testbench for RSS measurements

B.2 Simulation Environment Configuration File

Configuration File for Matlab Channel Simulation

Room	-	
|----------> length	7,25	*m*
|----------> width	2,3	*m*
|----------> height	3,8	*m*
|----------> wall 1	-	
|----------> material	1	
wall 2	-	
|----------> material	3	
wall 3	-	
|----------> material	3	
wall 4	-	
|----------> material	1	
ceiling	-	
|----------> material	3	
floor	-	
|----------> material	3	
Transmitter	-	
|----------> x	1,15	*m*
|----------> y	0,85	*m*
|----------> z	0,8	*m*
|----------> power	23	*dBm*
|----------> antenna	-	
|----------> polarisation	3	
|----------> gain	8	*dBi*
|----------> frequency	867,1	*MHz*
Receiver	-	
|----------> x	1,15	*m*
|----------> y	-	
|----------> start	1,45	*m*
|----------> end	6,94	*m*
|----------> stepsize	0,01	*m*
|----------> z	0,8	*m*
|----------> antenna	-	
|----------> polarisation	1	
|----------> gain	2	*dBi*
Model		
|----------> type	7	

Materials	
Gypsum Board	1
Glass	2
Concrete	3
Gas Concrete	4
Light Concrete	5
Wood	6
Metal	7
Channel Models	
LOS	1
Nikitin	2
2 RAY	3
3 RAY	4
5 RAY	5
6 RAY	6
7 RAY	7
Polarisations	
Vertical	1
Horizontal	2
Circular	3

FIGURE B.3: Simulation environment configuration file

B.3 Typical Material Permittivities

Table B.1 lists the complex permittivities of different materials that can be used in the new simulation environment. Of course, other materials can be added. Values for their complex permittivities are given in the literature (see e.g. [262]).

TABLE B.1: Reflection surface materials in the simulation framework

Material	**Complex Permittivity $\epsilon_2 = \epsilon_2' + j\epsilon_2''$ [F/m]**
Gypsum Board	$6.2 + j0.69$
Glass	3
Concrete	$7.9 + j0.89$
Gas Concrete	$1.9 + j0.7$
Light Concrete	$2 + j0.5$
Wood	3

B.4 Plots Generated by the Simulation Environment

Figure B.4 shows a three-dimensional RSS simulation of the standard application scenario used in this work. In addition to the various RSS plots, also a three-dimensional drawing can be generated by the simulation environment that depicts all $N = 7$ signal paths, the locations of the tag and the interrogator and the coordinates of the reflection points. An example is shown in figure B.5.

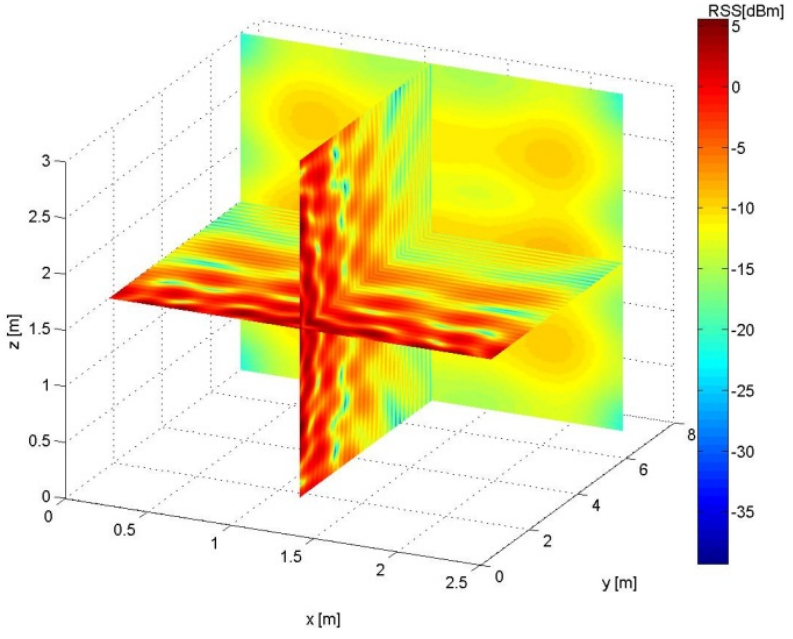

FIGURE B.4: Three-dimensional RSS simulation

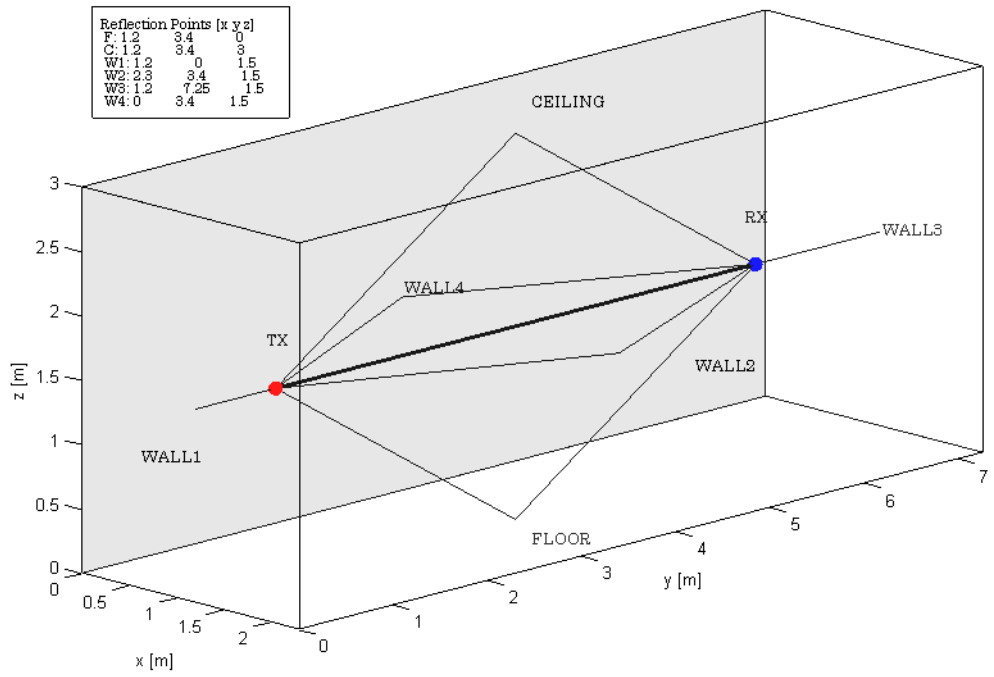

FIGURE B.5: Three-dimensional drawing of the RFID setup and the reflections

B.5 Tag Readability Estimation

In the design of a new RFID system installation, the most important factor is the tag read range which is the maximum distance from which the used interrogator is able to communicate with the tag. Several factors in the system setup influence the theoretical read range, e.g. the position and orientation of the interrogator antenna or the transmitter signal power of the interrogator. Usually, the Friis Transmission Equation is used to calculate the maximum read range of a tag [242, 247, 248]. In this work, it was shown that the interference between multipath signals leads to power fading. A commercially available passive UHF RFID tag has a typical sensitivity of -17 dBm. If the received signal power at the tag location is lower than this sensitivity, the tag cannot be activated and respond to interrogator queries. Thus, multipath leads to the formation of tag read and no-read zones and finally, to a reduced tag reading probability. In preliminary system designs, it is important to identify these locations and to adjust the system parameters in order to maximize the tag read regions.

B.5.1 Tag Readability

To determine if a tag at a certain location is readable, four system parameters have to be known:

1. The received signal power at the tag ($P_{\mathrm{Rx,tag}}$)
2. The sensitivity of the tag ($P_{\mathrm{sens,tag}}$)
3. The received signal power at the interrogator antenna ($P_{\mathrm{Rx,int}}$)
4. The sensitivity of the interrogator's receiver ($P_{\mathrm{sens,int}}$)

In the downlink, a passive UHF RFID tag is only readable if the received signal power at the tag is equal to or greater than the sensitivity of the tag:

$$P_{\mathrm{Rx,tag}} \geq P_{\mathrm{sens,tag}} \tag{B.1}$$

If a tag responds to a query, the interrogator can only decode the tag signal if the backscattered received signal power at the interrogator antenna is equal to or greater than the interrogator sensitivity:

$$P_{\mathrm{Rx,int}} \geq P_{\mathrm{sens,int}} \tag{B.2}$$

According to the literature, passive UHF RFID system are always downlink-limited [247, 263]. That means that a tag is readable from a certain interrogator position if the available interrogator transmitter power at the tag location is greater than the tag's sensitivity. In this case, the received backscattered signal power from the tag always exceeds the interrogator's receiver sensitivity. Under ideal conditions (e.g. no multipath), the available signal power at the tag in the downlink can be calculated from the Friis Transmission Equation. The maximum read range (interrogator-to-tag distance) $d_{\mathrm{max,down}}$ is reached when the received signal power at the tag is equal to the tag sensitivity $P_{\mathrm{sens,tag}}$:

$$d_{\mathrm{max,down}} = \frac{\lambda}{4\pi}\sqrt{\frac{P_{\mathrm{Tx,int}} G_{int} G_{\mathrm{tag}}}{P_{\mathrm{sens,tag}}}}. \tag{B.3}$$

$P_{\mathrm{Tx,int}}$ is the interrogator transmitter power, G_{int} is the maximum gain of the interrogator antenna, and G_{tag} is the maximum gain of the tag antenna.

As an example, the data-sheet of a typical tag IC (NXP G2XM [263]) includes a reference to equation (B.3) to estimate the tag read range. In this equation, the radicant is multiplied by an additional loss factor of $\eta = 0.5$ that accounts for matching and package losses of the tag IC. The combination of interrogator and tag antennas with different polarizations introduces an additional polarization loss of L_{pol} (e.g. $L_{\mathrm{pol}} = 0.5 = -3$ dBm for a combination of linearly and circularly polarized antennas). If the two losses are included in equation (B.3), the maximum tag read range is

$$d_{\mathrm{max,down}} = \frac{\lambda}{4\pi}\sqrt{\frac{P_{\mathrm{Tx,int}} G_{\mathrm{int}} G_{\mathrm{tag}}}{P_{\mathrm{sens,tag}}} \cdot \eta \cdot L_{\mathrm{pol}}}. \tag{B.4}$$

For the standard application scenario in this work, the maximum free-space read range is $d_{\mathrm{max,down}} = 6.9$ m. Through a real-world measurement in the same scenario, the quality of this read range estimation was investigated. After that, the readability was calculated using the enhanced transmission channel model and was compared with the measurement results. In addition to this basic LOS setup (called 'LOS1'scenario), a second scenario ('LOS2') used a larger room for the simulations and measurements. In a third scenario, an NLOS (non line-of-sight) situation was achieved by placing a high-frequency absorber in front of the interrogator antenna.

B.5.2 LOS1 Measurement and Simulation Results

Figure B.6 shows the setup for the tag readability measurement where a standard RFID system was placed into a university office room of size 7.25 m × 2.30 m × 3.00 m. There were no objects other than the RFID system present in the room. The interrogator antenna was placed to the center of the x-dimension of the room ($x = 1.15$ m) with a distance of 0.85 m to the wall at a height of 0.80 m. Seven tags ('a - g' in figure B.6) were arranged vertically on a wooden stand with a distance of 0.30 m to each other on the x-axis of the room at a height of 0.80 m. The distance of the first and the last tag to the walls of the room was 0.25 m. The measurement was started by placing the tags 0.60 m from the interrogator antenna and then moving the tags away in y-direction in 0.30 m steps. At each of the 19 measurement positions in the room ('1 - 19'in figure B.6), 1,000 interrogator-tag communication cycles were started. Tags with an EPC read rate of 90% or more were marked as readable. A total of 133 tag positions (denoted as 1a, ..., 19g) were considered in the measurement. All tag positions in the setup had a line-of-sight connection to the interrogator antenna. Details on the

used RFID system are listed in table B.2. The tag and interrogator sensitivities that were given in the data-sheets were confirmed through measurements. In addition to that, confirming measurements can be found in the literature [259, 260].

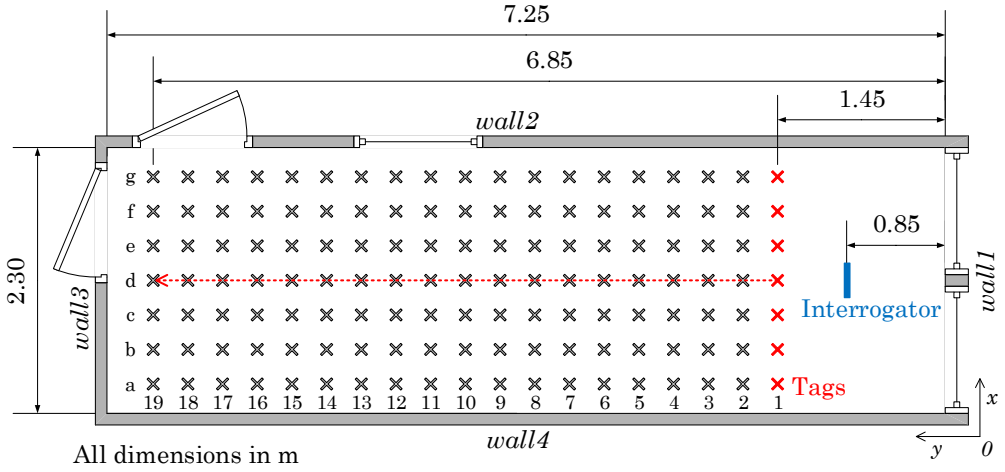

FIGURE B.6: Setup for the tag read range measurements (LOS1 scenario; top view)

TABLE B.2: RFID system setup for readability measurements

	Parameter	Value
Interrogator	Type	PUR-RMCU-500U by RF-Embedded
	Antenna Type	Poynting A-PATCH-0025 (circularly polarized patch)
	Max. Antenna Gain	7 dBi
	Sensitivity	-66 dBm
	Max. Tx Power	27 dBm
	Frequency	867.1 MHz ($\lambda = 0.345$ m)
	Baseband Coding	FM0 (40 kHz)
Tag	Type	UPM Raflatac DogBone
	IC	Impinj Monza 3
	IC Sensitivity	-15 dBm
	Antenna	Folded Dipole
	Max. Antenna Gain	2.1 dBi
	Overall Sensitivity	-17.1 dBm

Using equation (B.4), the read range for the used RFID system was calculated as $d_{\max} = d_{\max,\text{down}} = 6.9$ m. Because the maximum interrogator-to-tag distance in the used setup was 6.10 m, all considered tag positions should have been readable. Figure B.7 shows the results of the readability measurement. In contrast to the free-space estimation (dashed line), read (✓) and no-read (–) zones are existent in the room. Thus, it is not possible to define a maximum read range for this scenario.

For comparison, the received signal power at the tag location (downlink) and the received signal power at the interrogator location (uplink) were simulated to decide if a tag at a certain location in a specified RFID system setup is readable. The interrogator transmits a sinusoidal signal in the downlink to power the tag and to receive data from the tag in uplink. In the tag readability simulations, this additional downlink signal was not used. If a special system setup is considered and a certain tag position is readable in

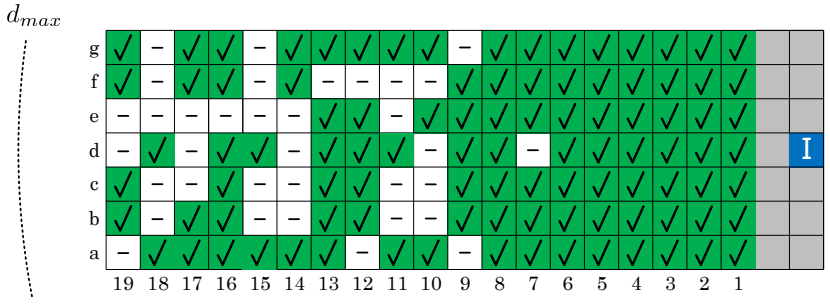

FIGURE B.7: Results of the tag read range measurement (LOS1 scenario)
I = interrogator, ✓ = tag readable, – = tag not readable,
dashed line = free-space read range

the downlink, enough power will reach the tag in the uplink because there are no more modulation losses present[1].

In the simulation environment, individual plots for the read-zones in the downlink (see figure B.8) and in the uplink (see figure B.9) were generated. It can be seen that the estimation of the tag readability cannot be based on the downlink alone. Different no-read zones can be found in both links that have to be combined to make a general prediction of the tag readability (see figure B.10). The matching of the measurement with the combined simulation results is shown in figure B.11. The readability of tags positioned to 116 out of 133 (87%) measurement locations were predicted correctly by the simulation. From the 17 wrongly predicted points, only eight (6%; f_0 points in figure B.11) were marked in the simulation as readable but they were not readable in the measurement.

[1]Considering an interrogator that transmits a QUERY command with amplitude modulation (90% modulation depth) and pulse interval encoding, it can be calculated that the power level of the sinusoidal signal from the interrogator in the uplink is 2.3 dB higher than the power of the modulated signal in the downlink.

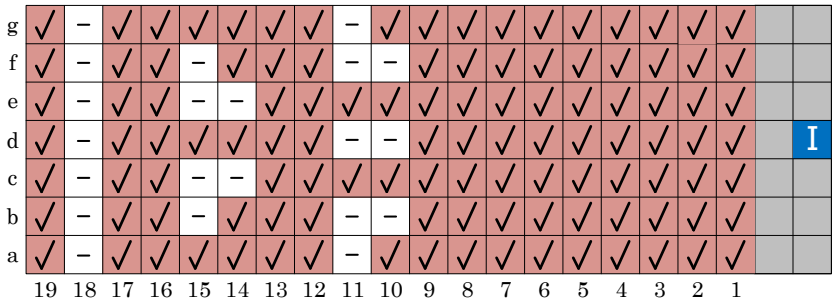

FIGURE B.8: Simulated read (✓) and no-read (–) zones in the downlink (interrogator → tag; LOS1 scenario)

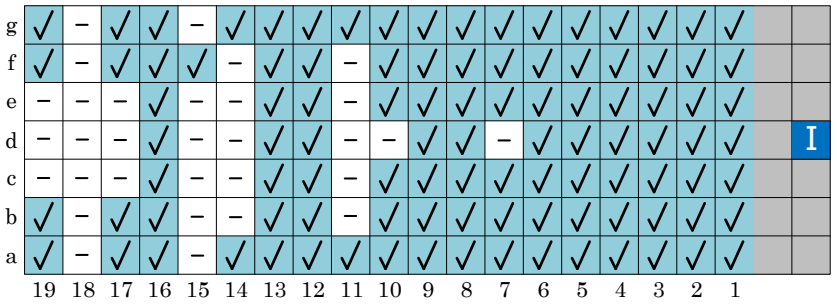

FIGURE B.9: Simulated read (✓) and no-read (–) zones in the uplink (tag → interrogator; LOS1 scenario)

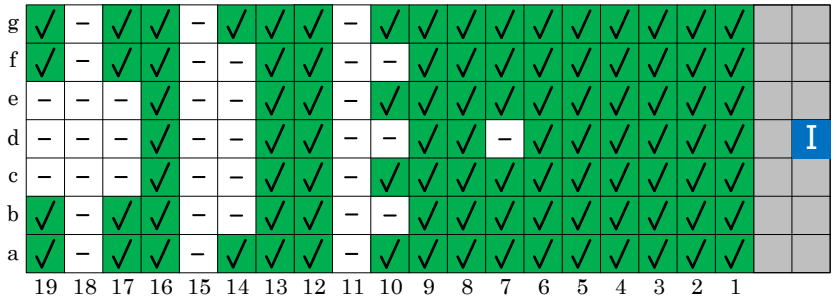

FIGURE B.10: Simulated overall read (✓) and no-read (–) zones (LOS1 scenario)

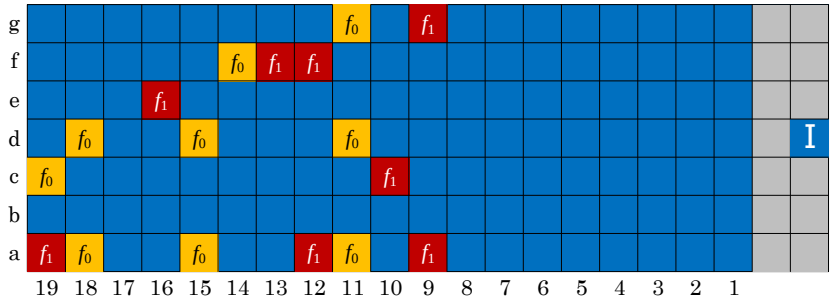

FIGURE B.11: Matching of the simulations and the measurements (LOS1 scenario) blue = match, f_0 = false no-read in simulation, f_1 = false read in simulation

B.5.3 LOS2 Measurement and Simulation Results

The tag readability setup was placed into a standard university seminar room of size 7.25 m × 4.70 m × 3.00 m to conduct a second measurement under line-of-sight conditions (see figure B.12). The interrogator antenna was placed to the center of the x-dimension of the room ($x = 2.35$ m) with a distance of 0.85 m to the wall at a height of 0.80 m. Fourteen tags ('a - n'in figure B.12) were arranged vertically on a wooden stand with a distance of 0.30 m to each other on the x-axis of the room at a height of 0.80 m. The distance of the first and the last tag to the walls of the room was 0.40 m. The measurement procedure was the same as described in the previous section. The measurement results are depicted in figure B.13. A simulation of the tag readability was conducted for the uplink and the downlink and combined to estimate the overall readability (see figure B.14). The matching of the simulation and the measurement results is shown in figure B.15. For 86% (228 locations) of the 266 measurement points, the readability was estimated correctly.

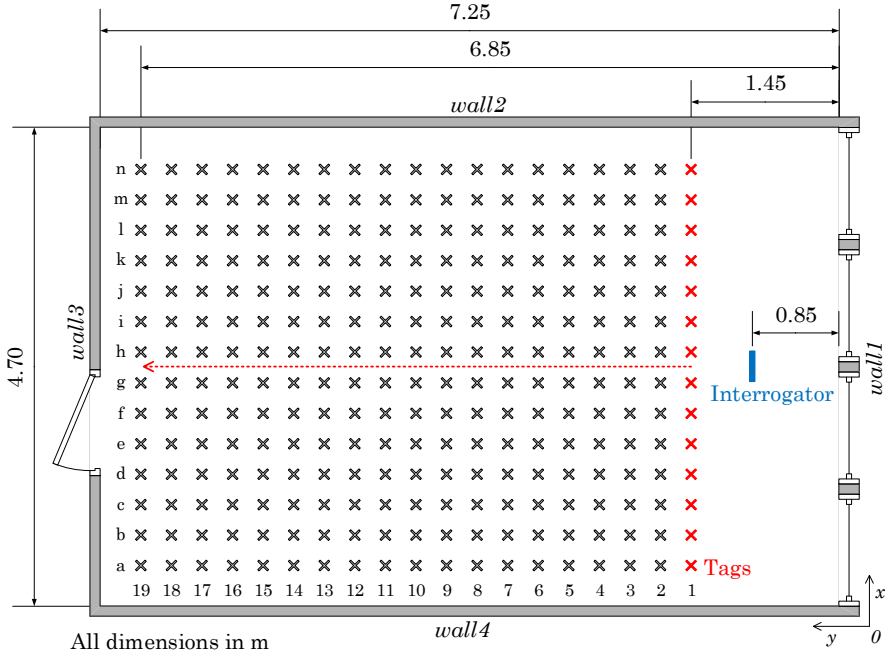

FIGURE B.12: Setup for the additional tag read range measurements (top view; LOS2 scenario)

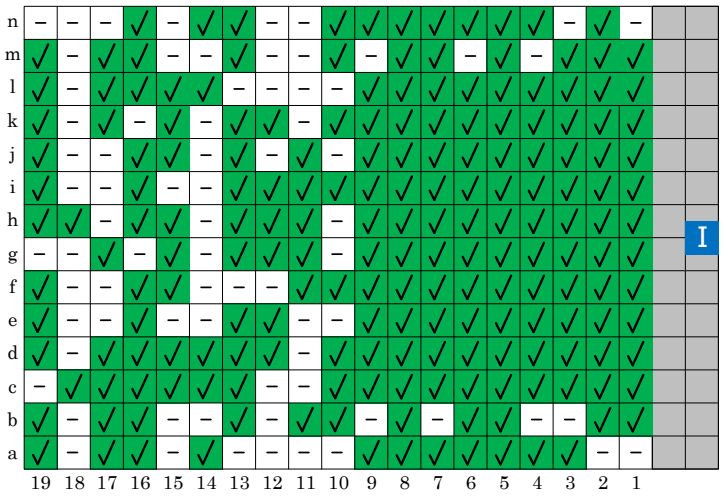

FIGURE B.13: Measurement of the read (✓) and no-read (–) zones (LOS2 scenario)

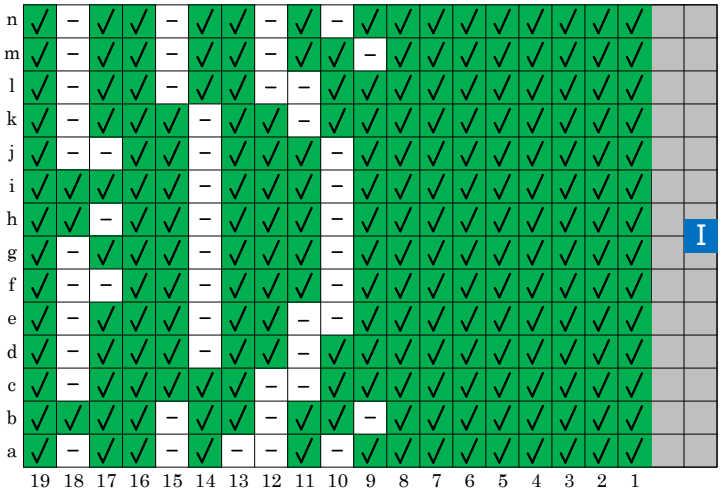

FIGURE B.14: Simulated overall read (✓) and no-read (–) zones (LOS2 scenario)

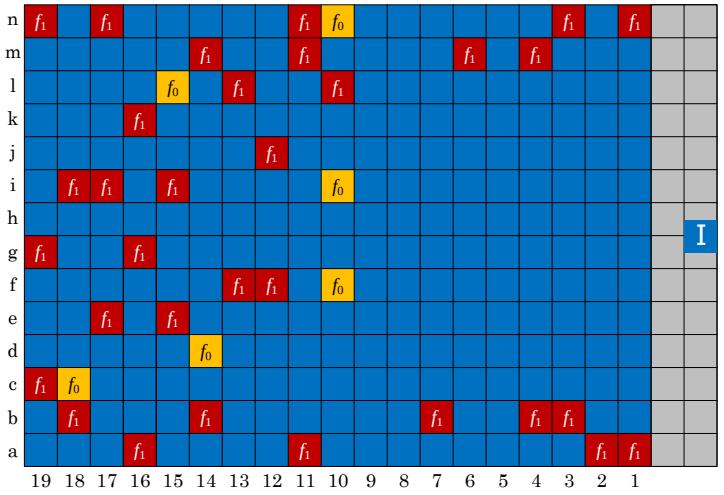

FIGURE B.15: Matching of the simulations and the measurements (LOS2 scenario)
blue = match, f_0 = false no-read in simulation, f_1 = false read in simulation

B.5.4 NLOS Measurement and Simulation Results

In this measurement, a high-frequency absorber of size 0.30 m × 0.50 m × 0.40 m was used to block the LOS path (and/or other multipath components) for different tag positions. Figure B.16 shows a top view drawing of the NLOS measurement setup. The measurement results are shown in figure B.17, the combined up-/downlink readability simulation in figure B.18, and the matching of the simulation and measurement results in figure B.19. As can be seen, the readability of 114 tag positions (88%) was estimated correctly in the simulation.

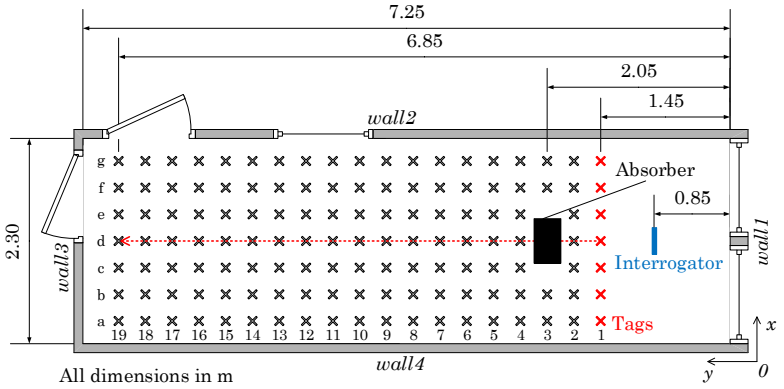

FIGURE B.16: Setup for the NLOS tag readability measurements (top view; NLOS scenario)

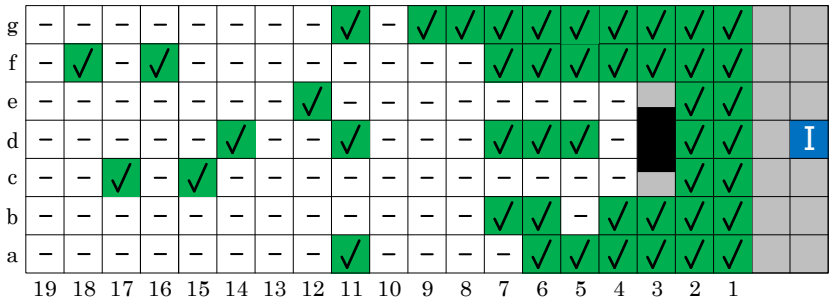

FIGURE B.17: Measurement of the read (✓) and no-read (–) zones (NLOS scenario)

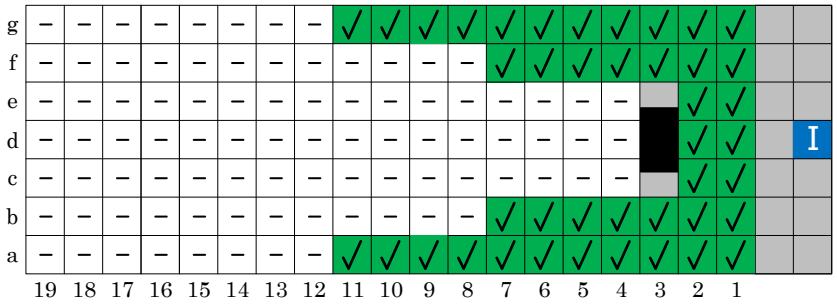

FIGURE B.18: Simulated read (✓) and no-read (–) zones (NLOS scenario)

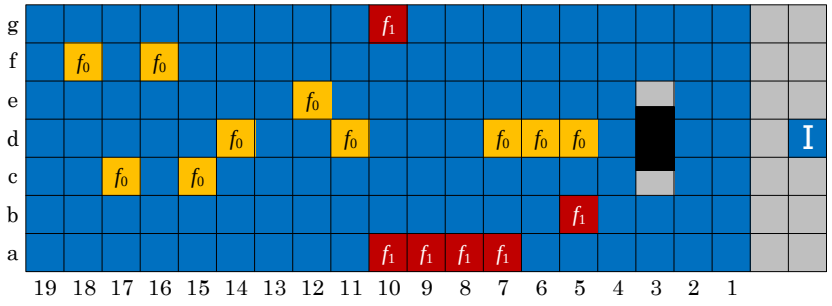

FIGURE B.19: Matching of the simulations and the measurements (NLOS scenario) blue = match, f_0 = false no-read in simulation, f_1 = false read in simulation

Appendix C

Receiver Beamforming Localization

C.1 FEKO Simulation Software

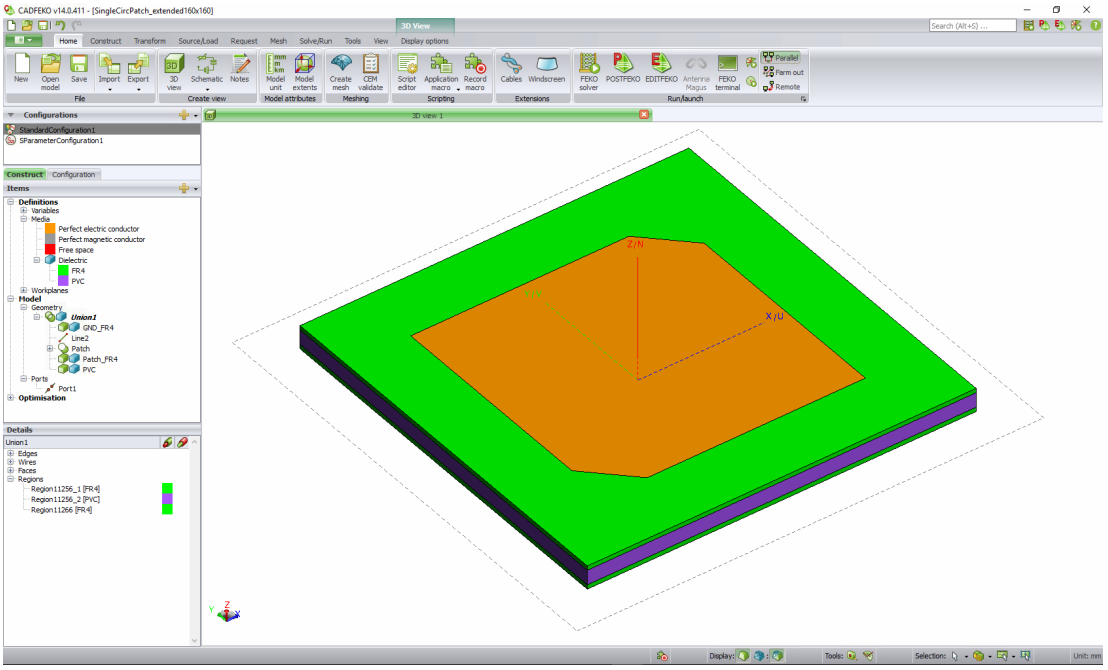

FIGURE C.1: Model of a microstrip patch antenna in CADFEKO

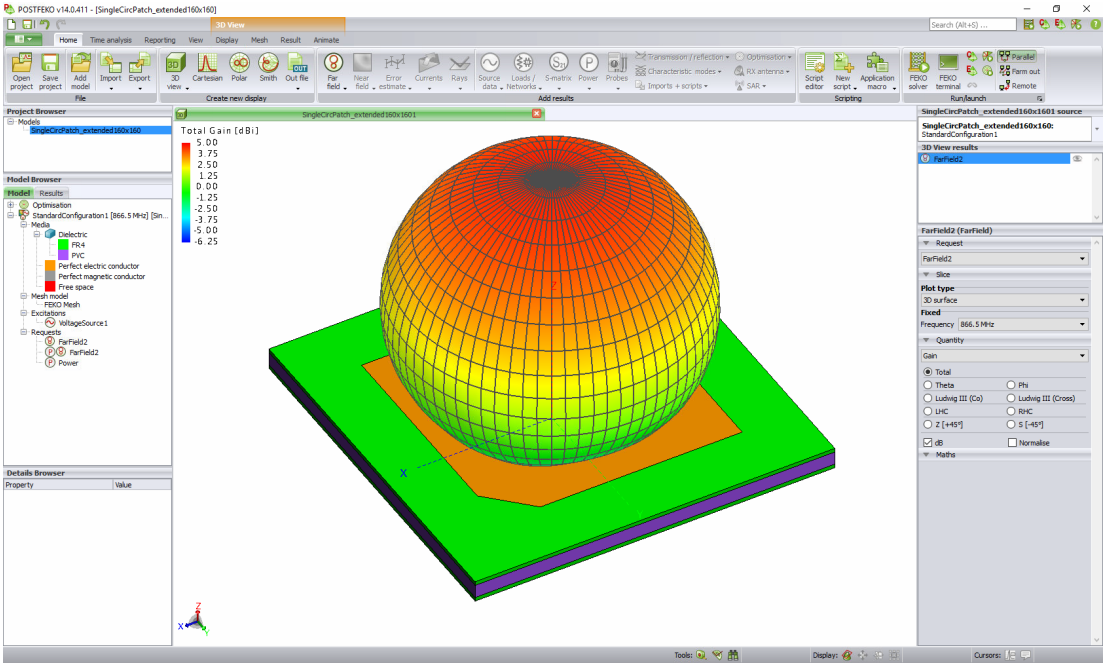

FIGURE C.2: Three-dimensional gain pattern of a microstrip patch antenna in POST-FEKO

C.2 Nearest Point Algorithm

After estimating the direction of the target tag from N different antenna array positions in the localization area, the localization task is to find the point P_m in space which has the minimum distance from all N lines connected to the target tag directions:

$$P_m = \arg\min_{P\in\mathbb{R}^3} \sum_{i=1}^{N} d^2(P, g_i) \tag{C.1}$$

where g_i is the line connected to one of the N direction estimates. The point P can be determined as follows if $N = 3$:

1. Compute the linear functions describing the straight line from antenna array i towards the estimated direction using the estimated angles ϕ_i and θ_i with $i = 1, 2, 3$.

   This can be done beneficially in parametric form where $t \in \mathbb{R}$ denotes the parameter:

   $$\begin{aligned} \begin{pmatrix} x \\ y \\ z \end{pmatrix} &= \vec{v}_{Ri} + t\vec{v}_{Di} \\ &= \begin{pmatrix} x_{Ri} \\ y_{Ri} \\ z_{Ri} \end{pmatrix} + t \begin{pmatrix} \cos\phi_i \sin\theta_i \\ \sin\phi_i \sin\theta_i \\ \cos\theta_i \end{pmatrix} \end{aligned} \tag{C.2}$$

   Note that the angles θ_i and ϕ_i are measured in the antenna-array-specific coordinate system

2. Consider the N skew lines $g_i = \{\vec{v}_i + t\vec{w}_i | t \in \mathbb{R}\}$ with $i = 1, 2, ..., N$ and the point $\vec{p}$. Then, the squared (minimum) distance between the line and the point is given by (see standard textbook on analytic algebra):

   $$d^2 = \frac{|(\vec{p} - \vec{v}_i) \times \vec{w}_i|^2}{|\vec{w}_i|^2},$$

   where $\times$ denotes the vector product.

Now assuming that, without loss of generality, the directional vectors $\vec{w}_i$ are normalized to $|\vec{w}_i| = 1$, one gets for the sum of squared Euclidean distances:

$$\begin{aligned} D = \sum_{i=1}^{N} d_i^2 &= \sum_{i=1}^{N} \left| \begin{pmatrix} p_x - v_{xi} \\ p_y - v_{yi} \\ p_z - v_{zi} \end{pmatrix} \times \begin{pmatrix} w_{xi} \\ w_{yi} \\ w_{zi} \end{pmatrix} \right|^2 = \sum_{i=1}^{N} \left| \begin{pmatrix} h_{xi} \\ h_{yi} \\ h_{zi} \end{pmatrix} \times \begin{pmatrix} w_{xi} \\ w_{yi} \\ w_{zi} \end{pmatrix} \right|^2 \\ &= \sum_{i=1}^{N} \left| ((h_{yi}w_{zi} - h_{zi}w_{yi}), (h_{zi}w_{xi} - h_{xi}w_{zi}), (h_{xi}w_{yi} - h_{yi}w_{xi}))^T \right|^2 \\ &= \sum_{i=1}^{N} \left((h_{yi}w_{zi} - h_{zi}w_{yi})^2 + (h_{zi}w_{xi} - h_{xi}w_{zi})^2 + (h_{xi}w_{yi} - h_{yi}w_{xi})^2 \right) \end{aligned}$$

3. This is a quadratic form, having only one minimum, calculated by setting the partial derivations with respect to the point coordinates equal to zero:

$$\begin{aligned} \frac{\partial D}{\partial p_x} &= \sum_{i=1}^{N} (0 + 2(h_{zi}w_{xi} - h_{xi}w_{zi})(-w_{zi}) + 2(h_{xi}w_{yi} - h_{yi}w_{xi})w_{yi}) \\ 0 &= \sum_{i=1}^{N} \big((w_{yi}^2 + w_{zi}^2)p_x - w_{xi}w_{yi}p_y - w_{xi}w_{zi}p_z + \\ &\qquad + (-(w_{yi}^2 + w_{zi}^2)v_{xi} + w_{xi}w_{yi}v_{yi} + w_{xi}w_{zi}v_{zi}) \big) , \end{aligned} \tag{C.3}$$

$$\begin{aligned} \frac{\partial D}{\partial p_y} &= \sum_{i=1}^{N} (2(h_{yi}w_{zi} - h_{zi}w_{yi})w_{zi} + 0 + 2(h_{xi}w_{yi} - h_{yi}w_{xi})(-w_{xi})) \\ 0 &= \sum_{i=1}^{N} \big(-w_{xi}w_{yi}p_x + (w_{xi}^2 + w_{zi}^2)p_y - w_{yi}w_{zi}p_z + \\ &\qquad + (w_{xi}w_{yi}v_{xi} - (w_{xi}^2 + w_{zi}^2)v_{yi} + w_{yi}w_{zi}v_{zi}) \big) \end{aligned} \tag{C.4}$$

and

$$\begin{aligned} \frac{\partial D}{\partial p_z} &= \sum_{i=1}^{N} (2(h_{yi}w_{zi} - h_{zi}w_{yi})(-w_{yi}) + 2(h_{zi}w_{xi} - h_{xi}w_{zi})w_{xi} + 0) \\ 0 &= \sum_{i=1}^{N} \big(-w_{xi}w_{zi}p_x - w_{yi}w_{zi}p_y + (w_{xi}^2 + w_{yi}^2)p_z + \\ &\qquad + (w_{xi}w_{zi}v_{xi} + w_{yi}w_{zi}v_{yi} - (w_{xi}^2 + w_{yi}^2)v_{zi}) \big) \end{aligned} \tag{C.5}$$

This results in the system of equations:

$$\begin{pmatrix} \sum_{i=1}^{N}(w_{yi}^2+w_{zi}^2) & -\sum_{i=1}^{N} w_{xi}w_{yi} & -\sum_{i=1}^{N} w_{xi}w_{zi} \\ -\sum_{i=1}^{N} w_{xi}w_{yi} & \sum_{i=1}^{N}(w_{xi}^2+w_{zi}^2) & -\sum_{i=1}^{N} w_{yi}w_{zi} \\ -\sum_{i=1}^{N} w_{xi}w_{zi} & -\sum_{i=1}^{N} w_{yi}w_{zi} & \sum_{i=1}^{N}(w_{xi}^2+w_{yi}^2) \end{pmatrix} \begin{pmatrix} p_x \\ p_y \\ p_z \end{pmatrix} = \\ = \begin{pmatrix} \sum_{i=1}^{N}(w_{yi}^2+w_{zi}^2)v_{xi} - w_{xi}w_{yi}v_{yi} - w_{xi}w_{zi}v_{zi} \\ \sum_{i=1}^{N} -w_{xi}w_{yi}v_{xi} + (w_{xi}^2+w_{zi}^2)v_{yi} - w_{yi}w_{zi}v_{zi} \\ \sum_{i=1}^{N} -w_{xi}w_{zi}v_{xi} - w_{yi}w_{zi}v_{yi} + (w_{xi}^2+w_{yi}^2)v_{zi} \end{pmatrix} \tag{C.6}$$

For the 2D case with $p_z = v_{zi} = w_{zi} = 0$ one finds:

$$\begin{pmatrix} \sum_{i=1}^{N} w_{yi}^2 & -\sum_{i=1}^{N} w_{xi}w_{yi} \\ -\sum_{i=1}^{N} w_{xi}w_{yi} & \sum_{i=1}^{N} w_{xi}^2 \end{pmatrix} \begin{pmatrix} p_x \\ p_y \end{pmatrix} = \begin{pmatrix} \sum_{i=1}^{N} w_{yi}^2 v_{xi} - w_{xi}w_{yi}v_{yi} \\ \sum_{i=1}^{N} -w_{xi}w_{yi}v_{xi} + w_{xi}^2 v_{yi} \end{pmatrix} \tag{C.7}$$

The advantage of the proposed algorithm is its ability to work for any number of target tag direction estimates and for both cases, the two-dimensional and three-dimensional one. The algorithm computes the optimum linear solution for the AoA problem related to minimum Euclidean distances to all estimates assuming a Gaussian error distribution in the x,y,z coordinates of the target.

A suboptimal solution can be formulated as follows: Assuming that estimates of the target tag direction from three different antenna arrays on the ground plane are available. Then the following steps can be performed to get an estimated position of the tag:

1. Compute the linear functions describing a straight line in the estimated direction from the measured angles-of-arrival θ_n for $n = 1, 2, 3$.

2. The point in space has to be found that has a minimum distance to all three skew lines that were constructed in 1. This problem should be solved in a minimum mean square sense. A practical approach is as follows:

   (a) Consider pairs of skew lines $g_i = \{\vec{v_i} + r\vec{w_i} | r \in \mathbb{R}\}$ and $g_j = \{\vec{v_j} + s\vec{w_j} | s \in \mathbb{R}\}$ and compute the minimum Euclidean distance between them as

   $$d_{ij} = \frac{|\,(\vec{v_j} - \vec{v_i}) \cdot (\vec{w_j} \times \vec{w_i})\,|}{|\vec{w_j} \times \vec{w_i}|}, \tag{C.8}$$

   where $\times$ denotes the vector product and $\cdot$ the scalar product.

   (b) The normal vector (length = 1) of the plane parallel to both lines is given as:

   $$\vec{n} = \frac{(\vec{w_j} \times \vec{w_i})}{|\vec{w_j} \times \vec{w_i}|} \tag{C.9}$$

(c) Compute the points on both lines belonging to the shortest line connecting both skew lines by solving the system of equations for t_m and s_m:

$$\vec{v_i} + t_m \vec{w_i} = \vec{v_j} + s_m \vec{w_j} + d_{ij} \vec{n} \tag{C.10}$$

which contains three equations for two unknowns.

(d) Repeat this for the two other pairs of skew lines.

(e) Determine the center points c_1, c_2, c_3 of the connecting lines of pairs (g_1, g_2), (g_1, g_3), (g_2, g_3) of skew lines. Connecting these center points results into a triangle of which the centroid can be used as an estimate for the tag position.

Alternatively, use a numerical approach to find the two points by running up one line and finding for each point the distance to the other line. Stop if the distance is minimum.

C.3 Experimental Testbed

C.3.1 DSP Unit

Figure C.3 shows a block diagram of the new, self-designed DSP unit for the phase-difference measurement of a tag signal. A three-element antenna array connects to the receiver inputs of three RF front-end modules. The main component of these modules is the integrated UHF RFID interrogator IC IDS Microchip R901G (or the equivalent AMS AS3991) that comprises all analogue (modulator, filter, etc.) and digital blocks to implement the full EPCglobal protocol. The transmitter path of RF front-end 3 is connected to a separate antenna. The local oscillator frequency for the demodulation process is provided by a LO (local oscillator) module that feeds the three interrogator modules with an in-phase sine signal generated by a synthesizer IC (Analog Devices ADF4360-7). The control and communications module includes an analog-to-digital converter (Maxim MAX1304) for sampling of the six IQ base-band signals generated by the RF front-ends and two microcontrollers (STmicroelectronics STM32F407 and STM32F405). It connects the AoA unit via RS232, Ethernet or USB to a PC that controls the measurement process and collects the AoAs from all connected units to angulate the position of the tag. A picture of the full AoA unit is depicted in figure C.4. For the calculation of the AoA, the RF front-end module 2 starts a communication cycle with the tag to read its Electronic Product Code. From the demodulated tag response, 250 samples (relating to around 70 symbols) are used for computing the correlation as described in section 5.3.1. As a measure for the received signal strength of the tag signal, the sum of the mean signal power of the received baseband IQ signals of the three antenna array elements is calculated.

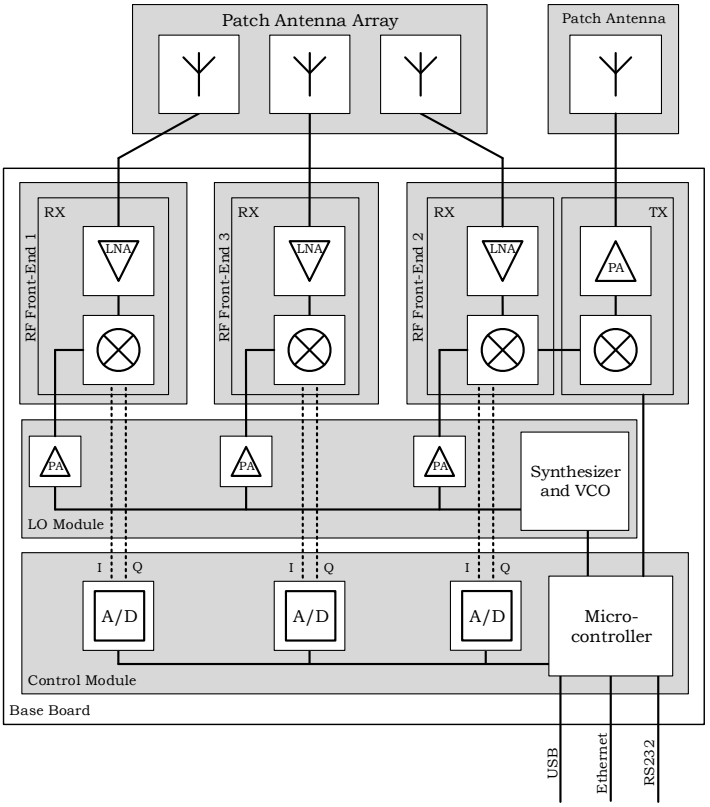

FIGURE C.3: Block diagram of the AoA unit

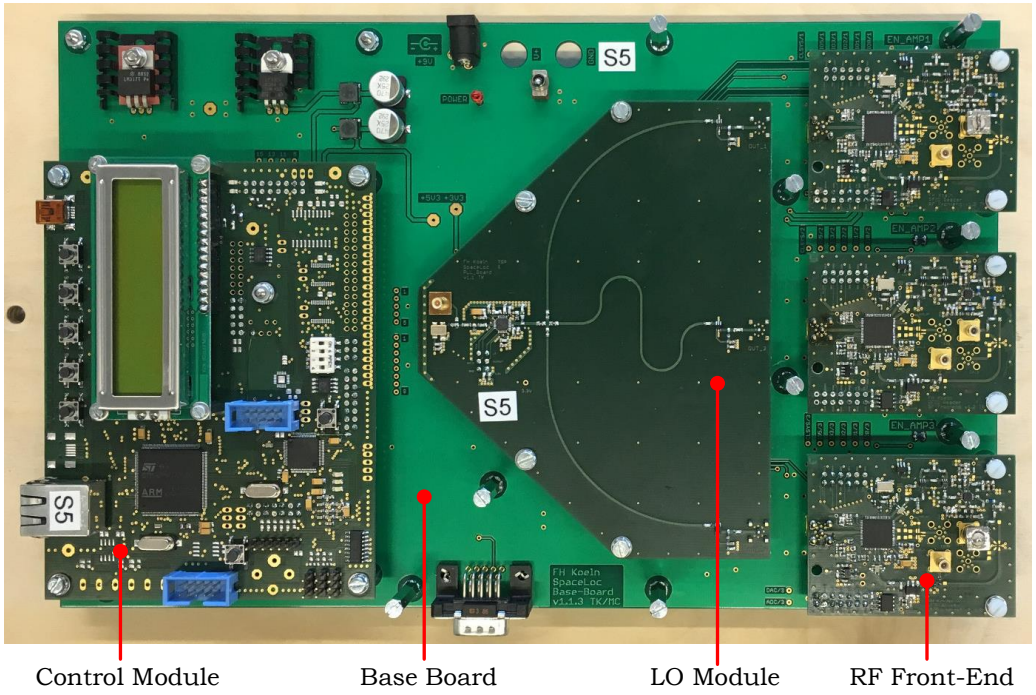

FIGURE C.4: Picture of the DSP unit

C.3.2 Circularly Polarized Transmitter Patch Antenna

The circularly polarized patch antenna that is displayed in figure C.5 is used as the AoA unit's transmitter antenna. It supports the current and the future European UHF RFID frequency ranges and is made of two aluminium plates: one square plate for the ground plane (222 mm × 222 mm) and one circular plate for the patch element (diameter 169 mm). Capacitive feeding is realized with two circular plates made of brass, arranged 1.5 mm behind the patch element. A 3-dB 90° branch-line coupler provides the necessary signals for circular polarization. The measured mean values of the antenna gain are 8.5 dBi (867.1 MHz) and 8.2 dBi (920.3 MHz). The corresponding 3-dB-beamwidths are 73.5° and 65°, respectively. The axial ratio is below 1 dB for 867.1 MHz and below 1.9 dB for 920.3 MHz.

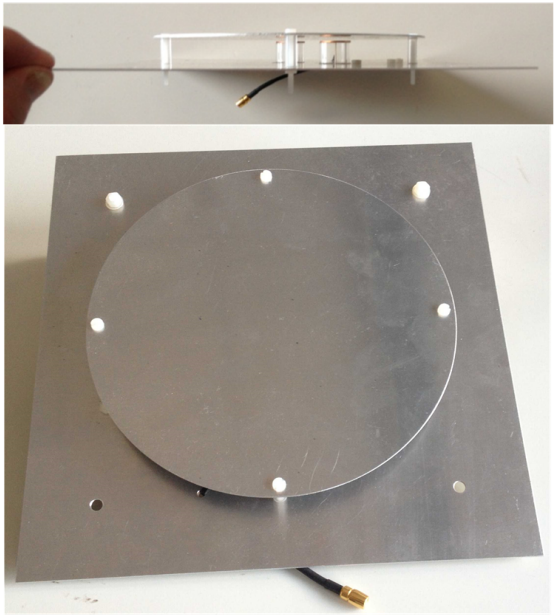

FIGURE C.5: Pictures of the circularly polarized patch antenna (side and top view)

C.3.3 AoA Unit

Figure C.6 shows a picture of the full AoA unit.

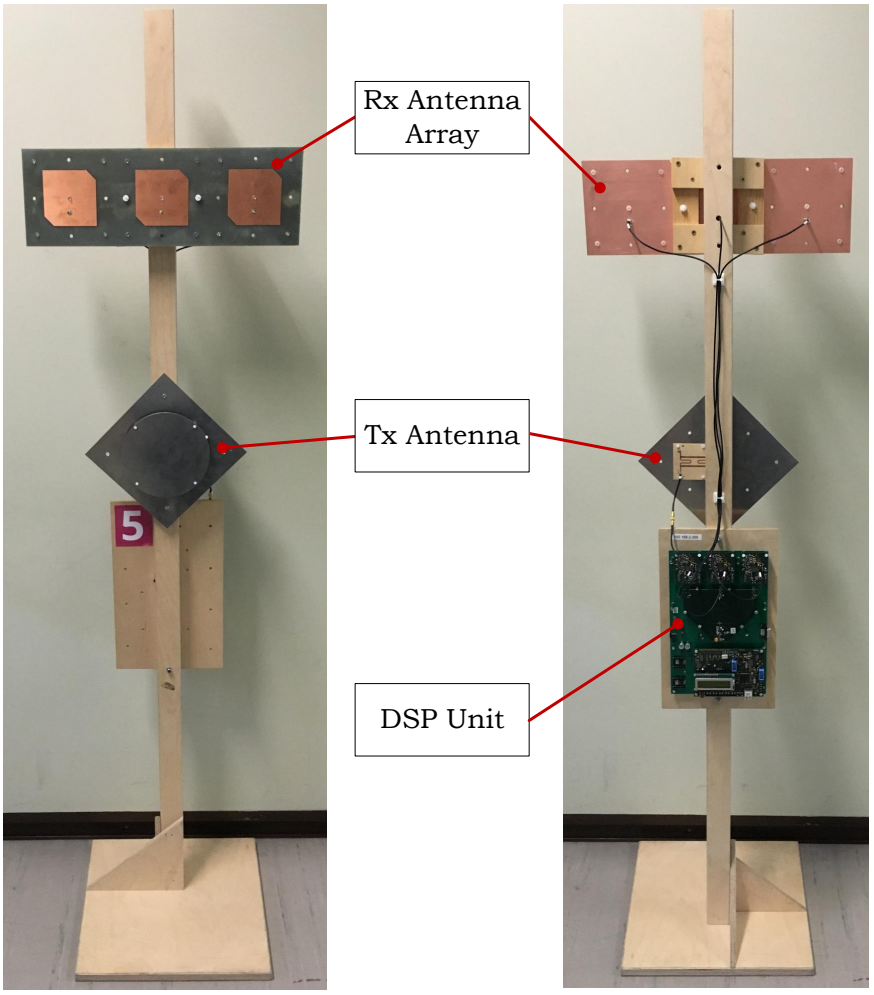

FIGURE C.6: Pictures of the AoA unit

C.3.4 Tags

The UPM RaflaTac DogBone label tag that is displayed in figure C.7 consists of Impinj tag IC and a folded dipole antenna. It operates in a frequency range between 860 MHz and 960 MHz and has a size of 97 mm × 27 mm.

FIGURE C.7: UPM RaflaTac DogBone label tag

Based on the passive UHF RFID tag IC G2XM by NXP, a tag was developed that is matched to a 50 Ω load and allows the connection of any 50Ω-matched antenna (e.g. a circularly polarized patch antenna). Figure C.8 shows a picture of this tag where the 50 Ω matching is realized by means of a transmission line transformation on FR4 board.

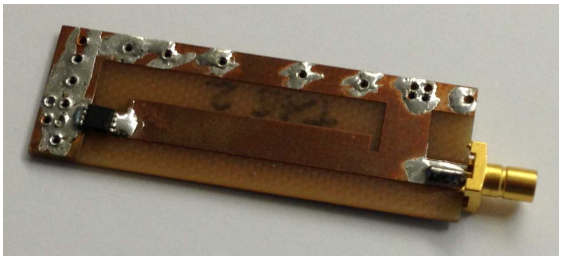

FIGURE C.8: Passive UHF RFID tag matched to 50 Ω

C.4 Measurement Setups

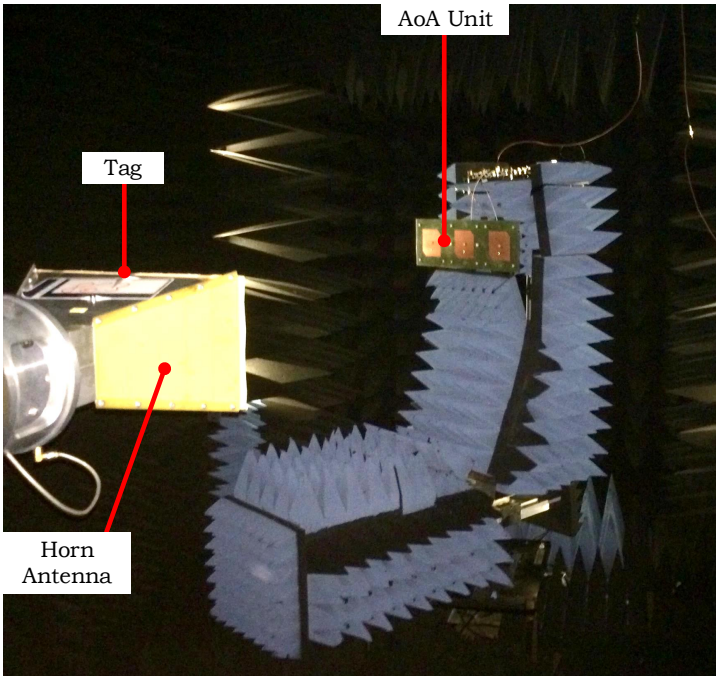

FIGURE C.9: Picture of the setup for the AoA measurements in the anechoic chamber

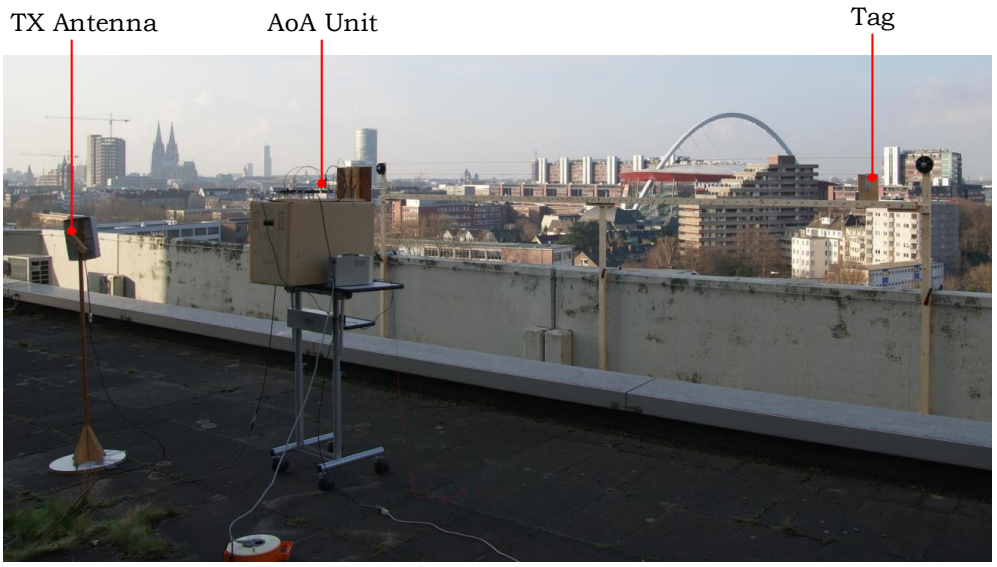

FIGURE C.10: Picture of the setup for the AoA measurements on the university balcony

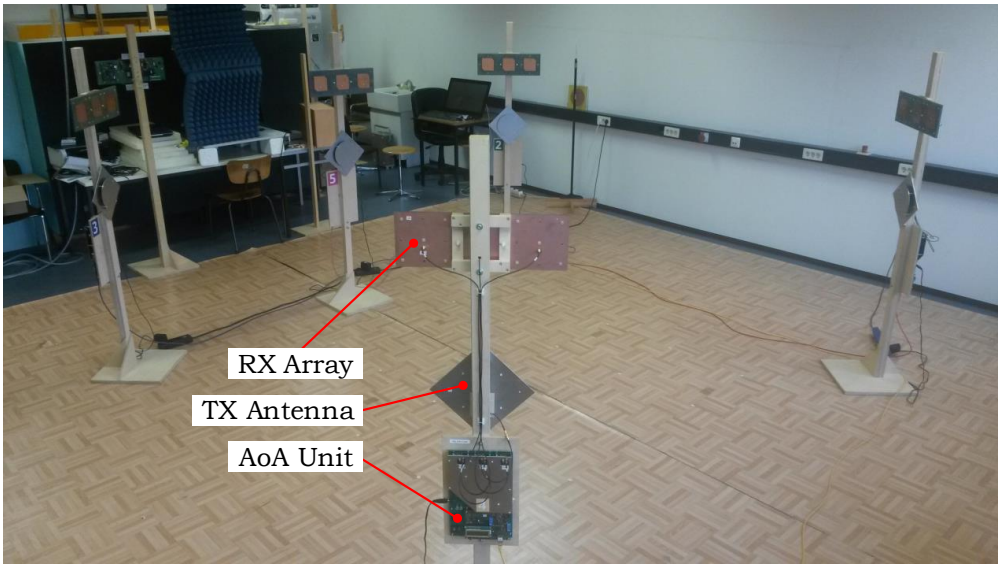

FIGURE C.11: Picture of the seminar room localization measurement

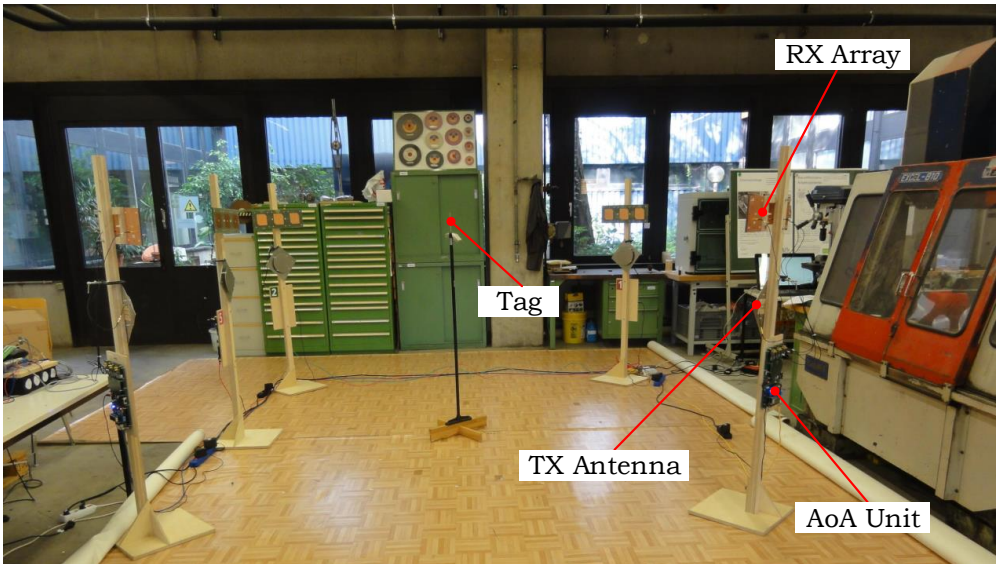

FIGURE C.12: Picture of the machine hall localization measurement

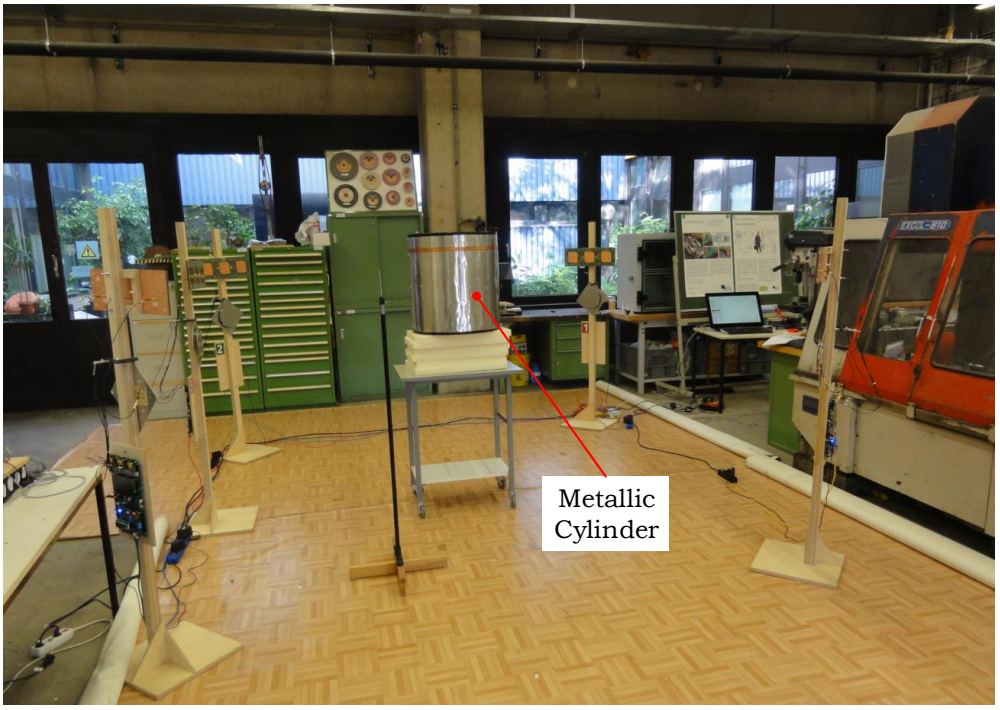

FIGURE C.13: Picture of the machine hall localization measurement with an additional scatterer

Appendix D

Transmitter Beamforming Localisation

D.1 AoAct Unit

Figure D.1 shows a block diagram of the new, self-developed AoAct unit. Each of the functional blocks was designed and built on separate circuit boards (see figure D.2). These modules are attached to a common base board which is used for power supply and signal distribution. In contrast to the AoA unit, the AoAct DSP unit is designed to match the size of the patch antenna array. Thus, it can be attached to the rear of the antenna array to form a single, compact unit.

The control module is built around a microcontroller (STMicroelectronics STM32F407) that synthesises the baseband transmitter signals and controls all other hardware modules. The six baseband signals (I and Q components for three RF front-ends) are generated using a digital-to-analog converter (DAC, Texas Instruments TLV5630). A second, auxiliary DAC is used to generate several reference signals for the RF front-end, such as the control voltages for the power amplifiers. For communication to a host PC, there are three different interfaces available: USB, Ethernet and RS232. The LO (Local Oscillator) module consists of an integrated synthesizer (Analog Devices ADF4360) that generates three synchronous high-frequency signals for the RF front-ends. The RF front-end is used to modulate the synthesized I and Q components onto the high-frequency carrier. It consists of an integrated modulator (Texas Instruments TRF3701), a power amplifier (RFMD RF5110G), and a power detector (Texas Instruments LMV225). RF front-end 2 is equipped with a low-noise amplifier (LNA, TriQuint TQP3M9007) and an integrated RFID interrogator (Austria Microsystems AS3991) that is used as a demodulator. It also includes all necessary filtering for the RF and the baseband signals.

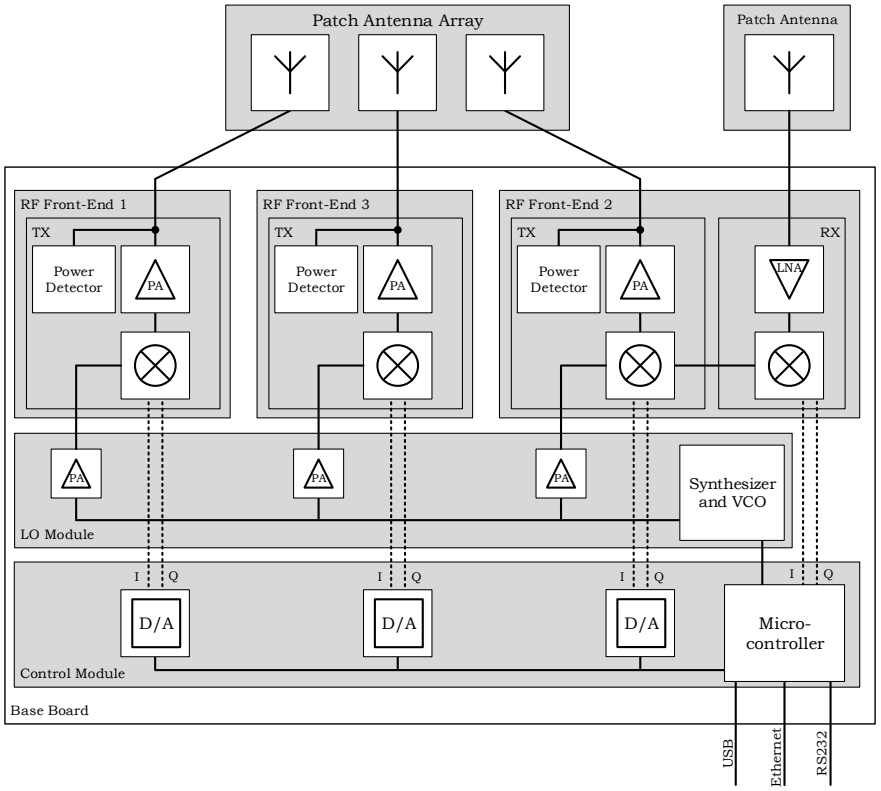

FIGURE D.1: Block diagram of the AoAct unit

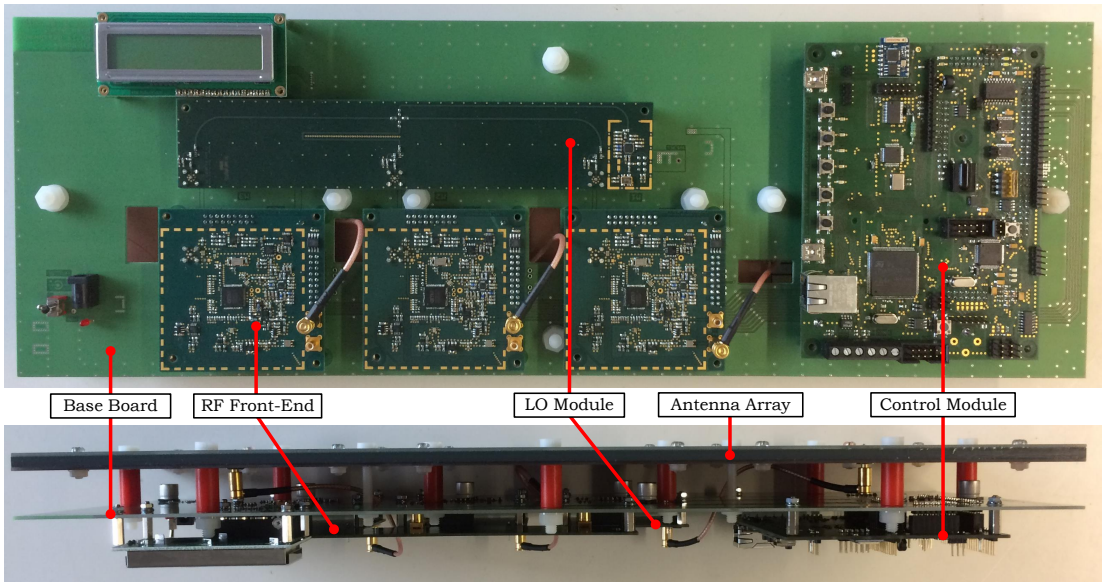

FIGURE D.2: Picture of the AoAct unit (top view and side view)

With this RF front-end, it is possible to receive and demodulate the response of the RFID tag. The firmware of the microcontroller on the control module includes all drivers to control the connected peripherals (e.g. the DACs) and to communicate with external host systems (e.g. USB). The full EPCglobal communication protocol is implemented, including the generation of the baseband I and Q components using the connected DAC. Additionally, the decoding of the received tag signal is realized. The phase of the transmitter signal can be set in 0.06° steps in a range of -180° to 180° and the level from -20 dBm to 27 dBm in 0.001 dB steps. To test the readability of a tag, a communication cycle to read the EPC (Electronic Product Code) of the tag is started. In the process of estimating the AoAct of a tag, it is marked as readable (or activated) if it is possible to receive and decode a valid EPC from the tag.

A circularly polarized patch antenna (see section C.3.2) is used as the receiver antenna for the AoAct unit and the new circularly polarized three-element patch antenna array as the transmitter antenna (see section 5.3.1).

A host PC Matlab software is implemented to control the AoAct unit (setting phases and levels for the desired beam pattern and executing the AoAct estimation algorithm). It also allows recording and plotting of the received signal powers and the tag readability. It should be noted that this software is only needed to visualize the measurement results during the AoAct estimation process. The process itself is fully executed on the AoAct unit.

The processing time for setting the three signal phases and levels to change the beam pattern is negligible. The implemented EPCglobal communication protocol supports data rates up to 80 KBit/s. At this data rate, the time to execute a full EPCglobal communication cycle to read the tag's EPC takes approximately 5 ms. The maximum angular beamsteering range of the used three-element array is ±52°, which equals phase differences of the transmit signals in the full range of ±180°. To sweep through this range in 1° phase steps while recording the tag readability takes approximately 1.8 seconds.

D.2 Beam Pattern Measurements

Figures D.3 and D.4 show measured beam patterns for equal transmitter power levels $P_{\mathrm{Tx},1} = P_{\mathrm{Tx},2} = P_{\mathrm{Tx},3} = 25$ dBm (i.e. equal absolute values $A_l = 1$ for the beam former weights w_l) for each array element, a fixed phase of $\varphi_1 = 0°$ for the center element and varying phases $\varphi_0 = \varphi, \varphi_2 = -\varphi$ for the outer elements. The designation of the single graphs in the figures is as follows: $\varphi_0, \varphi_1, \varphi_2$.

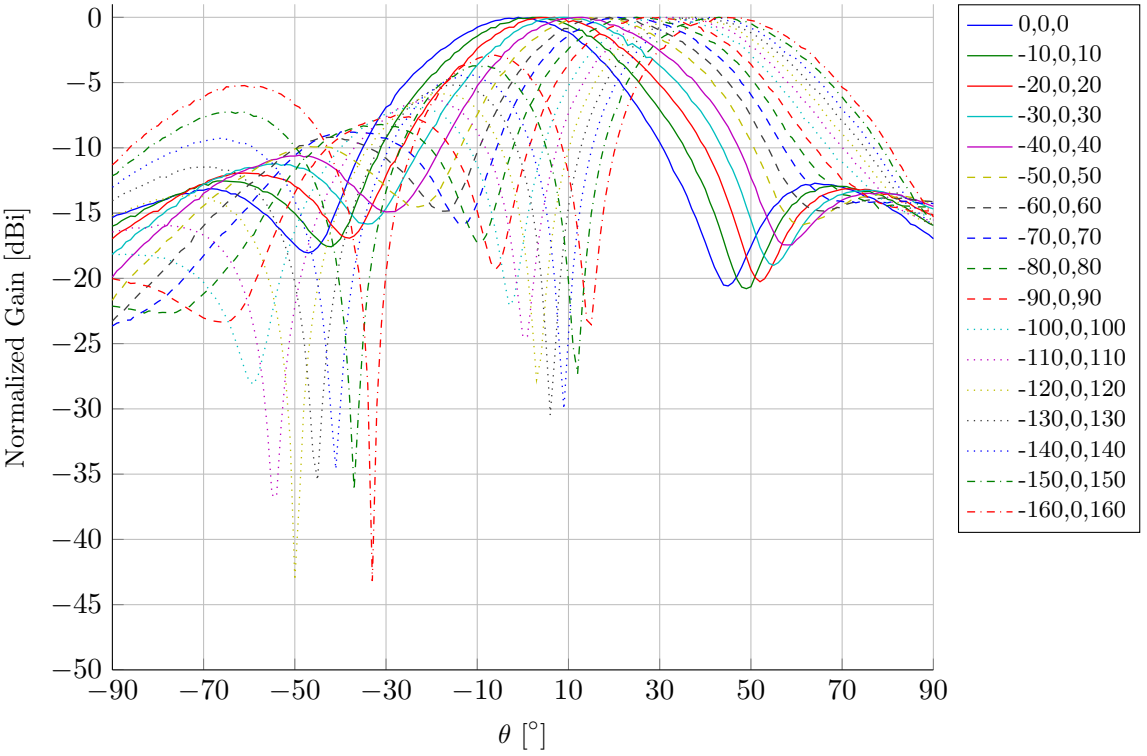

FIGURE D.3: Measured beam patterns for $\varphi = -160°, -150°, ..., 0°$

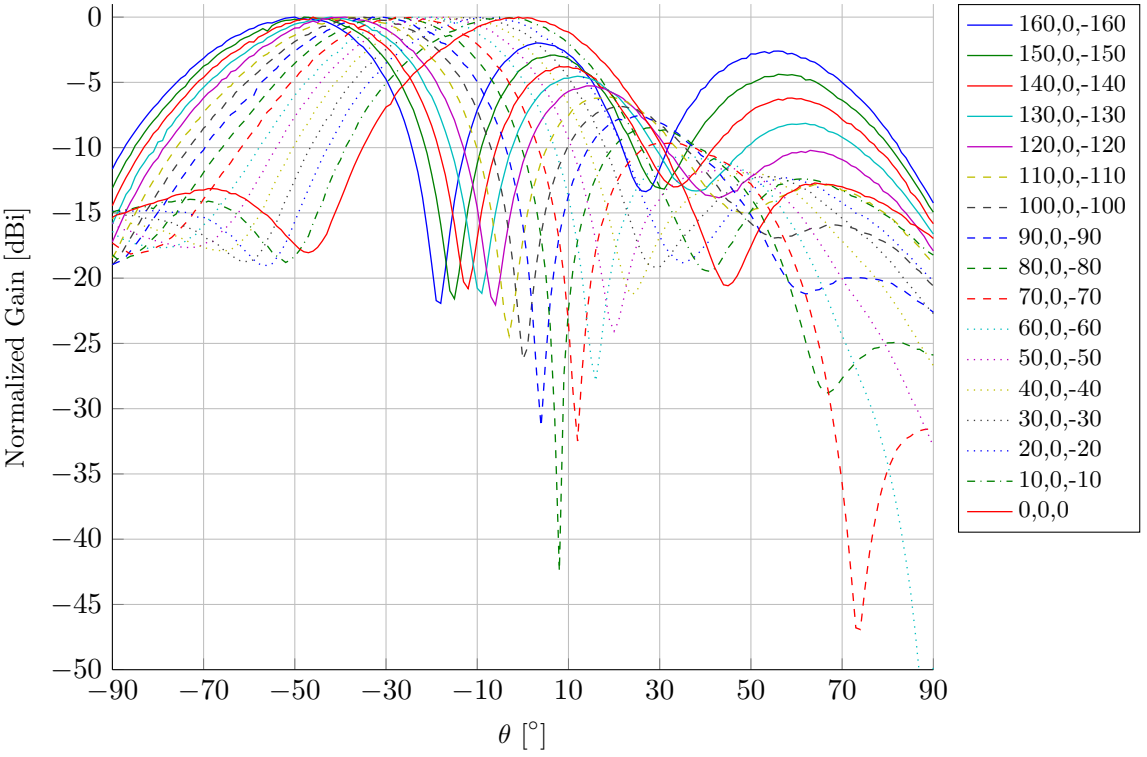

FIGURE D.4: Measured beam patterns for $\varphi = 0°, 10°, ..., 160°$

References

[1] O. Onalaja, *Advances in UWB-based Indoor Position Estimation and its Application in Fall Detection.* Dissertation, London South Bank University, United Kingdom, 2014.

[2] J. Koch, J. Wettach, E. Bloch, and K. Berns, "Indoor localisation of humans, objects, and mobile robots with RFID infrastructure," in *7th International Conference on Hybrid Intelligent Systems*, pp. 271–276, September 2007.

[3] T. Sanpechuda and L. Kovavisaruch, "A review of RFID localization: Applications and techniques," *5th International Conference on Electrical Engineering/-Electronics, Computer, Telecommunications and Information Technology*, vol. 2, pp. 769–772, May 2008.

[4] W. Lu, G. Q. Huang, and H. Li, "Scenarios for applying RFID technology in construction project management," *Automation in Construction*, vol. 20, pp. 101–106, March 2011.

[5] P. Daly, "Navstar GPS and GLONASS: global satellite navigation systems," *Electronics & Communications Engineering Journal*, vol. 5, pp. 349–357, December 1993.

[6] J. McIntire, *Supply Chain Visibility: From Theory to Practice.* Ashgate Publishing, Ltd., 2014.

[7] J. Wilson, "Toward things that think for the next millennium," *IEEE Computer*, vol. 33, pp. 72–76, January 2000.

[8] F. Shrouf, J. Ordieres, and G. Miragliotta, "Smart factories in industry 4.0: A review of the concept and of energy management approached in production based on the internet of things paradigm," in *IEEE International Conference on Industrial Engineering and Engineering Management*, pp. 697–701, December 2014.

[9] M. Vossiek, R. Miesen, and J. Wittwer, "RF identification and localization - recent steps towards the internet of things in metal production and processing,"

in *18th International Conference on Microwave Radar and Wireless Communications*, pp. 1–8, June 2010.

[10] H. Zhang and L. Zhu, "Internet of things: Key technology, architecture and challenging problems," in *IEEE International Conference on Computer Science and Automation Engineering*, vol. 4, pp. 507–512, June 2011.

[11] ITU-T, "Location matters: Spatial standards for the Internet of Things," *ITU News*, pp. 1–5, December 2015.

[12] Y. Gu, A. Lo, and I. Niemegeers, "A survey of indoor positioning systems for wireless personal networks," *IEEE Communications Surveys & Tutorials*, vol. 11, pp. 13–32, March 2009.

[13] F. Peyrard, C. Soutou, and J.-J. Mercier, "Mobile stations localization in a WLAN," in *25th Annual IEEE Conference on Local Computer Networks*, pp. 136–142, November 2000.

[14] B. Geiger, "Ranging in the IEEE 802.15.4a standard using energy detectors," in *IEEE EUROCON*, pp. 1956–1963, May 2009.

[15] J. M. Myerson, *RFID in the Supply Chain: A Guide to Selection and Implementation*, vol. 20. CRC Press, 2006.

[16] EPCglobal Inc., "Epcglobal class-1 generation-2 air interface protocol v1.2.0," October 2008.

[17] International Organization for Standardization, "ISO/IEC 18000-6:2013 - Information technology – Radio frequency identification for item management – Part 6: Parameters for air interface communications at 860 MHz to 960 MHz," January 2013.

[18] GS1, "Regulatory status for Using RFID in the EPC gen 2 band (860 to 960 MHz) of the UHF spectrum," October 2014.

[19] F. Kirsch, R. Miesen, and M. Vossiek, "Analytical study about the impact of multipath propagation on UHF-RFID ranging techniques," in *IEEE International Conference on Wireless Information Technology and Systems*, pp. 1–4, November 2012.

[20] The Guardian, "The internet of things is revolutionising our lives, but standards are a must." Website, 2015. `http://www.theguardian.com/media-network/2015/mar/31/the-internet-of-things-is-revolutionising-our-lives`.

[21] ABIresearch, "More than 30 billion devices will wirelessly connect to the internet of everything in 2020." Website, 2013. `https://www.abiresearch.com/press/more-than-30-billion-devices-will-wirelessly-conne/`.

[22] H. Chaouchi, *The Internet of Things: Connecting Objects*. John Wiley & Sons, 2013.

[23] T. Bauernhansl, *Industrie 4.0 in Produktion, Automatisierung und Logistik Anwendung, Technologien, Migration*. Springer Vieweg, 2014.

[24] O. Vermesan and P. Friess, *Internet of Things - Global Technological and Societal Trends*. River Publishers, 2011.

[25] Y. Bai, S. Wu, H. Wu, and K. Zhang, "Overview of RFID-based indoor positioning technology," in *29th Annual International Conference of the IEEE Engineering in Medicine and Biology Society*, pp. 1–10, August 2012.

[26] M. Hossain and W.-S. Soh, "A comprehensive study of bluetooth signal parameters for localization," in *IEEE 18th International Symposium on Personal, Indoor and Mobile Radio Communications*, pp. 1–5, September 2007.

[27] K. Sattlegger and U. Denk, "Navigating your way through the RFID jungle," 2014.

[28] L. Ni and A. Patil, "LANDMARC: Indoor location sensing using active RFID," in *First IEEE International Conference on Pervasive Computing and Communications*, pp. 407–415, March 2003.

[29] M. Bolic, D. Simplot-Ryl, and I. Stojmenovic, *RFID Systems: Research Trends and Challenges*. John Wiley & Sons, 2010.

[30] H. T. Friis, "A note on a simple transmission formula," *Proceedings of the IRE*, vol. 34, pp. 254–256, May 1946.

[31] K. Chawla, G. Robins, and L. Zhang, "Efficient RFID-based mobile object localization," in *IEEE International Conference on Wireless and Mobile Computing, Networking and Communications*, pp. 683–690, October 2010.

[32] J. Maneesilp, C. Wang, H. Wu, and N.-F. Tzeng, "RFID support for accurate 3D localization," *IEEE Transactions on Computers*, vol. 62, pp. 1447–1459, April 2013.

[33] J. S. Choi, H. Lee, R. Elmasri, and D. W. Engels, "Localization systems using passive UHF RFID," in *Fifth International Joint Conference on INC, IMS and IDC*, pp. 1727–1732, August 2009.

[34] R. Miesen, F. Kirsch, and M. Vossiek, "Holographic localization of passive UHF RFID transponders," in *IEEE International Conference on RFID*, pp. 32–37, April 2011.

[35] R. Miesen, F. Kirsch, and M. Vossiek, "UHF RFID localization based on synthetic apertures," *IEEE Transactions on Automation Science and Engineering*, vol. 10, pp. 807–815, January 2012.

[36] M. Hasani, J. Talvitie, L. Sydanheimo, E.-S. Lohan, and L. Ukkonen, "Hybrid WLAN-RFID indoor localization solution utilizing textile tag," *IEEE Antennas and Wireless Propagation Letters*, vol. 14, pp. 1358–1361, February 2015.

[37] T. Nick, S. Cordes, and J. Gotze, "Camera-assisted localization of passive RFID labels," in *International Conference on Indoor Positioning and Indoor Navigation*, pp. 13–15, November 2012.

[38] L. Catarinucci, R. Colella, L. Mainetti, L. Patrono, S. Pieretti, I. Sergi, and L. Tarricone, "Smart RFID antenna system for indoor tracking and behavior analysis of small animals in colony cages," *IEEE Sensors Journal*, vol. 14, pp. 1198–1206, April 2014.

[39] P. Perrissol, L. Lizzi, A. Diallo, P. Le Thuc, R. Staraj, and G. Carle, "RSSI measurements to achieve mouse localization in a cage," in *IEEE Conference on Antenna Measurements & Applications*, pp. 1–4, November 2014.

[40] A. Almaaitah, K. Ali, H. S. Hassanein, and M. Ibnkahla, "3D passive tag localization schemes for indoor RFID applications," *IEEE International Conference on Communications*, pp. 1–5, May 2010.

[41] M. Agatonovic, E. Di Giampaolo, P. Tognolatti, and B. Milovanovic, "Artificial neural networks for ranging of passive UHF RFID tags," in *11th International Conference on Telecommunications in Modern Satellite, Cable and Broadcasting Services*, vol. 02, pp. 505–508, October 2013.

[42] M. Y. Chia, K. C. Ang, K. Chee, and S. Leong, "A smart beam steering RFID interrogator for passive tags in item level tagging applications," in *IEEE MTT-S International Microwave Symposium Digest*, pp. 575–578, June 2008.

[43] G. Hislop, D. Lekime, M. Drouguet, and C. Craeye, "A prototype 2D direction finding system with passive RFID tags," in *Fourth European Conference on Antennas and Propagation*, pp. 1–5, April 2010.

[44] J. Foutz, A. Spanias, and M. K. Banavar, *Narrowband Direction of Arrival Estimation for Antenna Arrays.* Morgan & Claypool Publishers, 2008.

[45] T. S. Dhope, "Application of MUSIC, ESPRIT and ROOT MUSIC in DOA estimation," *World Journal of Science and Technology*, vol. 8, pp. 20–25, August 2011.

[46] D. Arnitz, U. Muehlmann, and K. Witrisal, "Characterization and modeling of uhf rfid channels for ranging and localization," *IEEE Transactions on Antennas and Propagation*, vol. 60, pp. 2491–2501, May 2012.

[47] T. S. Rappaport and C. D. McGillem, "UHF fading in factories," *IEEE Journal on Selected Areas in Communications*, vol. 7, pp. 40–48, January 1989.

[48] H. Hashemi, D. Tholl, and G. Morrison, "Statistical modeling of the indoor radio propagation channel. I," in *Vehicular Technology Society 42nd VTS Conference*, pp. 338–342, May 1992.

[49] F. Saez de Adana, O. Gutierrez Blanco, I. Gonzalez Diego, J. Perez Arriaga, and M. Catedra, "Propagation model based on ray tracing for the design of personal communication systems in indoor environments," *IEEE Transactions on Vehicular Technology*, vol. 49, pp. 2105–2112, November 2000.

[50] P. V. Nikitin and K. V. S. Rao, "Antennas and propagation in UHF RFID systems," in *IEEE International Conference on RFID*, pp. 277–288, April 2008.

[51] B. Sklar, *Digital Communications: Fundamentals and Applications*. Pearson Education Limited, 2014.

[52] H. Hile and G. Borriello, "Positioning and orientation in indoor environments using camera phones," *IEEE Computer Graphics and Applications*, vol. 28, pp. 32–39, July 2008.

[53] A. Kitanov, S. Bisevac, and I. Petrovic, "Mobile robot self-localization in complex indoor environments using monocular vision and 3D model," in *IEEE/ASME international conference on advanced intelligent mechatronics*, pp. 1–6, September 2007.

[54] M. Muffert, J. Siegemund, and W. Forstner, "The estimation of spatial positions by using an omnidirectional camera system," in *International Conference on Machine Control & Guidance*, pp. 1–11, January 2010.

[55] K. Sjo, D. G. Lopez, C. Paul, P. Jensfelt, and D. Kragic, "Object search and localization for an indoor mobile robot," *Journal of Computing and Information Technology*, vol. 17, pp. 67–80, January 2009.

[56] J. Kim and H. Jun, "Vision-based location positioning using augmented reality for indoor navigation," *IEEE Transactions on Consumer Electronics*, vol. 54, pp. 954–962, August 2008.

[57] M. Köhler, S. N. Patel, J. Summet, E. Stuntebeck, and G. Abowd, "TrackSense: Infrastructure free precise indoor positioning using projected patterns," in *5th International Conference on Pervasive Computing*, pp. 334–350, May 2007.

[58] T. Inc., "Sky-trax system." Website, 2016. `http://www.totaltraxinc.com/smart-forklift-solutions/the-sky-trax-system/`.

[59] A. Mulloni, D. Wagner, I. Barakonyi, and D. Schmalstieg, "Indoor positioning and navigation with camera phones," *IEEE Pervasive Computing*, vol. 8, pp. 22–31, April 2009.

[60] C. Jekeli, *Inertial Navigation Systems with Geodetic Applications*. Walter de Gruyter, 2001.

[61] Z. Sun, X. Mao, W. Tian, and X. Zhang, "Activity classification and dead reckoning for pedestrian navigation with wearable sensors," *Measurement Science and Technology*, vol. 20, pp. 1–7, November 2009.

[62] V. R. Okan Yalak, Phillip Tomé, "Hybridization of MEMS and assisted GPS," *Inside GNSS*, vol. 2, pp. 34–42, January 2007.

[63] P. Kemppi, T. Rautiainen, V. Ranki, F. Belloni, and J. Pajunen, "Hybrid positioning system combining angle-based localization, pedestrian dead reckoning and map filtering," in *International Conference on Indoor Positioning and Indoor Navigation*, pp. 1–7, September 2010.

[64] C. Keßler, C. Ascher, M. Flad, and G. F. Trommer, "Multi-sensor indoor pedestrian navigation system with vision aiding," *Gyroscopy and Navigation*, vol. 3, pp. 79–90, April 2012.

[65] J. Seitz, T. Vaupel, S. Meyer, J. G. Boronat, and J. Thielecke, "A hidden markov model for pedestrian navigation," in *7th Workshop on Positioning, Navigation and Communication*, pp. 120–127, March 2010.

[66] Y. M. Shin, Seung Hyuck; Kim, Hyun Wook; Park, Chan Gook; Yoo, "Sit-down & stand-up awareness algorithm for the pedestrian dead reckoning," in *European Navigation Conference on Global Navigation Satellite Systems*, pp. 1–6, May 2009.

[67] W. Liu, C. Hu, Q. He, M. Q.-H. Meng, and L. Liu, "An hybrid localization system based on optics and magnetics," in *IEEE International Conference on Robotics and Biomimetics*, pp. 1165–1169, December 2010.

[68] S. Song, C. Hu, M. Li, W. Yang, and M. Q.-H. Meng, "Real time algorithm for magnet's localization in capsule endoscope," in *IEEE International Conference on Automation and Logistics*, pp. 2030–2035, August 2009.

[69] J. Blankenbach and A. Norrdine, "Position estimation using artificial generated magnetic fields," in *International Conference on Indoor Positioning and Indoor Navigation*, pp. 1–5, September 2010.

[70] K. Atsuumi and M. Sano, "Indoor IR azimuth sensor using a linear polarizer," in *International Conference on Indoor Positioning and Indoor Navigation*, pp. 1–5, September 2010.

[71] D. Hauschildt and N. Kirchhof, "Advances in thermal infrared localization: Challenges and solutions," in *International Conference on Indoor Positioning and Indoor Navigation*, pp. 1–8, September 2010.

[72] F. Boochs, R. Schutze, C. Simon, F. Marzani, H. Wirth, and J. Meier, "Increasing the accuracy of untaught robot positions by means of a multi-camera system," in *International Conference on Indoor Positioning and Indoor Navigation*, pp. 1–9, September 2010.

[73] S. Sooyong Lee and J.-B. Jae-Bok Song, "Mobile robot localization using infrared light reflecting landmarks," in *2007 International Conference on Control, Automation and Systems*, pp. 674–677, IEEE, 2007.

[74] R. Mautz and W. Y. Ochieng, "A robust indoor positioning and auto-localisation algorithm," *Journal of Global Positioning Systems*, vol. 01, pp. 38–46, June 2007.

[75] M. Alloulah and M. Hazas, "An efficient CDMA core for indoor acoustic position sensing," in *International Conference on Indoor Positioning and Indoor Navigation*, pp. 1–5, September 2010.

[76] H. Schweinzer and M. Syafrudin, "LOSNUS: An ultrasonic system enabling high accuracy and secure TDoA locating of numerous devices," in *International Conference on Indoor Positioning and Indoor Navigation*, pp. 1–8, September 2010.

[77] A. Jiménez, J. Prieto, J. Ealo, J. Guevara, and F. Seco, "A computerized system to determine the provenance of finds in archaeological sites using acoustic signals," *Journal of Archaeological Science*, vol. 36, pp. 2415–2426, October 2009.

[78] C. V. L. Atri Mandal, "Beep: 3d indoor positioning using audible sound," in *Second IEEE Consumer Communications and Networking Conference*, pp. 348–353, May 2005.

[79] F. S. T. van Diggelen, *A-GPS: Assisted GPS, GNSS, and SBAS*. Artech House, 2009.

[80] M. B. Kjærgaard, H. Blunck, T. Godsk, T. Toftkjær, D. L. Christensen, and K. Grønbæk, "Indoor positioning using GPS revisited," in *8th International Conference on Pervasive Computing*, pp. 38–56, May 2010.

[81] B. L. Jiahuang Zhang, A. G. Dempster, and C. Rizos, "Evaluation of high sensitivity GPS receivers," in *International Symposium on GPS/GNSS*, pp. 1–6, March 2010.

[82] C. Kee, H. Jun, and D. Yun, "Indoor navigation system using asynchronous pseudolites," *The Journal of Navigation*, vol. 56, pp. 443–455, August 2003.

[83] C. Rizos, G. Roberts, J. Barnes, and N. Gambale, "Experimental results of locata: A high accuracy indoor positioning system," in *International Conference on Indoor Positioning and Indoor Navigation*, pp. 1–7, September 2010.

[84] K. Muthukrishnan, G. Koprinkov, N. Meratnia, and M. Lijding, "Using time-of-flight for WLAN localization: feasibility study." Technical Report, August 2006.

[85] C. Wong, R. Klukas, and G. G. Messier, "Using WLAN infrastructure for angle-of-arrival indoor user location," in *IEEE 68th Vehicular Technology Conference*, pp. 1–5, September 2008.

[86] F. Tappero, B. Merminod, and M. Ciurana, "IEEE 802.11 ranging and multilateration for software-defined positioning receiver," in *International Conference on Indoor Positioning and Indoor Navigation*, pp. 1–6, September 2010.

[87] F. Yu, M. Jiang, J. Liang, X. Qin, M. Hu, T. Peng, and X. Hu, "Expansion RSS-based indoor localization using 5G WiFi signal," in *International Conference on Computational Intelligence and Communication Networks*, pp. 510–514, November 2014.

[88] B. Parodi, H. Lenz, A. Szabo, J. Horn, J. Bamberger, and D. Obradovic, "Initialization and online-learning of RSS maps for indoor / campus localization," in *IEEE/ION Position, Location, And Navigation Symposium*, pp. 164–172, April 2006.

[89] J.-G. Park, B. Charrow, D. Curtis, J. Battat, E. Minkov, J. Hicks, S. Teller, and J. Ledlie, "Growing an organic indoor location system," in *8th International Conference on Mobile Systems, Applications, and Services*, pp. 271–284, June 2010.

[90] R. Hansen, R. Wind, C. S. Jensen, and B. Thomsen, "Algorithmic strategies for adapting to environmental changes in 802.11 location fingerprinting," in *International Conference on Indoor Positioning and Indoor Navigation*, pp. 1–10, September 2010.

[91] S. Gansemer, U. Grossmann, and S. Hakobyan, "RSSI-based Euclidean Distance algorithm for indoor positioning adapted for the use in dynamically changing WLAN environments and multi-level buildings," in *International Conference on Indoor Positioning and Indoor Navigation*, pp. 1–6, September 2010.

[92] L. Koski, T. Perala, and R. Piche, "Indoor positioning using WLAN coverage area estimates," in *International Conference on Indoor Positioning and Indoor Navigation*, pp. 1–7, September 2010.

[93] A. Kushki, K. N. Plataniotis, and A. N. Venetsanopoulos, *WLAN Positioning Systems: Principles and Applications in Location-Based Services.* Cambridge University Press, 2012.

[94] T. King, S. Kopf, T. Haenselmann, C. Lubberger, and W. Effelsberg, "Compass: A probabilistic indoor positioning system based on 802.11 and digital compasses," in *1st International Workshop on Wireless Network Testbeds, Experimental Evaluation & Characterization*, pp. 34–40, January 2006.

[95] S. A. Golden and S. S. Bateman, "Sensor measurements for Wi-Fi location with emphasis on time-of-arrival ranging," *IEEE Transactions on Mobile Computing*, vol. 6, pp. 1185–1198, October 2007.

[96] M. Ciurana, D. López, and F. Barceló-Arroyo, "Softoa: software ranging for toa-based positioning of wlan terminals," in *Location and Context Awareness: 4th International Symposium*, pp. 207–221, May 2009.

[97] G. Fischer, O. Klymenko, D. Martynenko, and H. Luediger, "An impulse radio UWB transceiver with high-precision TOA measurement unit," in *International Conference on Indoor Positioning and Indoor Navigation*, pp. 1–8, IEEE, September 2010.

[98] M. M. Pietrzyk and T. von der Grun, "Experimental validation of a TOA UWB ranging platform with the energy detection receiver," in *International Conference on Indoor Positioning and Indoor Navigation*, pp. 1–8, September 2010.

[99] M. Segura, H. Hashemi, C. Sisterna, and V. Mut, "Experimental demonstration of self-localized ultra wideband indoor mobile robot navigation system," in *International Conference on Indoor Positioning and Indoor Navigation*, pp. 1–9, September 2010.

[100] H. Kroll and C. Steiner, "Indoor ultra-wideband location fingerprinting," in *International Conference on Indoor Positioning and Indoor Navigation*, pp. 1–5, September 2010.

[101] K. Hausmair, K. Witrisal, P. Meissner, C. Steiner, and G. Kail, "SAGE algorithm for UWB channel parameter estimation," in *COST 2100 Management Committee Meeting*, February 2010.

[102] A. Molisch, "Ultrawideband propagation channels-theory, measurement, and modeling," *IEEE Transactions on Vehicular Technology*, vol. 54, pp. 1528–1545, September 2005.

[103] R. Mautz, "Indoor positioning technologies." Habilitationsschrift, 2012. ETH Zürich.

[104] A. S.-I. Noh, W. J. Lee, and J. Y. Ye, "Comparison of the mechanisms of the zigbee's indoor localization algorithm," in *Ninth ACIS International Conference on Software Engineering, Artificial Intelligence, Networking, and Parallel/Distributed Computing*, pp. 13–18, June 2008.

[105] J. Tsuji, H. Kawamura, K. Suzuki, T. Ikeda, A. Sashima, and K. Kurumat, "Zigbee based indoor localization with particle filter estimation," in *IEEE International Conference on Systems, Man and Cybernetics*, pp. 1115–1120, October 2010.

[106] L. Aalto, N. Göthlin, J. Korhonen, and T. Ojala, "Bluetooth and WAP push based location-aware mobile advertising system," in *2nd International Conference on Mobile Systems, Applications, and Services*, pp. 49–58, June 2004.

[107] M. S. Bargh and R. de Groote, "Indoor localization based on response rate of bluetooth inquiries," in *First ACM international workshop on mobile entity localization and tracking in GPS-less environments*, pp. 49–54, May 2008.

[108] M. Kranz, C. Fischer, and A. Schmidt, "A comparative study of DECT and WLAN signals for indoor localization," in *IEEE International Conference on Pervasive Computing and Communications*, pp. 235–243, March 2010.

[109] M. Rabinowitz and J. Spilker, "A new positioning system using television synchronization signals," *IEEE Transactions on Broadcasting*, vol. 51, pp. 51–61, March 2005.

[110] V. Moghtadaiee, A. G. Dempster, and S. Lim, "Indoor localization using FM radio signals: A fingerprinting approach," in *International Conference on Indoor Positioning and Indoor Navigation*, pp. 1–7, September 2011.

[111] A. Varshavsky, E. De Lara, J. Hightower, A. LaMarca, and V. Otsason, "GSM indoor localization," *Pervasive and Mobile Computing*, vol. 3, pp. 698–720, December 2007.

[112] S. N. Patel, E. P. Stuntebeck, and T. Robertson, "Pl-tags: Detecting batteryless tags through the power lines in a building," in *7th International Conference on Pervasive Computing*, pp. 256–273, May 2009.

[113] E. P. Stuntebeck, S. N. Patel, T. Robertson, M. S. Reynolds, and G. D. Abowd, "Wideband powerline positioning for indoor localization," in *10th International Conference on Ubiquitous Computing*, pp. 94–103, September 2008.

[114] M. Valtonen, J. Maentausta, and J. Vanhala, "Tiletrack: Capacitive human tracking using floor tiles," in *IEEE International Conference on Pervasive Computing and Communications*, pp. 1–10, March 2009.

[115] B. Richardson, K. Leydon, M. Fernstrom, and J. A. Paradiso, "Z-tiles: Building blocks for modular, pressure-sensing floorspaces," in *Extended Abstracts on Human Factors in Computing Systems*, pp. 1529–1532, January 2004.

[116] X. Liu, H. Makino, S. Kobayashi, and Y. Maeda, "An indoor guidance system for the blind using fluorescent lights–relationship between receiving signal and walking speed.," *Annual International Conference of the IEEE Engineering in Medicine and Biology Society*, vol. 1, pp. 1–3, January 2006.

[117] G.-Y. Jin, X.-Y. Lu, and M.-S. Park, "An indoor localization mechanism using active RFID tag," in *IEEE International Conference on Sensor Networks, Ubiquitous, and Trustworthy Computing*, vol. 1, pp. 40–43, June 2006.

[118] Y. Zhao, Y. Liu, and L. M. Ni, "VIRE: Active RFID-based localization using virtual reference elimination," in *International Conference on Parallel Processing*, pp. 56–56, September 2007.

[119] X. Jiang, Y. Liu, and X. Wang, "An enhanced approach of indoor location sensing using active RFID," in *WASE International Conference on Information Engineering*, vol. 1, pp. 169–172, July 2009.

[120] R. de Amorim Silva and P. A. da S. Goncalves, "Enhancing the efficiency of active RFID-based indoor location systems," in *IEEE Wireless Communications and Networking Conference*, pp. 1–6, April 2009.

[121] W. Li, J. Wu, and D. Wang, "A novel indoor positioning method based on key reference RFID tags," in *IEEE Youth Conference on Information, Computing and Telecommunication*, pp. 42–45, September 2009.

[122] C.-S. Wang, C.-H. Huang, Y.-S. Chen, and L.-J. Zheng, "An implementation of positioning system in indoor environment based on active RFID," in *Joint Conferences on Pervasive Computing*, pp. 71–76, December 2009.

[123] F. Tlili, N. Hamdi, and A. Belghith, "Accurate 3D localization scheme based on active RFID tags for indoor environment," in *IEEE International Conference on RFID-Technologies and Applications*, pp. 378–382, November 2012.

[124] W. Shi and V. W. S. Wong, "MDS-based localization algorithm for RFID systems," in *IEEE International Conference on Communications*, pp. 1–6, June 2011.

[125] C. Hekimian-Williams, B. Grant, X. Liu, Z. Zhang, and P. Kumar, "Accurate localization of RFID tags using phase difference," in *IEEE International Conference on RFID*, pp. 89–96, April 2010.

[126] G. Retscher and Q. Fu, "Continuous indoor navigation with RFID and INS," in *IEEE/ION Position, Location and Navigation Symposium*, pp. 102–112, May 2010.

[127] C. Alippi, D. Cogliati, and G. Vanini, "A statistical approach to localize passive RFIDs," in *IEEE International Symposium on Circuits and Systems*, pp. 343–346, May 2006.

[128] W. Zhu, J. Cao, Y. Xu, L. Yang, and J. Kong, "Fault-tolerant RFID reader localization based on passive RFID tags," in *IEEE International Conference on Computer Communications*, pp. 2183–2191, March 2012.

[129] Y. Guo, X. Guo, and G. Wang, "Using RFID in localization for indoor navigation of mobile robots," in *IEEE International Conference on Mechatronics and Automation*, pp. 1892–1897, August 2012.

[130] J. Lee, Y. Park, D. Kim, M. Choi, T. Goh, and S.-W. Kim, "An efficient localization method using RFID tag floor localization and dead reckoning," in *International Conference on Control, Automation and Systems*, pp. 1452–1456, October 2012.

[131] S. Park and H. Lee, "Self-recognition of vehicle position using UHF passive RFID tags," *IEEE Transactions on Industrial Electronics*, vol. 60, pp. 226–234, January 2013.

[132] X. Liu, J. Peng, and T. Liu, "A novel indoor localization system based on passive RFID technology," in *International Conference on Electronic & Mechanical Engineering and Information Technology*, pp. 4285–4288, August 2011.

[133] T. Jingwangsa, S. Soonjun, and P. Cherntanomwong, "Comparison between innovative approaches of RFID based localization using fingerprinting techniques for outdoor and indoor environments," in *International Conference on Advanced Communication Technology*, pp. 1511–1515, May 2010.

[134] S. S. Saab and Z. S. Nakad, "A standalone RFID indoor positioning system using passive tags," *IEEE Transactions on Industrial Electronics*, vol. 58, pp. 1961–1970, July 2011.

[135] E. Di Giampaolo and F. Martinelli, "A passive UHF-RFID system for the localization of an indoor autonomous vehicle," *IEEE Transactions on Industrial Electronics*, vol. 59, pp. 3961–3970, October 2011.

[136] P. Z. Peebles, *Probability, Random Variables, and Random Signal Principles.* McGraw-Hill, 1987.

[137] K. Hassan, T. A. Rahman, M. R. Kamarudin, and F. Nor, "The mathematical relationship between maximum access delay and the r.m.s delay spread," in *The Seventh International Conference on Wireless and Mobile Communications*, pp. 18–23, June 2011.

[138] A. Lazaro, D. Girbau, and D. Salinas, "Radio link budgets for UHF RFID on multipath environments," *IEEE Transactions on Antennas and Propagation*, vol. 57, pp. 1241–1251, April 2009.

[139] M. Bouet and A. L. dos Santos, "RFID tags: Positioning principles and localization techniques," in *1st IFIP Wireless Days*, pp. 1–5, November 2008.

[140] Z. Zhang, *Antenna design for mobile devices.* IEEE Press, 2011.

[141] A. Loeffler, U. Wissendheit, H. Gerhaeuser, and D. Kuznetsova, "A multi-purpose RFID reader supporting indoor navigation systems," in *IEEE International Conference on RFID-Technology and Applications*, pp. 43–48, June 2010.

[142] T. Shiraishi, N. Komuro, H. Ueda, H. Kasai, and T. Tsuboi, "Indoor location estimation technique using UHF band RFID," in *International Conference on Information Networking*, pp. 1–5, January 2008.

[143] N. Pathanawongthum and P. Chemtanomwong, "RFID based localization techniques for indoor environment," in *International Conference on Advanced Communication Technology*, pp. 1418–1421, February 2010.

[144] Y. Park, J. W. Lee, D. Kim, and S.-w. Kim, "Model-based iterative position estimation algorithm for RFID tag floor localization," in *IEEE International Midwest Symposium on Circuits and Systems*, pp. 1–4, August 2011.

[145] Z. Zhang, Z. Lu, V. Saakian, X. Qin, and Q. Chen, "Item-level indoor localization with passive UHF RFID based on tag interaction analysis," *IEEE Transactions on Industrial Electronics*, vol. 61, pp. 2122–2135, May 2014.

[146] S. Soonjun, D. Boontri, and P. Cherntanomwong, "A novel approach of RFID based indoor localization using fingerprinting techniques," in *15th Asia-Pacific Conference on Communications*, pp. 475–478, October 2009.

[147] E. Di Giampaolo, "A passive-RFID based indoor navigation system for visually impaired people," in *International Symposium on Applied Sciences in Biomedical and Communication Technologies*, pp. 1–5, November 2010.

[148] H. Malla, P. Purushothaman, S. V. Rajan, and V. Balasubramanian, "Object level mapping of an indoor environment using RFID," in *International Conference on Ubiquitous Positioning, Indoor Navigation and Location Based Service*, pp. 203–212, November 2014.

[149] R. C. Luo, C.-T. Chuang, and S.-S. Huang, "RFID-based indoor antenna localization system using passive tag and variable RF-attenuation," in *33rd Annual Conference of the IEEE Industrial Electronics Society*, pp. 2254–2259, November 2007.

[150] D. Boontrai, T. Jingwangsa, and P. Cherntanomwong, "Indoor localization technique using passive RFID tags," in *9th International Symposium on Communications and Information Technology*, pp. 922–926, September 2009.

[151] J. Zhou, H. Zhang, and L. Mo, "Two-dimension localization of passive RFID tags using AoA estimation," in *IEEE International Instrumentation and Measurement Technology Conference*, pp. 1–5, May 2011.

[152] M. Y. Ahmad and A. S. Mohan, "RFID reader localization using passive RFID tags," in *Asia Pacific Microwave Conference*, pp. 606–609, December 2009.

[153] S. K. Tan and Z. Fan, "Performance study of RFID localisation in a challenging indoor environment," in *IEEE International Conference on Dependable, Autonomic and Secure Computing*, pp. 311–316, December 2009.

[154] Z. Babic, M. Ljubojevic, and V. Risojevic, "Indoor RFID localization improved by motion segmentation," in *International Symposium on Image and Signal Processing and Analysis*, pp. 271–276, September 2011.

[155] S. Gong, H. Liu, Y. Hu, J. Zhang, and H. Kong, "ROS-based object localization using RFID and laser," in *IEEE International Conference on Information and Automation*, pp. 406–411, June 2012.

[156] H. Wang, G. Bauer, F. Kirsch, and M. Vossiek, "Hybrid RFID system-based pedestrian localization: A case study," in *Workshop on Positioning, Navigation and Communication*, pp. 1–6, March 2013.

[157] A. Papapostolou and H. Chaouchi, "Simulation-based analysis for a heterogeneous indoor localization scheme," in *7th IEEE Consumer Communications and Networking Conference*, pp. 1–5, January 2010.

[158] S. P. Subramanian, J. Sommer, S. Schmitt, and W. Rosenstiel, "INR indoor navigator with RFID locator," in *Third International Conference on Next Generation Mobile Applications, Services and Technologies*, pp. 176–181, September 2009.

[159] E. Di Giampaolo and F. Martinelli, "Robot localization by sparse and passive RFID tags," *IEEE International Symposium on Industrial Electronics*, pp. 1937–1942, July 2010.

[160] V. P. Munishwar, S. Singh, C. Mitchell, K. Gopalan, and N. B. Abu-Ghazaleh, "On the accuracy of RFID-based localization in a mobile wireless network testbed," in *IEEE International Conference on Pervasive Computing and Communications*, pp. 1–6, March 2009.

[161] F. Manzoor, Y. Huang, and K. Menzel, "Passive RFID-based indoor positioning system, an algorithmic approach," in *IEEE International Conference on RFID-Technology and Applications*, pp. 112–117, June 2010.

[162] F. Manzoor and K. Menzel, "Indoor localisation for complex building designs using passive RFID technology," in *General Assembly and Scientific Symposium*, pp. 1–4, August 2011.

[163] L. Ni, D. Zhang, and M. Souryal, "RFID-based localization and tracking technologies," *IEEE Wireless Communications*, vol. 18, pp. 45–51, April 2011.

[164] X. Zheng, H. Liu, J. Yang, Y. Chen, J.-A. Francisco, R. P. Martin, and X. Li, "Characterizing the impact of multi-frequency and multi-power on localization accuracy," in *IEEE International Conference on Mobile Ad-hoc and Sensor Systems*, pp. 156–165, November 2010.

[165] S. Shao and R. J. Burkholder, "Passive UHF RFID tag localization using reader antenna spatial diversity," in *IEEE International Conference on Wireless Information Technology and Systems*, pp. 1–4, November 2012.

[166] J. Brchan, L. Zhao, J. Wu, R. Williams, and L. Perez, "A real-time RFID localization experiment using propagation models," in *IEEE International Conference on RFID*, pp. 141–148, April 2012.

[167] T. Nick, M. Z. I. Khan, J. Gotze, and W. John, "Localization of passive UHF RFID label with Unscented Kalman Filter based on angle-dependent RSSI measurements," in *5th International Conference on Signal Processing and Communication Systems*, pp. 1–7, December 2011.

[168] T. Nick, J. Gotze, and W. John, "Fuzzy-adaptive Kalman filter for RFID localization," in *International Conference on Ubiquitous Positioning, Indoor Navigation, and Location Based Service*, October 2012.

[169] J.-M. Akre, X. Zhang, S. Baey, B. Kervella, A. Fladenmuller, M. Zancanaro, and M. Fonseca, "Accurate 2-D localization of RFID tags using antenna transmission power control," in *IFIP Wireless Days*, pp. 1–6, November 2014.

[170] J. Choi, H. Lee, D. W. Engels, and R. Elmasri, "Passive UHF RFID-based localization using detection of tag interference on smart shelf," *IEEE Transactions on Systems, Man, and Cybernetics, Part C: Applications and Reviews*, vol. 42, pp. 268–275, March 2011.

[171] D. Fortin-Simard, K. Bouchard, S. Gaboury, B. Bouchard, and A. Bouzouane, "Accurate passive RFID localization system for smart homes," in *IEEE 3rd International Conference on Networked Embedded Systems for Every Application*, pp. 1–8, December 2012.

[172] J. Vongkulbhisal, "An RFID-based indoor localization system using antenna beam scanning," in *International Conference on Electrical Engineering/Electronics, Computer, Telecommunications and Information Technology*, pp. 1–4, May 2012.

[173] Y. Liu and Y. Qiu, "An indoor localization of UHF RFID using a hybrid approach," in *International Conference on Consumer Electronics, Communications and Networks*, pp. 1653–1656, April 2012.

[174] T. Wada, N. Uchitomi, Y. Ota, T. Hori, K. Mutsuura, and H. Okada, "A novel scheme for spatial localization of passive RFID Tags; Communication Range Recognition (CRR) scheme," in *IEEE International Conference on Communications*, pp. 1–6, June 2009.

[175] X. Zhang, J. Peng, and X. Cao, "RFID indoor localization algorithm based on dynamic netting," *International Conference on Computational and Information Sciences*, pp. 428–431, December 2010.

[176] F. Schwiegelshohn, T. Nick, and J. Gotze, "Localization based on fusion of RFID and stereo image data," in *Workshop on Positioning, Navigation and Communication*, pp. 1–6, March 2013.

[177] C. Men, L. Mao, and L. Wu, "The research of RFID localization technology based on bi-directional RSSI," in *International Conference on Wireless Communications, Networking and Mobile Computing*, pp. 1–4, September 2012.

[178] M. Elsayeh, M. Haroon, B. Tawfik, and S. Fahmy, "RFID-based indoors localization of tag-less objects," *5th Cairo International Biomedical Engineering Conference*, pp. 61–65, December 2010.

[179] J. S. Choi, B. R. Son, H. K. Kang, and D. H. Lee, "Indoor localization of unmanned aerial vehicle based on passive UHF RFID systems," in *International Conference on Ubiquitous Robots and Ambient Intelligence*, pp. 188–189, November 2012.

[180] B. Wagner, D. Timmermann, G. Ruscher, and T. Kirste, "Device-free user localization utilizing artificial neural networks and passive RFID," in *International Conference on Ubiquitous Positioning, Indoor Navigation, and Location Based Service*, pp. 1–7, October 2012.

[181] A. Parr, R. Miesen, F. Kirsch, and M. Vossiek, "A novel method for UHF RFID tag tracking based on acceleration data," in *IEEE International Conference on RFID*, pp. 110–115, April 2012.

[182] E. DiGiampaolo and F. Martinelli, "Mobile robot localization using the phase of passive UHF RFID signals," *IEEE Transactions on Industrial Electronics*, vol. 61, pp. 365–376, January 2014.

[183] F. Martinelli, "A robot localization system combining RSSI and phase shift in UHF-RFID signals," *IEEE Transactions on Control Systems Technology*, vol. 23, pp. 1782–1796, September 2015.

[184] F. Lombardini, F. Viviani, P. Nepa, and A. Buffi, "Robust coherent localization of moving UHF-RFID tags by a SAR-like approach," in *10th European Conference on Synthetic Aperture Radar*, pp. 1–4, June 2014.

[185] A. Buffi, P. Nepa, and F. Lombardini, "A phase-based technique for localization of UHF-RFID tags moving on a conveyor belt: Performance analysis and test-case measurements," *IEEE Sensors Journal*, vol. 15, pp. 387–396, January 2015.

[186] J. Wang, Y. Ma, Y. Zhao, and K. Liu, "A multipath mitigation localization algorithm based on MDS for passive UHF RFID," *IEEE Communications Letters*, vol. 19, pp. 1652–1655, September 2015.

[187] M. Scherhaufl, M. Pichler, and A. Stelzer, "UHF RFID localization based on phase evaluation of passive tag arrays," *IEEE Transactions on Instrumentation and Measurement*, vol. 64, pp. 913–922, April 2015.

[188] M. Scherhaufl, M. Pichler, and A. Stelzer, "Robust localization of passive UHF RFID tag arrays based on phase-difference-of-arrival evaluation," in *IEEE Topical Conference on Wireless Sensors and Sensor Networks*, pp. 47–49, January 2015.

[189] M. Scherhaufl, M. Pichler, and A. Stelzer, "UHF RFID localization based on evaluation of backscattered tag signals," *IEEE Transactions on Instrumentation and Measurement*, vol. 64, pp. 2889–2899, November 2015.

[190] P. V. Nikitin, R. Martinez, S. Ramamurthy, H. Leland, G. Spiess, and K. V. S. Rao, "Phase based spatial identification of UHF RFID tags," in *IEEE International Conference on RFID*, pp. 102–109, April 2010.

[191] A. Povalac and J. Sebesta, "Phase difference of arrival distance estimation for RFID tags in frequency domain," in *IEEE International Conference on RFID-Technologies and Applications*, pp. 188–193, September 2011.

[192] A. Wille, M. Broll, and S. Winter, "Phase difference based RFID navigation for medical applications," in *IEEE International Conference on RFID*, pp. 98–105, April 2011.

[193] M. Abbak and I. Tekin, "RFID coverage extension using microstrip-patch antenna array," *IEEE Antennas and Propagation Magazine*, vol. 51, pp. 185–191, February 2009.

[194] S. Balon, J. A. Buyco, and J. J. Marciano, "Sectorization of UHF RFID tags using a steerable phased antenna array," in *IEEE Student Conference on Research and Development*, pp. 16–20, December 2010.

[195] M. Del Prete, D. Masotti, N. Arbizzani, and A. Costanzo, "A flag-shaped printed dipole array for ambient scanning," in *IEEE International Conference on RFID-Technologies and Applications*, pp. 244–247, November 2012.

[196] Y. Zhang, M. G. Amin, and S. Kaushik, "Localization and tracking of passive RFID tags based on direction estimation," *International Journal of Antennas and Propagation*, vol. 2007, October 2007.

[197] M. J. Abedin and A. S. Mohan, "RFID localization using planar antenna arrays with arbitrary geometry," *Asia-Pacific Microwave Conference*, pp. 1–4, December 2008.

[198] M. J. Abedin and A. S. Mohan, "Use of smart antennas for the localization of RFID reader," in *Asia Pacific Microwave Conference*, pp. 1036–1039, December 2009.

[199] A. Paulraj, V. Reddy, T. Shan, and T. Kailath, "Performance analysis of the music algorithm with spatial smoothing in the presence of coherent sources," in *IEEE Military Communications Conference*, vol. 3, pp. 41.5.1–41.5.5, IEEE, October 1986.

[200] H. L. van Trees, *Optimum Array Processing: Detection, Estimation and Modulation Theory*. Wiley, 2002.

[201] A. Bouzakis and L. Overmeyer, "RFID tag positioning with the aid of an active electronically-steered array," in *IEEE 23rd International Symposium on Personal, Indoor and Mobile Radio Communications*, pp. 2483–2488, September 2012.

[202] P. Salomen, M. Keskilammi, L. Syddnheimo, and M. Kivikoski, "An intelligent 2.45 GHz multidimensional beam-scanning X-array for modern RFID reader," in *IEEE Antennas and Propagation Society International Symposium*, vol. 1, pp. 190–193, July 2000.

[203] J.-D. Tseng, R.-J. Ko, and W.-D. Wang, "Switched beam antenna array for UHF band RFID system," in *International Workshop on Anti-Counterfeiting, Security and Identification*, pp. 92–95, April 2007.

[204] N. C. Karmakar, P. Zakavi, and M. Kumbukage, "Development of a phased array antenna for universal UHF RFID reader," in *IEEE Antennas and Propagation Society International Symposium*, pp. 1–4, July 2010.

[205] T.-J. Huang, P.-H. Pan, and H.-T. Hsu, "Adaptive beam steering smart antenna system for ultra-high-frequency radio frequency identification applications," in *International Symposium on Computer, Consumer and Control*, pp. 713–716, June 2012.

[206] L. Weisgerber and A. Popugaev, "Multibeam antenna array for rfid applications," in *European Microwave Conference*, pp. 84–87, October 2013.

[207] M. Ould-Elhassen, M. Mabrouk, A. Ghazel, and P. Benech, "Improved coverage of phased array antennas used for RFID applications," in *IEEE International Symposium on Phased Array Systems and Technology*, pp. 553–558, October 2013.

[208] F. E. Fakoukakis, K. A. Gotsis, G. A. Kyriacou, and J. N. Sahalos, "Beam steering for RFID readers with inherent antenna diversity," in *8th European Conference on Antennas and Propagation*, pp. 2210–2214, April 2014.

[209] Q. Liu, V. Fusco, D. Linton, and D. Zelenchuk, "Frequency scanning antenna for target location applications," in *8th European Conference on Antennas and Propagation*, pp. 2059–2061, April 2014.

[210] P. N. Hsi-Tseng Chou, Chien-Te Yu, Kai-Te Wang, "A simple design of patch antenna array with an optimized field distribution in the near-zone for RFID applications," *IEEE Antennas and Wireless Propagation Letters*, vol. 13, pp. 257–260, February 2014.

[211] H.-T. Chou, M.-Y. Lee, and C.-T. Yu, "Subsystem of phased array antennas with adaptive beam steering in the near-field RFID applications," *IEEE Antennas and Wireless Propagation Letters*, vol. 14, pp. 1746–1749, April 2015.

[212] W.-S. Lee, H.-S. Tae, and J.-W. Yu, "Quadruple-feed beam-controlled antenna array for the localisations of ultra-high-frequency radio-frequency identification tags," *IET Microwaves, Antennas & Propagation*, vol. 9, pp. 923–932, June 2015.

[213] B. Wardrop, "Digital beamforming and adaptive techniques," in *IEEE Tutorial Meeting on Phased Array Radar*, pp. 1–29, October 1989.

[214] H. Krim and M. Viberg, "Two decades of array signal processing research: the parametric approach," *IEEE Signal Processing Magazine*, vol. 13, pp. 67–94, July 1996.

[215] M. S. Bartlett, "Smoothing periodograms from time-series with continuous spectra," *Nature*, vol. 161, pp. 686–687, May 1948.

[216] J. Capon, "High-resolution frequency-wavenumber spectrum analysis," *Proceedings of the IEEE*, vol. 57, pp. 1408–1418, August 1969.

[217] A. Barabell, "Improving the resolution performance of eigenstructure-based direction-finding algorithms," in *IEEE International Conference on Acoustics, Speech, and Signal Processing*, vol. 8, pp. 336–339, April 1983.

[218] R. Roy and T. Kailath, "ESPRIT-estimation of signal parameters via rotational invariance techniques," *IEEE Transactions on Acoustics, Speech, and Signal Processing*, vol. 37, pp. 984–995, July 1989.

[219] V. Krishnaveni, T. Kesavamurthy, and A. B, "Beamforming for direction-of-arrival (doa) estimation-a survey," *International Journal of Computer Applications*, vol. 61, pp. 4–11, January 2013.

[220] J. Xiong and K. Jamieson, "ArrayTrack: A fine-grained indoor location system," in *10th USENIX Symposium on Networked Systems Design and Implementation*, pp. 71–84, May 2013.

[221] B. Van Veen and K. Buckley, "Beamforming: a versatile approach to spatial filtering," *IEEE ASSP Magazine*, vol. 5, pp. 4–24, April 1988.

[222] S. N. Bhuiya, F. Islam, and M. A. Matin, "Analysis of direction of arrival techniques using uniform linear array," *International Journal of Computer Theory & Engineering*, vol. 4, pp. 931–934, January 2012.

[223] C.-L. Chang, C.-H. Wu, and C.-H. Tseng, "A miniaturized electronic beam-scanning phased-array antenna for radio-frequency identification (RFID) applications," in *International Workshop on Anti-Counterfeiting, Security and Identification*, pp. 1–4, August 2012.

[224] A. A. M. Saleh and R. Valenzuela, "A statistical model for indoor multipath propagation," *IEEE Journal on Selected Areas in Communications*, vol. 5, pp. 128–137, February 1987.

[225] R. Bultitude, "Measurement, characterization and modeling of indoor 800/900 MHz radio channels for digital communications," *IEEE Communications Magazine*, vol. 25, pp. 5–12, June 1987.

[226] A. Affandi, G. El Zein, and J. Citerne, "Investigation on frequency dependence of indoor radio propagation parameters," in *IEEE VTS 50th Vehicular Technology Conference*, vol. 4, pp. 1988–1992, September 1999.

[227] D. Wong and D. Cox, "Estimating local mean signal power level in a Rayleigh fading environment," *IEEE Transactions on Vehicular Technology*, vol. 48, pp. 956–959, May 1999.

[228] D. Kim, M. A. Ingram, and W. W. Smith, "Small-scale fading for an indoor wireless channel with modulated backscatter," in *IEEE VTS 54th Vehicular Technology Conference*, vol. 3, pp. 1616–1620, October 2001.

[229] D. Kim, M. A. Ingram, and J. Smith W.W., "Measurements of small-scale fading and path loss for long range RF tags," *IEEE Transactions on Antennas and Propagation*, vol. 51, pp. 1740–1749, August 2003.

[230] W. Su, K. M. Beilke, and T. T. Ha, "A reliability study of RFID technology in a fading channel," in *Forty-First Asilomar Conference on Signals, Systems and Computers*, pp. 2124–2127, November 2007.

[231] S. E. Alexander, "Radio propagation within buildings at 900 MHz," *Electronics Letters*, vol. 18, pp. 913–914, October 1982.

[232] R. Krigslund, P. Popovski, G. F. Pedersen, and K. Olesen, "Interference helps to equalize the read range and reduce false positives of passive RFID tags," *IEEE Transactions on Industrial Electronics*, vol. 59, pp. 4821–4830, December 2012.

[233] H. Hashemi, D. Lee, and D. Ehman, "Statistical modeling of the indoor radio propagation channel. II," in *Vehicular Technology Society 42nd VTS Conference*, pp. 839–843, May 1992.

[234] W. Tam and V. Tran, "Propagation modelling for indoor wireless communication," *Electronics & Communications Engineering Journal*, vol. 7, pp. 913–914, October 1995.

[235] S. Banerjee, R. Jesme, and R. Sainati, "Performance analysis of short range UHF propagation as applicable to passive RFID," in *IEEE International Conference on RFID*, pp. 30–36, March 2007.

[236] T.-I. Kvaksrud, "Range measurements in an open field environment." TI Design Note, 2008. `http://www.ti.com/lit/an/swra169a/swra169a.pdf`.

[237] G. Marrocco, E. Di Giampaolo, and R. Aliberti, "Estimation of UHF RFID reading regions in real environments," *IEEE Antennas and Propagation Magazine*, vol. 51, pp. 44–57, December 2009.

[238] S. Seidel and T. Rappaport, "Site-specific propagation prediction for wireless in-building personal communication system design," *IEEE Transactions on Vehicular Technology*, vol. 43, pp. 879–891, November 1994.

[239] P. Bosselmann and B. Rembold, "Planning and analysis of UHF RFID systems for consumer goods logistics using ray tracing predictions," in *RFID Eurasia*, pp. 1–7, September 2007.

[240] J. Tarng, W. Chang, and B. Hsu, "Three-dimensional modeling of 900-MHz and 2.44-GHz radio propagation in corridors," *IEEE Transactions on Vehicular Technology*, vol. 46, pp. 519–527, May 1997.

[241] K. A. Remley, H. R. Anderson, and A. Weisshar, "Improving the accuracy of ray-tracing techniques for indoor propagation modeling," *IEEE Transactions on Vehicular Technology*, vol. 49, pp. 2350–2358, November 2000.

[242] Y. Gao, Z. Zhang, H. Lu, and H. Wang, "Calculation of read distance in passive backscatter RFID systems and application," *Journal of System and Management Sciences*, vol. 2, pp. 40–49, May 2012.

[243] J. Griffin and G. Durgin, "Complete link budgets for backscatter-radio and RFID systems," *IEEE Antennas and Propagation Magazine*, vol. 51, pp. 11–25, April 2009.

[244] K. W. Kark, *Antennen und Strahlungsfelder*. Vieweg+Teubner Verlag, 2 ed., 2006.

[245] N. Najibi and S. Jin, "Physical reflectivity and polarization characteristics for snow and ice-covered surfaces interacting with gps signals," *Remote Sensing*, vol. 5, pp. 4006–4030, May 2013.

[246] T. A. Milligan, *Modern Antenna Design*. John Wiley & Sons, 2 ed., 2005.

[247] R. Chakraborty, S. Roy, and V. Jandhyala, "Revisiting RFID link budgets for technology scaling: Range maximization of RFID tags," *IEEE Transactions on Microwave Theory and Techniques*, vol. 59, pp. 496–503, February 2011.

[248] Z. Fan, S. Qiao, H.-F. Jiang Tao, and L.-X. Ran, "Signal descriptions and formulations for long range UHF RFID readers," *Progress In Electromagnetics Research*, vol. 71, pp. 109–127, October 2007.

[249] Naval Air Warfare Center Weapons Division, *Electronic Warfare and Radar Systems - Engineering Handbook*. S. O'Neil, 4 ed., 2013.

[250] J. M. Kim and Younggyun, "Antenna Diversity Strengthens Wireless LANs," *Communication Systems Design*, pp. 15–22, January 2003.

[251] M. Rahnema, *UMTS Network Planning, Optimization, and Inter-Operation with GSM*. John Wiley & Sons, 2008.

[252] D. Brennan, "Linear Diversity Combining Techniques," *Proceedings of the IRE*, vol. 47, pp. 1075–1102, June 1959.

[253] J. D. Gibson, *Mobile Communications Handbook, Third Edition*. CRC Press, 2012.

[254] ETSI, "Electromagnetic compatibility and radio spectrum matters (ERM); Methods, parameters and test procedures for cognitive interference mitigation towards ER-GSM for use by UHF RFID using Detect-And-Avoid (DAA) or other similar techniques," tech. rep., ETSI, August 2013.

[255] C. Balanis and P. Ioannides, *Introduction to Smart Antennas*. Morgan & Claypool Publishers, 2007.

[256] D. Pozar, "Microstrip antennas," *Proceedings of the IEEE*, vol. 80, pp. 79–91, August 1992.

[257] R. Garg, *Microstrip Antenna Design Handbook*. Artech House, 2001.

[258] K. F. Warnick, "Antennas and Propagation for Wireless Communications," tech. rep., BYU Electrical & Computer Engineering, 2015.

[259] L. Catarinucci, D. De Donno, M. Guadalupi, F. Ricciato, and L. Tarricone, "Performance analysis of passive UHF RFID tags with GNU-Radio," in *IEEE International Symposium on Antennas and Propagation*, pp. 541–544, July 2011.

[260] Y.-P. Luh and Y.-C. Liu, "Measurement of effective reading distance of UHF RFID passive tags," *Modern Mechanical Engineering*, vol. 03, pp. 115–120, August 2013.

[261] R. Schmidt, "Multiple emitter location and signal parameter estimation," *IEEE Transactions on Antennas and Propagation*, vol. 34, pp. 276–280, March 1986.

[262] H. Xu, B. Li, S. Xu, and H. Feng, "The measurement of dielectric constant of the concrete using single-frequency CW radar," *First International Conference on Intelligent Networks and Intelligent Systems*, pp. 588–591, November 2008.

[263] NXP, "SL3ICS1002/2303 UCODE G2XM and G2XL." Datasheet, 2013.